

**UC Davis**

**UC Davis Electronic Theses and Dissertations**

**Title**

High-speed Exercise and Fetlock Kinematics Affect the Development of Stress-Reactions in Racehorse Proximal Sesamoid Bones

**Permalink**

<https://escholarship.org/uc/item/8dx9b2d2>

**Author**

Shaffer, Sarah Kinsey

**Publication Date**

2021

Peer reviewed|Thesis/dissertation

High-speed Exercise and Fetlock Kinematics Affect the Development of Stress-Reactions in  
Racehorse Proximal Sesamoid Bones

By

SARAH KINSEY SHAFFER  
DISSERTATION

Submitted in partial satisfaction of the requirements for the degree of

DOCTOR OF PHILOSOPHY

in

Mechanical Engineering

in the

OFFICE OF GRADUATE STUDIES

of the

UNIVERSITY OF CALIFORNIA

DAVIS

Approved:

---

David P. Fyhrie, Chair

---

Susan M. Stover

---

Michael R. Hill

Committee in Charge

2021

## **Acknowledgements**

I would like to thank all the individuals in the J.D. Wheat Veterinary Orthopedic Research Laboratory at UC Davis who made my time in graduate school enjoyable. Importantly, I want to thank Sue Stover and Dave Fyhrie. I could not have hoped for better mentors and have learned so much from you over the years. I am so lucky to have been able to work on this project with both of you. You made this work both interesting and fun – whether I was counting microcracks or backcountry skiing. Also, I want to thank Tanya Garcia, our laboratory manager, for patiently training me on lab protocols and helping me with technical difficulties over the years.

Finally, I would like to thank my parents, Dan and Sharon, who have always encouraged and supported me. Without you two, I would never have developed my love of learning or animals. In high-school you encouraged me to try robotics and I was hooked on engineering. In undergrad, you encouraged me to take Beau, my horse, to compete for and win a world title in reining. When I told you two I needed to move across the country to pursue a PhD that would combine engineering and horses, you helped me pack up my truck, dog, and horse. So thank you, without you two, I would never have made it this far.

## Abstract

Stress-fractures of bone are similar to fatigue fractures in engineering materials as both are caused by microdamage accumulation under repetitive loading. However, stress-fractures have a biologic component, since bone tissue is capable of repairing damage and/or adding mass in response to damaging loading. The cellular damage repair processes cause transient porosities to develop in bone tissue, which temporarily reduce modulus and increase the damage accumulation rate if damaging loading is continued. Consequently, the stress fracture process is an interaction between bone's mechanical response to high-levels of loading (damage accumulation), and the biological responses of repair and hypertrophy that change tissue modulus.

This work focuses on stress-reactions, bone tissue changes that precede a stress-fracture, in athletes. Specifically, racehorse proximal sesamoid bone (PSB) fracture is used as a naturally occurring model of an osteochondral stress fracture. The PSBs are a pair of bones in the metacarpophalangeal (fetlock) joint of the distal forelimb and PSB fracture is one of the most common fatal musculoskeletal injuries associated with race training. In this work, morphologic tissue properties between PSB from racehorses with (Case) and without (Control) a unilateral biaxial PSB are compared. Both Case and Control horses were in race-training at the time of death and their training histories were known. The observed tissue properties are related to exercise. In addition, a compartment model of bone's turnover cycle is introduced and used to explain the associations among morphologic variables and exercise. The collected morphologic data is used to solve for the model's steady-state rate constants. Finally, the relationship between PSB kinematics and how PSB motion may impact PSB fracture risk is explored.

Our primary finding was that horses in higher intensity training develop a subchondral stress-reaction (lesion). A subchondral bone lesion was consistently found in the abaxial aspect of medial PSB from both Case fractured and Case intact contralateral PSB. This lesion was not found in Control PSBs.



The lesion was characterized by low bone volume fraction, low tissue mineral density, and higher microdamage compared to surrounding tissue. The bilaterality of this lesion in Case horses coupled with the observed tissue properties make the lesion consistent with stress-reactions in subchondral tissue that develop before a complete stress-fracture. Within the subchondral lesion, bone volume fraction was negatively associated with exercise intensity and microcrack areal density was positively associated with exercise intensity. These findings imply the lesion was more severe in horses with more intense training. Generally, Controls had a less intense training program compared to Cases. Additionally, the bone volume fraction was higher in the internal trabecular bone of Case proximal sesamoid bones compared to Controls. At this internal site, microdamage was not observed and bone volume fraction increased with exercise intensity. Steady-state model rate constants were determined based on the observed morphologic tissue properties at these two locations. Modeling results suggest that the different relationships between exercise and tissue properties within the subchondral and internal sites will occur if model rate constants depend on exercise intensity in a location-specific manner. We hypothesize that the different relationships are due to a strain difference between the two regions that causes a damage-repair response in the subchondral region and an adaptive-response in the internal region. In vitro axial limb loading indicated that the PSBs may experience an articular incongruity at high-speed gallop loads. Further, kinematic analysis indicated that the medial PSB experienced external rotation at high-speed gallop loads, which may cause the stress-reaction to form on the abaxial surface of the medial PSB.

The presented work is clinically relevant because the identified abaxial subchondral site can be examined for a lesion in vivo to test whether a horse has or is developing a stress reaction that puts it at risk of fracture. Also, the lesion was found to develop 1- 8 months after an increase in exercise intensity, making this time-frame an important period for clinical examinations. Finally, the calibrated compartment model could be incorporated into a predictive dynamic simulation to predict the effects of exercise on PSB morphology and lesion development.

## Table of Contents

List of Figures .....	ix
List of Tables .....	xii
List of Equations.....	xv
Chapter 1: Introduction .....	1
1.1 Motivation and Research Aims .....	1
1.2 Bone Structure and Function .....	2
1.2.1 Bone as a Composite Material .....	4
1.2.2 Bone Cell Types .....	5
1.3 Bone Modeling and Remodeling .....	6
1.3.1 Bone’s Response to Damage .....	8
1.3.2 Bone’s Response to Mechanical Loads .....	10
1.3.3 Stress Fractures .....	11
1.4 Finite Element Methods (FEM) for Modeling Bone .....	13
1.4.1 Symmetry Assumptions.....	13
1.4.2 Homogeneity Assumptions .....	15
1.4.3 Material Evolution Equations .....	16
1.5 Racehorse Anatomy and Musculoskeletal Injuries .....	18
1.5.1 The Equine Fetlock Joint: Anatomy and Function .....	19
1.5.2 Fetlock Joint Kinematics .....	21
1.5.3 Proximal Sesamoid Bones Fracture Characteristics .....	22
1.5.4 Stress Fractures in Racehorses.....	23
1.5.5 Prediction & Prevention of Proximal Sesamoid Bone Fractures.....	24
1.6 Research Aims & Hypothesis.....	25
1.7 References.....	27
Chapter 2: Subchondral Focal Osteopenia Associated with Proximal Sesamoid Bone Fracture in Thoroughbred Racehorses.....	37
2.1 Abstract .....	37
2.2 Introduction.....	38
2.3 Materials and Methods .....	39
2.3.1 Study 1 – Morphologic study.....	40
2.3.2 Study 2 – Tissue morphometric study.....	42
2.4 Results .....	44

2.4.1	Study 1 – Morphological findings.....	45
2.4.2	Study 2 – Tissue morphometric findings.....	53
2.5	Discussion.....	54
2.6	Manufacturer’s Addresses.....	60
2.7	Supplementary Information A: Selection of Study Horses.....	61
2.8	Supplementary Information B: Qualitative Variable Definition and Classification Levels.....	63
2.9	References.....	71
Chapter 3: Exercise History Predicts Focal Differences in Bone Volume Fraction, Mineral Density, and Microdamage in the Proximal Sesamoid Bones of Thoroughbred Racehorses.....		
3.1	Abstract.....	74
3.2	Introduction.....	75
3.3	Materials & Methods.....	77
3.3.1	Subject specific exercise history.....	77
3.3.2	Specimen preparation.....	78
3.3.3	Densitometric Assessment.....	78
3.3.4	Microdamage Quantification.....	79
3.3.5	Statistical Analysis.....	81
3.4	Results.....	82
3.4.1	Densitometric and Microdamage Results by Presence of Subchondral Bone Lesion.....	87
3.4.2	Relationship between Microcracks and Densitometric Measures.....	87
3.4.3	Differences in Exercise History among Case & Control Racehorses.....	88
3.4.4	Relationships between Exercise History, Microcracks and Densitometry.....	89
3.5	Discussion.....	91
3.5.1	Relationship of Exercise to Densitometric & Microdamage Variables.....	92
3.6	Acknowledgements.....	96
3.7	Supplemental Material A: Exercise history and relationship to densitometric and microdamage measures.....	97
3.8	Supplemental Material B: Densitometric and Microdamage Data.....	111
3.9	Supplemental Material C: Equilibrium Solution for Bone Compartment Model.....	119
3.10	References.....	121
Chapter 4: Training Drives Turnover Rates in Racehorse Proximal Sesamoid Bones.....		
4.1	Abstract.....	124
4.2	Introduction.....	125
4.3	Methods.....	128

4.3.1	Study Design .....	128
4.3.2	Model Description .....	130
4.3.3	Derivation of the Dependence of TMD on Remodeling Rates .....	132
4.3.4	Mineralization Law .....	133
4.3.5	Average Mineralization .....	135
4.3.6	Relating Morphometric Data to Volume Fractions and Tissue Mineral Density.....	136
4.3.7	Selection of a Fixed Primary Mineralization Rate ( $k_3$ ) .....	138
4.3.8	Determining Steady-State Rate Constants.....	139
4.3.9	Racehorse exercise data.....	141
4.3.10	Statistical Analysis .....	142
4.4	Results .....	143
4.4.1	Effect of $k_3$ .....	143
4.4.2	Group Differences among Rate Constants.....	144
4.4.3	Correlations among Steady-State Rate Constants and morphometric Data .....	145
4.4.4	Regressions between Morphometric Data and Steady-State Rate Constants.....	146
4.5	Discussion.....	149
4.6	Acknowledgements.....	156
4.7	Supplemental Material A: Steady-State Solution for Bone Compartment Model.....	157
4.8	Supplementary Material B: Exercise History Regressions.....	161
4.9	Supplementary Material C: Sensitivity of $k_1$ to Input Distributions in Non-Damaged ROI .....	164
4.10	References.....	165
Chapter 5: In Vitro Assessment of the Motion of Equine Proximal Sesamoid Bones Relative To The Third Metacarpal Bone Under Physiologic Midstance Loads.....		170
5.1	Abstract .....	170
5.2	Introduction.....	171
5.3	Materials and Methods .....	173
5.3.1	Sample .....	173
5.3.2	Biomechanical testing .....	174
5.3.3	Radiographic measurements.....	176
5.3.4	Statistical analysis.....	178
5.4	Results .....	179
5.5	Discussion.....	182
5.6	Acknowledgments.....	188

5.7	Footnotes .....	188
5.8	References.....	189
Chapter 6: In Vitro Motions of the Medial and Lateral Proximal Sesamoid Bones under Mid-Stance Load Conditions are Consistent with Racehorse Fracture Configurations.....		
6.1	Abstract .....	191
6.2	Introduction.....	192
6.3	Materials and Methods .....	194
6.3.1	Sample Selection .....	194
6.3.2	Limb Instrumentation.....	195
6.3.3	Biomechanical Testing.....	196
6.3.4	Data Reduction.....	197
6.3.5	Data Analysis .....	198
6.4	Results .....	199
6.5	Discussion.....	202
6.6	Acknowledgements.....	208
6.7	References.....	209
Chapter 7: Conclusion.....		
7.1	Summary: Aim 1 .....	212
7.3	Summary Aim 2 .....	215
7.2	Summary Aim 3 .....	216
7.4	Study Strengths & Limitations.....	217
7.5	Future Opportunities.....	220
7.5.1	In Vivo Assessment of Morphological Changes within the PSBs.....	220
7.5.2	PSB Motion Studies .....	222
7.5.3	Finite Element Modeling .....	223
7.6	Summary .....	225
7.7	References.....	226
Appendix: Description of Exercise Trends in a Subset of California Racehorses with and without Proximal Sesamoid Bone Fracture .....		
8.1	Description of Exercise History Information .....	229
8.2	Principal Component Analysis.....	230
8.3	Classification & Regression Tree (CART) Analysis for Distinguishing Between Groups .....	233
8.4	Descriptive Statistics of Study Groups.....	239

## List of Figures

Figure 1.1	Linear microcracks shown in the subchondral tissue of an equine proximal sesamoid bone	9
Figure 1.2	The fetlock region of the equine forelimb	19
Figure 1.3	Soft tissue structures and geometry of the bones in the metacarpophalangeal (fetlock) joint	20
Figure 1.4	Proximal sesamoid bone fracture configurations	23
Figure 2.1	Standardized regions of interest for analysis of tissue properties	43
Figure 2.2	Typical location of subchondral surface abnormality, on the abaxial side of the mid-sagittal plane.	44
Figure 2.3	Microcomputed tomography porosity maps highlighting the focal subchondral osteopenic abnormality found in Case racehorses	45
Figure 2.4	Focal subchondral discoloration surrounded by sclerosis in Case proximal sesamoid bones	47
Figure 2.5	Subchondral sites of focal osteopenia shown on microcomputed tomography sagittal images	50
Figure 2.6	Representative histology of Case and Control proximal sesamoid bones stained with Hematoxylin & Eosin	52
Figure SA-2.7.1	Receiver-operator characteristic curve for the regression shown in Table SA-2.7.1	61
Figure SA- 2.7.2	Probability of a horse being a Case, determined by the Logistic Regression shown in Table SA 2.7.1	62
Figure SB- 2.8.1	Regions examined in Study 1 (Section 2.3.1) shown on a sagittal section and fracture faces of a proximal sesamoid bone	63
Figure 3.1	Compartment model of the bone turnover cycle	76
Figure 3.2	Sagittal plane regions of interest for microcomputed tomography and microdamage analysis	80
Figure 3.3	Basic fuchsin stained histology sections show in internal and calcified cartilage microcracks on Control, Case Contralateral Intact, and Case Fractures proximal sesamoid bones	84
Figure 3.4	Selected exercise robust linear regressions for bone volume fraction and number of subchondral microcracks with horse exercise	90
Figure 3.5	Magnetic resonance image (MRI) of the left fetlock joint of a living racehorses from a different racing population showing a bone bruise at the same location as the low density lesions identified in this study	95
Figure 4.1	Compartment model of the bone "tissue turnover cycle"	128
Figure 4.2	Flowchart of study methods	129
Figure 4.3	Root-mean square error curve fits of Equation 4.3 from rabbit and sheep data	134
Figure 4.4	Stained crack area fraction, shown on a representative histology section, in the Damaged region of interest.	138

Figure 4.5	Volume fraction surfaces for the Non-Damaged region of interest are shown in terms of rate constant ratios	140
Figure 4.6	Non-Damaged ROI and Damaged ROI solutions for resorption rate ( $k_1$ ) and osteoid formation rate ( $k_2$ ) shown against the measured bone volume fraction and tissue mineral density	146
Figure 4.7	Damaged region of interest solutions for damage formation rate ( $K_4$ ) plotted against the stained microcrack area fraction	146
Figure 4.8	Robust regressions among $k_1$ and $k_2$ in the Non-Damaged ROI and horse exercise	148
Figure 4.9	Robust regression among $k_2$ and Events per Year in the Damaged ROI	148
Figure 4.10	Robust regression between the damage formation rate ( $k_4$ ) and cumulative works 4 months before death	149
Figure 5.1	Dorsopalmar radiographic image and photograph of the metacarpophalangeal (fetlock) region of an equine cadaveric forelimb that depict placement of lead markers and instrumentation of the PSBs to facilitate data collection during biomechanical testing in an in vitro study conducted to assess the motion of the PSBs relative to the MC3 condyle under physiologic loads consistent with standing (1.8 kN) and midstance walking (3.6 kN), trotting (4.5 kN), and galloping (10.5 kN).	175
Figure 5.2	Lateromedial radiographic image of the fetlock region of an equine forelimb under 1.8 kN of axial compression (i.e., physiologic load consistent with standing) with annotations depicting the measurements obtained during the study described in Figure 5.1	176
Figure 5.3	Schematic of the transverse plane of the distal aspect of MC3 for an equine forelimb of the study described in Figure 5.1 that depicts the positions of the PSBs relative to MC3 and apparent movement of the 2 LVDTs when the limb was unloaded and loaded during biomechanical testing	178
Figure 5.4	Plot of fetlock angle versus load for 8 equine forelimbs that underwent biomechanical testing as described in Figure 5.1.	180
Figure 5.5	Scatterplots of AS angle (A) and PSB-TR distance (B) versus fetlock angle for 8 equine forelimbs when biomechanically tested at loads consistent with standing (diamonds), walking (square), trotting (triangle), and galloping (circle) as described in Figure 5.1.	181
Figure 6.1	Dorsopalmar radiographic projection of intact proximal sesamoid bone and examples of common fracture configurations	193
Figure 6.2	Lateral (A), lateropalmar (B), and palmar (C) views illustrating instrumentation of a left forelimb in the material testing system showing MC3-P1 sign conventions for the flexion-extension, internal-external rotation, and abduction-adduction joint angles.	195
Figure 6.3	Lateral (A), lateropalmar (B), and palmar (C) views illustrating instrumentation and sign conventions for the MC3-PSB flexion-extension, internal-external rotation, and abduction-adduction joint angles are shown on a left forelimb.	196

Figure 6.4	Linear regressions and 95% confidence intervals for the change in medial MC3-PSB (red long-dashed line) and lateral MC3-PSB (black short-dashed line) angles from the Stand load condition for MC3-PSB flexion-extension angle (A), internal-external rotation angle (B), and abduction-adduction angle (C).	201
Figure 6.5	Non-sagittal plane rotations of the proximal phalanx (P1) and the proximal sesamoid bones (PSBs) relative to the third metacarpal bone (MC3) and the potential interaction between these rotations and metacarpophalangeal joint ligaments at gallop equivalent load.	205
Figure 6.6	Dorsopalmar radiographs illustrate characteristic fractures in the proximal sesamoid bones (PSBs), third metacarpal bone (MC3), and proximal phalanx (P1). A	207
Figure 7.1	Flowchart of how the compartment model could be linked within a larger finite element modeling scheme	224
Figure 7.2	A two-element finite element model	225
Figure 8.1	Scree Plot showing proportion of variance explained by each principal component and cumulative variance.	231
Figure 8.2	Principal component analysis results	233
Figure 8.3	CART results for Group 1, variable Set A	236
Figure 8.4	CART results for Group 2, variable Sets A-C	237
Figure 8.5	CART results for Group 3, variable Set A	238
Figure 8.6	CART results for variable Set A using all horses.	238



## List of Tables

Table 2.1	Contingency table for presence of focal radiolucencies observed on high-detail radiographs of sagittal sections.	46
Table 2.2	Relationship of subchondral focal radiolucency with subchondral discoloration and sclerosis for all PSBs.	49
Table 2.3	Tissue properties (mean (95% CIs)) in the subchondral lesion and control sites in FX-PSBs, CLI-PSBs, and CTRL-PSB	54
Table SA-2.7.1	Descriptive values (mean (95% CI)) for the exercise variable selected from a multivariable stepwise logistic regression (LR) used to select the subset of Case and Control Horses for Study 1 (Section 2.3.1)	61
Table SA-2.7.2	Descriptive values (mean (95% CI)) for the exercise variable selected from a multivariable stepwise logistic regression (LR) used to select the subset of Case and Control Horses for Study 1 (Section 2.3.1) when applied to Study 2 horses (Section 2.3.4)	62
Table SB- 2.8.1	Description of variables classified in Study 1 (Section 2.3.1)	64
Table 3.1	Least Square Means $\pm$ Standard Error from ANOVA or Raw Means $\pm$ Standard Deviation from ranked ANOVA for tissue properties in each region of interest in all three study groups	82
Table 3.2	Raw Means (Standard Deviation) of microdamage variables for Group and Region of Interest (ROI).	85
Table 3.3	Raw Means (Standard Deviation) of calcified cartilage microcrack variables for Group and Region of Interest (ROI).	86
Table 3.4	Linear regression slope ( $R^2$ ) between microdamage and densitometric measures in the CS $\mu$ ROI with the CD hROI and whole bone hROIs.	87
Table 3.5	Median (Minimum, Maximum) and Mean (Standard Deviation) of selected exercise history variables for Case (n= 10) and Control (n=10) horses.	88
Table SA - 3.7.1	Exercise variable definitions	97
Table SA - 3.7.2	Median (Minimum, Maximum) and Mean (Standard Deviation) of exercise history variables.	100
Table SA - 3.7.3	Robust univariate linear regressions between densitometric and exercise history variables.	104
Table SA - 3.7.4	Robust univariate linear regressions between microdamage and exercise history variables for selected regions of interest.	107
Table SA - 3.7.5	Univariate logistic regressions (LR) predicting presence of calcified cartilage cracks in the Central Subchondral histology ROI based on exercise history variables.	110
Table SB - 3.8.1	Least Square Means (Standard Error) from ANOVA or Raw Means (Standard Deviation) from ranked ANOVA for Bone Volume Fraction, Apparent Mineral Density, and Tissue Mineral Density for all Groups and the four Regions of Interest.	111
Table SB - 3.8.2	Raw Means (Standard Deviation) of microdamage variables for Group and Region of Interest.	113

Table SB - 3.8.3	Least Square Means (Standard Error) of total damage found in Case fracture, Case contralateral intact, and Control proximal sesamoid bones.	114
Table SB - 3.8.4	Raw Means (Standard Deviation) of tissue morphometry variables for region of interest and presence or absence of a subchondral lesion on the microcomputed tomography scan.	115
Table SB - 3.8.5	Raw Means (Standard Deviation) of microdamage variables for region of interest (ROI) depending on lesion presence (Yes, No) on the microcomputed tomography scan.	117
Table SB - 3.8.6	Raw Means (Standard Deviation) of calcified cartilage microdamage variables for region of interest (ROI) depending on lesion presence (Yes, No) on the microcomputed tomography scan.	118
Table 4.1	Parameter values used to solve for rate constants.	140
Table 4.2	Least Square Means $\pm$ Standard Error from ANOVA or Raw Means $\pm$ Standard Deviation from ranked ANOVA for bone volume fraction, tissue mineral density, and stained crack area fraction in each region of interest in all three study groups.	143
Table 4.3	Summary [Mean (Standard Deviation)] of derived steady-state rate constants.	145
Table 4.4	Summary of how the rate constants, mineralized bone volume fraction, and tissue mineral density changed with exercise intensity.	152
Table SB - 4.8.1	Robust linear regressions results [Slope ( $R^2$ )] between $k_1$ or $\ln(k_1)$ and exercise variables.	161
Table SB - 4.8.2	Robust linear regressions results [Slope ( $R^2$ )] between $k_2$ or $\ln(k_2)$ and exercise variables. Regressions were performed in both the Damaged and Non-Damaged regions of interest.	162
Table SB - 4.8.3	Robust linear regressions results [Slope ( $R^2$ )] between $k_4$ and $\ln(k_4)$ and exercise variables	163
Table 5.1	Least squares mean $\pm$ standard error values for measurements obtained during biomechanical testing of 8 equine cadaveric forelimbs in an in vitro study conducted to assess the motion of the PSBs relative to the third metacarpal bone condyle under physiologic midstance loads consistent with standing (1.8 kN), walking (3.6 kN), trotting (4.5 kN), and galloping (10.5 kN).	179
Table 6.1	Least Square Mean $\pm$ Standard Error of MC3-P1 angles at Stand, Walk, Trot, and Gallop load conditions and the Change in metacarpophalangeal joint angles from the Stand load condition	199
Table 6.2	Least Square Mean $\pm$ Standard Error of third metacarpal bone-proximal sesamoid bone joint angles from the Stand load condition for the Walk, Trot, and Gallop load conditions.	200
Table 6.3	Partial Spearman correlation coefficients (r values) for the change of third metacarpal bone-first phalanx angle and third metacarpal bone-proximal sesamoid bone joint angles from the Stance load condition for the Walk, Trot, and Gallop load conditions.	202
Table SA-8.2.1	Description of horse ages and genders.	228
Table SA-8.2.2	Cause of Death for Affected and Control Horses.	229
Table SA-8.2.3	Base Variables from Exercise History.	230

Table SA-8.2.4	Variable Sets A, B, & C for CART Analysis	234
Table SA-8.2.5	Groups for CART Analysis; Note that groups differ based on control group membership.	234
Table SA-8.2.6	CART Results for all Groups and All Variable Combinations	235
Table SA-8.2.7	Descriptive Statistics for selected rate variables.	240
Table SA-8.2.8	Descriptive Statistics for selected rate variables.	241
Table SA-8.2.9	Univariate Odds Ratios for selected exercise variables.	241

## List of Equations

Equation 1.1	Apparent density	15
Equation 1.2	Apparent modulus of cancellous and compact bone	15
Equation 1.3	Example minimization function used in bone finite element models	18
Equation 1.4	Example minimization function used in bone finite element models	18
Equation 3.9.1	Time derivative of undamaged mineralized bone volume derived from compartment model shown in Figure 3.1	119
Equation 3.9.2	Time derivative of damaged mineralized bone derived from compartment model shown in Figure 3.1	119
Equation 3.9.3	Time derivative of osteoid volume derived from compartment model shown in Figure 3.1	119
Equation 3.9.4	Time derivative of marrow volume derived from compartment model shown in Figure 3.1	119
Equation 3.9.5	Steady-state solution for undamaged mineralized bone volume fraction	119
Equation 3.9.6	Steady-state solution for damaged mineralized bone volume fraction	119
Equation 3.9.7	Steady-state for osteoid volume fraction	119
Equation 3.9.8	Steady-state for marrow volume fraction	119
Equation 3.9.9	Partial derivative of undamaged bone volume fraction with respect to damage formation rate; derived from compartment model shown in Figure 3.1	120
Equation 3.9.10	Partial derivative of marrow volume fraction with respect to damage formation rate; derived from compartment model shown in Figure 3.1	120
Equation 3.9.11	Partial derivative of osteoid volume fraction with respect to damage formation rate; derived from compartment model shown in Figure 3.1	120
Equation 3.9.12	Partial derivative of damaged bone volume fraction with respect to damage formation rate; derived from compartment model shown in Figure 3.1	120
Equation 4.1a	Summation of compartment model volumes	130
Equation 4.1b	Summation of compartment model volume fractions	132
Equation 4.2	Tissue mineral density expressed as an expected value	132
Equation 4.3	Secondary mineralization law	133
Equation 4.4	Exponential probability distribution	135
Equation 4.5	Tissue mineral density of the undamaged mineralized bone volume	135
Equation 4.6	Tissue mineral density of the damaged mineralized bone volume	136
Equation 4.7	Mineralized bone volume fraction of the compartment model	136
Equation 4.8	Tissue mineral density for the compartment model's mineralized bone volume fraction	136
Equation 4.9	Unmineralized bone volume fraction	136
Equation 4.7.1	Time derivative of undamaged mineralized bone volume for compartment model shown in Figure 4.1	157
Equation 4.7.2	Time derivative of damaged mineralized bone for compartment model shown in Figure 4.1	157

Equation 4.7.3	Time derivative of osteoid volume for compartment model shown in Figure 4.1	157
Equation 4.7.4	Time derivative of marrow volume for compartment model shown in Figure 4.1	157
Equation 4.7.5	Matrix formulation of the time derivatives of the steady-state compartment model, as shown in Figure 4.1	157
Equation 4.7.6	Null space of compartment model (Figure 4.1)	158
Equation 4.7.7a	General solution for steady-state compartment model	158
Equation 4.7.7b	General solution for steady-state compartment model	158
Equation 4.7.8	Steady-state undamaged mineralized bone volume fraction for the compartment model shown in Figure 4.1	158
Equation 4.7.9	Steady-state damaged mineralized bone volume fraction for the compartment model shown in Figure 4.1	158
Equation 4.7.10	Steady-state osteoid volume fraction for the compartment model shown in Figure 4.1	158
Equation 4.7.11	Steady-state marrow volume fraction for the compartment model shown in Figure 4.1	158
Equation 4.7.12	Steady-state unmineralized bone volume fraction for the compartment model shown in Figure 4.1	159
Equation 4.7.13	Steady-State mineralized bone volume fraction for the compartment model shown in Figure 4.1	159
Equation 4.7.14	Partial derivative of mineralized bone volume fraction with respect to resorption rate for the compartment model shown in Figure 4.1	159
Equation 4.7.15	Partial derivative of mineralized bone volume fraction with respect to osteoid formation rate for the compartment model shown in Figure 4.1	159
Equation 4.7.16	Partial derivative of mineralized bone volume fraction with respect to primary mineralization rate for the compartment model shown in Figure 4.1	159
Equation 4.7.17	Partial derivative of mineralized bone volume fraction with respect to damage formation rate for the compartment model shown in Figure 4.1	159
Equation 4.7.18	Partial derivative of mineralized bone volume fraction with respect to damage removal rate for the compartment model shown in Figure 4.1	159
Equation 4.7.19	Non-damaged model steady state solution for the undamaged mineralized bone volume fraction	159
Equation 4.7.20	Non-damaged model steady state solution for the osteoid volume fraction	159
Equation 4.7.21	Non-damaged model steady state solution for the marrow volume fraction	160
Equation 4.7.22	Non-damaged model steady state solution for the unmineralized bone volume fraction	160
Equation 4.7.23	Partial derivative of the mineralized bone volume fraction with respect to resorption rate for a region without damage	160
Equation 4.7.24	Partial derivative of the mineralized bone volume fraction with respect to osteoid formation rate for a region without damage	160
Equation 4.7.25	Partial derivative of the mineralized bone volume fraction with respect to primary mineralization rate for a region without damage	160

## **Chapter 1: Introduction**

### **1.1 Motivation and Research Aims**

The etiology and prediction of non-traumatic bone fractures, especially those seen frequently in a patient population (e.g., vertebral collapse in post-menopausal women), has been a topic of interest in the medical field for decades. One subset of non-traumatic fractures are stress fractures in athletes, which are generally believed to result from accumulation of microscopic tissue defects (microdamage) incurred with repetitive physiologic loads. In bone, microdamage refers to tissue damage, often appearing as small (< 1mm) cracks, that cause mechanical property degradation. Stress fractures are like engineering fatigue fractures, as both are dependent on loading and microdamage accumulation. However, in bones, the stress fracture process is complicated by biology. Bone cells respond to mechanical loads, microdamage, and nutrition and can repair damage, modify bone mass density and shape as a result of their response. The biological responses to load, damage and nutrition present practical difficulties when computationally modeling stress fractures, as they change material properties separate from the changes directly resulting from the accumulation of fatigue damage. Additionally, while bone's damage response to the narrow stress states in laboratory fatigue testing is fairly well established, the dependence of fatigue damage on the combined stresses that occur during real-world training activities is not.

This dissertation focuses on the etiology of stress fractures in the Proximal Sesamoid Bones (PSBs) of California Thoroughbred racehorses. PSB fractures are the most common fatal musculoskeletal injury in the California racehorse population.<sup>1</sup> Currently, there are few reliable screening methods to predict which horses are at risk for a PSB fracture. The primary goal of this work is to link observable pathologic changes of the PSBs to training and specific loading conditions. Additionally, a compartment model of bone's tissue turnover cycle that can be directly correlated, through histomorphometric measures, to

specific training activities is introduced. We plan to use this compartment model within a predictive finite element modeling framework for PSB fractures.

The research presented in this dissertation is related to understanding 1) densitometric and histomorphologic features associated with subchondral bone stress-reactions (tissue changes) that precede stress fractures; 2) unique features of a stress-reactions that promote a complete stress fracture; 3) loading circumstances associated with stress-reactions and complete fracture development; and 4) the interaction of bone's biological turnover and repair processes with microdamage accumulation involved in stress fracture development. The Thoroughbred racehorse provides an opportunity to investigate these aims, specifically in the proximal sesamoid bones (PSBs) of the distal forelimb, which are commonly injured and available for study. Racehorse PSBs provide exercise-induced in vivo model for osteochondral (joint surface) stress fractures; this type of fracture is very difficult to model in vitro. The following sections provide a brief introduction of bone structure, function, biological response to damage and loading within the context of stress fractures. Additionally, because this work uses racehorse PSBs, equine anatomy and racehorse fractures are also briefly reviewed.

## **1.2 Bone Structure and Function**

The main roles of the skeletal system are to transmit forces, protect organs from damage, and help maintain mineral homeostasis.<sup>2</sup> To meet these demands, bone has evolved a highly organized, hierarchical, composite of organic and inorganic materials. Distinct structural units are observed at different length scales; the organization and composition of these structural units contribute to bone's continuum-level mechanical properties. In most mammalian bone, four length scales are defined for bone's structural levels: the macroscale, mesoscale, microscale, and nanoscale.

At the macroscale, bone tissue is classified as compact or cancellous based on its porosity. Compact bone is very dense, with a porosity between 5-10%, and generally forms the outer "shell" (i.e.,

cortex) of bones.<sup>3</sup> Cancellous bone, or trabecular bone, has a porosity between 75-95%.<sup>3</sup> It is found inside the ends of long bones (e.g., femoral head), inside flat bones (e.g., pelvis), and inside cuboidal bones (e.g., wrist).<sup>3</sup> Macroscale mechanical properties are highly dependent on organ geometry and substructure (e.g., volume-average density, cancellous bone connectivity, collagen-crosslinking, etc.).<sup>4</sup> At the mesoscale, structural differences can be observed between compact and cancellous bone. Additionally, both types can be identified as lamellar or woven depending on collagen fibril organization. Lamellar bone is organized, consisting of mineralized collagen fibrils (lamellae) arranged in layers; in woven bone, the fibers are less organized.<sup>5</sup> However, woven bone can be rapidly formed, an advantage during rapid growth and repair circumstances. In adults, lamellar bone is found in cortices in either circumferential lamellae or in osteons embedded within an interstitial matrix. Osteons are approximately cylindrical structures composed of concentric lamellae surrounding a central cavity that contains a blood vessel (Haversian canal); osteons are 1-10mm long with a diameter of about 0.2 mm and generally are parallel with the long axis of the bone.<sup>3</sup> (Osteons often branch and rejoin in a complex network, but this detail of structure is not important in this discussion.) Secondary osteons (i.e., osteons formed through remodeling of pre-existing bone tissue) have a lower elastic modulus than the interstitial matrix and are separated from the interstitial matrix by a low-shear strength interface called a cement line.<sup>6</sup> These interfaces help extend bone's fatigue life by resisting crack growth.<sup>7</sup> There are numerous holes in the mineralized tissue that create tissue porosity. These include lacunae, small pores that contain osteocytes (a type of bone cell), and canaliculi, small <1  $\mu\text{m}$  diameter tunnels that form an interconnected network that allows for osteocyte communication. While these pores are small, accounting for  $\sim 1.45\%$  of the bone tissue volume, they are numerous; there are an estimated 15,000-35,000 lacunae/mm<sup>3</sup>.<sup>8</sup> Remodeled cancellous bone is a network of bony struts called trabeculae with a surrounding and connected marrow and vascular space. Trabeculae of remodeled cancellous bone are often described as struts (0.1-0.3 mm diameter) or plates



(of similar thickness) composed of trabecular packets separated from the interstitial matrix by cement lines.

At the microscale, lamellae are the primary structural units and many macroscale material properties of bone depend on the direction of the collagen fibers within the lamellae and the relative orientation between layers of lamellae.<sup>5</sup> At the nanoscale, mineralized collagen fibrils are the basic structural units. Hydroxyapatite mineral crystals, small amounts of non-collagenous organic proteins, and water are embedded within the collagen fibrils and also contribute to mechanical properties (e.g., bone strength, hardness, brittleness, fracture toughness).<sup>3,9,10</sup>

### **1.2.1 Bone as a Composite Material**

Due to its structural organization, bone is analogous to a composite material and is often modeled as such by engineers. Using this analogy, compact bone is like a fiber-reinforced composite with osteons as the fibers. Strength is determined by multiple factors, including the organization of lamellae within osteons, degree of mineralization, and porosity.<sup>11</sup> Since osteons are generally aligned with the long axis of a bone, strength is highest longitudinally (in the direction of the osteons) and lower in the radial and circumferential directions. Most studies report a 3:1:1 tensile and compressive longitudinal to radial to circumferential strength ratio.<sup>11</sup> (Note also that, mineralized bone tissue is stronger in compression than in tension, caused by the weakness of the mineral in tension as compared to compression.) Because of this structure, the moduli of compact bone are often approximately transversely isotropic. Apparent density (i.e., the mass of hydrated mineralized bone tissue within a given volume) and bone volume fraction (i.e., the volume of mineralized tissue in a given volume) have been experimentally related both to modulus and strength following power laws.<sup>4,6,12-14</sup> Mineralization (i.e., the amount of mineral in a specific mineralized tissue volume) affects fracture toughness, strength, and modulus.<sup>6,15</sup> Less mineralized bone has lower modulus and strength, but highly mineralized bone usually has lower initiation and

propagation fracture toughnesses.<sup>16</sup> Adding mineralization to volume fraction in empirical fits to predict mechanical properties can improve the power-law relationship for modulus.<sup>15</sup>

Cancellous bone is similar to an open celled porous foam; it behaves similarly to a porous foam when deformed – there is an initial region of elastic behavior, followed by a collapse plateau, and then a rapid increase in modulus as the pores compact (densification).<sup>17–19</sup> Strength of cancellous bone is related to the total mass of the tissue, mineralization of trabeculae, porosity, trabecular orientation, history of mechanical loading (as it affects hard tissue damage) and various histomorphometric measures, where many of these are not fully independent.<sup>11</sup> Experimentally, trabecular orientation greatly influences the strength anisotropy.<sup>20</sup> Empirically, both modulus and strength are dependent on several structural measures, most importantly, the apparent density.<sup>21,22</sup>

### **1.2.2 Bone Cell Types**

An overview of bone structure and function is incomplete without describing the bone cells, as they are the main effectors responsible for maintenance, damage repair, and bone's loading response. The four main types of bone cells are: osteocytes, osteoblasts, osteoclasts, and bone lining cells. Osteocytes are the most numerous cell type and are found inside small pores called lacunae in the bone matrix. Osteocytes form an interconnected network (syncytium) within micro-channels called canaliculi and are the primary mechanosensory bone cell. They are responsible for mechanotransduction, initiating structural changes and repair processes, and mineral transport.<sup>23,24</sup> Not all of the mechanisms of mechanotransduction are known – but strain-induced fluid flow around osteocyte processes within canaliculi is considered one of the major contributors.<sup>2,23</sup> Osteoblasts are mononuclear, cuboidal cells that produce the organic portion of the bone matrix (i.e., osteoid). Osteoclasts are large, multinucleated cells that resorb (remove) mineralized bone. Bone lining cells connect osteocytes to the outer surface of

bone, help osteocytes signal osteoclasts, receive systemically circulating chemical signals, and play a role in mineral transport.<sup>2</sup>

### **1.3 Bone Modeling and Remodeling**

In healthy bone, cells modify the quantity of bone and turnover rate in response to the load environment, damage, mineral homeostasis and other stimuli.<sup>25</sup> Bone reacts to these stimuli through two primary processes: modeling and remodeling. The cellular processes of modeling and remodeling are similar, except for their spatial and temporal coupling. During remodeling the actions of osteoclasts (bone removal) and osteoblasts (bone formation) are spatially and temporally linked: resorption, then formation, occurs at a location. During modeling, the processes are not coupled. In healthy adults, remodeling is approximately balanced and results in no net bone loss.<sup>26</sup> However, unbalanced remodeling can cause net changes in the amount of bone tissue at a location. Often the balance is negative (e.g., the formation of Haversian canals during compact bone remodeling), but a positive balance is also possible (e.g., in cancellous bone a positive remodeling balance can be induced with parathyroid hormone).<sup>27,28</sup> Remodeling is estimated to turnover (i.e., replace) ~3% of compact bone and 25-30% of cancellous bone per year in adult humans; however, the turnover rate varies with skeletal location, age, species and other factors.<sup>29</sup> Modeling is associated with a change in shape of the tissue with or without a net change in bone mass. Modeling can be internal (e.g., an increase in trabecular width or location) or external (e.g., altering bone curvature or width). Both modeling and remodeling can occur throughout an individual's life, however, modeling of the external shape of a bone primarily occurs during growth.<sup>29</sup>

Both modeling and remodeling are controlled by many local, systemic, and exogenous factors. The exact nature of the cell signaling, biochemical reactions, and biomineralization processes that occur during these processes are an active area of bone research. While the specifics are still being investigated, remodeling is sometimes defined as a five-step process consisting of: activation, resorption, reversal,

formation, and mineralization.<sup>25,29</sup> Teams of osteoblasts and osteoclasts called basic multicellular units (BMUs) follow these steps in a coupled way during remodeling; during modeling, only some of the steps take place as formation and resorption are not coupled. During activation, osteocytes signal osteoclasts to resorb bone.<sup>25,30</sup> During resorption, osteoclasts carve out resorption bays in the form of a cylindrical canal the size of an osteon in compact bone or a trench the size of a hemi-osteon in cancellous bone. Cellular activity is switched between osteoclasts and osteoblasts during the reversal phase. During formation, osteoblasts radially fill the resorbed region with organic matrix (i.e., osteoid).<sup>2</sup> After osteoid is deposited, it first matures and then undergoes mineralization.<sup>24</sup> The osteoid maturation time (i.e., the average time between deposition of osteoid and mineralization at a bone-forming site)<sup>31</sup> is between 15-20 days in humans.<sup>32</sup> In humans, the total time for one BMU to complete is 4-6 months.<sup>25,29</sup> Most mineralization occurs within days of osteoid maturation; however, full mineralization takes months to years.<sup>33,34</sup> Because newly formed tissue has a lower mineral density than older tissue, tissue mineral density is often used as an indicator of relative tissue age.<sup>35</sup> The end result of remodeling is a new secondary osteon in compact bone or a new hemi-osteon in trabecular bone.

Generally the mineralization process is defined as occurring in two stages, a rapid primary mineralization stage where 70% of maximum mineral density is reached within a few days and a slower secondary mineralization stage where 70-95% of maximum possible mineral density accumulates over months to years.<sup>36</sup> Primary mineralization is assumed to occur rapidly (i.e., over several days) because many more high mineral density osteons are observed than low density osteons,<sup>36,37</sup> mineralization rate studies observe newly mineralized tissue at early time points,<sup>33,38</sup> and newly formed bone has been found to mineralize faster than quiescent (older tissue, where cells are not acting) bone by a factor of two.<sup>39</sup> Bone mineral is not purely hydroxyapatite ( $\text{Ca}_{10}(\text{PO}_4)_6(\text{OH})_2$ ), but instead contains a wide variety of anionic (e.g.  $\text{CO}_3^{2-}$ ) and cationic (e.g.  $\text{Na}^+$ ) substitutions in the hydroxyapatite lattice.<sup>40</sup> The mineralization rate of

chemical species occurs at different rates in bone tissue.<sup>41</sup> Therefore, while bone mineralization occurs in a rapid primary and slower secondary phase, an exact mineralization time profile is unknown.

### **1.3.1 Bone's Response to Damage**

Physiological loads can cause fatigue damage to bone tissue;<sup>42</sup> simply, this means that bones can accumulate damage at loads an organism experiences during daily living.<sup>43</sup> Damage is material changes that result in a modulus decrease; in bone, damage is normally referred to as microdamage because of the small size of the discrete tissue failures visible after histological staining (Figure 1.1). Microdamage includes linear microcracks, diffuse microcracks, and complete microfracture of trabeculae, but which microdamage is present depends on the loading direction and the lamellar patterning. Linear microcracks preferentially form in areas of compressive stress and diffuse microdamage forms preferentially in areas of tensile stress.<sup>2,43,44</sup> Linear microcracks are between 40 – 100  $\mu\text{m}$  long when viewed in transverse cross-sections of long bones and are usually found between osteons in the interstitial tissue of compact bone tissue (Figure 1.1).<sup>45</sup> Diffuse cracks are less than 10  $\mu\text{m}$  across and occur in clusters in both compact and trabecular bone. Microfractures of trabeculae result in complete collapse of individual trabecular struts;<sup>2</sup> however, this damage type appears to be less common than either diffuse or linear microcracking.<sup>19</sup> In both cortical and cancellous bone, the accumulation of more instances of microdamage (i.e., their number), not microdamage size, is associated with decreases in tissue modulus, strength, and fracture initiation toughness.<sup>46–48</sup> Microdamage formation allows for energy absorption without causing catastrophic failure (i.e., full bone fracture) and bone tissue has many inherent toughening mechanisms that prevent progression of microcracks (e.g., cement lines around osteons). However, even with these toughening mechanisms, accumulation of too much microdamage will cause complete failure.<sup>2,43</sup> Medically, this type of fracture is called a stress fracture when one also includes the medically important effects of the cell response to tissue damage.

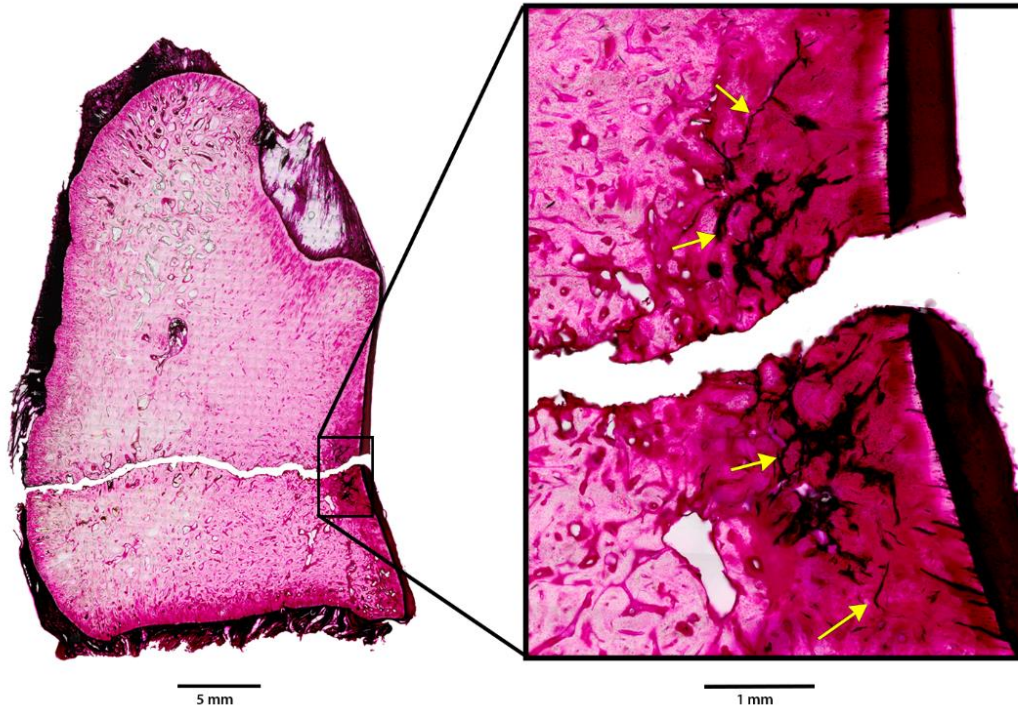


**Figure 1.1:** Linear microcracks shown in the subchondral tissue of an equine proximal sesamoid bone that has fractured. The microcracks are stained with basic fuchsin, a common histology stain.

Microdamage causes a local remodeling response (i.e., targeted remodeling)<sup>26,49,50</sup> that appears to target the repair of linear microcracks, but not diffuse damage.<sup>26,50</sup> The remodeling process has a role in stress fracture development since it can remove cracks and prevent their accumulation. However, the remodeling process is believed also to play a further role in stress fractures because it temporarily increases porosity and reduces tissue mineralization at the location where damage is occurring (i.e., it causes a stress-reaction). These transient changes can accelerate the progression to a stress fracture when high levels of loading are continued, since the new porosities and reduced modulus can elevate strain and promote the formation of more microdamage. The hypothesis that resorption porosity causes an increase in damage rate is supported by the observation of the formation of microdamage near resorption bays in remodeling cancellous bone and from computational-modeling evidence that resorption bays are stress risers.<sup>51,52</sup> If these regions of high-microdamage low-density tissue are sufficiently mechanically compromised, a stress fracture can occur through these locations.<sup>1,2,53–55</sup>

### 1.3.2 Bone's Response to Mechanical Loads

There have been many experiments to determine which aspects of mechanical loading cause changes in the amount of bone tissue; three main empirical observations, or rules, governing bone's response to loads are generally considered.<sup>25,29,56</sup> First, dynamic loads are required to initiate an anabolic response (i.e., bone formation). Strain rate accounts for nearly 70% of the variation in bone adaptation to applied load.<sup>2,57</sup> Under physiologic strain magnitudes, more bone formation is observed under higher strain rates;<sup>58</sup> however, non-physiologic vibrations (e.g., standing on a vibrating plate) does not consistently alter bone formation.<sup>59,60</sup>

Significant dynamic loads are required to maintain normal appendicular bone mass in adult mammals. In one classic disuse study in dogs, 40 weeks of forelimb immobilization resulted in a loss of nearly half the limb's bone mass; however, in limbs immobilized for 32 weeks and then reloaded, nearly 70% of the bone mass was recovered after 28 weeks.<sup>61,62</sup> Second, bone has a memory of its loading history; however, this memory effect is not fully understood. As previously mentioned, the stimulus sensed by osteocytes to trigger bone formation (or resorption) is unknown but appears to be related to strain. Experimental evidence indicates a strain threshold may be required to initiate bone formation; this threshold is location-specific and depends, at least, on the bone's past routine loading conditions.<sup>57</sup> For example, when the same strains were applied to rat ulnas, more bone formation was found in regions with lower physiologic strain-levels compared to regions with high-physiologic strains.<sup>63</sup> Therefore, the mechanical loading (or lack of loading) required to induce bone formation (or removal) is site specific. Third, only a short duration of loading is required to initiate an anabolic response. In studies performed on turkeys and rats, only a small number of load cycles were needed to induce bone remodeling, and continued load application did not cause further increase in the amount of bone formation.<sup>64,65</sup> Further, bone cells appear to have a refractory period and, therefore, loading bouts must be separated in time to

maximize bone formation.<sup>66</sup> These three rules also imply that a change in routine could be more influential in starting an anabolic or catabolic event than is the bone's long-term load history.

### **1.3.3 Stress Fractures**

Both modeling and remodeling play a role in stress fracture development. As discussed, both damage accumulation and the transient porosities that develop during damage removal can alter tissue modulus and (are believed) to interact in a vicious cycle when high levels of loading are continued. However, since bone can respond to damaging (high) strains by adding mass, the stress fracture process is often considered a "competition" between bone's response to high-levels of loading and the biologically distinct repair process. In medical literature, there is a fuzzy boundary between the tissue changes preceding a stress-fracture and the stress fracture itself. However, the tissue changes that precede a stress fracture are often called a stress-reaction. We will distinguish the two from an engineering standpoint, rather than using clinical symptoms, and define a stress fracture as a fracture occurring from single load to failure after the bone was weakened due to a localized stress-reaction. The stress-reaction forms due to the interaction of repetitive physiologic loads (exercise), modeling, remodeling, and other factors (e.g., health status).

A classic morphometric indicator of a stress reaction is accumulated microdamage and transient porosities (a bone lesion) caused by a local repair response. Lesions can be detected clinically, depending on the equipment used (i.e., computed tomography resolution). Other clinically observable indicators of a stress-reaction include co-localized bone formation on the periosteal (outside) or endosteal (inside) surface, bone pain (which can result in abnormal movement/lameness), overlying skin reddening or warmth, external swelling, and/or bone marrow edema.<sup>55,67</sup> In some cases, a fracture line will occur through one cortex of a long bone with a coincident periosteal bone formation.<sup>55</sup> Generally, it is hypothesized that the periosteal or endosteal bone formation occurs to mechanically stabilize the



low-density lesion. If the stress-reaction occurs below a joint surface (i.e., in subchondral bone), periosteal bone formation cannot occur. However, in the subchondral cancellous bone, compacted bone is often found surrounding a focal lesion.<sup>68,69</sup> It is unknown if this region of dense tissue forms prior to the lesion (likely due to the same high-load intensity that cause the lesion) or after the lesion (in an attempt to buttress the local weakness).

Stress fractures can be prevented if the stress reaction is identified early and activity levels are reduced. In racehorses, both forelimbs are similarly loaded, and a stress fracture in one forelimb is often associated with a stress-reaction in the same location in the other, non-fractured limb.<sup>70</sup> One of the goals of this work is to relate exercise programs with the tissue changes that occur within a stress-reaction location. Other factors besides mechanical loading, such as nutrition and hormone balance, affect stress fracture risk and the development of stress-reactions.<sup>67</sup> Note that these factors also affect bone modeling and remodeling.<sup>71</sup>

The interaction effects between these bone modeling and remodeling, their time-scales, and other factors make it difficult to bridge the gap between in vitro and in vivo laboratory fatigue testing, which are tightly controlled, and “real-world” training practices. For example, in racehorses, there appears to be a balance between low-speed and high-speed exercise that must be maintained to prevent stress fractures. High intensity training is linked to both stress fractures and soft tissue injuries;<sup>1</sup> when non-fatal, these injuries result in the horse being temporarily removed from work (a layup). In the racing industry, layups are considered 60 or more days without intensive training. Unfortunately, the first 2 months during which a racehorse returns to high-speed work following a layup is one of the times these animals are at the highest risk for a complete stress fracture.<sup>1</sup> Likely, there are specific training practices that are protective against a stress-fracture – that allow for bone mass to be maintained (i.e., no resorption of tissue due to disuse) while preventing excessive damage (i.e., that do not cause a damage-repair feedback cycle) – one goal of this research is to begin to find them. It has been shown that easing the physical

demands on military recruits, while still maintaining a sufficiently rigorous exercise schedule for training, reduces stress fracture rates.<sup>72</sup> Similarly, in both humans and horses, a stress fracture often occurs after an abrupt change in exercise intensity.<sup>1,55</sup> Epidemiological studies on racehorses support the idea of training programs that are protective against stress fractures, but have been unable to parse specifics (e.g., miles/day). Case-control studies of stress fracture are impractically expensive in horses since they would require the animals to be euthanized. However, computational modeling has been used in humans (e.g., marathon runners)<sup>73</sup> to predict which exercise programs may be more likely to increase fracture risk and could be applied for use in horses.

## **1.4 Finite Element Methods (FEM) for Modeling Bone**

Finite element methods (FEM) are frequently used to calculate the stress and strain in the tissue that are assumed to determine bone tissue's response to damage and applied loads. Three main assumptions are made when modeling bone with FEM: material symmetry, degree of material homogeneity, and the equations governing material evolution.

### **1.4.1 Symmetry Assumptions**

As previously discussed, bone tissue has anisotropic material properties that can evolve as loading conditions change and different bone tissue types have different properties for equivalent loading conditions. Multiphase material models for bone, require porosity ( $p$ ) and, minimally, some indication of anisotropy such as a fabric tensor ( $\underline{H}$ ) to define the material properties.<sup>74</sup> Porosity is the lowest complexity measure of local microstructure (it is a scalar) and measures the void fraction. The fabric tensor is a higher order measure (second order tensor) characterizing the arrangement of the material surface distribution.<sup>74,75</sup> Fabric tensors are experimentally determined via stereological measurement; for bone, ellipsoids fitted to the 3D measurement of the mean intercept lengths between bone and marrow interfaces are used to define a fabric tensor.<sup>75,76</sup>

Porosity ( $\rho$ ) and the second order fabric tensor ( $\underline{H}$ ) can be related to the elastic stiffness tensor ( $\underline{C}$ ) used for stress-strain calculations. When the modulus tensor  $\underline{C}$  is expressed as a function of  $\rho$  and  $\underline{H}$ , full anisotropy (e.g., triclinic symmetry) cannot be represented because the assumption of a second order fabric restricts the model. The least material symmetry represented using  $\rho$  and  $\underline{H}$  is orthotropy.<sup>74</sup> However, experiments determining the fabric tensor to predict volume-averaged moduli lead to the conclusion that trabecular bone is often orthotropic, and compact bone is often transversely isotropic; therefore, bone's anisotropy can often be well represented using  $\underline{H}$  and  $\rho$ .<sup>74,77</sup> Despite this, isotropic models of bone are the most common due to the difficulty of measuring  $\underline{H}$  and the lack of experimental information on the relationship between changes of  $\underline{H}$  and changes in loading direction.<sup>78</sup>

Isotropic models are used for three main reasons: 1) Bone's natural tendency to align material symmetry axes with the most common loading direction reduces shear coupling, so isotropic symmetry can be assumed in models using physiological loading conditions. When no shear coupling exists, reducing material symmetry from aligned orthotropic to isotropic does not change the form of the stiffness matrix.<sup>79</sup> So, under physiological loading conditions increasing material symmetry past isotropic may not improve a model's predictive capability.<sup>80</sup> 2) Isotropic models are computationally simpler than orthotropic models. 3) Existing publications on bone mechanical properties do not fully define the connection between porosity, the fabric tensor, and material properties. However, there is good data for the isotropic relationship between Young's modulus and porosity that appears valid for most species. There are few validated models for orthotropic properties, and none are available for equine bones. Therefore, significantly more experimental work would be needed to use orthotropic material properties. Considering (1) with (2) and (3), isotropic constitutive models are an appropriate initial choice for modeling physiologic loads in bone.

## 1.4.2 Homogeneity Assumptions

Continuum mechanics is the mathematical basis underlying finite element methods (FEM). Bone tissue, which is filled with numerous pores, is clearly not a continuum. To avoid violating continuum assumptions, most FEM models bone use one of three approaches.<sup>81</sup> First, methods to include microstructural effects (e.g., homogenization theory or representative volume elements) can be used. Second, bone can be modeled at the substructure level to avoid discontinuities in the tissue. In this method, hard tissue and porous spaces are individually modeled. Third, one can ignore the fact that bone is not a continuum. In this latter method, apparent material properties are used for tissue volumes that are large enough to contain several pores –averaging out the effect of individual pores in the volume. This approach does not require the material to be homogeneous at the continuum level, as the apparent characteristics can be different for different volume elements. The third method is (arguably) the most practical when predicting changes within an entire bone and is historically the most common. Both sub-structural and microstructural effect models are more computationally intense and not easily performed in commercial software. Additionally, the detail provided by sub-structural models is not needed for most clinical applications (e.g., modeling whole bones).

Using the apparent property method, an assumption about material symmetry must be made before the stiffness matrix is constructed. Assuming isotropy, apparent mass density ( $\rho_a$ , Eqn. 1.1) is sufficient to determine the apparent modulus for cancellous and compact bone ( $E_a$ , Eqn. 1.2).<sup>2,12,13,21,81</sup>

$$\rho_a = \frac{1}{V} \int_V \rho dV \quad \begin{array}{l} \text{with } \rho = \text{true hard tissue mass density} \\ V = \text{volume of interest} \end{array} \quad \text{Eqn. 1.1}$$

$$E_a = C\rho_a^n \quad \begin{array}{l} \text{with } C = \text{experimentally determined constant} \\ n = \text{experimentally determined constant} \end{array} \quad \text{Eqn. 1.2}$$

Apparent density is a suitable substitute to porosity when defining a scalar measure of material structure.<sup>74</sup> The averaging volume ( $V$ ) depends on the size of the microstructure and limits the maximum

spatial derivative of apparent density, apparent stress, apparent strain and apparent moduli. A conservative estimate for the upper limit of the spatial derivative of  $\rho_a$  ( $d\rho_a/dx$ ) is  $2.0 \text{ g*cm}^{-3}\text{mm}^{-1}$ .<sup>3,81</sup> When  $E_a$  is used in finite element computations, the computed stress (and strain) values are expected (averaged) values within the volume ( $V$ ) – rather than true values at a material point.

### 1.4.3 Material Evolution Equations

As discussed earlier, bone modeling and remodeling occur on multiple structural and temporal levels. Since both modeling and remodeling can alter structure and density at a timescale that is relevant for computer modeling problems of interest to orthopedic researchers, these changes should be accounted for in mathematical models. Few research groups have attempted to simulate external bone modeling (i.e., shape changes) with finite element methods, as it requires movement of element nodes or addition of elements mid-simulation to allow for changes to the external model geometry.<sup>82</sup> External modeling occurs in small amounts in adult humans, so the simplification to only allow for internal modeling (e.g., density/internal structure changes) and remodeling (e.g., damage repair) is still useful for many clinical applications.

Models governing the evolution of bone tissue in response to loading and/or damage can be considered mechanistic, phenomenological, or mixed. Phenomenological models do not directly simulate physiological mechanisms and instead focus on observed empirical relationships between mechanical and morphologic properties. Examples include those proposed by Carter, Fyhrie, Schaffler, Weinans, Huiskes, and others.<sup>79,81,83,84</sup> Mechanistic models include detailed mathematical descriptions of physiological pathways (e.g., the effect of RANK-RANKL-OPG pathways<sup>85</sup>). As more is learned about the cellular signaling pathways in bone tissue, mechanistic models are becoming more popular. However, at this time not enough detail is known about bone biology to develop a complete mechanistic model of bone. Therefore, most mechanistic models must also include phenomenological components and can be considered mixed or semi-mechanistic; examples of mixed models include those by Hazelwood, Mullender, van Oers, and many

others.<sup>86-90</sup> Regardless of the algorithm type, mathematical models of bone modeling and remodeling need to be developed in terms of variables that can be measured in real bones that have known relationships to mechanical properties in order for the model to be useful to test hypotheses related to bone adaptation.<sup>91</sup>

Most phenomenological and mixed models assume the biological processes that change bone's structure are driven by error signals. These error signals are functions of the local structure and stress. If an error signal exists and causes structural changes, an objective function (F) can be formulated to drive models to an equilibrium state. In current formulations for bone's response to loading and/or damage, F is designed to be minimal at equilibrium.<sup>81,83,84,86,92</sup>

Finite element formulations using apparent properties generally simulate internal modeling and remodeling via changes in element apparent mass density ( $\rho_a$ ). This is done by defining  $d\rho_a/dt$  as the objective function to minimize (Eqn. 1.3). Frequently,  $d\rho_a/dt$  is formulated as a first order differential equation where some function,  $\phi$ , measures how close bone is to a goal state G (Eqn. 1.4);  $\phi$  and G are arbitrary (since the exact biological stimulus remains unknown) and many different formulations for  $\phi$  and G have been implemented in FEM models.<sup>81</sup> Examples include strain energy density, change in accumulated damage, and effective stress.<sup>81,83,87,91,93</sup> Often, F is non-linear in  $\rho_a$  resulting in numerical and spatial instabilities in the solutions that do not reproduce "real world" responses of bone to mechanical load.<sup>81</sup> This is unfortunate, as the instabilities severely limit the use of these models in clinical settings. Often, post-hoc modifications have been made to impose stability criteria.<sup>87</sup> In Chapters 3 & 4 of this dissertation, we propose a compartment model of bone's turnover cycle that could easily be linked to an objective function (F) that is linear in terms of apparent density. Development of validated linear differential equations with known numerical stability properties will improve the quality of solutions and make it possible to predict damage quantitatively for the equine proximal sesamoid bones.

$$\frac{d\rho_a}{dt} = F(\sigma, \varepsilon, \dot{\varepsilon}, \rho_a, d, \dots) \text{ where } 0 \leq \rho_a \leq \rho_{a,\max} \quad \text{with } \sigma = \text{stress field} \quad \text{Eqn. 1.3}$$

$\varepsilon = \text{strain field}$   
 $\rho_a = \text{apparent density}$   
 $d = \text{damage variable}$   
 $\rho_{a,\max} = \text{empirical max } \rho_a$

$$\frac{d\rho_a}{dt} = B*(\varphi(\sigma, \varepsilon, \dot{\varepsilon}, \rho_a, d, \dots)-G) \quad \text{with } B = \text{Curve-Fitted Constant} \quad \text{Eqn. 1.4}$$

$G = \text{Proposed Goal State}$

## 1.5 Racehorse Anatomy and Musculoskeletal Injuries

Musculoskeletal injuries (MSI) are a significant welfare issue in horse racing. Many of these MSIs are considered catastrophic injuries, meaning an injured horse is euthanized or permanently removed from racing due to the injury. Nearly one horse dies from an injury during racing and training for every 24 Thoroughbreds and every 44 Quarter Horses that start in a race.<sup>94</sup> Although the incidence of deaths from MSI per race is low, MSIs occur often enough to seriously affect horse welfare, jockey welfare, racing economics, and public perception.<sup>1</sup> Worldwide, MSIs are the leading cause of racehorse deaths directly associated with racing or training.<sup>94-96</sup> MSIs are also the leading cause of jockey falls- often injuring both the jockey riding the injured horse and others who fall when their mount collides with the injured horse.<sup>97,98</sup> Jockeys are 162 times more likely to fall and 171 times more likely to be injured when riding a horse that died during a race than otherwise.<sup>98</sup>

Among MSIs, bone fractures are the most common fatal injury type in racehorses.<sup>1,95,99</sup> The most common site of fatal MSI is in the metacarpophalangeal joint (i.e., the fetlock joint).<sup>100-102</sup> The most common fatal fetlock injury is fracture of the proximal sesamoid bones (PSBs).<sup>95,101-104</sup> The population of horses studied in this dissertation are from California, so some specific facts about fetlock and PSB fractures in California follow. Between 1992-2018 in California, fetlock failure caused 50% of fatal injuries, affecting 2,384 racehorses. In this time-period, PSB fracture accounted for 82% of fatal fetlock injuries and 48% of all fatal MSIs – totaling nearly 1,924 fatal injuries.<sup>105</sup>

### 1.5.1 The Equine Fetlock Joint: Anatomy and Function

The fetlock joint of the distal equine forelimb consists of four bones: the medial PSB, lateral PSB, the third metacarpal bone (MC3), and the proximal phalanx (P1). The MC3 and P1 are long bones and the PSBs are a pair of pyramidal-shaped bones intercalated in the ligaments of the fetlock's suspensory apparatus (Figure 1.2 and Figure 1.3).<sup>106</sup> The medial PSB is typically shorter (proximodistally) and wider (mediolaterally) than the lateral PSB.<sup>107,108</sup> The PSBs and P1 articulate with the MC3, but not with one another. The articular surface of the distal condyle of the MC3 has two distinct curvatures to allow for articulation with both the PSBs and P1. The palmar surface of MC3 is congruent with the PSBs, and the dorsal surface of MC3 is congruent with the P1. The curvature of the dorsal articular surface is higher than the palmar surface and the transverse ridge delineates the change in curvature.<sup>109–111</sup> Additionally, the sagittal ridge of the MC3 interdigitates within a sagittal groove on the proximal condyle of the P1 and between the two PSBs (Figure 1.3).

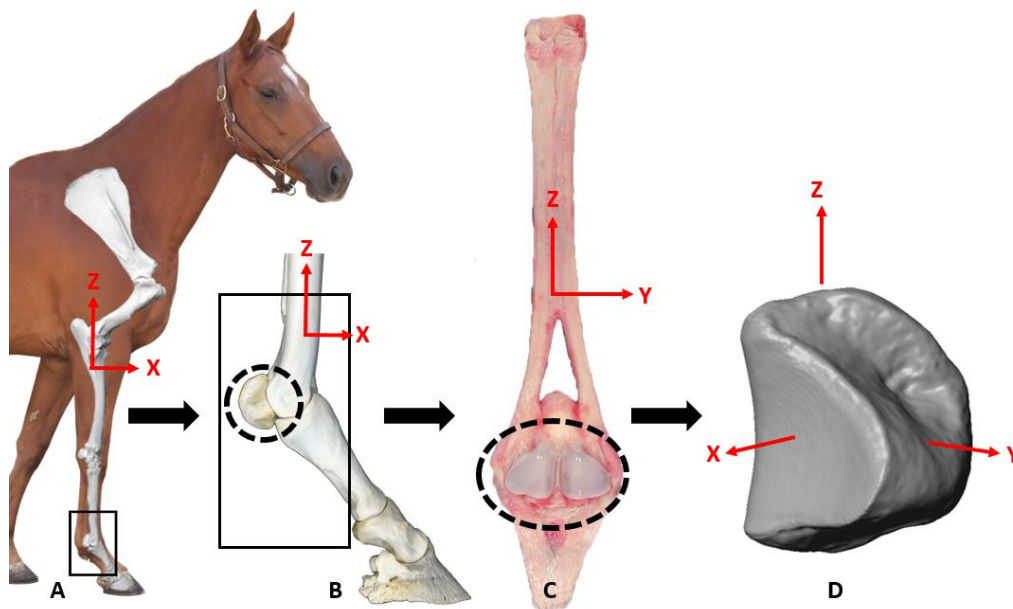


**Figure 1.2** The fetlock region of the equine forelimb. A) Anatomical position of bones of the equine forelimb with the fetlock region indicated by the box. B) Lateral view of equine forelimb bones, location of PSBs indicated with dashed circle. C) Dorsal view of suspensory apparatus with intercalated PSBs indicated by dashed circle. D) 3-D model of PSB created from microcomputed tomography images, illustrating the pyramidal shape. PSBs have an average height (z-axis) of 37mm, width (y-axis) of 32mm, and depth (x-axis) of 25mm.<sup>112</sup>



The suspensory apparatus supports the fetlock joint during locomotion and contains three structures in series: the suspensory ligament, the PSBs, and distal ligaments of the PSBs (alternately known as the distal sesamoidean ligaments; Figure 1.3). If any of these structures rupture or fracture, the suspensory apparatus is not able to sustain loads. The suspensory ligament originates at the proximopalmar aspect of the MC3 and inserts into the apex of the PSBs. The bases of the PSBs are bound tightly to the proximal and middle phalanges (P1 and P2, respectively) by four sets of distal sesamoidean ligaments. Of the four sets of distal sesamoidean ligaments, the straight and oblique distal sesamoidean ligaments are the most substantive. The PSBs are bound to each other along their axial borders, on their respective sides of the sagittal ridge, by the intersesamoidean ligament.

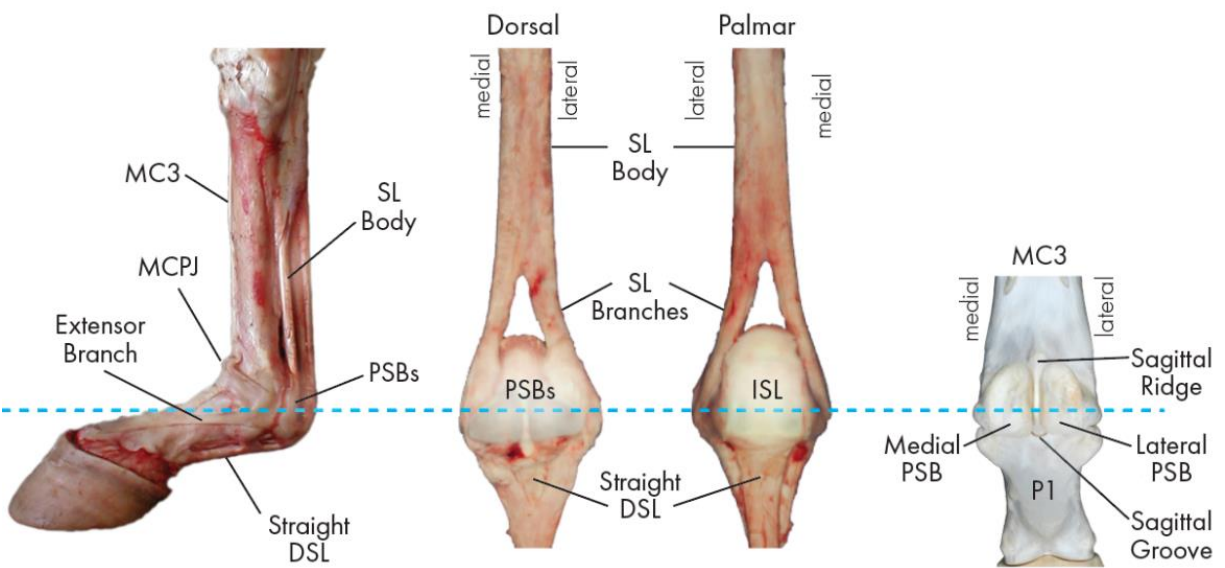


**Figure 1.3:** Soft tissue structures and geometry of the bones of the metacarpophalangeal joint (MCPJ or fetlock joint) help confine fetlock motion to flexion-extension in the sagittal plane. Soft tissue components include the suspensory ligament (SL) and its medial, lateral, and extensor branches, the intersesamoidean ligament (ISL), and the distal sesamoidean ligaments (DSLs, distal ligaments of the proximal sesamoid bones (PSBs)). Bones of the MCPJ include the third metacarpal bone (MC3), proximal phalanx (P1), and medial and lateral PSBs. The sagittal ridge of the MC3 condyle interdigitates with both the sagittal groove on the proximal articular surface of P1 and the ISL between the two PSBs.

The sagittal ridge of the third metacarpal bone, the suspensory apparatus, and other soft tissue structures (i.e. collateral sesamoidean ligaments, extensor branches of suspensory ligament) help confine fetlock movement to flexion-extension in the sagittal plane (Figure 1.3). At the gallop (~25mph), each

forelimb supports loads in excess of 170% of equine body weight – this can exceed 10 kN.<sup>113</sup> The suspensory apparatus is the primary structure that supports this load during stride and prevents the fetlock from hyperextending. Many consider the extreme fetlock extension observed at the gallop to be hyperextension, as the P1 can contact the dorsal surface of the MC3 causing chip fractures at racing-speeds. Regardless, without the suspensory apparatus, the fetlock joint would drop to the ground when the forelimb is loaded.<sup>106</sup> During locomotion and stance, compressive loads are applied to the articular surface of each PSB as they impact the third metacarpal bone and tensile loads are applied proximally and distally by the ligaments of the suspensory apparatus to resist fetlock extension.<sup>114</sup>

### **1.5.2 Fetlock Joint Kinematics**

In nearly all existing literature, the kinematics described for the fetlock joint only describe the articulation of the third metacarpal bone (MC3) relative to the proximal phalanx (P1; i.e., MC3-P1 joint angles). There is a significant body of work describing the 3D kinematics of the MC3-P1 articulation both in vivo and in vitro. The primary motion of the MC3-P1 articulation is flexion and extension in the sagittal plane. Maximum extension occurs during the support phase of stance (i.e., mid-stance) when the peak vertical ground reaction force occurs.<sup>115</sup> In a majority of in vivo studies, a small amount of non-sagittal plane motion is reported. Specifically, up to 5° MC3-P1 external rotation and 10-12° MC3 or MC3-P1 abduction occur during MC3-P1 extension.<sup>116,117</sup> The direction of the axial rotation (i.e., internal or external rotation) appears to vary both among and within horses. The non-sagittal plane movements reported by in vitro studies performed at a neutral hoof position (e.g., flat hoof position) are smaller than those recorded in vivo.<sup>118</sup> However, larger non-sagittal plane motions can be induced in vitro using wedges inserted beneath the medial or lateral aspect of the hoof; this may mimic the effect of uneven or banked racetracks on in vivo motion.<sup>118</sup> Despite the high prevalence of PSB fractures, PSB kinematics have not been explored in vivo.

Generally, motion outside of the sagittal plane (i.e., any movement that is not flexion/extension) could contribute to fetlock injury – since the joint is designed to move within the sagittal plane. Shoeing, uneven footing, turning a corner, and landing a jump affect the non-sagittal plane movement of MC3-P1 articulation.<sup>118–121</sup> Wearing shoes has been shown to increase the abduction/adduction range of the MC3 during locomotion.<sup>119</sup> Uneven footing alters both the abduction/adduction direction and the internal/external rotation direction of the MC3.<sup>118</sup> Turning a corner also changes the abduction or adduction of the forelimb compared to straight line movement.<sup>120</sup> Landing a jump also increases abduction and external rotation.<sup>121</sup> Currently, it is unknown how these non-sagittal plane motions of the MC3-P1 interaction affect PSB kinematics. Changes in PSB kinematics are expected to alter the loading pattern of the MC3-PSB interaction; this may alter the strain distribution and affect PSB fracture risk.

### **1.5.3 Proximal Sesamoid Bones Fracture Characteristics**

Clinically, PSB fractures are classified by location, fracture orientation, and the number of fragments (Figure 1.4). There are four main fracture locations: basilar (i.e., within the distal portion), mid-body (i.e., through center), apical (i.e., through proximal portion), and axial avulsion (i.e., longitudinal fracture along the adjacent bone margins). Mid-body and basilar fractures are the most common.<sup>108</sup> At these locations, the fracture orientation is most often transverse or oblique. Simple fractures (i.e., those with only 2 fragments) are more common than comminuted fractures (i.e.,  $\geq 3$  fragments).<sup>108</sup> PSB fracture occurs equally in both forelimbs or is more frequently found in left limbs, depending on the racing population.<sup>1,108</sup>



**Figure 1.4:** Proximal Sesamoid Bone fracture configurations. A) Articular surface of intact PSBs is shown, PSBs are embedded in suspensory apparatus ligaments. B) PSBs with a biaxial fracture; lateral bone (left) shows a simple oblique fracture and medial bone (right) shows simple transverse basilar fracture. C) PSBs with a biaxial transverse midbody fracture of both bones; medial bone (left) has a simple midbody fracture and lateral bone (right) has a comminuted fracture.

In 55% - 80% of fatal cases, the medial and lateral PSBs fracture at the same time; this is considered a biaxial fracture.<sup>108</sup> In cases involving only one PSB, medial PSB fractures occur more often (15.9%) compared to lateral PSB fractures (4.1%).<sup>105</sup> Biaxial PSB fractures are especially damaging because the integrity of the suspensory apparatus is disrupted – this prevents the horse from bearing weight on the affected limb. The prognosis for surgical repair of biaxial PSB fracture is bleak.<sup>122</sup> Therefore, horses who sustain biaxial PSB fractures are usually humanely euthanized.

#### 1.5.4 Stress Fractures in Racehorses

Most catastrophic musculoskeletal injuries (MSIs) in racehorses, including PSB fractures, are believed to be stress-fractures resulting from the repetitive loads that occur during racing and training.<sup>1,123,124</sup> This idea is supported by the following observations: 1) fractures occur in specific anatomic sites, 2) the fractures have typical patterns, 3) incomplete fractures are often found in the contralateral intact limb, 4) pre-existing pathology (i.e., a periosteal callus, focal remodeling) often precedes a catastrophic fracture, 5) these fractures have been associated with specific trends in training program (i.e., more intensive training is associated with fracture) and 6) these fracture types do not occur in horses without habitual training and performance at high-speeds.

Pre-existing abnormalities in bone tissue have been observed in fractured PSBs. For example, bone volume fraction and trabecular thickness are greater in PSBs that have fractured than in those from

control horses.<sup>125,126</sup> Regional changes in bone volume fraction, with greater changes in bone volume fraction between case and control bones along the flexor (palmar) surface have been observed.<sup>125</sup> These differences likely reflect local bone responses to high loads and/or microdamage. Additionally, radiolucent bone lesions have been observed in the trabecular bone adjacent to the palmar surface.<sup>103,127</sup> These lesions are thought to be signs of stress remodeling that facilitate fracture initiation.<sup>70,125,128,129</sup> These lesions have also been found in the contralateral limb of horses that sustain unilateral biaxial PSB fracture. Since both forelimbs experience nearly equivalent loading patterns, pathological changes in both forelimbs are expected in horses that experienced a stress fracture in one limb. However, specific loading conditions that cause the pathologic changes are unknown. If the fracture had been the result of a traumatic incident, these changes would not be seen in the opposite forelimb's non-fractured PSBs. Anecdotally, subchondral bone abnormalities have been observed at necropsy in medial transverse midbody or basilar PSB fractures; these observations are described in detail in Chapters 2 and 5. Finally, epidemiologic studies indicate that horses with more intensive training are at higher risk for PSB fracture.<sup>130-132</sup> However, the specific nature of the exercise programs that lead to PSB fractures are unknown.

### **1.5.5 Prediction & Prevention of Proximal Sesamoid Bone Fractures**

While pathological evidence (e.g., periosteal callus) allows for clinical methods to screen many skeletal sites (i.e., scapula) at risk for a bone fracture prior to an exercise event, no reliable methods exist to pre-screen horses for PSBs fracture risk. The main reason no clinical methods exist is the location of the PSBs within the fetlock joint and the lack of understanding of the specific etiology of PSB fracture. The anatomy of the fetlock joint makes clinical radiographs isolating the PSBs difficult to obtain and the small density changes that precede a stress fracture cannot be identified in radiographic views where multiple bones overlap. Additionally, the anatomy of the fetlock joint makes it difficult to palpate the PSBs (e.g., they are embedded within a thick ligament). Recently, positron emission tomography (PET) scanning was

introduced at the Santa Anita racetrack in California to identify the subchondral lesion described in Chapters 2 and 5.<sup>133</sup> This method may prove a useful tool in identifying horses at risk for PSB fracture in the future. However, PET scanning is not widely available for clinical use, is expensive, and would have to be repeated at regular intervals to identify at risk horses.

While opportunities exist to enhance screening methods for horses at risk for PSB fracture, especially if etiology of PSB fracture were improved, these screening methods do not address the underlying relationship between racehorse exercise and PSB fracture. Assuming PSB fractures are stress fractures (which is supported by significant clinical evidence), there are likely training programs that put horses at a low-risk for PSB fractures. Epidemiological studies imply ‘high-intensity training’ puts horses at risk for PSB fracture, however, the complex interactions between exercise, race-surface properties, and bone remodeling have prevented recommendation of specific training programs to reduce fracture risk.<sup>95,130,131</sup> A case-control study with live racehorses to determine the effect of specific training programs on PSB fracture-risk is impractical; the requirement that animals be euthanized to collect research endpoints is prohibitively expensive and inhumane. Therefore, computer modeling is the most accessible method to determine how the complex interactions between exercise history, training- and race-surface properties, and bone’s innate repair process affect PSB fracture-risk.

## **1.6 Research Aims & Hypothesis**

Racehorse proximal sesamoid bones provide a naturally occurring model of osteochondral stress fractures. The research that follows has three Aims, all related to the etiology of Thoroughbred racehorse proximal sesamoid bone stress fractures. Most of this work has been published, or submitted for publication, as indicated.

**Aim One:** To compare microstructural and macrostructural features of PSBs from Thoroughbred racehorses with and without unilateral biaxial PSB fractures to identify bone abnormalities that precede

fracture. This work is novel in that it characterizes changes associated with PSB fracture within the subchondral tissue of racehorse PSBs. This work was published as:

Shaffer, SK., To, C., Garcia, TC., Fyhrie, DP., Stover, SM. Subchondral focal osteopenia associated with proximal sesamoid bone fracture in Thoroughbred racehorses. *Equine Veterinary Journal*. 2021. doi: 10.1111/evj.13291

**Aim Two:** To determine if the structural measures identified in Aim 1 are linked to horse exercise and to determine if a novel compartmental model of bone remodeling can be used to explain and predict the observed changes. The compartment model introduced for this Aim is novel. Additionally, the relationships found in this Aim between histomorphological measures and exercise add to the body of evidence indicating that PSB fractures in racehorses are stress fractures. This work has not been published, but a portion has been submitted for publication.

**Aim Three:** To determine the motion of the proximal sesamoid bones at racing-speed load conditions and if their motions may contribute to the formation of the abnormalities observed in Aim 1. This work is novel in that the three-dimensional movement of the PSBs have not been previously described. This work was published or accepted for publication pending revisions as:

Shaffer, SK., Sachs, N., Garcia, TC., Fyhrie, DP., Stover, SM. In vitro assessment of the motion of equine proximal sesamoid bones relative to the third metacarpal bone under physiologic midstance loads. *American Journal of Veterinary Research*. 2021. doi: 10.2460/ajvr.82.3.198

Shaffer, SK., Shelley, K., Garcia, TC., Samol, MA., Hill, AE., Fyhrie, DP., Stover, SM. In Vitro Motions of the Medial and Lateral Proximal Sesamoid Bones under Mid-Stance Load Conditions are Consistent with Racehorse Fracture Configurations. Accepted pending revisions to the *Journal of Biomechanics*.

## 1.7 References

1. Stover SM. The Epidemiology of Thoroughbred Racehorse Injuries. *Clin Tech Equine Pract.* 2003;2(4):312-322. doi:10.1053/j.ctep.2004.04.003
2. Martin RB, Burr DB, Sharkey NA, Fyhrie DP. *Skeletal Tissue Mechanics*. 2nd ed. New York, NY: Springer New York; 2015. doi:10.1007/978-1-4939-3002-9
3. Martin RB, Burr DB, Sharkey NA, Fyhrie DP. Skeletal Biology. In: *Skeletal Tissue Mechanics*. New York, NY: Springer New York; 2015:35-95. doi:10.1007/978-1-4939-3002-9
4. Hodgkinson R, Currey JD. Effects of Structural Variation on Young's Modulus of Non-Human Cancellous Bone. *Proc Inst Mech Eng Part H J Eng Med.* 1990;204(1):43-52. doi:10.1243/PIME\_PROC\_1990\_204\_227\_02
5. Boivin G, Farlay D, Bala Y, Doublier A, Meunier PJ, Delmas PD. Influence of remodeling on the mineralization of bone tissue. *Osteoporos Int.* 2009;20(6):1023-1026. doi:10.1007/s00198-009-0861-x
6. Currey JD. The structure and mechanics of bone. *J Mater Sci.* 2012;47(1):41-54. doi:10.1007/s10853-011-5914-9
7. Martin RB, Burr DB, Sharkey NA, Fyhrie DP. Fatigue and Fracture Resistance of Bone. In: *Skeletal Tissue Mechanics*. New York, NY: Springer New York; 2015:423-483. doi:10.1007/978-1-4939-3002-9
8. Yu B, Pacureanu A, Olivier C, Cloetens P, Peyrin F. Assessment of the human bone lacuno-canalicular network at the nanoscale and impact of spatial resolution. *Sci Rep.* 2020;10(1):4567. doi:10.1038/s41598-020-61269-8
9. Beniash E. Biominerals- hierarchical nanocomposites : the example of bone. *Wiley Interdiscip Rev Nanomed Nanobiotechnol.* 2011;3(1):47-69. doi:10.1002/wnan.105.Biominerals-
10. Donnelly E, Boskey AL, Baker SP, van der Meulen MCH. Effects of tissue age on bone tissue material composition and nanomechanical properties in the rat cortex. *J Biomed Mater Res Part A.* 2009;9999A(3):NA-NA. doi:10.1002/jbm.a.32442
11. Martin RB, Burr DB, Sharkey NA, Fyhrie DP. Mechanical Properties of Bone. In: *Skeletal Tissue Mechanics*. New York, NY: Springer New York; 2015:355-414. doi:10.1007/978-1-4939-3002-9
12. Hodgkinson R, Currey JD. Young's modulus, density and material properties in cancellous bone over a large density range. *J Mater Sci Mater Med.* 1992;3(5):377-381. doi:10.1007/BF00705371
13. Keller TS, Carter DR, Hernandez CJ, Beaupre GS. The Influence of Bone Volume Fraction and Ash Fraction on Bone Strength and Modulus. 2001;29(1):74-78.
14. Schaffler MB, Burr DB. Stiffness of compact bone: Effects of porosity and density. *J Biomech.* 1988;21(1):13-16. doi:10.1016/0021-9290(88)90186-8



15. Currey JD. The effect of porosity and mineral content on the Young's modulus of elasticity of compact bone. *J Biomech.* 1988;21(2):131-139. doi:10.1016/0021-9290(88)90006-1
16. Ciarelli TE, Fyhrie DP, Parfitt AM. Effects of vertebral bone fragility and bone formation rate on the mineralization levels of cancellous bone from white females. *Bone.* 2003;32(3):311-315. doi:10.1016/S8756-3282(02)00975-4
17. Goldstein SA. The mechanical properties of trabecular bone depend on anatomic location and function. *J Biomech.* 1987;20(11-12):1055-1061. doi:10.1016/0021-9290(87)90023-6
18. Meyers MA, Chawla K. *Mechanical Behavior of Materials.* Vol 81. 2nd ed. Cambridge University Press; 2009. doi:10.1108/aeat.2009.12781bae.001
19. Fyhrie DP, Schaffler MB. Failure mechanisms in human vertebral cancellous bone. *Bone.* 1994;15(1):105-109. doi:10.1016/8756-3282(94)90900-8
20. Goulet RW, Goldstein SA, Ciarelli MJ, Kuhn JL, Brown MB, Feldkamp LA. The relationship between the structural and orthogonal compressive properties of trabecular bone. *J Biomech.* 1994;27(4). doi:10.1016/0021-9290(94)90014-0
21. Rice JC, Cowin SC, Bowman JA. On the dependence of the elasticity and strength of cancellous bone on apparent density. *J Biomech.* 1988;21(2):155-168. doi:10.1016/0021-9290(88)90008-5
22. Hernandez CJ, Lambers FM, Widjaja J, Chapa C, Rimnac CM. Quantitative relationships between microdamage and cancellous bone strength and stiffness. *Bone.* 2014;66:205-213. doi:10.1016/j.bone.2014.05.023
23. Buenzli PR, Sims NA. Quantifying the osteocyte network in the human skeleton. *Bone.* 2015;75:144-150. doi:10.1016/j.bone.2015.02.016
24. Atkins GJ, Findlay DM. Osteocyte regulation of bone mineral: A little give and take. *Osteoporos Int.* 2012;23(8):2067-2079. doi:10.1007/s00198-012-1915-z
25. Robling AG, Castillo AB, Turner CH. Biomechanical and Molecular Regulation of Bone Remodeling. *Annu Rev Biomed Eng.* 2006;8(1):455-498. doi:10.1146/annurev.bioeng.8.061505.095721
26. Herman BC, Cardoso L, Majeska RJ, Jepsen KJ, Schaffler MB. Activation of bone remodeling after fatigue: Differential response to linear microcracks and diffuse damage. *Bone.* 2010;47(4):766-772. doi:10.1016/j.bone.2010.07.006
27. Hodsmann A., Kisiel M, Adachi J., Fraher L., Watson P. Histomorphometric evidence for increased bone turnover without change in cortical thickness or porosity after 2 years of cyclical hPTH(1-34) therapy in women with severe osteoporosis. *Bone.* 2000;27(2):311-318. doi:10.1016/S8756-3282(00)00316-1
28. Bradbeer JN, Arlot ME, Meunier PJ, Reeve J. Treatment of osteoporosis with parathyroid peptide (hPTH 1-34) and oestrogen: increase in volumetric density of iliac cancellous bone may depend on reduced trabecular spacing as well as increased thickness of packets of newly formed bone. *Clin Endocrinol (Oxf).* 1992;37(3):282-289. doi:10.1111/j.1365-2265.1992.tb02323.x

29. Martin RB, Burr DB, Sharkey NA, Fyhrie DP. Growth, Modeling, and Remodeling of Bone. In: *Skeletal Tissue Mechanics*. 2nd ed. New York, NY: Springer New York; 2015:95-168. doi:10.1007/978-1-4939-3002-9
30. Vashishth D, Verborgt O, Divine G, Schaffler MB, Fyhrie DP. Decline in osteocyte lacunar density in human cortical bone is associated with accumulation of microcracks with age. *Bone*. 2000;26(4):375-380. doi:10.1016/S8756-3282(00)00236-2
31. Dempster DW, Compston JE, Drezner MK, et al. Standardized nomenclature, symbols, and units for bone histomorphometry: A 2012 update of the report of the ASBMR Histomorphometry Nomenclature Committee. *J Bone Miner Res*. 2013;28(1):2-17. doi:10.1002/jbmr.1805
32. Parfitt AM, Han Z-H, Palnitkar S, Rao DS, Nelson D. Effects of Ethnicity and Age or Menopause on the Remodeling and Turnover of Iliac Bone: Implications for Mechanisms of Bone Loss. *J Bone Miner Res*. 1997;12(4):498-508. doi:10.1359/jbmr.1997.12.4.498
33. Fuchs RK, Allen MR, Ruppel ME, et al. In situ examination of the time-course for secondary mineralization of Haversian bone using synchrotron Fourier transform infrared microspectroscopy. *Matrix Biol*. 2008;27(1):34-41. doi:10.1016/j.matbio.2007.07.006
34. Bala Y, Farlay D, Delmas PD, Meunier PJ, Boivin G. Time sequence of secondary mineralization and microhardness in cortical and cancellous bone from ewes. *Bone*. 2010;46(4):1204-1212. doi:10.1016/j.bone.2009.11.032
35. Grynpas M. Age and disease-related changes in the mineral of bone. *Calcif Tissue Int*. 1993;53(1 Supplement). doi:10.1007/BF01673403
36. Parfitt AM. The Physiologic and Clinical Significance of Bone Histomorphometric Data. In: Recker RR, ed. *Bone Histomorphometry : Techniques and Interpretation*. ; 1983:143-224.
37. Amprino R, Engström A. STUDIES ON X RAY ABSORPTION AND DIFFRACTION OF BONE TISSUE. *Cells Tissues Organs*. 1952;15(1-2):1-22. doi:10.1159/000140734
38. Marotti G, Favia A, Zallone AZ. Quantitative analysis on the rate of secondary bone mineralization. *Calcif Tissue Res*. 1972;10(1):67-81. doi:10.1007/BF02012537
39. Lukas C, Ruffoni D, Lambers FM, et al. Mineralization kinetics in murine trabecular bone quantified by time-lapsed in vivo micro-computed tomography. *Bone*. 2013;56(1):55-60. doi:10.1016/j.bone.2013.05.005
40. Von Euw S, Wang Y, Laurent G, et al. Bone mineral: new insights into its chemical composition. *Sci Rep*. 2019;9(1):8456. doi:10.1038/s41598-019-44620-6
41. Wergedal J, Baylink D. Electron microprobe measurements of bone mineralization rate in vivo. *Am J Physiol Content*. 1974;226(2):345-352. doi:10.1152/ajplegacy.1974.226.2.345
42. Schaffler MB, Radin EL, Burr DB. Long-term fatigue behavior of compact bone at low strain magnitude and rate. *Bone*. 1990;11(5):321-326. doi:10.1016/8756-3282(90)90087-F

43. Seref-Ferlengez Z, Kennedy OD, Schaffler MB. Bone microdamage, remodeling and bone fragility: how much damage is too much damage? *Bonekey Rep.* 2015;4(September 2014):1-7. doi:10.1038/bonekey.2015.11
44. Boyce TM, Fyhrie DP, Glotkowski MC, Radin EL, Schaffler MB. Damage type and strain mode associations in human compact bone bending fatigue. *J Orthop Res.* 1998;16(3):322-329. doi:10.1002/jor.1100160308
45. Schaffler MB, Choi K, Milgrom C. Aging and matrix microdamage accumulation in human compact bone. *Bone.* 1995;17(6):521-525. doi:10.1016/8756-3282(95)00370-3
46. Yeni YN, Fyhrie DP. Fatigue damage-fracture mechanics interaction in cortical bone. *Bone.* 2002;30(3):509-514. doi:10.1016/S8756-3282(01)00696-2
47. Burr DB, Turner CH, Naick P, et al. Does microdamage accumulation affect the mechanical properties of bone? *J Biomech.* 1998;31:337-345.
48. Fletcher L, Codrington J, Parkinson I. Effects of fatigue induced damage on the longitudinal fracture resistance of cortical bone. *J Mater Sci Mater Med.* 2014;25(7):1661-1670. doi:10.1007/s10856-014-5213-5
49. Burr DB. *Remodeling and Repair of Fatigue Damage.* Vol 53. London; 1993. doi:10.1007/BF01673407
50. Bentolila V, Boyce TM, Fyhrie DP, Drumb R, Skerry TM, Schaffler MB. Intracortical remodeling in adult rat long bones after fatigue loading. *Bone.* 1998;23(3):275-281. doi:10.1016/S8756-3282(98)00104-5
51. Hernandez CJ, Gupta A, Keaveny TM. A Biomechanical Analysis of the Effects of Resorption Cavities on Cancellous Bone Strength. *J Bone Miner Res.* 2006;21(8):1248-1255. doi:10.1359/jbmr.060514
52. Slyfield CR, Tkachenko EV, Fischer SE, et al. Mechanical failure begins preferentially near resorption cavities in human vertebral cancellous bone under compression. *Bone.* 2012;50(6):1281-1287. doi:10.1016/j.bone.2012.02.636
53. Riggs CM. Fractures - A preventable hazard of racing thoroughbreds? *Vet J.* 2002;163(1):19-29. doi:10.1053/tvjl.2001.0610
54. Ferry AT, Graves T, Theodore GH, Gill TJ. Stress fractures in athletes. *Phys Sportsmed.* 2010;38(2):109-116. doi:10.3810/psm.2010.06.1788
55. Matcuk GR, Mahanty SR, Skalski MR, Patel DB, White EA, Gottsegen CJ. Stress fractures: pathophysiology, clinical presentation, imaging features, and treatment options. *Emerg Radiol.* 2016;23(4):365-375. doi:10.1007/s10140-016-1390-5
56. Turner CH. Three rules for bone adaptation to mechanical stimuli. *Bone.* 1998;23(5):399-407. doi:10.1016/S8756-3282(98)00118-5

57. Turner CH. Skeletal Adaptation to Mechanical Loading. *Clin Rev Bone Miner Metab.* 2007;5(4):181-194. doi:10.1007/s12018-008-9010-x
58. Hsieh Y-F, Turner CH. Effects of Loading Frequency on Mechanically Induced Bone Formation. *J Bone Miner Res.* 2001;16(5):918-924. doi:10.1359/jbmr.2001.16.5.918
59. Marin-Puyalto J, Gomez-Cabello A, Gonzalez-Agüero A, et al. Is Vibration Training Good for Your Bones? An Overview of Systematic Reviews. *Biomed Res Int.* 2018;2018:1-16. doi:10.1155/2018/5178284
60. Rubin C, Turner AS, Mallinckrodt C, Jerome C, Mcleod K, Bain S. Mechanical strain, induced noninvasively in the high-frequency domain, is anabolic to cancellous bone, but not cortical bone. *Bone.* 2002;30(3):445-452. doi:10.1016/S8756-3282(01)00689-5
61. Uththoff HK, Sékaly G, Jaworski ZF. Effect of long-term nontraumatic immobilization on metaphyseal spongiosa in young adult and old beagle dogs. *Clin Orthop Relat Res.* 1985. doi:10.1097/00003086-198501000-00040
62. Uththoff HK, Jaworski ZFG. Bone loss in response to long term immobilisation. *J Bone Jt Surg.* 1978.
63. Hsieh YF, Robling AG, Ambrosius WT, Burr DB, Turner CH. Mechanical loading of diaphyseal bone in vivo: The strain threshold for an osteogenic response varies with location. *J Bone Miner Res.* 2001;16(12):2291-2297. doi:10.1359/jbmr.2001.16.12.2291
64. Umemura Y, Ishiko T, Yamauchi T, Kurono M, Mashiko S. Five jumps per day increase bone mass and breaking force in rats. *J Bone Miner Res.* 1997;12(9):1480-1485. doi:10.1359/jbmr.1997.12.9.1480
65. Rubin C, Lanyon L. Bone remodeling in response to applied dynamic loads. *J Bone Jt Surg.* 1984;66-A(3):397-402.
66. Robling AG, Burr DB, Turner CH. Partitioning a Daily Mechanical Stimulus into Discrete Loading Bouts Improves the Osteogenic Response to Loading. *J Bone Miner Res.* 2000;15(8):1596-1602. doi:10.1359/jbmr.2000.15.8.1596
67. Aicale R, Tarantino D, Maffulli N. Overuse injuries in sport: A comprehensive overview. *J Orthop Surg Res.* 2018;13(1):1-11. doi:10.1186/s13018-018-1017-5
68. Riggs CM. Osteochondral injury and joint disease in the athletic horse. *Equine Vet Educ.* 2006;18(April):100-112.
69. Barr ED, Pinchbeck GL, Clegg PD, Boyde A, Riggs CM. Post mortem evaluation of palmar osteochondral disease (traumatic osteochondrosis) of the metacarpal/metatarsophalangeal joint in Thoroughbred racehorses. *Equine Vet J.* 2009;41(4):366-371. doi:10.2746/042516409X368372
70. Stover SM. Diagnostic Workup of Upper-Limb Stress Fractures and Proximal Sesamoid Bone Stress Remodeling. In: *AAEP Proceedings; In-Depth: Racing-Related Lameness.* Vol 59. ; 2013:427-435.

71. Martin RB, Burr DB, Sharkey NA, Fyhrie DP. *Mechanical Adaptability of the Skeleton*. 2nd ed. New York, NY: Springer New York; 2015. doi:10.1007/978-1-4939-3002-9
72. Milgrom C, Finestone AS. The effect of stress fracture interventions in a single elite infantry training unit (1983–2015). *Bone*. 2017;103:125-130. doi:10.1016/j.bone.2017.06.026
73. Hazelwood SJ, Castillo AB. Simulated effects of marathon training on bone density, remodeling, and microdamage accumulation of the femur. *Int J Fatigue*. 2007;29(6):1057-1064. doi:10.1016/j.ijfatigue.2006.10.001
74. Cowin SC. The Relationship Between the Elasticity Tensor and the Fabric Tensor. *Mech Mater*. 1985;4:137-147.
75. Fyhrie DP, Fazzalari NL, Goulet R, Goldstein SA. Direct calculation of the surface-to-volume ratio for human cancellous bone. *J Biomech*. 1993;26(8):955-967. doi:10.1016/0021-9290(93)90057-L
76. Moreno R, Smedby O, Borga M. Techniques for Computing Fabric Tensors: A Review. In: Westin C-F, Vilanova A, Burgeth B, eds. *Visualization and Processing of Tensors and Higher Order Descriptors for Multi-Valued Data*. Vol 1. Berlin: Springer; 2014:271-292. <http://drops.dagstuhl.de/opus/volltexte/2012/3444>.
77. Cowin SC, Mehrabadi MM. Identification of the elastic symmetry of bone and other materials. *J Biomech*. 1989;22(6-7):503-515. doi:10.1016/0021-9290(89)90001-8
78. Wirtz DC, Schiffers N, Forst R, Pandorf T, Weichert D, Radermacher K. Critical evaluation of known bone material properties to realize anisotropic FE-simulation of the proximal femur. *J Biomech*. 2000;33(10):1325-1330. doi:10.1016/S0021-9290(00)00069-5
79. Fyhrie DP, Carter DR. A unifying principle relating stress to trabecular bone morphology. *J Orthop Res*. 1986;4(3):304-317. doi:10.1002/jor.1100040307
80. Ün K, Çalık A. Relevance of inhomogeneous–anisotropic models of human cortical bone: a tibia study using the finite element method. *Biotechnol Biotechnol Equip*. 2016;30(3):538-547. doi:10.1080/13102818.2016.1154803
81. Fyhrie DP, Schaffler MB. The Adaptation of Bone Apparent Density to Applied Load. *J Biomech*. 1995;28(2):135-146.
82. Hart RT, Davy DT, Heiple KG. A Computational Method for Stress Analysis of Adaptive Elastic Materials With a View Toward Applications in Strain-Induced Bone Remodeling. *J Biomech Eng*. 2009;106(4):342. doi:10.1115/1.3138503
83. Weinans H, Huskies R, Grootenboer HJ. The Behavior of Adaptive Bone-Remodeling Simulation Models. *J Biomech*. 1992;25(12):1425-1441.
84. Beaupré G., Orr TE, Carter D. An approach for time-dependent bone modeling and remodeling - theoretical development. *J Orthop Res*. 1990;8(5):651-661.
85. Peterson MC, Riggs MM. A physiologically based mathematical model of integrated calcium

- homeostasis and bone remodeling. *Bone*. 2010;46(1):49-63. doi:10.1016/j.bone.2009.08.053
86. Hazelwood SJ, Martin RB, Rashid MM, Rodrigo JJ. A mechanistic model for internal bone remodeling exhibits different dynamic responses in disuse and overload. *J Biomech*. 2001;34(3):299-308. doi:10.1016/S0021-9290(00)00221-9
  87. Mullender MG, Huiskes R, Weinans H. A Physiological Approach to the Simulation of Bone Remodeling as a Self-Organizational Control Process. *J Biomech*. 1994;27(11):1389-1394.
  88. van Schaick E, Zheng J, Ruixo JJP, Gieschke R, Jacqmin P. A semi-mechanistic model of bone mineral density and bone turnover based on a circular model of bone remodeling. *J Pharmacokinet Pharmacodyn*. 2015;42(4):315-332. doi:10.1007/s10928-015-9423-3
  89. van Oers RFM, Ruimerman R, Tanck E, Hilbers PAJ, Huiskes R. A unified theory for osteonal and hemi-osteonal remodeling. *Bone*. 2008;42(2):250-259. doi:10.1016/j.bone.2007.10.009
  90. van Oers RFM, van Rietbergen B, Ito K, Huiskes R, Hilbers PAJ. Simulations of trabecular remodeling and fatigue: Is remodeling helpful or harmful? *Bone*. 2011;48(5):1210-1215. doi:10.1016/j.bone.2011.01.011
  91. Martin RB. The usefulness of mathematical models for bone remodeling. *Yearb Phys Anthropol*. 1985;28:227-236. doi:10.1002/ajpa.1330280512
  92. Martin RB. Mathematical model for repair of fatigue damage and stress fracture in osteonal bone. *J Orthop Res*. 1995;13(3):309-316. doi:10.1002/jor.1100130303
  93. Huiskes R. Adaptive Bone-Remodeling Theory Applied to Prosthetic-Design Analysis. *J Biomech*. 1987;29(11-12):1135-1150.
  94. Vallance SA, Case JT, Entwistle RC, et al. Characteristics of Thoroughbred and Quarter Horse racehorses that sustained a complete scapular fracture. *Equine Vet J*. 2012;44(4):425-431. doi:10.1111/j.2042-3306.2011.00481.x
  95. Johnson BJ, Stover SM, Daft BM, et al. Causes of death in racehorses over a 2 year period. *Equine Vet J*. 1994;26(4):327-330. doi:10.1111/j.2042-3306.1994.tb04395.x
  96. *California Horse Racing Board Postmortem Examination Program 2017-2018 Annual Report*. Davis, CA; 2019. [http://chr.ca.gov/postmortem\\_reports.html](http://chr.ca.gov/postmortem_reports.html).
  97. Hitchens PL, Hill AE, Stover SM. Jockey Falls, Injuries, and fatalities associated with thoroughbred and Quarter Horse racing in California, 2007-2011. *Orthop J Sport Med*. 2013;1(1):1-7. doi:10.1177/2325967113492625
  98. Hitchens PL, Hill AE, Stover SM. The role of catastrophic injury or sudden death of the horse in race-day jockey falls and injuries in California, 2007-2012. *Equine Vet J*. 2016;48(1):50-56. doi:10.1111/evj.12392
  99. Delay J. Postmortem findings in Ontario racehorses , 2003 – 2015. *J Vet Diagnostic Investig*. 2017;29(4). doi:10.1177/1040638717700690

100. Wylie CE, McManus P, McDonald C, Jorgensen S, McGreevy P. Thoroughbred fatality and associated jockey falls and injuries in races in New South Wales and the Australian Capital Territory, Australia: 2009–2014. *Vet J.* 2017;227:1-7. doi:10.1016/j.tvjl.2017.06.008
101. Spargo KE, Rubio-Martinez LM, Wheeler DP, Fletcher L, Carstens A. Catastrophic musculoskeletal injuries in Thoroughbred racehorses on racetracks in Gauteng, South Africa. *J S Afr Vet Assoc.* 2019;90:1019-9128. doi:10.4102/jsava.v90i0.1640
102. Sun TC, Riggs CM, Cogger N, Wright J, Al-Alawneh JI. Noncatastrophic and catastrophic fractures in racing Thoroughbreds at the Hong Kong Jockey Club. *Equine Vet J.* 2019;51(1):77-82. doi:10.1111/evj.12953
103. Stover SM. Personal Communication. 2015.
104. *Supplemental Tables of Equine Injury Database Statistics for Thoroughbreds.*; 2018.
105. Hill AE. *Unpublished Data.*; 2020.
106. Ferraro GL, Stover SM, Whitcomb MB. *Suspensory Ligament Injuries in Horses.* Davis; 1999.
107. Beccati F, Gialletti R, Giontella A, Davanzo S, Di Meo A, Pepe M. Morphologic radiographic study of the proximal sesamoid bones of the forelimb in thoroughbred racehorses in training. *J Vet Med Ser C Anat Histol Embryol.* 2014;43(5):403-407. doi:10.1111/ahe.12075
108. Anthenill LA, Stover SM, Gardner IA, et al. Association between findings on palmarodorsal radiographic images and detection of a fracture in the proximal sesamoid bones of forelimbs obtained from cadavers of racing Thoroughbreds. *Am J Vet Res.* 2006;67(5):858-868. doi:10.2460/ajvr.67.5.858
109. Janes JG, Kennedy LA, Garrett KS, Engiles JB. Common lesions of the distal end of the third metacarpal/metatarsal bone in racehorse catastrophic breakdown injuries. *J Vet Diagnostic Investig.* 2017;29(4):431-436. doi:10.1177/1040638717717948
110. Pool R, Meagher D. Pathologic findings and pathogenesis of racetrack injuries. *Vet Clin North Am Equine Pract.* 1990;6(1):1-30. doi:10.1016/S0749-0720(15)30891-4
111. Park RD. Equine Diagnostic Imaging - Part 1 Radiology. In: Stashak TS, ed. *Adams' Lameness in Horses.* 5th Editio. Philadelphia: Lippincott Williams & Wilkins; 2002:228-231.
112. Wang D, Shi L, Griffith JF, Qin L, Yew DTW, Riggs CM. Comprehensive surface-based morphometry reveals the association of fracture risk and bone geometry. *J Orthop Res.* 2012;30(8):1277-1284. doi:10.1002/jor.22062
113. Swanstrom MD, Stover SM, Hubbard M, Hawkins DA. Determination of passive mechanical properties of the superficial and deep digital flexor muscle-ligament-tendon complexes in the forelimbs of horses. *Am J Vet Res.* 2004;65(2):188-197. doi:10.2460/ajvr.2004.65.188
114. Young DR, Nunamaker DM, Markel MD. Quantitative evaluation of the remodeling response of the proximal sesamoid bones to training-related stimuli in Thoroughbreds. *Am J Vet Res.*

1991;52(8):1350-1356. doi:0096-1523/92

115. Setterbo J, Garcia T, Campbell I, Kim S, Hubbard M, Stover S. Forelimb Kinematics of Galloping Thoroughbred Racehorses Measured on Dirt, Synthetic, and Turf Track Surfaces (P235). In: *The Engineering of Sport 7*. Paris: Springer Paris; 2009:437-446. doi:10.1007/978-2-287-99056-4\_54
116. Chateau H, Degueurce C, Denoix J-M. Evaluation of three-dimensional kinematics of the distal portion of the forelimb in horses walking in a straight line. *Am J Vet Res*. 2004;65(4):447-455. doi:10.2460/ajvr.2004.65.447
117. Clayton HM, Sha D, Stick J, Elvin N. 3D Kinematics of the equine metacarpophalangeal joint at walk and trot. *Vet Comp Orthop Traumatol*. 2007;(20):86-91. doi:10.1160/VCOT-07-01-0011
118. Chateau H, Degueurce C, Jerbi H, et al. Normal three-dimensional behaviour of the metacarpophalangeal joint and the effect of uneven foot bearing. *Equine Vet J*. 2001;33(S33):84-88. doi:10.1111/j.2042-3306.2001.tb05366.x
119. Stutz JC, Vidondo B, Ramseyer A, Maninchedda UE, Cruz AM. Effect of three types of horseshoes and unshod feet on selected nonpodal forelimb kinematic variables measured by an extremity mounted inertial measurement unit sensor system in sound horses at the trot under conditions of treadmill and soft geotextile su. *Vet Rec Open*. 2018;5(1):1-12. doi:10.1136/vetreco-2017-000237
120. Chateau H, Degueurce C, Denoix J-M. Three-dimensional kinematics of the equine distal forelimb: effects of a sharp turn at the walk. *Equine Vet J*. 2010;37(1):12-18. doi:10.2746/0425164054406946
121. Childs B, Pugliese B, Carballo C, Miranda D, Brainerd E, Kirker-Head C. Three-dimensional kinematics of the equine metacarpophalangeal joint using x-ray reconstruction of moving morphology – a pilot study. *Vet Comp Orthop Traumatol*. 2017;30(04):1-8. doi:10.3415/VCOT-16-06-0095
122. Trumble TN, Arnoczky S, Stick J, Stickle R. Clinical relevance of the microvasculature of the equine proximal sesamoid bone. *Am J Vet Res*. 1995;56(6):720-724.
123. Martig S, Chen W, Lee PVS, Whitton RC. Bone fatigue and its implications for injuries in racehorses. *Equine Vet J*. 2014;46(4):408-415. doi:10.1111/evj.12241
124. Stover SM. Nomenclature, classification, and documentation of catastrophic fractures and associated preexisting injuries in racehorses. *J Vet Diagnostic Investig*. 2017;29(4):396-404. doi:10.1177/1040638717692846
125. Cresswell EN, McDonough SP, Palmer SE, Hernandez CJ, Reesink HL. Can Quantitative Computed Tomography Detect Bone Morphological Changes Associated with Catastrophic Proximal Sesamoid Bone Fracture in Thoroughbred Racehorses? *Equine Vet J*. 2018:1-8. doi:10.1111/evj.12965
126. Peloso JG, Vogler JB, Cohen ND, et al. Association of catastrophic biaxial fracture of the proximal sesamoid bones with bony changes of the metacarpophalangeal joint identified by standing



- magnetic resonance imaging in cadaveric forelimbs of Thoroughbred racehorses. *J Am Vet Med Assoc.* 2015;246(6):661-673. doi:10.2460/javma.246.6.661
127. Anthenill LA, Gardner IA, Pool R, Garcia TC, Stover SM. Palmar Lesions and Trabecular Bone Compaction Likely Precede Proximal Sesamoid Bone Mid- Body Fractures in Thoroughbred Racehorses. 2009;55:2009.
  128. Anthenill LA, Gardner IA, Pool RR, Garcia TC, Stover SM. Comparison of macrostructural and microstructural bone features in Thoroughbred racehorses with and without midbody fracture of the proximal sesamoid bone. *Am J Vet Res.* 2010;71(7):755-765. doi:10.2460/ajvr.71.7.755
  129. McKerney E, Collar E, Stover SM. Fatal Musculoskeletal Injuries of the Metacarpophalangeal and Metatarsophalangeal (Fetlock) Joint in California Racehorses: One Hundred and Thirty-Nine Cases. In: *Fatal Musculoskeletal Injuries of the Metacarpophalangeal and Metatarsophalangeal (Fetlock) Joint in California Racehorses: One Hundred and Thirty-Nine Cases.* AAEP Proceedings; 2013:402.
  130. Hill AE, Gardner IA, Carpenter TE, Stover SM. Effects of injury to the suspensory apparatus, exercise, and horseshoe characteristics on the risk of lateral condylar fracture and suspensory apparatus failure in forelimbs of Thoroughbred racehorses. *Am J Vet Res.* 2004;65(11):1508-1517. doi:10.2460/ajvr.2004.65.1508
  131. Anthenill LA, Stover SM, Gardner IA, Hill AE. Risk factors for proximal sesamoid bone fractures associated with exercise history and horseshoe characteristics in Thoroughbred racehorses. *Am J Vet Res.* 2007;68(7):760-771. doi:10.2460/ajvr.68.7.760
  132. Carrier T, Estberg L, Stover SM, et al. Association between long periods without high-speed workouts and risk of complete humeral or pelvic fracture in Thoroughbred racehorses: 54 Cases (1991-1994). *Javma.* 1998;212(10):1582-1587.
  133. Spriet M, Espinosa P, Kyme AZ, et al. 18F-sodium fluoride positron emission tomography of the equine distal limb: Exploratory study in three horses. *Equine Vet J.* 2018;50(1):125-132. doi:10.1111/evj.12719

## **Chapter 2: Subchondral Focal Osteopenia Associated with Proximal Sesamoid**

### **Bone Fracture in Thoroughbred Racehorses**

This chapter has been published as:

Shaffer, S.K., To, C., Garcia, T.C., Fyhrie, D.P., Uzal, F.A., Stover, S.M., 2021. Subchondral focal osteopenia associated with proximal sesamoid bone fracture in Thoroughbred racehorses. *Equine Veterinary Journal*, 53, 294-305. <https://doi.org/10.1111/evj.13291>

#### **2.1 Abstract**

**Background:** Proximal sesamoid bone (PSB) fracture is the most common fatal injury in Thoroughbred (TB) racehorses in the United States. Epidemiological and pathological evidence indicate PSB fracture is likely the acute culmination of a chronic stress-related process. However, the etiopathogenesis of PSB fracture is poorly understood.

**Objective:** To characterize bone abnormalities that precede PSB fracture.

**Study design:** Two retrospective case-control groups of PSBs from TB racehorses with, and without, unilateral biaxial PSB fracture.

**Methods:** Proximal sesamoid bones were harvested postmortem from TB racehorses euthanized for unilateral biaxial PSB fracture (cases) or causes unrelated to PSB fracture (controls) while racing or training. The fractured medial PSB (FX-PSB) and contralateral intact medial PSB (CLI-PSB) from racehorses that sustained PSB fracture, and an intact medial PSB (CTRL-PSB) from racehorses that did not have a PSB fracture were collected as case and control specimens. *Study 1*) distributions of morphologic features were compared among case and control groups using visual examination, photographs, radiographs, and histology of whole PSBs and serial sagittal sections (10 FX-PSB, 10 CLI-PSB, 10 CTRL-PSB). *Study 2*) local

bone volume fraction and mineral densities were compared among case and control PSBs using microcomputed tomography (9 FX-PSB, 9 CLI-PSB, 9 CTRL-PSB).

**Results:** A focal subchondral lesion characterized by co-localized focal discoloration, radiolucency, osteopenia, low tissue mineral density, and a surrounding region of dense cancellous bone was identified in most case horses but not in controls. This subchondral lesion was found in a slightly abaxial mid-body location and was bilaterally present in most case horses.

**Main limitations:** The postmortem samples may not represent the spectrum of abnormalities that occur throughout the development of the subchondral lesion. Lateral PSBs were not examined, so their contribution to biaxial PSB fracture pathogenesis is unknown.

**Conclusion:** Abaxial subchondral lesions are consistent with pre-existing injury and likely associated with PSB fracture.

## 2.2 Introduction

Musculoskeletal injuries have an adverse effect on the racing industry, often resulting in racehorse death or permanent removal from racing and in jockey injury. Musculoskeletal injuries are the most common cause of racehorse death associated with racing or training.<sup>1,2</sup> The most common fatal injury in the United States is fracture of the proximal sesamoid bones (PSBs) – accounting for 45-50% and 37-40% of fatal injuries to Thoroughbred and Quarter Horse racehorses, respectively.<sup>1,3,4</sup>

Epidemiological evidence supports the premise that PSB fractures are the acute manifestation of chronic repetitive loading.<sup>5</sup> Racehorses in intensive training are at higher risk for PSB fracture.<sup>6</sup> Racehorses that spend more time in active training and racing, compete in more events, have higher high speed exercise intensities in the 6-12 months before death, and greater cumulative distances in their career than

their cohort are at a higher risk for PSB fracture.<sup>6-9</sup> Therefore, common recommendations to prevent PSB fracture include limitations on exercise intensity and the amount of continual time racing.<sup>6</sup>

Understanding the mechanism of PSB fracture is necessary to reduce fracture risk and determine links between risk factors and fracture prevention. Two theories have been proposed to explain PSB fracture: 1) disproportionate rates of bone and ligament strengthening in response to training cause the PSBs to be the weakest link in the suspensory apparatus and 2) transient changes in PSBs due to an imbalance in the rates of damage accumulation and repair create a focal site for fracture initiation.<sup>4,5,10</sup> Racehorse third metacarpal, scapular, and cervical spine fractures are associated with preexisting focal bone changes that degrade material properties and predispose the bone to fracture.<sup>11,12</sup> These preexisting changes are often observed in the contralateral, non-fractured limb, due to the bilateral nature of repetitive overuse injuries; clinical fracture occurs in the more severely affected limb.<sup>13-15</sup>

Proximal sesamoid bones were examined to determine if pre-existing abnormalities are associated with PSB fracture. It was hypothesized that horses with unilateral biaxial PSB fracture will have bilateral evidence of focal stress remodeling associated with PSB fracture and that fractured PSBs will have more severe changes than contralateral intact PSBs.

## **2.3 Materials and Methods**

Two independent studies were performed that each compared findings among different sets of 3 groups of PSBs: fractured medial PSBs from case racehorses that sustained PSB fracture (FX-PSB), the contralateral intact medial PSB from case racehorses that sustained PSB fracture (CLI-PSB), and intact medial PSBs from control racehorses that died from a cause unrelated to PSB fracture (CTRL-PSB). *Study 1* examined morphologic findings from whole PSBs and serial sagittal sections. *Study 2* compared tissue morphometric properties from microcomputed tomography ( $\mu$ CT) scans. Bones were harvested from

Thoroughbred racehorses that died during racing or training and were necropsied for the California Horse Racing Board from 2000-2017. The suspensory apparatus was excised from the forelimb during necropsy, within 1-4 days of death after storage at 4C, and excised PSBs were stored in saline soaked towels in watertight bags at -20C until studied.

### **2.3.1 Study 1 – Morphologic study**

Ten case (1 female, 5 gelding, 4 stallion; 2-8 years old, median age 3 years old) and 10 control (3 female, 5 gelding, 2 stallion; 2-7 years old, median age 3 years old) horses were selected from a set of 96 Thoroughbred racehorses (39 case horses, 2-14 years old, median age 4 years old; 57 control horses, 2-8 years old, median age 3 years old) that were euthanized because of an injury that occurred during racing or training. Study horses were selected to span different exercise intensity training histories because PSB fracture has been associated with high intensity training and racing.<sup>6,9</sup> Therefore, the study sample of 10 case and 10 control horses was selected using a multivariable stepwise logistic regression of exercise history variables reduced from races and official timed work-outs from official records [Jockey Club Information Systems]<sup>A</sup> to predict case status, similar to previous studies.<sup>16</sup> The regression (max-rescaled  $r^2 = 0.35$ , area under ROC = 0.80) was used to predict the probability that a horse was a case (Supplementary Item 1) [SAS 9.4]<sup>B</sup>. From this model, stratified sampling was used to select 10 case and 10 control horses, distributed among the full range of probabilities. This selection of 10 case and 10 control horses provided 10 FX-PSB, 10 CLI-PSB, and 10-CTRL-PSBs. Case horses were euthanized due to unilateral forelimb (8 left, 2 right) biaxial PSB fracture; control horses were euthanized due to fracture to the carpus (2), humerus (2), third metacarpal bone (2), proximal phalanx (2), pelvis (1), or radius (1).

All PSBs were excised from the suspensory apparatus. Fracture surfaces and dorsal, palmar, axial, and abaxial surfaces of whole PSBs and reconstructed FX-PSBs were photographed and scanned using  $\mu$ CT [ $\mu$ CT 35C;  $18.5\mu\text{m}^3$  voxels, 7 kVP, 114  $\mu\text{A}$ , 2.5s integration time; calibrated with ScanCo phantom].

Subsequently PSBs were embedded in polymethyl-methacrylate (PMMA) and cut into 3mm thick serial sagittal sections using a circular saw [IsoMet 1000 Precision Cutter]<sup>D</sup>. Axial and abaxial sides of each section were photographed and high-detail contact radiographs were obtained with the abaxial side in contact with the radiography film [43855N X-Ray System Faxitron Series<sup>E</sup>, 35 kVp, 40 kVp, 2 minute exposures; Oncology Portal Pack for Localization<sup>F</sup>].

Photographs and high detail contact radiographic images were respectively evaluated for discoloration (presence, location, severity, distribution), focal radiolucency, density pattern, fracture pattern, and fracture surface incongruities (Supplementary Item 2). Areas of focal radiolucency observed on high-detail radiographs of the sagittal sections were confirmed using the  $\mu$ CT images. Photographs, high detail radiographs, and  $\mu$ CT images were evaluated twice by one observer (SKS) with a Kappa agreement statistic (0.8 median, range 0.54-1; evaluation over three week time period) for features that could be correlated with adaptive and/or pathologic processes [SAS 9.4]<sup>B</sup>. Categorical variables with discrepancies between the two attempts were re-evaluated a third time by the same observer and all three attempts were compared to choose final classification.

Differences in the distributions for variables among FX-PSB, CLI-PSB, and CTRL-PSB groups were assessed using Fisher's Exact Tests [SAS 9.4]<sup>B</sup>. Correlations among variables were assessed using Spearman's correlation coefficient ( $r$ ) [SAS 9.4]<sup>B</sup>. A  $p \leq 0.05$  was considered statistically significant.

Sagittal sections for histology were selected based on the presence of gross discoloration; if no discoloration was present in a PSB's sections, a section was selected from a similar location as those with discoloration. Sections were fixed in buffered formalin, decalcified, embedded in paraffin, cut into 4  $\mu$ m thick sections, stained with Hematoxylin & Eosin (H&E), and examined using brightfield microscopy (Olympus VS120 Virtual Slide Microscope, 20x objective; Olympus Soft Imaging Solutions VC50 camera). Histologic findings are described.

### 2.3.2 Study 2 – Tissue morphometric study

Nine case (5 female, 2 gelding, 2 stallions; 3-4 years old, median age 4) and 9 Control Thoroughbred racehorses (6 female, 1 gelding, 2 stallions; 2-4 years old, median age 3) provided 9 medial FX-PSBs, 9 medial CLI-PSBs, and 18 bilateral medial CTRL-PSBs. Case horses were euthanized due to unilateral biaxial PSB fracture and had focal semi-circular subchondral discoloration on the fracture surface. Control horses were euthanized due to carpal bone fracture (1), hindlimb PSB fracture (1), laminitis (1), pneumonia (3), radius fracture (1), humeral fracture (1), and sudden death of unknown cause (1). Bones from 2 control horses were also used in Study 1.

Bones were imaged with a high-resolution  $\mu$ CT specimen scanner [Siemens Inveon CT<sup>G</sup>, 80 kVP, 315 uA, 1650 ms exposure time, 35.7  $\mu\text{m}^3$  voxels, 1081 projections per 360 degrees]. Bone volume fraction (BVF), apparent mineral density (AMD), tissue mineral density (TMD), trabecular number (Tb.N), and trabecular thickness (Tb.Th) were determined for two half-cylindrical regions of interest (ROI) [ScanCO  $\mu$ CT Evaluation Software v6.5-3]<sup>C</sup>. The first ROI (ROI-1) was drawn surrounding the focal region that was co-located with subchondral discoloration (Fig 2.1). A second ROI (ROI-2), a within bone control region, was centered at one-third of the maximum width of ROI-1 away from the most axial point of ROI-1 (this region was not obtainable on all FX-PSBs). In PSBs without focal radiolucency (CTRL-PSBs), ROIs were drawn at locations that corresponded to locations of focal radiolucency in other PSBs (Fig 2.1). Bone tissues in the reconstructed images were segregated from soft tissues using a standard threshold.

The effects of PSB group on tissue morphometric variables were assessed using a mixed model ANOVA and post-hoc pairwise comparisons [SAS 9.4]<sup>B</sup>. Group (FX-PSB, CLI-PSB, CTRL-PSB) and ROI (ROI-1, ROI-2) were treated as fixed effects, horse was treated as a random effect, and repeated measures within horse were accounted for. A  $p \leq 0.05$  was considered statistically significant. Normality of the ANOVA residuals were checked using the Shapiro-Wilks statistic [SAS 9.4]<sup>B</sup>. Post hoc power was assessed for non-

statistically significant comparisons [SAS 9.4]<sup>B</sup>. Exercise histories from horses selected in Study 2 were compared to those selected in Study 1 (Supplementary Item 1).

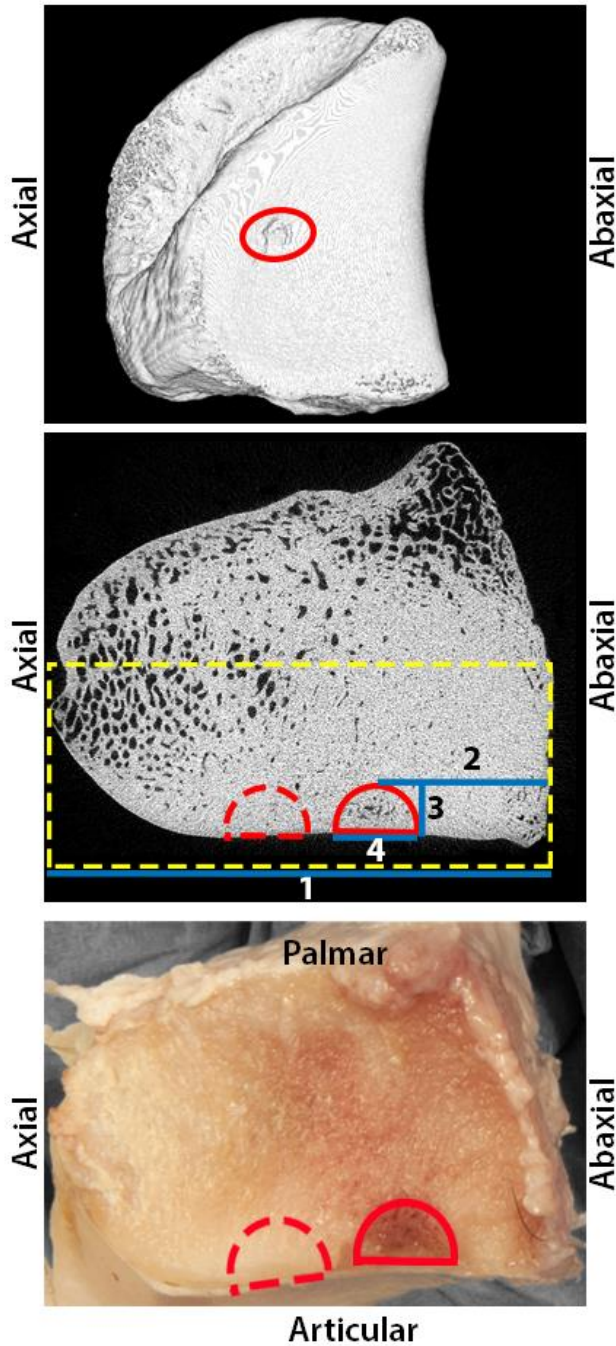


**Figure 2.1:** Standardized regions of interest for analysis of tissue properties. Level of analysis shown on whole proximal sesamoid bones (PSB; top), and ROIs shown on microcomputed tomography transverse slice (center) and on fracture surface (bottom). In PSBs with focal subchondral radiolucencies (top image, red circle), the proximal-distal center of radiolucency was located and the distance from the bone apex was located as a proportion of full bone height. The transverse section at the center of the focal radiolucency was used to center ROI-1 and ROI-2. ROI-1 was drawn to surround the lesion (solid red crescent). The caliper-width of PSB (dashed yellow box, width illustrated by line 1), maximum lesion width (line 4), maximum lesion depth (line 3), and the abaxial-to-axial distance to lesion center (line 2) were determined at this transverse section. ROI-2 (red dashed line in middle image) was drawn one-third of ROI-1 width away from most axial point of ROI-1. In PSBs without lesions, ROI-1 and ROI-2 were drawn at the median values for the given proportions and standardized to PSB size. In bottom image, a solid ROI surrounds subchondral discoloration (ROI-1) and dashed ROI indicates control subchondral region (ROI-2).



## 2.4 Results

Abnormal findings were observed in two specific locations within the PSB: one in subchondral bone on the abaxial half of the PSB, and a second along the palmar surface. Most abnormal findings were in a subchondral region within the abaxial half of the bone at a proximodistal level that corresponded to complete transverse PSB fracture (Figs. 2.1, 2.2, & 2.3). The palmar location was less common and corresponded to the location of the lesion previously reported by Anthenill.<sup>3</sup>

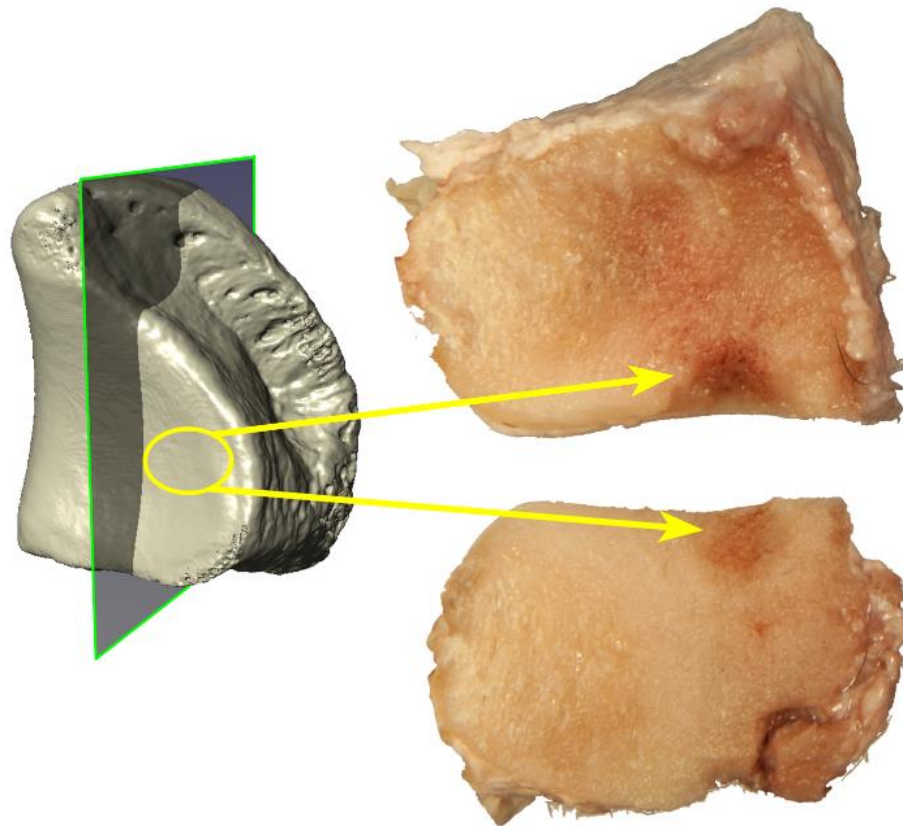


**Figure 2.2:** Typical location of subchondral surface abnormality was to the abaxial side of the mid-sagittal plane. Example shown (right) on opposing fracture faces.

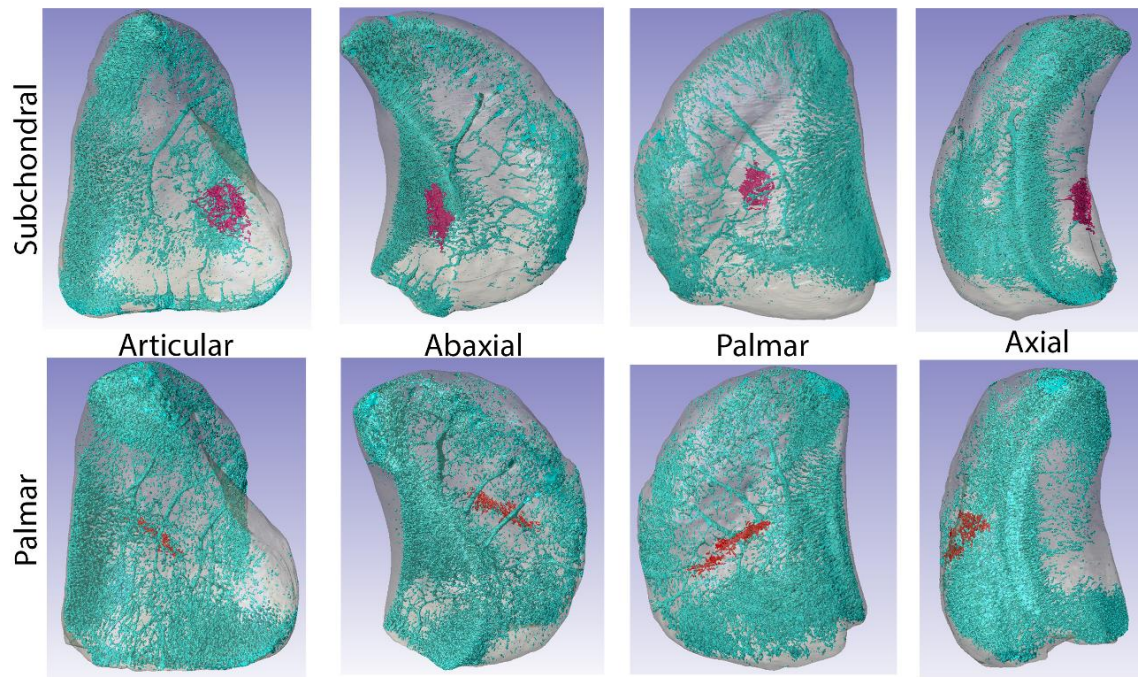


**Figure 2.3:** Microcomputed tomography porosity maps highlighting focal subchondral osteopenic abnormality. Porosity maps (shown in aquamarine) of case contralateral intact proximal sesamoid bone illustrating, in 3D, the subchondral (top row) and palmar (bottom row) abnormal osteopenic foci (red). These visualizations were created from  $\mu$ CT scans, porosities were identified using a standard threshold. Osteopenia foci (red) were visually identified on  $\mu$ CT slices and then a region growing tool was used to determine their extent.

#### 2.4.1 Study 1 – Morphological findings

A well-demarcated, focal, semicircular-shaped subchondral discoloration, that was contiguous with the fracture plane of FX-PSBs and present at a corresponding level in CLI-PSBs, was frequently observed grossly on fracture surfaces and sagittal sections (Table 1; Figs 2.2 and 2.4). Subchondral discoloration was bilateral in 70% of case horses and occurred more frequently in FX-PSBs and CLI-PSBs than in CTRL-PSBs ( $p < 0.001$ ). The distributions of discoloration between FX-PSBs and CLI-PSBs were not statistically different ( $p=0.629$ ). Two case horses had no subchondral discoloration and one case had discoloration only in the FX-PSB. The only CTRL-PSB with subchondral discoloration had a diffuse discoloration (see Supplementary Item 2). The most frequently found subchondral discoloration pattern

was: well-demarcated, focal, and crescent-shaped; this pattern was found in 80% of FX-PSBs, 60% of CLI-PSBs, and none of the CTRL-PSBs.

**Table 2.1:** Contingency table for presence of focal radiolucencies observed on high-detail radiographs of sagittal sections. Statistically significant differences ( $p < 0.05$ ) in distributions among groups are indicated by \*

Group	Bone	Focal Discoloration		Focal Radiolucency					
		Subchondral*		Subchondral*		Palmar		Any*	
		No	Yes	No	Yes	No	Yes	No	Yes
Case	FX-PSB	2	8	4	6	6	4	2	8
	CLI-PSB	4	6	5	5	9	1	5	5
Control	CTRL-PSB	10	0	10	0	8	2	8	2

(FX-PSB, fractured proximal sesamoid bone; CLI-PSB, contralateral intact proximal sesamoid bone; CTRL-PSB, control intact proximal sesamoid bone; Subchondral, only subchondral focal radiolucency; Palmar, only palmar radiolucency; Any, subchondral and/or palmar radiolucency)

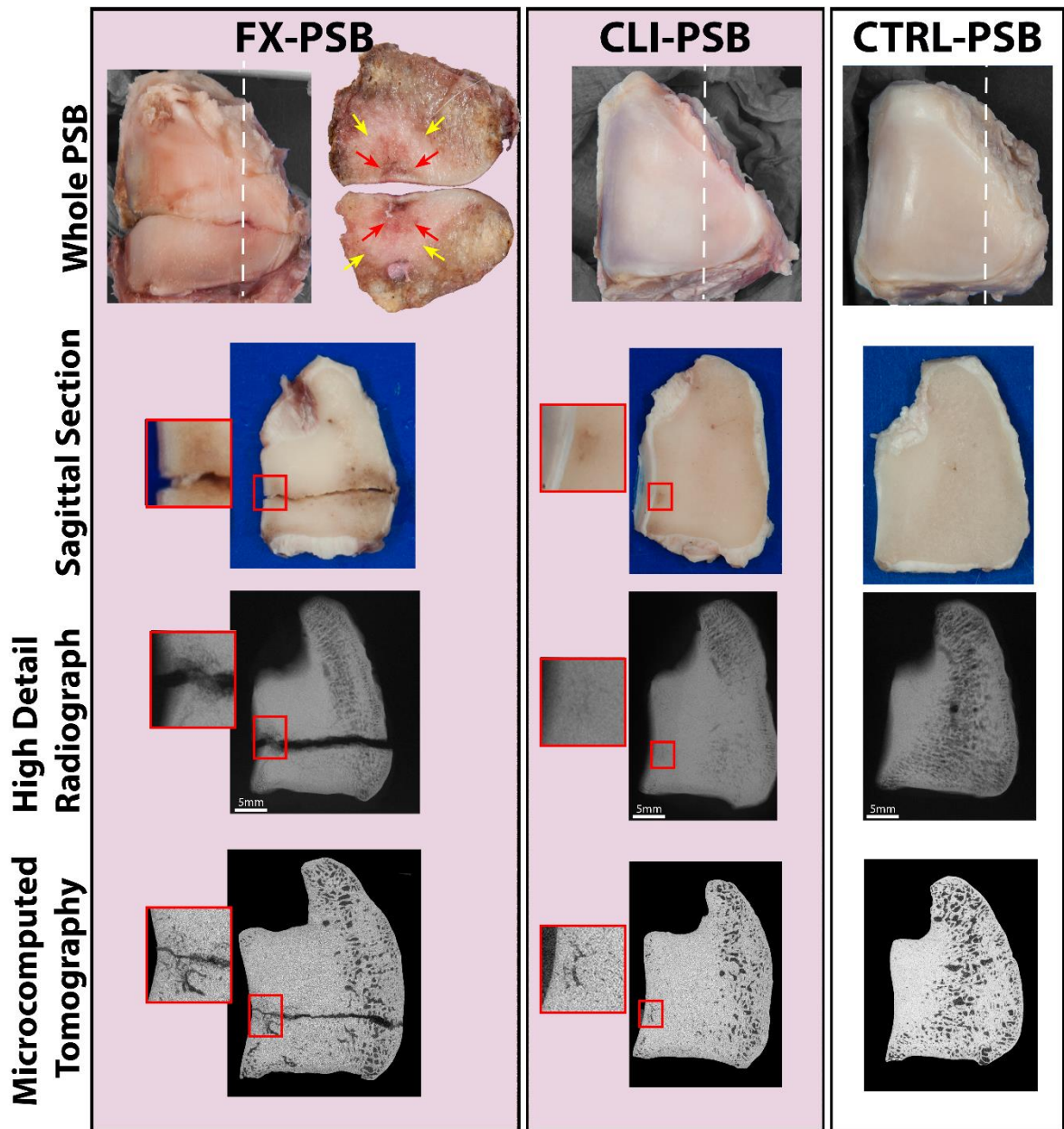


**Figure 2.4:** Focal subchondral discoloration surrounded by sclerosis in Case proximal sesamoid bones .Focal subchondral discoloration (red arrows) surrounded by sclerosis (yellow arrows) on fracture surfaces of fractured proximal sesamoid bones (FX-PSB) and on abaxially located sagittal section of FX-PSB and contralateral limb proximal sesamoid bones (CLI-PSB) from the same case horse (red box, slice taken at level of section indicated by white dashed lines); but not on the control proximal sesamoid bones (CTRL-PSB). Focal osteopenia (red boxes) on high detail radiographs and microcomputed tomography of case bones co-localized with focal discoloration.

Focal subchondral discoloration was more severe for FX-PSBs than CLI-PSBs ( $p = 0.006$ ). Specifically, this discoloration was graded severe in 2 FX-PSBs, moderate in 4 FX-PSBs and 2 CLI-PSBs, and mild in 2 FX-PSBs and 5 CLI-PSBs. Additionally, focal subchondral discoloration on sagittal sections correlated with the presence of subchondral fracture surface discoloration ( $r = 0.66$ ). Most FX-PSBs (90%) had visible discoloration on the fracture surface; most commonly in a crescent pattern in 70% FX-PSBs (Fig 2.4).

Subchondral radiolucency found on high detail radiographic images of sagittal sections, confirmed via sagittal  $\mu$ CT images, was focal and predominantly bilateral in case horses and not apparent in control horses ( $p = 0.012$ ) (Figs 2.4 and 2.5, Table 1). These focal subchondral radiolucencies were found in 70% of case horses (4 bilateral, 2 unilateral in FX-PSB, 1 unilateral in CLI-PSB). Subchondral radiolucency occurred more frequently in FX-PSBs and CLI-PSBs than in CTRL-PSBs ( $p = 0.012$  comparing all groups,  $p = 0.033$  comparing CLI-PSBs and CTRL-PSBs,  $p = 0.012$  comparing FX-PSBs and CTRL-PSBs). The distributions of subchondral radiolucency between FX-PSBs and CLI-PSBs were not statistically different ( $p = 1.0$ ). Retrospective review of  $\mu$ CT images revealed subchondral radiolucencies in two additional case horses and showed small radiolucencies in additional CLI-PSBs; a total of 6 bilateral subchondral radiolucencies and 3 unilateral subchondral radiolucencies in FX-PSBs were found. The focal subchondral radiolucencies were co-located with focal subchondral discoloration and contiguous with the fracture line (Fig 2.4). Presence of a focal subchondral radiolucency correlated with the presence of focal subchondral discoloration on sagittal sections ( $r = 0.66$ ,  $p < 0.001$ ), and the pattern of subchondral sclerosis ( $r = 0.33$ ,  $p = 0.01$ ; Table 2). All PSBs had some degree of subchondral sclerosis; case horses (FX-PSB & CLI-PSBs) tended to have more severe subchondral sclerosis than controls ( $p = 0.09$ ).

**Table 2.2:** Relationship of subchondral focal radiolucency with subchondral discoloration and sclerosis for all PSBs. Spearman’s Correlation Coefficient (r) and Fisher’s Exact p-value are listed

Subchondral Focal Radiolucency	Subchondral Discoloration									Subchondral Sclerosis					
	Presence		Pattern			Severity				Presence		Pattern			
	No	Yes	None	Focal	Diffuse	None	Mild	Moderate	Severe	No	Yes	Edge	Thin Crescent	Wide Crescent	Full
No	14	5	14	4	1	14	3	1	1	0	19	2	2	12	3
Yes	0	11	0	10	1	0	5	5	1	0	11	0	0	3	8
	p < 0.001 r = 0.71		p < 0.001 r = 0.66			p < 0.001 r = 0.55				N/A		p = 0.01 r = 0.33			



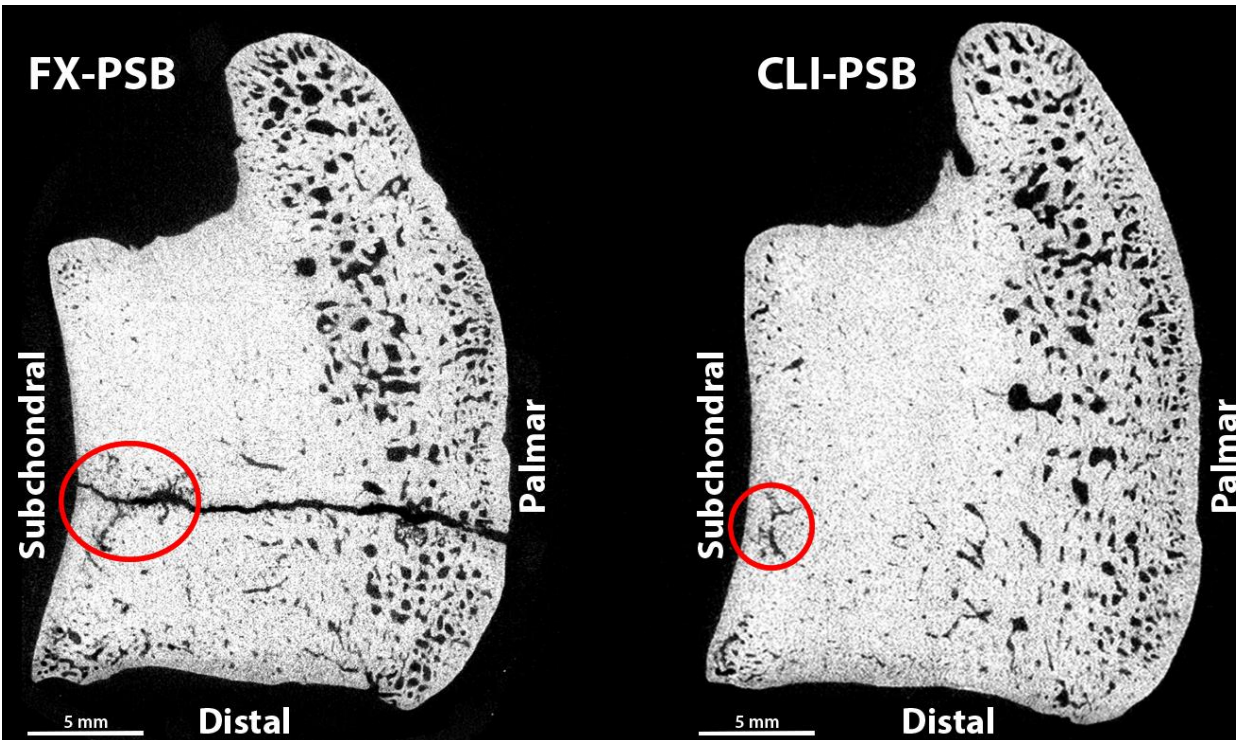


**Figure 2.5:** Subchondral sites of focal osteopenia illustrated on uCT sagittal images. Regions of focal osteopenia (red circles) are shown on bilateral (fractured proximal sesamoid bone (FX-PSB) & contralateral intact PSB (CLI-PSB) limbs of a case horse with unilateral biaxial PSB fracture.

Palmar discoloration did not differ among groups (presence, pattern, and severity;  $p = 0.6$ ;  $p = 0.2$ ,  $p = 0.6$ ); 19 of 30 horses had mild discoloration along the palmar border in the sagittal sections, either well-demarcated along the entire border ( $n=8$ ), diffuse along part of the border ( $n=3$ ), or focal ( $n=8$ ). Presence of palmar discoloration in sagittal sections was not correlated to presence of a palmar radiolucency ( $r = 0.03$ ). The pattern of palmar discoloration on the fracture face did not correlate to presence of a palmar radiolucency ( $r = 0.16$ ).

Palmar focal radiolucencies were less prevalent in our sample set than subchondral focal radiolucencies (Table 1), and not statistically different among groups ( $p = 0.4$ ). The only focal radiolucencies found in CTRL-PSBs were palmar (2 CTRL-PSBs). Four case horses had palmar focal radiolucencies (1 bilateral, 3 unilateral in FX-PSB), three of the four case horses with palmar focal

radiolucencies also had subchondral focal radiolucencies. Palmar radiolucencies were contiguous with the fracture line in FX-PSBs were they were present.

Any radiolucency (subchondral or palmar) occurred more frequently in FX-PSBs than in CTRL-PSBs ( $p = 0.023$ ). The distributions of any radiolucency between CLI-PSBs with FX-PSBs and with CTRL-PSBs were not statistically different ( $p=0.350$ ,  $p=0.350$ , respectively).

All FX-PSBs had incongruent fracture lines or were missing pieces of bone on the high-detailed radiographs and images of sagittal sections – either on the palmar aspect, subchondral aspect, or both. No significant associations between fracture type (comminuted ( $n=6$ ) or simple ( $n=4$ )) and other variables were found.

Histological sections stained with H&E were examined for differences between case and control PSBs along the subchondral surface. Subchondral bone tears (STs) were found in both case and control PSBs; however, STs were tightly clustered in a crescent shape at the level of the focal radiolucency in case horses (present in 9/10 CLI-PSBs, 10/10 FX-PSBs; Fig 2.6). Subchondral bone tears were observed in 7 CTRL-PSBs, but were much less numerous and only tightly clustered in 2 CTRL-PSBs. Calcified cartilage tears (CCTs) were often found clustered adjacent to STs in case horses (present in 5/10 CLI-PSBs, 8/10 FX-PSBs; Fig 2.6). The two CTRL-PSBs with CCTs had clustered STs (Fig 2.6). In case FX-PSBs, STs and CCTs were tightly clustered in a half-crescent shaped region on proximal and distal sides of the fracture line (Fig 2.6). In both Case and Control bones, bone matrix tears were more prevalent along the subchondral (dorsal) surface than the palmar surface. Sample cellularity was poor and presence of resorption bays could not be confirmed; however, porosities with scalloped edges were frequently found near SMT clusters in the subchondral region. In addition, islands of calcified cartilage were found within subchondral matrix of most PSBs; they tended to be deeper beneath the subchondral surface in CTRL-PSBs. Islands of subchondral bone were found within the calcified cartilage matrix of most PSBs.



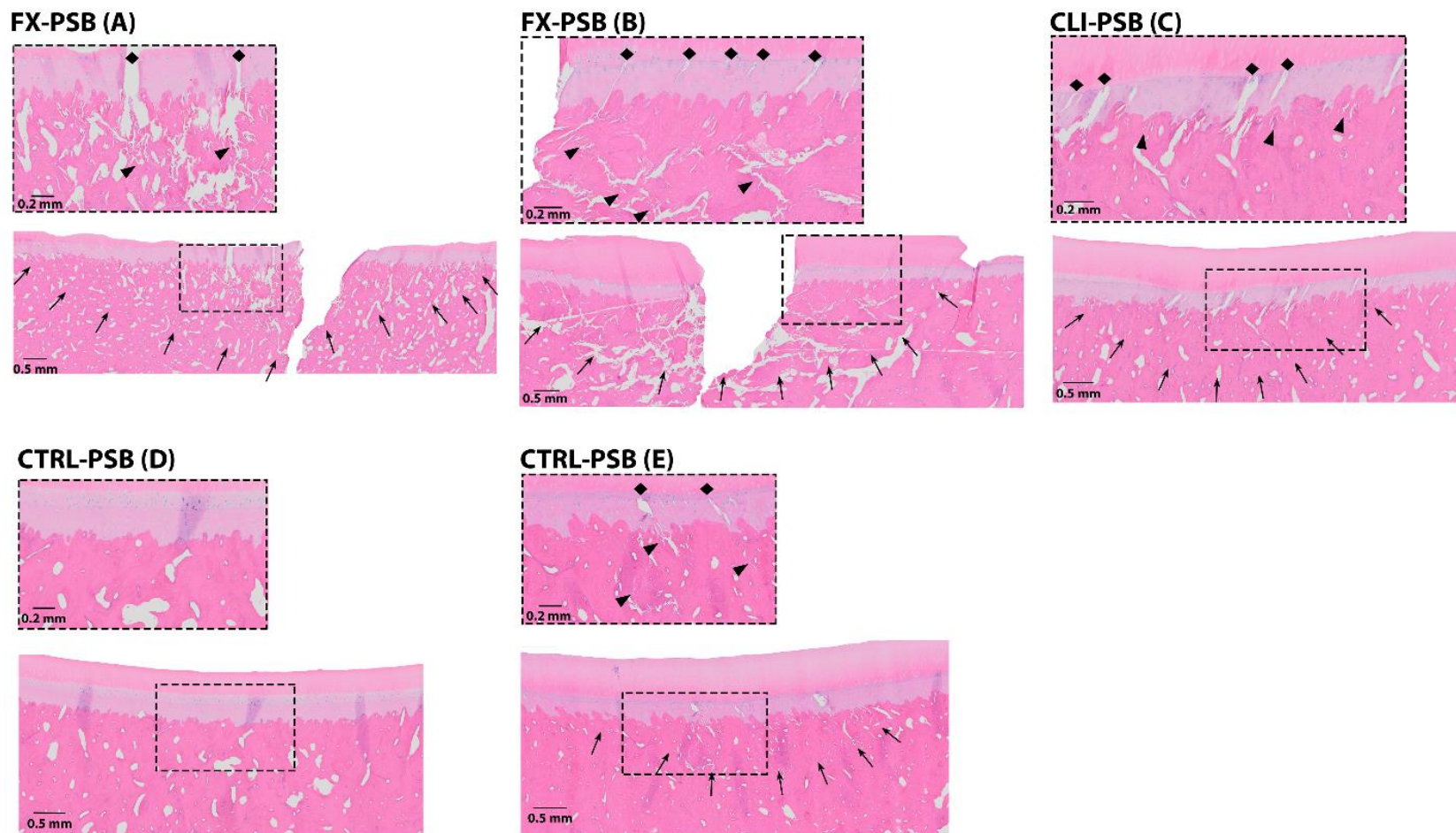


**Figure 2.6:** Representative histology of case and control PSBs stained with Hematoxylin & Eosin. A) Case fractured proximal sesamoid bones (FX-PSB) with severe subchondral bone matrix tears (arrowhead) clustered in crescent-shape (black-arrows) near fracture line with some tearing in calcified cartilage matrix (diamonds). B) Case FX-PSB with typical subchondral matrix tears (arrowheads) and calcified cartilage matrix tears (diamonds) in crescent-shaped region around fracture line (arrowheads). C) Case contralateral limb proximal sesamoid bones (CLI-PSB) with typical subchondral matrix tears (arrowheads) and calcified cartilage matrix tears (diamonds) in crescent-shaped region at the corresponding location to fracture in the contralateral FX-PSB (arrowheads). D) Typical control PSB with no subchondral or calcified cartilage matrix tears. E) Control PSB with the most tears, still occur in the corresponding, but smaller, area as in typical case CLI-PSBs and FX-PSBs.

#### 2.4.2 Study 2 – Tissue morphometric findings

At the subchondral focal radiolucent site (ROI-1), BVF, AMD, TMD and Tb.Th were statistically lower and Tb.N was statistically higher in FX-PSBs than CLI-PSBs and CTRL-PSBs ( $p < 0.05$ ; Table 3). Tissue properties in CLI-PSBs were intermediate between those of FX-PSBs and CTRL-PSBs, but not statistically different from CTRL-PSBs (Table 3). P-values comparing CLI-PSBs to CTRL-PSBs ranged from 0.16 to 0.91; post hoc power ranged from 0.14-0.39. Within ROI-1, BVF was 12% lower ( $p = 0.03$ ), AMD was 9% lower ( $p = 0.02$ ), TMD was 5% lower ( $p = 0.004$ ), Tb.Th was 54% lower ( $p = 0.008$ ), and Tb.N was 47% higher ( $p = 0.003$ ) in FX-PSBs compared to CTRL-PSBs. Tissue properties in ROI-1 could not accurately be measured in 3 of 9 FX-PSBs due to fracture plane interference with construction of ROIs. The mean cross-sectional area of ROI-1 was 8.19 mm<sup>2</sup> for CLI-PSBs and 7.93 mm<sup>2</sup> for FX-PSBs.

Tissue morphometric properties at the intra-bone control site were not different between case and control horses (CLI-PSBs and CTRL-PSBs) (ROI-2, Table 3). P-values ranged from 0.19 to 0.66; post hoc power ranged from 0.10 to 0.65. Due to interference from the fracture line, tissue properties at ROI-2 were not measured in FX-PSBs.

**Table 2.3:** Tissue properties (mean (95% CIs)) in the subchondral lesion (ROI-1) and control (ROI-2) sites in FX-PSBs, CLI-PSBs, and CTRL-PSBs. Within site for each variable, values that do not share a superscript are statistically different at  $p < 0.05$

	Subchondral Discoloration Site (ROI-1)			Intra-Bone Control Site (ROI-2)	
	FX-PSB n=6	CLI-PSB n=9	CTRL-PSB n=9	CLI-PSB n=9	CTRL-PSB n=9
<b>Bone Volume Fraction (%)</b>	82 <sup>A</sup> (67, 97)	92 <sup>B</sup> (81,100)	94 <sup>B</sup> (91, 97)	99 <sup>α</sup> (99, 100)	98 <sup>α</sup> (98, 99)
<b>Apparent Mineral Density (mgHA/cc)</b>	685 <sup>A</sup> (632, 737)	727 <sup>B</sup> (684, 771)	750 <sup>B</sup> (733, 766)	793 <sup>α</sup> (777, 809)	801 <sup>α</sup> (785, 817)
<b>Tissue Mineral Density (mgHA/cc)</b>	730 <sup>A</sup> (705, 754)	756 <sup>B</sup> (738, 773)	771 <sup>B</sup> (760, 781)	798 <sup>α</sup> (782, 813)	809 <sup>α</sup> (795, 823)
<b>Trabecular Thickness (mm)</b>	0.5 <sup>A</sup> (0.3, 0.6)	0.9 <sup>B</sup> (0.6, 1.1)	1.0 <sup>B</sup> (0.8, 1.1)	1.4 <sup>α</sup> (1.1, 1.6)	1.3 <sup>α</sup> (1.1, 1.4)
<b>Trabecular Number (#/mm<sup>3</sup>)</b>	3.0 <sup>A</sup> (2.6, 3.6)	2.2 <sup>B</sup> (1.6, 2.8)	2.1 <sup>B</sup> (1.9, 2.3)	1.6 <sup>α</sup> (1.3, 1.9)	1.7 <sup>α</sup> (1.5, 1.9)

(FX-PSB, fractured proximal sesamoid bone; CLI-PSB, contralateral intact proximal sesamoid bone; CTRL-PSB, control intact proximal sesamoid bone)

## 2.5 Discussion

Proximal sesamoid bones were examined from Thoroughbred racehorses that died from either PSB fracture (cases) or a non-PSB fracture cause (controls) to determine if pre-existing abnormalities are associated with PSB fracture. Case horses had evidence of pre-existing abnormalities on the subchondral surface characterized by co-localized focal surface discoloration, focal osteopenia, subchondral bone sclerosis, and focal fragmentation of subchondral bone and calcified cartilage matrix. All subchondral pathologic changes were more numerous in case horses than control horses and more severe in affected (fractured) limbs than contralateral intact limbs. A focal palmar radiolucency (lesion) was found infrequently in both case and control horses; it was not associated with a particular pattern of discoloration on sagittal sections.

Our laboratory previously reported linear palmar defects (lesions) in PSBs from horses with simple transverse mid-body PSB fractures<sup>16</sup>. However, only 2 of 8 case horses in that study (1 fracture, 2 contralateral intact PSBs) were reported to have palmar lesions.<sup>16,17</sup> In the current study, focal radiolucent regions on the palmar surface were found in both case and control PSBs (4 Case-FX, 1 Case-CLI, and 2 Controls) and the distributions among groups were not significantly different. While not measured, it is likely these palmar radiolucent regions were osteopenic. Palmar discoloration pattern (i.e. focal discoloration) was weakly correlated with presence of a palmar focal radiolucent lesion. Few bone matrix tears were noted along the palmar surface of case or controls.

In the current study, focal subchondral lesions defined by co-localized subchondral discoloration, osteopenia, low tissue mineral density, and subchondral bone and calcified cartilage tears on decalcified histology sections were associated with fracture in case horses. These subchondral lesions occurred in a consistent, focal, mid-body, slightly abaxial location in case horses. Subchondral lesions were found in 7 of 10 case horses (6/10 FX-PSB, and 5/10 CLI PSBs; these lesions were biaxial in 4 Case horses. Retrospective review of microcomputed tomography scans showed additional radiolucent lesions in two additional case horses; resulting in 9 of 10 case horses with subchondral lesions (biaxial in 6 case horses, unilateral in 3 FX-PSBs). Proximal sesamoid bones with the subchondral lesion always had advanced densification of the perilesional subchondral bone. Histology could not confirm the presence of resorption bays at the lesion site, due to poor cellularity; however, scalloped porosities (similar in morphology to resorption bays) were present at the level of the subchondral lesion. Crescent-shaped clusters of subchondral bone tears and calcified cartilage tears were more frequently found in the decalcified H&E sections of Case horses than Control horses; these tears were co-localized with the focal osteopenia and focal discoloration. While these tears may be processing artifacts, they likely represent pre-existing microdamage or matrix fragility at this focal site.<sup>18,19</sup> Case FX-PSBs had more advanced pathological changes at the subchondral lesion site than Case CLI-PSBs. Specifically, FX-PSBs had a statistically lower

bone volume fraction and tissue mineral density ( $p < 0.05$ ) within the lesion site than a comparable location in CLI-PSBs and Controls. The lack of statistical differences in bone volume fraction and mineral densities at the lesion site between CLI-PSBs and CTRL-PSBs are likely related to the relatively small observed effect size and the small sample size. There were also no statistically significant differences for tissue properties between CLI-PSBs and CTRL-PSBs at the intra-bone control site that was distant to the lesion. Mean differences and confidence intervals at the intra-bone control site were smallest of all comparisons, providing evidence that bones from case and control horses were less different in respects other than the presence of a lesion. Fractured PSBs also had more severe focal subchondral discoloration than CLI-PSBs. Subchondral cracks in FX-PSBs and small subchondral intertrabecular spaces resembling resorption cavities have been reported in horses that sustained PSB fractures, these may be precursors to the subchondral lesions found in this study.<sup>16</sup>

The role of microdamage and tissue remodeling in the formation of these subchondral lesions is supported by co-localization of focal osteopenia, discoloration, and matrix tearing; bilateral lesions among Case-FX and Case-CLI PSBs; and the lack of pathologic changes in Control horses. The left and right forelimbs experience similar stresses that induce damage and remodeling and bilateral changes were seen in Case horses, so it is likely that observed subchondral changes are the result of loading conditions causing damage with insufficient time for full recovery and repair. Presence of advanced subchondral sclerosis in Case horses and compaction of trabecular bone tissue within the Case PSBs indicates an adaptive response to increased mechanical loading in Case horses. The observed tearing of subchondral bone and calcified cartilage on decalcified histology sections likely represents microdamage, which induces bone turnover and repair.<sup>18</sup> A previous study indicated fracture does not appear to be associated with trabecular bone microfractures in the central area of the PSBs;<sup>20</sup> however, more focused analysis along the subchondral regions may yield evidence of microdamage consistent with the tearing seen in our

histology samples. Additionally, the focal osteopenia and low tissue mineral density at the lesion location is consistent with the transient effect damage resorption and repair has on bone tissue.

The tissue changes observed within this subchondral lesion are like those observed in stress fractures in compact, cortical bone with the exception of periosteal callus. Long bone stress fractures are a result of focal intracortical remodeling to high bone strains due to exercise and exercise-induced microdamage; these focal sites develop transient porosities, compromising bone material properties and leading to fracture.<sup>5,21</sup> Bilateral periosteal callus is commonly found in racehorses that unilateral complete fracture of the humerus, scapula, and metacarpus.<sup>4,12,14</sup> However, periosteal callus cannot be formed on the subchondral surface of the PSB due to overlying articular cartilage. As an alternative to a periosteal callus, the peri-lesional sclerotic change surrounding the focal osteopenia in the subchondral bone may be an attempt to buttress the underlying osteopenic weakness, like the endosteal callus that also accompanies cortical stress fractures. Similar peri-lesional changes are observed in palmar osteochondral disease of the third metacarpal bone (MC3), which occurs in an anatomic location where periosteal callus cannot form.<sup>22,23</sup> In the current study, the peri-lesional sclerosis is superimposed on more generalized subchondral sclerosis that is an adaptive response to increased loading with increasing training and racing intensity.

Loading conditions experienced by the PSBs during equine locomotion support the development of both subchondral and palmar lesions. The PSBs are part of the fetlock's suspensory apparatus. With fetlock extension, the PSBs experience both proximodistal tension, from the suspensory ligament and distal sesamoidean ligaments, and dorsopalmar compression, from the MC3. Compressive forces from the MC3 act on the articular PSB surface during equine locomotion and the contact area of the PSBs on the MC3 condyle increases with load;<sup>24</sup> these compressive forces may cause focal microdamage on the subchondral surface. Tensile forces from the suspensory ligament and distal sesamoidean ligaments act

on the palmar region of the PSB during locomotion and may be high enough to cause microdamage in a focal region on the palmar surface. Since bone volume fraction is highly correlated to Young's Modulus of trabecular bone, the osteopenic lesion at either location could act as a stress-riser and play a role in fracture initiation.<sup>25</sup>

Proximal sesamoid bone subchondral lesions may share a similar pathogenesis to palmar osteochondral disease (POD) lesions reported in the MC3 of horses that experienced MC3 condylar fracture. The PSBs articulate with the palmar aspect of the metacarpal condyle in a similar location that POD lesions occur. Horses that sustained PSB fractures often have the degenerative lesions of the metacarpal condyle associated with POD.<sup>4</sup> Additionally, PSB and POD lesions are associated with changes to subchondral bone and bluish discoloration of the subchondral bone visible through grossly normal articular cartilage<sup>23</sup>. Similar subchondral matrix fragility tears are associated with POD lesions and microdamage has been reported in the same location.<sup>15,18</sup> Finally, POD lesions occur in a similar crescent-shape as those observed in this study.<sup>18,26</sup> The POD lesions and the reported subchondral PSB lesions occur in opposing joint surfaces. Palmar osteochondral disease scores in the MC3 condyles were not evaluated in the current study; however, determining the relationship between the degree of POD and presence of these subchondral lesions may help explain the biomechanical pathogenesis of fetlock breakdown in racehorses.

One limitation of the study is inclusion of only medial PSBs. Biaxial PSB fractures are more common than uniaxial fractures and it is unknown which PSB fails first in catastrophic biaxial PSB fracture.<sup>1</sup> The medial PSB was selected because it fractures more commonly in unilateral fracture and the medial aspect of the fetlock joint is thought to bear more load during locomotion.<sup>27</sup> It is unknown whether similar abnormalities associated with catastrophic biaxial PSB fracture would be found in the lateral PSB. Another potential limitation of this study is the inclusion of control horses that died due to non-PSB

musculoskeletal injuries (MSIs). By using horses with fractures in bones other than the PSB as Controls, this study highlights changes in the PSBs specifically associated with PSB-fracture in a population of actively performing racehorses. Determining differences between the PSBs of horses who died from PSB-fracture and other MSIs is useful for determining horses at higher risk for PSB fracture; potentially differentiating insufficiency fractures of long bones from overuse fracture of the PSBs. Typically, horses with humeral or scapular fractures experience insufficiency fractures early in their career or after a lay-up due to insufficient adaptation to increasing stresses associated with increases in training intensity<sup>7,28</sup>. However, PSB fractures occur in older horses associated with long-periods of intense exercise without opportunity for recovery.<sup>6,9</sup> Notably, no control PSBs in this study had a subchondral lesion – regardless of whether the control horse died from other MSIs or not (e.g., pneumonia, laminitis, sudden death). Another limitation of this study is the examination of PSBs from only 36 racehorses from one geographic population (California). Although similar lesions are likely to occur in racehorses in other racing jurisdictions that train and race under similar circumstances as in California, it is unknown if the results of this study apply to racehorses in other racing jurisdictions. A larger sample size may also have elucidated differences between CLI-PSBs and CTRL-PSBs.

The subchondral focal discoloration could be used at necropsy to identify bones with subchondral lesions, since presence of a lesion was highly correlated to focal discoloration on the fracture faces; highlighting the importance of systematic examination and documentation when reporting racehorse injuries<sup>11</sup>. However, the lesions are small relative to the resolution of clinical densitometric techniques (e.g., radiographs) that could be used for lesion detection. The recent introduction of positron emission tomography (PET scan) to the veterinary clinic may allow detection of high bone turnover in the slightly abaxial location of the subchondral lesion.<sup>29</sup> It is possible that PET scanning may be made sufficiently accurate to identify horses at risk for a catastrophic fracture of the PSBs.



In conclusion, subchondral lesions observed in the medial PSBs of racehorses may have predisposed racehorses to catastrophic biaxial mid-body PSB fracture. In this study, subchondral lesions were found more frequently than palmar lesions in horses that died from mid-body PSB fracture.

## **2.6 Manufacturer's Addresses**

- a) Jockey Club Information Systems, Lexington, KY, USA
- b) SAS 9.4, SAS Institute Inc., Cary, North Carolina, USA.
- c)  $\mu$ CT 35 , Scanco Medical, Bassersdorf, Switzerland.
- d) Isomet 1000 Precision Cutter, Buehler, Lake Bluff, Illinois, USA.
- e) 43855N X\_ray System Faxitron Series, Hewlett-Packard, Palo Alto, USA.
- f) Oncology Portal Pack for Localization, Carestream Health, Rochester, NY, USA.
- g) Siemens Inveon CT, Siemens, Munich, Germany.

## 2.7 Supplementary Information A: Selection of Study Horses

**Table SA – 2.7.1:** Descriptive values (mean (95% CI)) for the exercise variable selected from a multivariable stepwise logistic regression (LR) used to select the subset of Case and Control Horses for Study 1 (Section 2.3.1); model max-rescaled  $r^2$  value is 0.35 and the area under (AUC) the receiver-operator characteristic curve (ROC) is 0.80. The logistic regression odds ratio (OR; OR (95% CI)) is given, as well as the risk increase for being a case horse when the variable is increased by the difference in group means.

Exercise History Variable (Units)	Case	Control	Difference in Group Means	LR Odds Ratio for being Case (95% CI)	Odds Of Being Case for Difference in Group Means	LR p-value
	Mean (95% CI)					
Number of High-Speed Furlongs 6 Months Before Death (furlongs)	80.0 (71.0, 89.0)	42.3 (33.6, 51.0)	37.7	1.04 (1.02, 1.06)	4.39	< 0.001

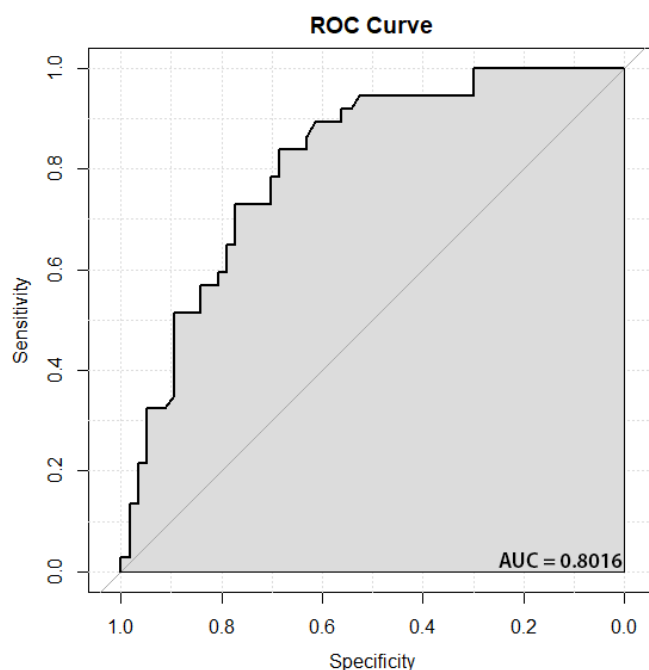


**Figure 2.7.1:** Receiver-operator characteristic curve for the regression shown in Table SA-2.7.1

Probability of a horse being a Case, as determined by the LR, is given in the Figure 2.7.2.

Stratified random sampling was used to select 9-10 horses from each decile, plus an additional horse

from the extreme high end of the probability prediction. Within each decile, at least three horses from the minority subset were selected to ensure Case and Controls animals were captured from the entire range of exercise histories present.

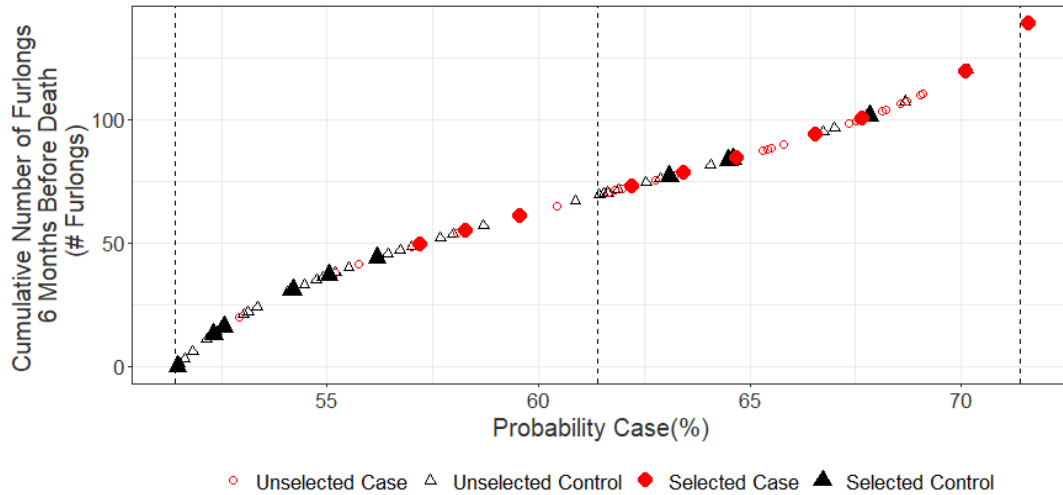


**Figure 2.7.2:** Probability of a horse being a Case, determined by the Logistic Regression shown in Table SA 2.7.1

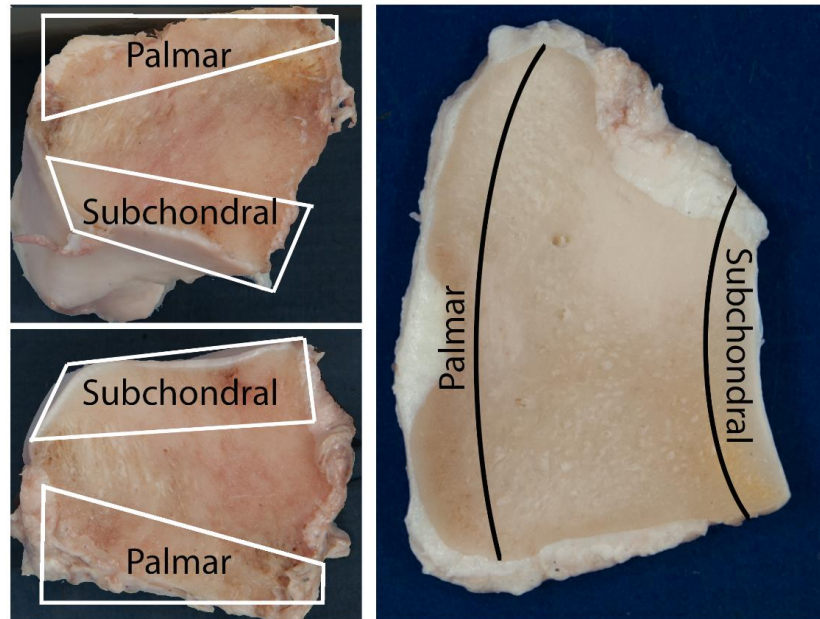
When the same LR was run over the 18 horses selected for Study 2 (where Cases were chosen based on fracture face discoloration and Controls were randomly selected), the max re-scaled  $r^2$  value was 0.61 and ROC AUC was 0.88. Results indicate that the selected exercise history variable (cumulative number of high-speed furlongs 6 months before death) was sufficient to separate horses into Case and Control groups. These are shown in Table SA-2.7.2.

**Table SA-2.7.2:** Descriptive values (mean (95% CI)) for the exercise variable selected from a multivariable stepwise logistic regression (LR) used to select the subset of Case and Control Horses for Study 1 (Section 2.3.1) when applied to Study 2 horses (Section 2.3.4)

Exercise History Variable (Units)	Case	Control	Difference in Group Means	LR OR for being Case (95% CI)	Odds Of Being Case for Difference in Group Means	LR p-value
	Mean (95% CI)					
Number of High-Speed Furlongs 6 Months Before Death (furlongs)	83.5 (68.8, 98.2)	31.1 (4.9, 57.2)	52.4	1.06 (1.01, 1.12)	21.2	0.021

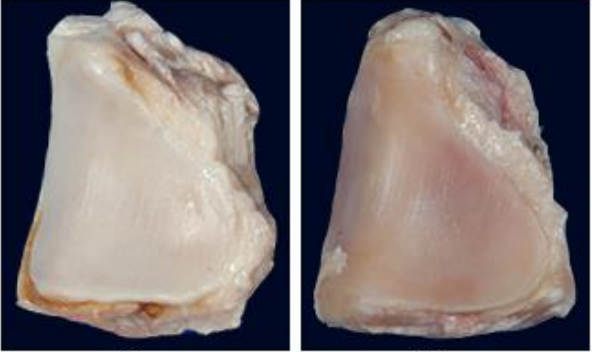
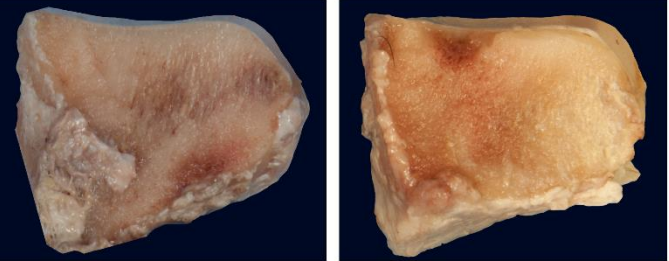
## 2.8 Supplementary Information B: Qualitative Variable Definition and Classification Levels.

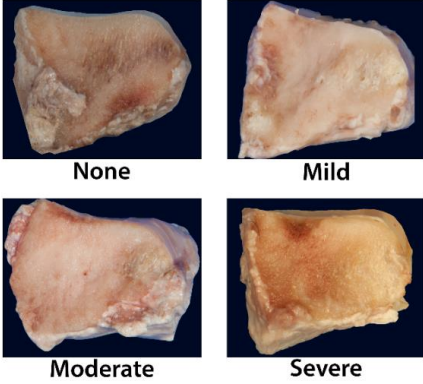
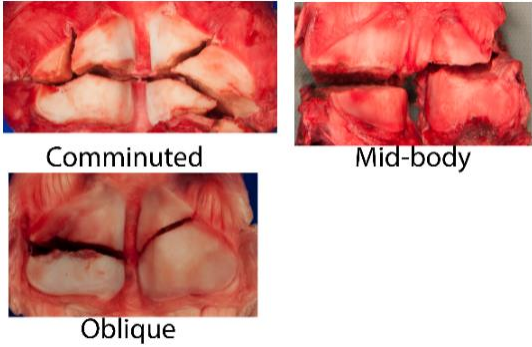
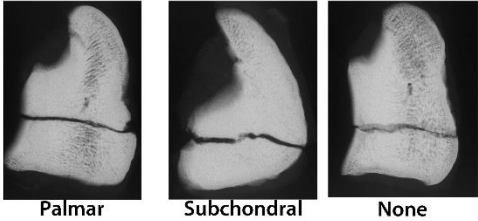
For variables assessed on sagittal sections– all sectioned pieces were analyzed as a group (i.e. “yes” discoloration on one section put the bone in the “yes” category). For variables captured from the opposing transversely oriented fracture surfaces – the proximal and distal fragments were considered together for analysis. Figure 2.8.1 defines the regions identified on the PSBs (Palmar vs Subchondral) on the fracture faces (left) and sagittal sections (right).

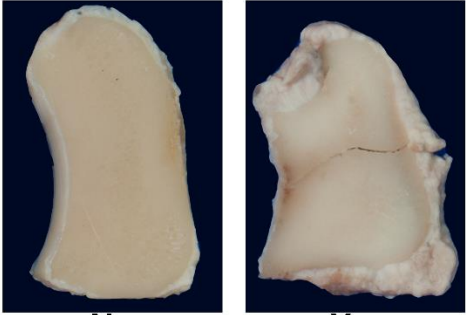
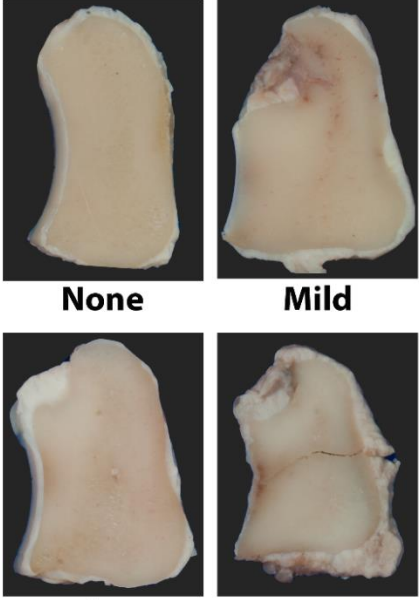


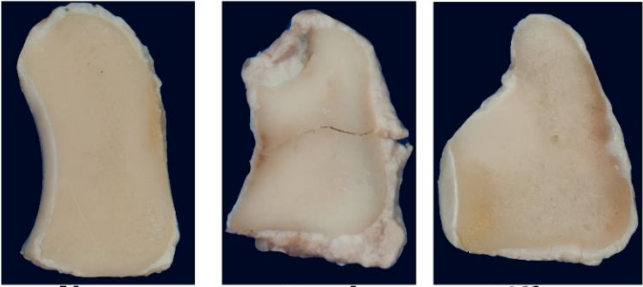
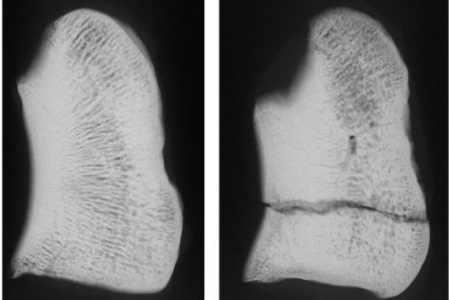
**Figure SB-2.8.1:** Regions examined in Study 1 (Section 2.3.1) shown on a sagittal section and fracture faces of a proximal sesamoid bone

**Table SB-2.8.1:** Description of variables classified in Study 1 (Section 2.3.1)

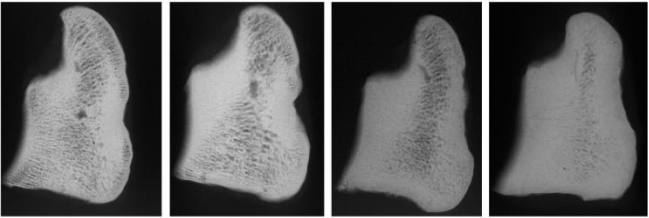
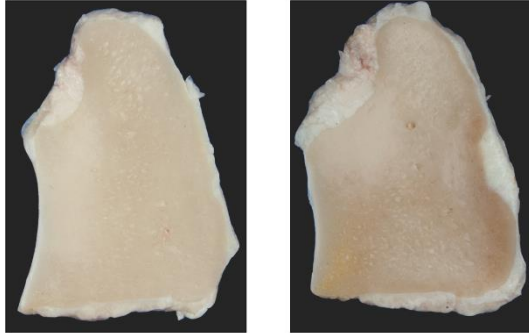
Category/ Location	Variable	Levels and Images	Definition	Specimen Type	Method Or Source
Articular Surface	Presence of Axial Articular Surface Discoloration	 <p style="text-align: center;">No                      Yes</p>	Presence (Yes) or absence (No) of discoloration along axial aspect of the articular surface	Whole Bone	Photograph
Fracture Surface	Presence of Subchondral Discoloration	 <p style="text-align: center;">No                      Yes</p>	Presence (Yes) or absence (no) of discoloration on subchondral side of open fracture surface  * Note this 'No' illustration has a focal palmar discoloration	Whole Bone, Fracture Face	Photograph

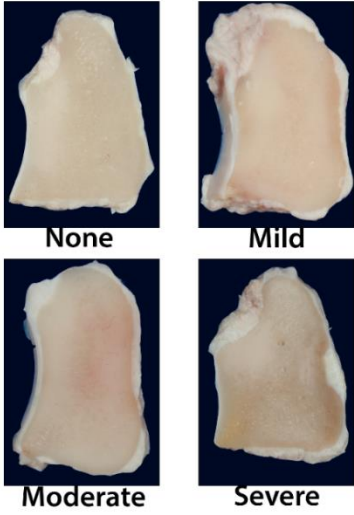
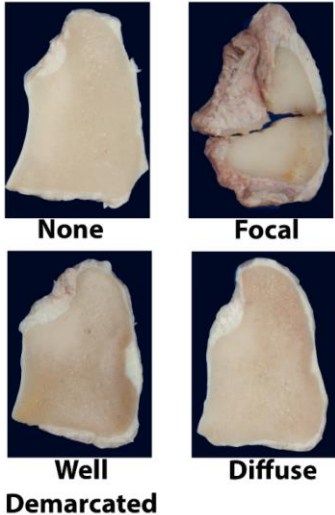
Fracture Surface	Severity of Subchondral Discoloration	 <p>None Mild Moderate Severe</p>	<p>Severity of Discoloration, ranked none (nothing present), mild (yellow/light red/light brown), moderate (red/brown), or severe (dark red/brown)</p> <p>* Note this 'None' illustration has a focal palmar discoloration</p>	Whole Bone, Fracture Face	Photograph
	Fracture Pattern	 <p>Comminuted Mid-body Oblique</p>	<p>Biaxial Comminuted, Simple Biaxial Mid-body (both medial and lateral PSB fracture into 2 pieces, with fracture through midline), Simple Mid-body &amp; Oblique (both PSBs in two pieces, one with fracture line through mid-body, other with fracture line at oblique angle)</p>	Whole Bone	Photograph
	Fracture Incongruity	 <p>Palmar Subchondral None</p>	<p>Location (if present) where fracture line appeared to be incongruent between two pieces of bone; this could be on the subchondral surface, palmar surface, or none (no incongruity).</p>	Sagittal Sections	High-detail Radiograph

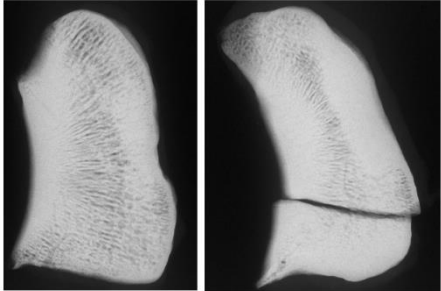
Subchondral Surface	Presence of Discoloration	 <p style="text-align: center;"><b>No</b>                      <b>Yes</b></p>	Presence (Yes) or absence (No) of subchondral discoloration, dorsal aspect of the bone slices beneath the articular cartilage	Sagittal Sections	Photograph
	Severity of Discoloration	 <p style="text-align: center;"><b>None</b>                      <b>Mild</b></p> <p style="text-align: center;"><b>Moderate</b>                      <b>Severe</b></p>	<p>Severity of Discoloration, ranked based on color. Mild (yellow/light red/light brown), moderate (red/brown), or severe (dark red/brown)</p> <p>Bones were rinsed prior to analysis, so should not be due to residual blood on surface</p>	Sagittal Sections	Photograph

<p>Pattern of Discoloration</p>	 <p style="text-align: center;"><b>None                  Focal                  Diffuse</b></p>	<p>Morphologic pattern of discoloration on subchondral aspect of the section.</p> <p>Discoloration can be more than 20% of bone length (Diffuse) or less than 20% of bone length (Focal)</p>	<p>Sagittal Sections</p>	<p>Photograph</p>
<p>Presence of Subchondral Lesion</p>	 <p style="text-align: center;"><b>No                  Yes</b></p>	<p>Presence (yes) or absence (no) of focal radiolucency on subchondral aspect of sagittal sections</p>	<p>Sagittal Sections</p>	<p>HD-Radiograph, Confirmed with <math>\mu</math>CT</p>



	Subchondral Sclerosis	 <p style="text-align: center;"> <b>Thin</b>      <b>Proximal Half</b>      <b>Full Dorsal Edge</b>      <b>Deep Dorsal</b> </p>	Levels of Subchondral Sclerosis, based on amount and location of opaque subchondral tissue. Ranked Thin (articular edge opaque), Proximal Half (articular edge and proximal subchondral tissue opaque), Full dorsal edge (proximal and distal subchondral tissue opaque), deep dorsal (subchondral tissue and internal tissue past dorsal shelf opaque)	Sagittal Sections	HD-radiographs
Palmar Surface	Presence of Discoloration	 <p style="text-align: center;"> <b>No</b>                      <b>Yes</b> </p>	Presence (Yes) or absence (No) of discoloration on sliced palmar sections. Normal sections appear white/pale yellow	Sagittal Sections	Photograph

<p>Severity of Discoloration</p>	 <p>None Mild Moderate Severe</p>	<p>Severity of Discoloration, ranked mild (yellow/light red/light brown), moderate (red/brown), or severe (dark red/brown)</p>	<p>Sagittal Sections</p>	<p>Photograph</p>
<p>Pattern of Discoloration</p>	 <p>None Focal Well Demarcated Diffuse</p>	<p>Morphologic pattern of discoloration on palmar aspect of the bone section. Discoloration can be along more than 20% of bone length but with high density (Well-Demarcated), more than 20% of bone length with low density (Diffuse) or less than 20% of bone length (Focal)</p>	<p>Sagittal Sections</p>	<p>Photograph</p>

	Presence of Palmar Lesion	 <p style="text-align: center;"><b>No</b>                      <b>Yes</b></p>	Presence (yes) or absence (no) of focal radiolucency on palmar aspect of sagittal sections	Sagittal Sections	HD-Radiograph, Confirmed with $\mu$ CT
--	---------------------------	---	--	-------------------	--

(FX-PSB, fractured proximal sesamoid bone; CLI-PSB, contralateral intact proximal sesamoid bone; CTRL-PSB, control intact proximal sesamoid bone)

## 2.9 References

1. Johnson BJ, Stover SM, Daft BM, et al. 1994. Causes of death in racehorses over a 2 year period. *Equine Vet. J.* 26(4):327–330 Available from: <http://doi.wiley.com/10.1111/j.2042-3306.1994.tb04395.x>.
2. 2019. California Horse Racing Board Postmortem Examination Program 2017-2018 Annual Report. Davis, CA. 2–13 p. Available from: [http://chr.ca.gov/postmortem\\_reports.html](http://chr.ca.gov/postmortem_reports.html).
3. Anthenill LA, Stover SM, Gardner IA, et al. 2006. Association between findings on palmarodorsal radiographic images and detection of a fracture in the proximal sesamoid bones of forelimbs obtained from cadavers of racing Thoroughbreds. *Am. J. Vet. Res.* 67(5):858–868 Available from: <http://avmajournals.avma.org/doi/abs/10.2460/ajvr.67.5.858>.
4. Stover SM. 2013. Diagnostic Workup of Upper-Limb Stress Fractures and Proximal Sesamoid Bone Stress Remodeling. In: *AAEP Proceedings; In-Depth: Racing-Related Lameness*. p 427–435.
5. Stover SM. 2003. The Epidemiology of Thoroughbred Racehorse Injuries. *Clin. Tech. Equine Pract.* 2(4):312–322.
6. Anthenill LA, Stover SM, Gardner IA, Hill AE. 2007. Risk factors for proximal sesamoid bone fractures associated with exercise history and horseshoe characteristics in Thoroughbred racehorses. *Am. J. Vet. Res.* 68(7):760–771 Available from: <http://avmajournals.avma.org/doi/abs/10.2460/ajvr.68.7.760>.
7. Carrier T, Estberg L, Stover SM, et al. 1998. Association between long periods without high-speed workouts and risk of complete humeral or pelvic fracture in Thoroughbred racehorses: 54 Cases (1991-1994). *Javma* 212(10):1582–1587.
8. Hill AE, Gardner IA, Carpenter TE, Stover SM. 2004. Effects of injury to the suspensory apparatus, exercise, and horseshoe characteristics on the risk of lateral condylar fracture and suspensory apparatus failure in forelimbs of Thoroughbred racehorses. *Am. J. Vet. Res.* 65(11):1508–1517.
9. Kristoffersen M, Parkin TDH, Singer ER. 2010. Catastrophic biaxial proximal sesamoid bone fractures in UK Thoroughbred races (1999-2004): Horse characteristics and racing history. *Equine Vet. J.* 42(5):420–424.
10. Trumble TN, Arnoczky S, Stick J, Stickle R. 1995. Clinical relevance of the microvasculature of the equine proximal sesamoid bone. *Am. J. Vet. Res.* 56(6):720–24.
11. Stover SM. 2017. Nomenclature, classification, and documentation of catastrophic fractures and associated preexisting injuries in racehorses. *J. Vet. Diagnostic Investig.* 29(4):396–404.
12. Entwistle RC, Sammons SC, Bigley RF, et al. 2009. Material properties are related to stress fracture callus and porosity of cortical bone tissue at affected and unaffected sites. *J. Orthop. Res.* 27(10):1272–1279.
13. Vallance SA, Spriet M, Stover SM. 2011. Catastrophic scapular fractures in Californian racehorses:

- Pathology, morphometry and bone density. *Equine Vet. J.* 43(6):676–685.
14. Stover SM, Johnson BJ, Daft BM, et al. 1992. An association between complete and incomplete stress fractures of the humerus in race horses. *Equine Vet. J.* 24:260–263.
  15. Riggs CM, Whitehouse GH, Boyde A. 1999. Pathology of the distal condyles of the third metacarpal and third metatarsal bones of the horse. *Equine Vet. J.* 31(2):140–148 Available from: <http://doi.wiley.com/10.1111/j.2042-3306.1999.tb03803.x>.
  16. Anthenill LA, Gardner IA, Pool RR, et al. 2010. Comparison of macrostructural and microstructural bone features in Thoroughbred racehorses with and without midbody fracture of the proximal sesamoid bone. *Am. J. Vet. Res.* 71(7):755–765 Available from: <http://avmajournals.avma.org/doi/abs/10.2460/ajvr.71.7.755>.
  17. Anthenill LA, Gardner IA, Pool R, et al. 2009. Palmar Lesions and Trabecular Bone Compaction Likely Precede Proximal Sesamoid Bone Mid- Body Fractures in Thoroughbred Racehorses. *Equine Vet. J.* 55:2009.
  18. Norrdin RW, Kawcak CE, Capwell BA, McIlwraith CW. 1998. Subchondral bone failure in an equine model of Overload Arthrosis. *Bone* 22(2):133–139.
  19. Lacourt M, Gao C, Li A, et al. 2012. Relationship between cartilage and subchondral bone lesions in repetitive impact trauma-induced equine osteoarthritis. *Osteoarthr. Cartil.* 20(6):572–583.
  20. Kristoffersen M, Hetzel U, Parkin TDH, Singer ER. 2010. Are bi-axial proximal sesamoid bone fractures in the british thoroughbred racehorse a bone fatigue related fracture?: A histological study. *Vet. Comp. Orthop. Traumatol.* 23(5):336–342.
  21. Martig S, Chen W, Lee PVS, Whitton RC. 2014. Bone fatigue and its implications for injuries in racehorses. *Equine Vet. J.* 46(4):408–415.
  22. Riggs CM. 2006. Osteochondral injury and joint disease in the athletic horse. *Equine Vet. Educ.* 18(April):100–112.
  23. Barr ED, Pinchbeck GL, Clegg PD, et al. 2009. Post mortem evaluation of palmar osteochondral disease (traumatic osteochondrosis) of the metacarpo/metatarsophalangeal joint in Thoroughbred racehorses. *Equine Vet. J.* 41(4):366–371 Available from: <http://doi.wiley.com/10.2746/042516409X368372>.
  24. Easton KL, Kawcak CE. 2007. Evaluation of Increased Subchondral Bone Density in Areas of Contact in the Metacarpophalangeal Joint During Joint Loading in Horses. *Am. J. Vet. Res.* 68(8):816–821.
  25. Kabel J, Odgaard A, Van Rietbergen B, Huiskes R. 1999. Connectivity and the elastic properties of cancellous bone. *Bone* 24(2):115–120.
  26. Norrdin RW, Stover SM. 2006. Subchondral bone failure in overload arthrosis: A scanning electron microscopic study in horses. *J. Musculoskelet. Neuronal Interact.* 6(3):251–257.

27. Schnabel L V., Redding WR. 2018. Diagnosis and management of proximal sesamoid bone fractures in the horse. *Equine Vet. Educ.* 30(8):450–455 Available from: <http://doi.wiley.com/10.1111/eve.12615>.
28. Vallance SA, Case JT, Entwistle RC, et al. 2012. Characteristics of Thoroughbred and Quarter Horse racehorses that sustained a complete scapular fracture. *Equine Vet. J.* 44(4):425–431.
29. Spriet M, Espinosa P, Kyme AZ, et al. 2018. <sup>18</sup>F-sodium fluoride positron emission tomography of the equine distal limb: Exploratory study in three horses. *Equine Vet. J.* 50(1):125–132.

**Chapter 3: Exercise History Predicts Focal Differences in Bone Volume Fraction, Mineral Density, and Microdamage in the Proximal Sesamoid Bones of Thoroughbred Racehorses**

**3.1 Abstract**

Medial proximal sesamoid bones from Thoroughbred racehorses that did (Case) or did not (Control) experience unilateral biaxial proximal sesamoid bone fracture were evaluated for bone volume fraction, apparent mineral density, tissue mineral density, and microdamage in Case Fractured, Case Contralateral Limb Intact, and Control bones. Case bones had a subchondral lesion with high microdamage density, and low bone volume fraction, apparent mineral density, and tissue mineral density. Lesion microdamage and densitometric measures were associated with training history by robust linear regression. Exercise intensity was negatively related to bone volume fraction ( $0.07 \leq R^2 \leq 0.12$ ) and positively related to microcrack areal density ( $0.21 \leq R^2 \leq 0.29$ ) in the lesion; however, in an undamaged site, the relationships were opposite in direction. Regardless of location, tissue mineral density decreased with event frequency for both Case and Control, suggesting increased bone remodeling with exercise. Measures of how often animals were removed from active training (layups) predicted a decrease in tissue mineral density, apparent mineral density, bone volume fraction, and microdamage at regions away from the lesion site. A steady-state compartment model was used to organize the differences in the correlations between variables within the data set. The overall conclusions are that at the osteopenic lesion site, repair of microdamage by remodeling was not successful (e.g., lower bone mass, increased damage, lower mineralization) but that in regions away from the lesion remodeling successfully controlled damage (e.g., higher bone mass, less microdamage, lower mineralization).

## 3.2 Introduction

Proximal sesamoid bone (PSB) fracture is a common fatal injury among Thoroughbred racehorses.<sup>1-3</sup> A subchondral bone lesion has been observed in medial PSBs from both forelimbs of racehorses that sustain unilateral biaxial PSB fracture.<sup>3-5</sup> Bilateral bone lesions, consistent fracture configurations, and association with high-speed exercise support that PSB fractures are stress fractures.<sup>4-7</sup>

Stress fractures are similar to fatigue fractures of non-living materials. However, unlike in non-living materials, bone reacts to damage, mechanical loads, and environmental factors.<sup>8-10</sup> In healthy bone, cells modulate the quantity of bone and turnover rate in response to the load environment and to repair damaged tissue.<sup>11</sup> Bone reacts to these stimuli through two processes: modeling and remodeling. During remodeling the cellular processes of bone resorption and formation are coupled, but they are uncoupled during modeling. Microdamaged tissue is removed and replaced with undamaged tissue by remodeling. The newly formed tissue mineralizes, with the time and rate of mineralization partially controlled by bone cells.<sup>12</sup> Resorption reduces the apparent elastic modulus by forming pores that can be stress risers at the site of damage repair.<sup>13</sup> Consequently, damage formation and porosity may increase at the repair site in a vicious cycle if training is not reduced.<sup>1,6,9,14,15</sup> In healthy adults, the amount of tissue removed and formed during remodeling are approximately the same (i.e., balanced). However, both negative (e.g., the formation of Haversian canals during remodeling of primary cortical bone) and positive (e.g., in cancellous bone a positive remodeling balance can be induced with parathyroid hormone)<sup>16,17</sup> remodeling balances are possible.

A compartment model for the “bone tissue turnover cycle” is proposed (Figure 3.1). It separates bone tissue into four volumes: undamaged mineralized bone ( $BV_{UD}$ ), damaged mineralized bone ( $BV_D$ ), osteoid (OV), and marrow or vascular space (MV). These tissue types are defined histologically<sup>18</sup> and completely fill the tissue volume ( $TV = BV_D + BV_{UD} + MV + OV$ ). Tissue types can transform along designated



paths at the corresponding rates ( $k_1 - k_5$ ; Figure 3.1; Supplementary Material C). The rates are known to vary with mechanical loading (e.g., strain frequency, magnitude, etc.), age, and other biological factors. Each compartment is a volumetric average within the tissue volume. Volume averaging of tissue types is analogous to many morphometric measures, which define properties relative to a set referent (i.e., measure *per volume*).<sup>18</sup> The four tissue types are related to histological measures, including microcomputed tomography measured mineralized bone volume fraction ( $BVF = BV_M/TV = (BV_D + BV_{UD})/TV$ ) and void space ( $1 - BV_M/TV$ ).

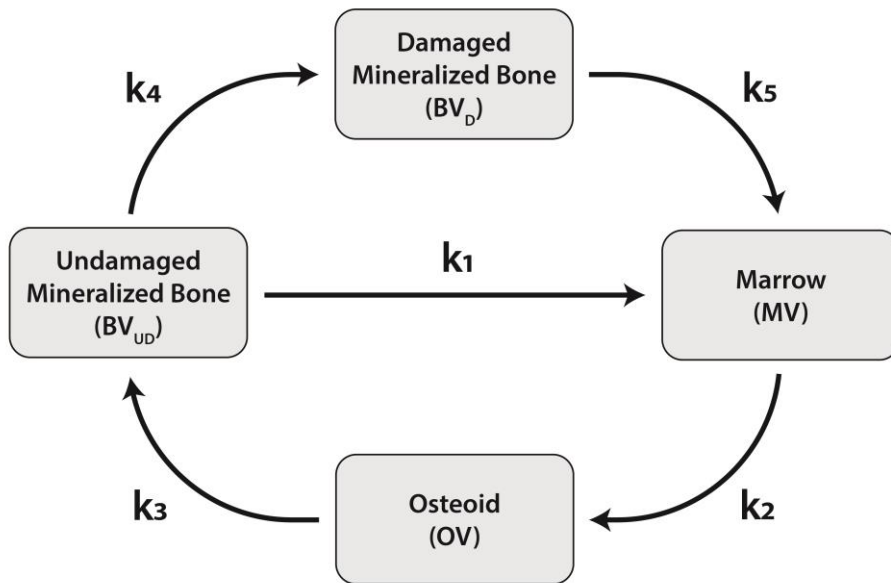


**Figure 3.1:** Compartment model of bone's tissue turnover cycle that assumes a volume of bone tissue can be classified into four volume types: Undamaged Mineralized Bone, Damaged Mineralized Bone, Osteoid, and Marrow. The arrows indicate the path a tissue volume can follow to transform into the different tissue types and  $k_i$  are the transformation rates.

The tissue turnover cycle (Figure 3.1) represents both bone modeling and remodeling. However, changes to any volume fraction cannot be directly attributed to either process. When bone is mathematically characterized using volume fractions, the internal surfaces are lost and, therefore, the distinction between bone remodeling and pure internal (i.e., trabecular surface) modeling is also lost. For example, an increase in mineralized bone volume fraction could occur by unbalanced positive remodeling, modeling to widen trabeculae, and/or other additive changes, but the model cannot distinguish the processes used to increase mineralized tissue volume fraction. This model retains the concept of modeling

on anatomical bone surfaces since exterior surfaces remain after volume averaging. However, in the current study, we are only considering internal changes in tissue fractions below the joint surface, therefore the model represents changes in volume fractions due to internal modeling and remodeling.

Objectives were to 1) compare densitometric and microdamage measures in the medial PSBs of racehorses that did (Case) and did not (Control) sustain unilateral biaxial PSB fracture, 2) determine relationships between measures and high-speed exercise, and 3) assess the model as a mechanism to understand the results.

### **3.3 Materials & Methods**

Densitometric and microdamage parameters were measured in 10 fractured medial PSBs (FX-PSB) from Case racehorses euthanized due to unilateral biaxial PSB fracture (1 female, 5 castrated males, 4 males; 2-8 years old), 10 contralateral limb intact medial PSBs (CLI-PSBs) from the same Case racehorses, and 10 medial PSBs from Control racehorses (CTRL-PSBs) euthanized for injuries unrelated to PSB fracture (3 female, 5 castrated males, 2 males; 2-7 years old). Specimens were collected at necropsy and stored until studied, as previously reported.<sup>4</sup> This study was exempt from Institutional Animal Care and Use Committee approval.

#### **3.3.1 Subject specific exercise history**

The date and distance for all official lifetime gallop-speed activities were acquired (Jockey Club Information Systems). Individual Events were classified as a Race (i.e., a competition) or Work (i.e., a training activity). Sixty-seven derived variables represented four categories: lifetime exercise, exercise intensity, layup ( $\geq 60$  days without an Event), and exercise intensity in the year before death (Table SA-3.7.1).<sup>7</sup>

### 3.3.2 Specimen preparation

PSBs were imaged using microcomputed tomography ( $\mu$ CT;  $\mu$ CT 35, ScanCo Medical;  $18.5 \mu\text{m}^3$  cubic voxels at 7kVP, 114  $\mu\text{A}$ , 2.5s integration time) calibrated to a phantom and segmented at the same threshold. A global threshold of 540 mgHA/ccm was determined by examining candidate thresholds and choosing that which best segregated the tissue into solid and void at the trabecular level as determined by one observer (SKS).

PSBs were previously assessed for focal discoloration, presence of a radiolucent bone lesion, and sectioned into 3mm thick serial sagittal sections. The section with the greatest focal subchondral discoloration was selected for microdamage measurement since it correlated with lesion presence.<sup>4</sup> Similarly located sections were selected for PSBs without focal discoloration.

Sections were stored in 70% ethanol for 8 days then *en bloc* stained in 1% basic fuchsin (F98-10, Fischer Chemical) in ascending grades of ethanol (80%, 90%, 100%; 6 days/grade) under vacuum<sup>19-21</sup>. Stained samples were infused in glycol methacrylate resin (Technovit 7200, Exakt Technologies Inc/Kulzer) in descending grades of ethanol (70%, 30%, 0%; 7 days/grade) under vacuum, placed in a mold, and cured for 8 hours of white then blue light (Histolux, Exakt Technologies Inc.). Hardened blocks were mounted (Technovit 4000 and 7210) on plastic slides, sectioned to 400  $\mu\text{m}$ , then ground and polished to 70  $\mu\text{m}$  thickness (Exakt 400 CS grinder, Exakt Apparateau GmbH & Co., Germany; Buehler MicroPolish 1 micron, Lake Bluff, IL). Brightfield digital microscopy images (Olympus VS120; Olympus OlyVia) were manually stitched (Adobe Photoshop) for microdamage quantification.

### 3.3.3 Densitometric Assessment

Bone volume fraction (BVF), apparent mineral density (AMD), and tissue mineral density (TMD) were quantified in four, 166.5  $\mu\text{m}$  wide, regions of interest ( $\mu$ ROIs) on  $\mu$ CT reconstructions (Figure 3.2A;

ScanCo  $\mu$ CT Evaluation Software v6.5-3; ScanCo Medical) by one observer. In bones with a lesion,  $\mu$ ROIs were created on the sagittal  $\mu$ CT slice with maximum lesion area. In PSBs without a lesion, the  $\mu$ ROIs were created on the sagittal  $\mu$ CT slice at 34.5% of the axial-abaxial width from the most abaxial slice, the mean location of maximum lesion sagittal area in CLI-PSBs. The four  $\mu$ ROIs were: Central Subchondral (CS), Central Subchondral Border (CSB), Proximal Subchondral (PS), and Trabecular (TB)  $\mu$ ROI (Figure 3.2A).

### **3.3.4 Microdamage Quantification**

Microdamage was quantified for six histology ROIs (hROIs) by one observer, blinded to group (CLI and CTRL, but not FX) and horse (ImageJ).<sup>22</sup> Three 1.5 mm deep quadrilateral regions equally divided the articular surface and formed the Proximal Subchondral (PS), Central Subchondral (CS), and Distal Subchondral (DS) hROIs. The Proximal Deep (PD), Central Deep (CD), and Distal Deep (DD) hROIs were duplicated palmarly (Figure 3.2B). Microdamage was not assessed for 2 CTRL-PSBs = as the tissue was inadvertently destroyed during grinding.

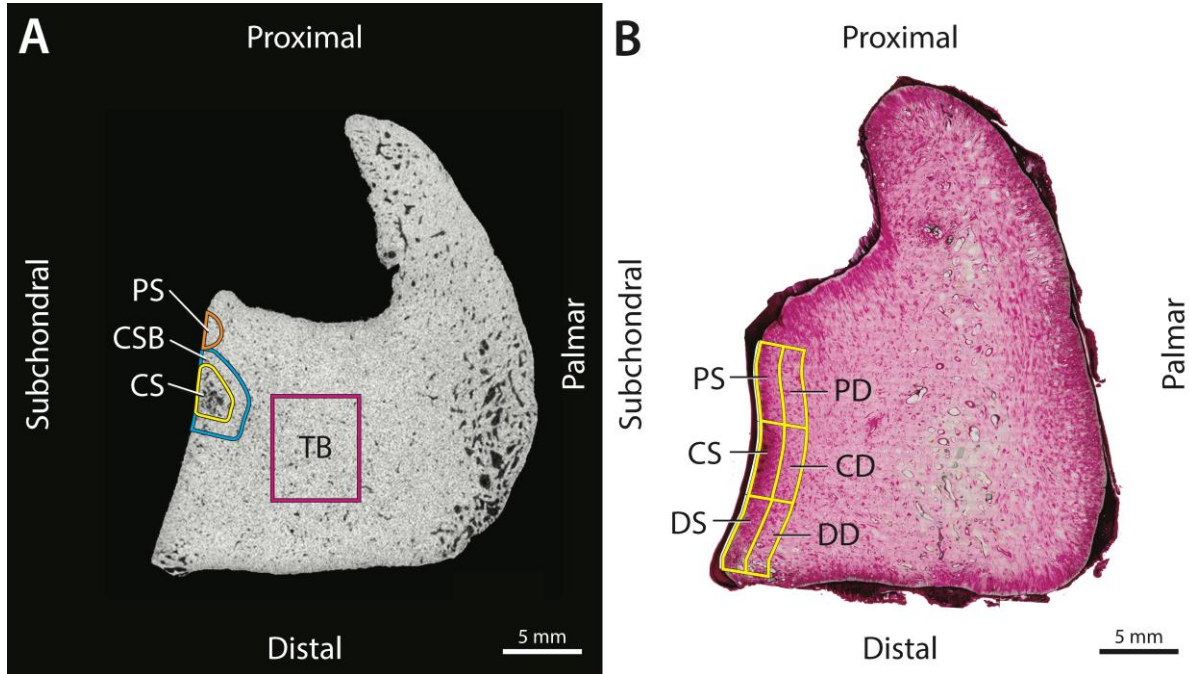


**Figure 3.2:** **A)** Sagittal-plane microcomputed tomography ( $\mu$ CT) from a Case Contralateral Intact (CLI) proximal sesamoid bone (PSB). Microcomputed tomography regions of interest ( $\mu$ ROI) are: Central Subchondral (CS), Central Subchondral Border (CSB), Proximal Subchondral  $\mu$ ROI (PS), and Trabecular  $\mu$ ROI (TB). The CS  $\mu$ ROI surrounded the lesion, if present, or was a  $0.09 \text{ cm}^2$  semi-circle at 39% of the proximodistal height (i.e. average lesion size and location in CLI-PSBs). The CSB  $\mu$ ROI was a 1 mm thick border around the CS  $\mu$ ROI. The PS  $\mu$ ROI was a  $0.06 \text{ cm}^2$  semi-circle whose distal edge was 0.5 mm from the proximal edge of the CS  $\mu$ ROI. The TB  $\mu$ ROI was a  $0.60 \text{ cm}^2$  square drawn 5 mm from the subchondral bone surface and the proximal PSB border. **B)** Basic fuchsin stained section from a CLI-PSB showing histology regions of interest (hROI) in a CLI-PSB. The six hROIs are: Proximal Subchondral hROI (PS), Central Subchondral hROI (CS), Distal Subchondral hROI (DS), Proximal Deep hROI (PD), Central Deep hROI (CD), and Distal Deep (DD) hROIs. Mean hROI area was  $7.9 \text{ mm}^2$  in FX-PSB,  $8.7 \text{ mm}^2$  in CLI-PSBs, and  $8.8 \text{ mm}^2$  in CTRL-PSBs; in FX-PSBs, tissue gaps were excluded from hROI and  $\mu$ ROI areas.

Subchondral bone microcracks (Cr) were defined as deeply stained linear features with a surrounding halo of basic fuchsin.<sup>23</sup> Calcified cartilage microcracks (Md.Cg.Cr) were defined as linear features extending from the tidemark with a surrounding halo of dark staining in subchondral hROIs.<sup>19</sup> The number of microcracks (N.Cr, N.Md.Cg.Cr), length of individual microcracks (Cr.Le, Md.Cg.Cr.Le), microcrack length sum ( $\Sigma$ Cr.Le,  $\Sigma$ Md.Cg.Cr.Le where summation is zero in the absence of cracks), proximal angle between articular surface and calcified cartilage microcrack, hROI area (B.Ar), and articular surface length (Cg.Bd) were quantified. The microcrack areal density (N.Cr/B.Ar; number/ $\text{mm}^2$ ), microcrack length per area ( $\Sigma$ Cr.Le/B.Ar; mm/ $\text{mm}^2$ ), average microcrack length ( $\Sigma$ Cr.Le/N.Cr; mm), calcified cartilage crack number per articular surface length (N.Md.Cg.Cr/Cg.Bd; number/ $\text{mm}^2$ ), average calcified cartilage crack

length ( $\Sigma\text{Md.Cg.Cr.Le}/\text{N.Md.Cg.Cr}$ ; mm), average proximal angle (degrees), and calcified cartilage crack length per articular surface length ( $\Sigma\text{Md.Cg.Cr.Le}/\text{Cg.Bd}$ ; mm/mm) were derived. Whole bone microcrack variables were estimated by combining data from all hROIs.

Measurement repeatability for N.Md.Cg.Cr and N.Cr was tested by interrater reliability (IRR; Shrout-Fleiss fixed set reliability statistic), t-tests, and Bland-Altman plots. N.Cr IRR was 0.65 – 0.92 among hROIs and 0.92 for whole bone; N.Md.Cg.Cr IRR was 0.79-0.96 among hROIs and 0.95 for whole bone. No significant differences ( $p \leq 0.05$ ) or biases were observed.

### **3.3.5 Statistical Analysis**

Exercise history variables were compared between Groups (Case, Control) using a two-sided t-test or Wilcoxon test depending on data normality (Shapiro-Wilks statistic,  $W \geq 0.9$ ). The effects of Group (CLI, CTRL, and FX-PSB) and  $\mu\text{ROI}$  or hROI on densitometric and microcrack variables were assessed using ANOVA or ranked ANOVA depending on ANOVA residual normality (SAS 9.4).<sup>1</sup> Group, ROI, and their interaction were fixed effects and horse was a random effect. The effects of a lesion (Present, Absent) and ROI on densitometric and microcrack variables were assessed similarly. Linear regression was used to assess the relationships between microdamage and densitometric measures in the following ( $\mu\text{ROI}$ , hROI) pairs: (CS, CS), (PS, PS), (Whole Bone, CS), (Whole Bone, TB). The relationships between densitometric and microcrack variables with exercise history variables were determined using robust linear regressions (SAS 9.4)<sup>24</sup> using data from CLI and CTRL-PSBs in all  $\mu\text{ROIs}$  and the CS, PS, PD, and whole bone hROIs. The relationships between the presence of calcified cartilage cracks and exercise history were assessed using univariate logistic regressions since 60% of samples had N.Md.Cg.Cr = 0. For all analyses,  $p \leq 0.05$  was considered statistically significant.

### 3.4 Results

Averaged over  $\mu$ ROIs, mean TMD was lower in FX-PSBs than CLI-PSBs. Averaged over Groups, AMD, TMD, and BVF differed among  $\mu$ ROIs (Table SB-3.8.1). The interaction between Group and  $\mu$ ROI was significant for AMD and BVF (Table 3.1).

**Table 3.1:** Least Square Means  $\pm$  Standard Error from ANOVA or Raw Means  $\pm$  Standard Deviation from ranked ANOVA<sup>¶</sup> for tissue properties in each region of interest in all three study groups. Significant ANOVA effects indicated by variable superscripts: <sup>†</sup>(ROI), <sup>§</sup>(Group), <sup>‡</sup>(Group\*ROI). Pairwise comparisons of ROIs within a group (down column) are indicated by superscripts (A,B,C). Pairwise comparisons of Groups for each ROI (across row), are indicated by subscripts ( $\alpha$ , $\beta$ ). For all comparisons, significant comparisons are indicated by \* and variables that do not share a superscript are significantly different at  $p \leq 0.05$ .

Region of Interest (ROI)	BVF <sup>¶,†,‡</sup>		
	CTRL*	CLI*	FX*
Central Subchondral*	0.98 (0.04) <sub><math>\alpha</math></sub> <sup>A</sup>	0.96 (0.04) <sub><math>\alpha</math>,<math>\beta</math></sub> <sup>A</sup>	0.90 (0.09) <sub><math>\beta</math></sub> <sup>A</sup>
Central Subchondral Border	0.97 (0.05) <sub><math>\alpha</math></sub> <sup>A</sup>	0.98 (0.05) <sub><math>\alpha</math></sub> <sup>B</sup>	0.99 (0.01) <sub><math>\alpha</math></sub> <sup>B</sup>
Trabecular	0.90 (0.09) <sub><math>\alpha</math></sub> <sup>B</sup>	0.97 (0.03) <sub><math>\alpha</math></sub> <sup>A</sup>	0.96 (0.03) <sub><math>\alpha</math></sub> <sup>A,B</sup>
Proximal Subchondral	0.97 (0.04) <sub><math>\alpha</math></sub> <sup>A</sup>	0.96 (0.07) <sub><math>\alpha</math></sub> <sup>A,B</sup>	0.96 (0.07) <sub><math>\alpha</math></sub> <sup>B</sup>
	AMD <sup>†,‡</sup> (mg HA/cc)		
	CTRL	CLI*	FX*
Central Subchondral*	796.06 (13.40) <sub><math>\alpha</math></sub> <sup>A</sup>	782.19 (13.40) <sub><math>\alpha</math></sub> <sup>A</sup>	733.08 (13.40) <sub><math>\beta</math></sub> <sup>A</sup>
Central Subchondral Border	814.90 (13.40) <sub><math>\alpha</math></sub> <sup>A</sup>	822.67 (13.40) <sub><math>\alpha</math></sub> <sup>A,B</sup>	817.05 (13.40) <sub><math>\alpha</math></sub> <sup>B</sup>
Trabecular	782.41 (13.40) <sub><math>\alpha</math></sub> <sup>A</sup>	827.57 (13.40) <sub><math>\beta</math></sub> <sup>B</sup>	816.65 (13.40) <sub><math>\alpha</math>,<math>\beta</math></sub> <sup>B</sup>
Proximal Subchondral	791.75 (13.40) <sub><math>\alpha</math></sub> <sup>A</sup>	795.41 (13.40) <sub><math>\alpha</math></sub> <sup>A,B</sup>	786.66 (14.70) <sub><math>\alpha</math></sub> <sup>B</sup>
	TMD <sup>†,§</sup> (mg HA/cc)		
	CTRL*	CLI*	FX*
Central Subchondral*	812.37 (5.79) <sub><math>\alpha</math></sub> <sup>A</sup>	809.15 (5.79) <sub><math>\alpha</math></sub> <sup>A</sup>	790.55 (5.79) <sub><math>\beta</math></sub> <sup>A</sup>
Central Subchondral Border	837.61 (5.79) <sub><math>\alpha</math></sub> <sup>B</sup>	838.84 (5.79) <sub><math>\alpha</math></sub> <sup>B</sup>	830.26 (5.79) <sub><math>\alpha</math></sub> <sup>B,C</sup>
Trabecular	843.47 (5.79) <sub><math>\alpha</math></sub> <sup>B</sup>	852.94 (5.79) <sub><math>\alpha</math></sub> <sup>B</sup>	842.63 (5.79) <sub><math>\alpha</math></sub> <sup>B</sup>
Proximal Subchondral	811.62 (5.79) <sub><math>\alpha</math></sub> <sup>A</sup>	819.54 (5.79) <sub><math>\alpha</math></sub> <sup>A</sup>	812.77 (6.32) <sub><math>\alpha</math></sub> <sup>C</sup>

Note: AMD (apparent mineral density), BVF (Bone volume fraction), CLI (Case Contralateral Intact Group), CTRL (Control Group), FX (Case Fractured Group), TMD (Tissue mineral density)

Group densitometric differences were observed in the CS and TB  $\mu$ ROIs (Table 3.1; Table SB-3.8.1). BVF, TMD, and AMD in the CS  $\mu$ ROI were 9%, 8% and 3% lower in the FX-PSB compared to CTRL-PSBs. However, BVF, AMD, and TMD in the CS  $\mu$ ROI of CLI-PSBs had intermediate values similar to CTRL-PSBs. In contrast, AMD in the TB  $\mu$ ROI was 6% lower in CTRL-PSBs than in CLI-PSBs.

Regional densitometric differences within Groups were most apparent in FX-PSBs and CLI-PSBs (Table 3.1). BVF, AMD, and TMD were lowest in the CS  $\mu$ ROI of FX-PSBs and CLI-PSBs. In FX-PSBs the CS  $\mu$ ROI BVF was 10.1% lower than in the CSB  $\mu$ ROI and 6.8% lower than in the PS  $\mu$ ROI. In contrast, CTRL-PSBs TB  $\mu$ ROI BVF was nearly 8% lower than all other CTRL  $\mu$ ROIs and no differences were apparent for AMD among all CTRL  $\mu$ ROIs.

All PSBs contained subchondral bone microcracks. The fracture line passed through the CD hROI in all FX-PSBs, the CS in 9/10 FX-PSBs, the PD in 2/10 FX-PSBs, and the PS in 1/10 FX-PSBs. Regardless of Group, microdamage was greatest in the CS, PS, and CD hROIs and least in PD and DD hROIs (Table 3.2; Figure 3.3; Table SB-3.8.2 & SB-3.8.3). The CS and PS hROI N.Cr and N.Cr/B.Ar were not significantly different among Groups; however, the  $\Sigma$ Cr.Le/N.Cr in FX-PSB CS hROI was 41% higher compared to CTRL or CLI-PSBs, and FX-PSB CD hROI N.Cr/B.Ar was 65% higher than in CTRL-PSBs.

Calcified cartilage microcracks were more numerous and larger in Case PSBs (CLI and FX-PSB) than in CTRL-PSBs (Table SB-3.8.2 & SB-3.8.3); they were found in 10/10 FX-PSBs, 9/10 CLI-PSBs, and 2/10 CTRL-PSBs. Case PSBs CS hROI had higher N.Md.Cg.Cr, N.Md.Cg.Cr/Cg.Bd,  $\Sigma$ Md.Cg.Cr.Le/N.Md.Cg.Cr, and  $\Sigma$ Md.Cg.Cr.Le/Cg.Bd than the CTRL-PSBs (Table 3.3). In the PS and DS hROIs, calcified cartilage variables were not different among Groups (Table 3.3). While not statistically different, the mean proximal angle changed from being  $>100^\circ$  in the PS and CS hROIs to  $\sim 56^\circ$  in the DS hROI (Table SB-3.8.2).



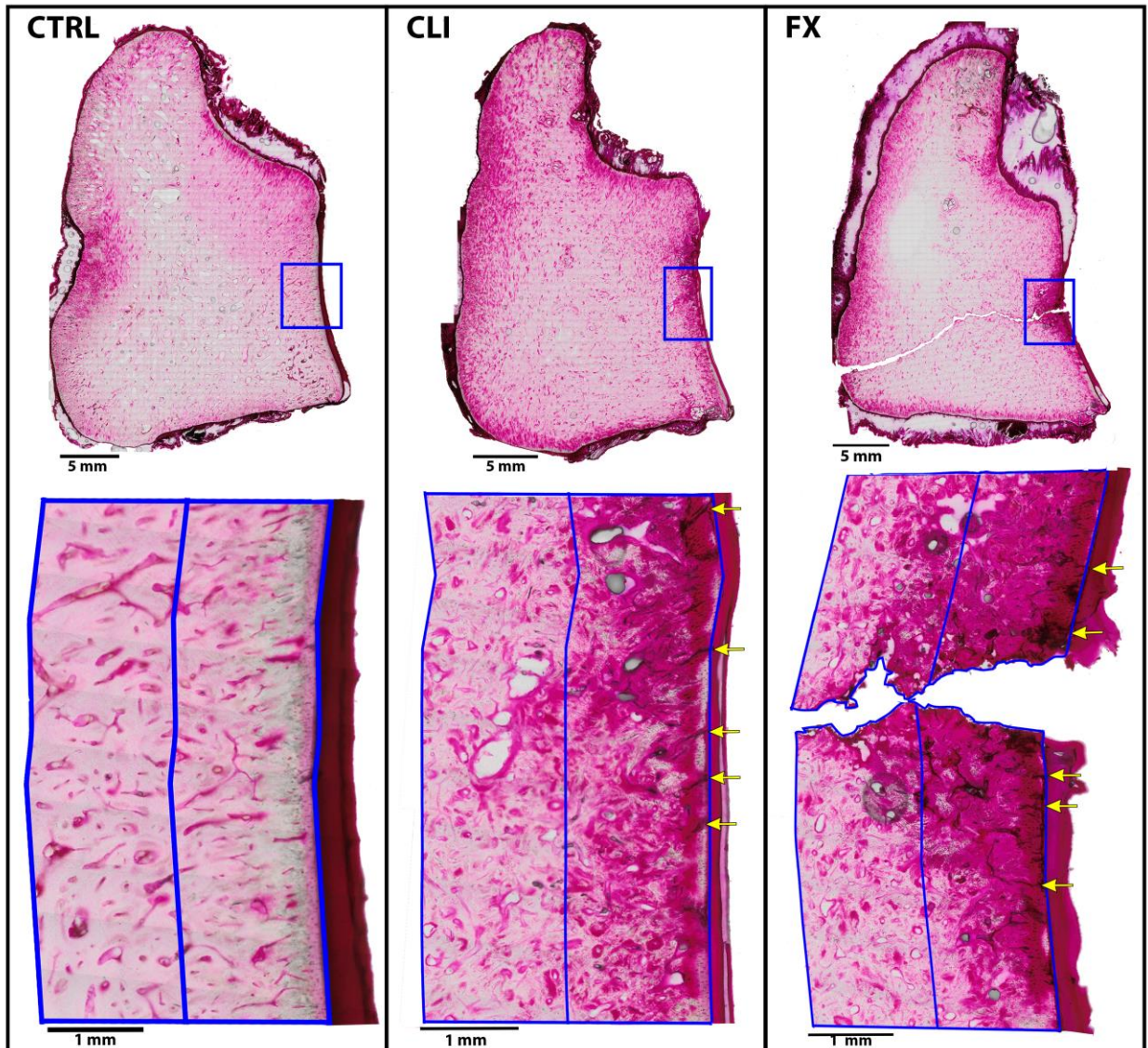


**Figure 3.3:** Basic Fuchsin stained histology sections showing internal and calcified cartilage microcracks on Control (CTRL; Left), Case Contralateral Intact (CLI; Center), and Case Fractured (FX; Right) proximal sesamoid bones (PSBs). The top row shows the entire stained sagittal section, where the blue box encompasses the Central Subchondral and Central Deep histology regions of interest (hROI). The bottom row shows the Central Deep hROI and Central Subchondral hROI from the CTRL, CLI, and FX PSB in more detail. The yellow arrows indicate calcified cartilage microcracks.

**Table 3.2:** Raw Means (Standard Deviation) of microdamage variables for Group and Region of Interest (ROI). Significant ANOVA effects indicated by variable superscripts: †(ROI), §(Group), ‡(Group\*ROI). Pairwise comparisons of ROIs within a group (down column) are indicated by letters (A,B,C,D). Pairwise comparisons of Groups for each ROI (across row), are indicated by Greek letters ( $\alpha$ , $\beta$ ). For all comparisons, significance is indicated by \* and variables that do not share a superscript are significantly different at  $p \leq 0.05$ .

	<b>N.Cr<sup>†</sup></b> (#)		
	<b>CTRL*</b>	<b>CLI*</b>	<b>FX*</b>
<b>Proximal Subchondral</b>	11.0 (11.3) $_{\alpha}^{A,B}$	29.1 (33.7) $_{\alpha}^{A,B}$	13.7 (15.0) $_{\alpha}^{B,C}$
<b>Central Subchondral</b>	19.8 (22.0) $_{\alpha}^A$	52.0 (39.0) $_{\alpha}^A$	60.9 (40.5) $_{\alpha}^A$
<b>Distal Subchondral</b>	6.1 (9.7) $_{\alpha}^{B,C}$	11.6 (13.4) $_{\alpha}^{B,C}$	9.4 (7.3) $_{\alpha}^{B,C}$
<b>Proximal Deep</b>	4.3 (4.9) $_{\alpha}^{C,D}$	4.9 (5.8) $_{\alpha}^{B,C}$	3.0 (3.0) $_{\alpha}^{D,C}$
<b>Central Deep</b>	6.9 (9.7) $_{\beta}^{A,B}$	14.5(10.8) $_{\alpha,\beta}^{A,B,C}$	15.6 (9.4) $_{\alpha}^{A,B}$
<b>Distal Deep</b>	2.2 (3.2) $_{\alpha}^D$	1.5 (3.3) $_{\alpha}^C$	2.0 (2.4) $_{\alpha}^D$
	<b>N.Cr/B.Ar<sup>†</sup></b> (#/mm <sup>2</sup> )		
	<b>CTRL*</b>	<b>CLI*</b>	<b>FX*</b>
<b>Proximal Subchondral</b>	1.1(1.0) $_{\alpha}^{A,B}$	3.1 (3.4) $_{\alpha}^{A,B}$	1.6 (1.5) $_{\alpha}^{B,C}$
<b>Central Subchondral</b>	2.1 (2.1) $_{\alpha}^A$	6.0 (4.1) $_{\alpha}^A$	7.6 (5.1) $_{\alpha}^A$
<b>Distal Subchondral</b>	0.6 (1.0) $_{\alpha}^{B,C}$	1.3 (1.4) $_{\alpha}^{B,C}$	1.3 (1.1) $_{\alpha}^{B,C}$
<b>Proximal Deep</b>	0.4 (0.5) $_{\alpha}^{B,C}$	0.5 (0.6) $_{\alpha}^{C,D}$	0.4 (0.5) $_{\alpha}^{D,C}$
<b>Central Deep*</b>	0.7 (0.9) $_{\beta}^{A,B,C}$	1.6 (1.0) $_{\alpha,\beta}^{A,B}$	2.0 (1.2) $_{\alpha}^{A,B}$
<b>Distal Deep</b>	0.2 (0.3) $_{\alpha}^C$	0.2 (0.4) $_{\alpha}^D$	0.3 (0.4) $_{\alpha}^D$
	<b><math>\Sigma</math>Cr.Le/N.Cr<sup>†,§</sup></b> (mm)		
	<b>CTRL</b>	<b>CLI*</b>	<b>FX*</b>
<b>Proximal Subchondral</b>	0.07(0.02) $_{\alpha}^A$	0.07 (0.04) $_{\alpha}^A$	0.06 (0.03) $_{\alpha}^{B,C}$
<b>Central Subchondral*</b>	0.07 (0.02) $_{\alpha}^A$	0.07 (0.03) $_{\alpha}^A$	0.12 (0.05) $_{\beta}^A$
<b>Distal Subchondral</b>	0.04 (0.04) $_{\alpha}^A$	0.05 (0.03) $_{\alpha}^{A,B}$	0.04 (0.03) $_{\alpha}^C$
<b>Proximal Deep</b>	0.05 (0.04) $_{\alpha}^A$	0.03 (0.03) $_{\alpha}^{A,B}$	0.07 (0.06) $_{\alpha}^{A,B,C}$
<b>Central Deep</b>	0.07 (0.05) $_{\alpha}^A$	0.07 (0.04) $_{\alpha}^{A,B}$	0.10 (0.06) $_{\alpha}^{A,B}$
<b>Distal Deep</b>	0.05(0.07) $_{\alpha}^A$	0.02(0.03) $_{\alpha}^B$	0.05(0.056) $_{\alpha}^C$
	<b><math>\Sigma</math>Cr.Le/B.Ar<sup>†</sup></b> (mm/mm <sup>2</sup> )		
	<b>CTRL*</b>	<b>CLI*</b>	<b>FX*</b>
<b>Proximal Subchondral</b>	0.09 (0.10) $_{\alpha}^{A,B}$	0.27 (0.34) $_{\alpha}^{A,B}$	0.12 (0.14) $_{\alpha}^{B,C}$
<b>Central Subchondral*</b>	0.17 (0.22) $_{\beta}^A$	0.50 (0.36) $_{\alpha,\beta}^A$	0.91 (0.54) $_{\alpha}^A$
<b>Distal Subchondral</b>	0.06 (0.11) $_{\alpha}^B$	0.08 (0.08) $_{\alpha}^{B,C}$	0.08 (0.08) $_{\alpha}^{B,C,D}$
<b>Proximal Deep</b>	0.03 (0.03) $_{\alpha}^B$	0.03 (0.03) $_{\alpha}^{D,C}$	0.05 (0.08) $_{\alpha}^{C,D}$
<b>Central Deep*</b>	0.06 (0.09) $_{\beta}^{A,B}$	0.11 (0.07) $_{\alpha,\beta}^{A,B}$	0.19 (0.14) $_{\alpha}^{A,B}$
<b>Distal Deep</b>	0.02 (0.03) $_{\alpha}^B$	0.01 (0.02) $_{\alpha}^D$	0.02 (0.03) $_{\alpha}^D$

Note: CLI (Case Contralateral Intact Group), CTRL (Control Group), FX (Case Fractured Group), N.Cr (microcrack number), N.Cr/B.Ar (microcrack density),  $\Sigma$ Cr.Le/B.Ar (microcrack length per area),  $\Sigma$ Cr.Le/N.Cr (Average microcrack length)

**Table 3.3:** Raw Means (Standard Deviation) of calcified cartilage microcrack variables for Group and Region of Interest (ROI). Significant ANOVA effects indicated by variable superscripts: <sup>†</sup>(ROI), <sup>§</sup>(Group), <sup>‡</sup>(Group\*ROI). Pairwise comparisons of ROIs within a group (down column) are indicated by letters (A,B,C,D). Pairwise comparisons of Groups for each ROI (across row), are indicated by Greek letters ( $\alpha$ , $\beta$ ). For all comparisons, significance is indicated by \* and variables that do not share a superscript are significantly different at  $p \leq 0.05$ .

	<b>N.Md.Cg.Cr<sup>†,§</sup></b> (#)		
	<b>CTRL</b>	<b>CLI*</b>	<b>FX*</b>
<b>Proximal Subchondral</b>	0.8 (1.5) $\alpha^A$	2.0 (2.7) $\alpha^{A,B}$	1.5 (1.5) $\alpha^{A,B}$
<b>Central Subchondral*</b>	0.1 (0.4) $\alpha^A$	2.6(2.4) $\beta^A$	5.1(4.1) $\beta^A$
<b>Distal Subchondral</b>	0.0 (0.0) $\alpha^A$	0.3 (0.7) $\alpha^B$	1.7 (2.6) $\alpha^B$
	<b>N.Md.Cg.Cr/Cg.Bd<sup>†,§</sup></b> (#/mm)		
	<b>CTRL</b>	<b>CLI*</b>	<b>FX*</b>
<b>Proximal Subchondral</b>	0.1 (0.2) $\alpha^A$	0.3 (0.4) $\alpha^{A,B}$	0.3 (0.2) $\alpha^{A,B}$
<b>Central Subchondral*</b>	0.0 (0.1) $\alpha^A$	0.5 (0.5) $\beta^A$	0.9 (0.6) $\beta^A$
<b>Distal Subchondral</b>	0.0 (0.0) $\alpha^A$	0.1 (0.1) $\alpha^B$	0.3 (0.5) $\alpha^B$
	<b><math>\Sigma</math>Md.Cg.Cr.Le/N.Md.Cg.Cr<sup>†,§</sup></b> (mm)		
	<b>CTRL</b>	<b>CLI*</b>	<b>FX</b>
<b>Proximal Subchondral</b>	0.07 (0.15) $\alpha^A$	0.12 (0.13) $\alpha^{A,B}$	0.08 (0.08) $\alpha^A$
<b>Central Subchondral*</b>	0.01 (0.04) $\alpha^A$	0.18 (0.16) $\beta^A$	0.18 (0.11) $\beta^A$
<b>Distal Subchondral</b>	0 (0) $\alpha^A$	0.06 (0.13) $\alpha^B$	0.09 (0.15) $\alpha^A$
	<b><math>\Sigma</math>Md.Cg.Cr.Le/Cg.Bd<sup>†,§</sup></b> (mm/mm)		
	<b>CTRL</b>	<b>CLI*</b>	<b>FX*</b>
<b>Proximal Subchondral</b>	0.03 (0.08) $\alpha^A$	0.08 (0.11) $\alpha^{A,B}$	0.03 (0.03) $\alpha^B$
<b>Central Subchondral*</b>	0.00 (0.01) $\alpha^A$	0.12 (0.13) $\beta^A$	0.17 (0.13) $\beta^A$
<b>Distal Subchondral</b>	0 (0) $\alpha^A$	0.01 (0.03) $\alpha^B$	0.09 (0.16) $\alpha^B$

**Note:** N.Md.Cg.Cr (calcified cartilage crack number), N.Md.Cg.Cr/Cg.Bd (number of calcified cartilage cracks per articular surface length),  $\Sigma$ Md.Cg.Cr.Le/Cg.Bd (calcified cartilage crack length per articular surface length),  $\Sigma$ Md.Cg.Cr.Le/N.Md.Cg.Cr (average calcified cartilage crack length).

### 3.4.1 Densitometric and Microdamage Results by Presence of Subchondral Bone Lesion

Densitometric and microdamage observations in PSBs with or without a lesion largely paralleled Group differences. Bilateral lesions were observed in 7/10 Case PSBs and unilateral lesions in 2/10 FX-PSBs; one Case PSBs contained no lesion.<sup>4</sup> Lesions were not observed in CTRL-PSBs.<sup>4</sup>

The greatest differences between PSBs with, and without, a lesion occurred in the CS and TB ROIs (Table SB-3.8.4 & SB-3.8.5). The CS  $\mu$ ROI of PSBs with a lesion had 7.5% lower BVF, 7.8% lower AMD, and 2.8% lower TMD than PSBs without a lesion. The TB BVF in PSBs with a lesion were significantly higher than those without. In PSBs with a lesion, N.Cr and N.Cr/B.Ar were highest in the CS hROI; however, N.Cr and N.Cr/B.Ar were not different in the three subchondral hROIs of PSBs without a lesion. Calcified cartilage cracks were found in 16/16 PSBs with a lesion and 5/14 PSBs without a lesion. Additionally, BVF in the PS and CSB  $\mu$ ROIs were higher in PSBs with a lesion than those without.

### 3.4.2 Relationship between Microcracks and Densitometric Measures

Variance in whole bone N.Md.Cg.Cr/Cg.Bd explained the largest amount of variance for BVF, AMD, and TMD in the CS  $\mu$ ROI (Table 3.4). Whole bone and CS hROI N.Md.Cg.Cr and N.Md.Cg.Cr/Cg.Bd were negatively related to CS  $\mu$ ROI TMD, AMD, and BVF.

**Table 3.4:** Linear regression slope ( $R^2$ ) between microdamage and densitometric measures in the CS  $\mu$ ROI with the CD hROI and whole bone hROIs. Reported regressions are significant at  $p \leq 0.05$ , non-significant regressions are indicated by NS.

		Central Subchondral hROI				Whole Bone Microdamage			
		N.Md.Cg.Cr (#)	N.Md.Cg.Cr/ Cg.Bd (#/mm)	N.Cr (#)	N.Cr/ B.Ar (#/mm <sup>2</sup> )	N.Md.Cg.Cr (#)	N.Md.Cg.Cr/ Cg.Bd (#/mm)	N.Cr (#)	N.Cr/ B.Ar (#/mm <sup>2</sup> )
Central Subchondral $\mu$ ROI	AMD (mg HA/cc)	-7.55 (0.29)	-46.33 (0.31)	NS	NS	-6.2 (0.40)	-113.79 (0.45)	NS	NS
	TMD (mg HA/cc)	-2.86 (0.31)	-17.39 (0.33)	-0.19 (0.17)	-1.76 (0.21)	-2.06 (0.34)	-37.51 (0.37)	NS	NS
	BVF	-0.01 (0.23)	-0.06 (0.25)	NS	NS	-0.01 (0.36)	-0.15 (0.40)	NS	NS

### 3.4.3 Differences in Exercise History among Case & Control Racehorses

Case horses participated in over twice as many lifetime Works and Events, accumulated nearly twice the lifetime Work and Event distance, had over twice as much time in training since last layup, and performed nearly twice the distance, Events, and Works each month 1 to 12 months before death (Table 3.5). Average Event distances and Race variables were not different between Case and Control horses; other exercise intensity variables were not different or marginally insignificant ( $0.10 \leq p < 0.05$ ; Table SA-3.7.2).

**Table 3.5:** Median (Minimum, Maximum) and Mean (Standard Deviation) of selected exercise history variables for Case (n= 10) and Control (n=10) horses. Within a row, Group means that share a superscript are not significantly different at  $p \leq 0.05$  (\* indicates marginal significance at  $p \leq 0.10$ ). Variables with non-normal distributions (Shapiro-Wilks  $W > 0.90$ ) are indicated by †. Variable definitions and full results are given in Supplement A.

Variable Type	Variable (Unit)	Median (Minimum, Maximum)		Mean (Standard Deviation)	
		Case	Control	Case	Control
Lifetime Exercise	Age <sup>†</sup> (Years)	3.54 (2.34, 7.84)	3.38 (2.61, 7.37)	3.95 <sup>A</sup> (1.58)	3.81 <sup>A</sup> (1.53)
	Number of Events <sup>†</sup> (events)	28.0 (14.00, 153.00)	15.50 (4.00, 78.00)	43.60 <sup>A</sup> (41.19)	24.60 <sup>B</sup> (23.68)
	Number of Races <sup>†</sup> (races)	8.00 (0.00, 32.00)	5.00 (0.00, 26.00)	10.70 <sup>A</sup> (9.92)	7.00 <sup>A</sup> (8.38)
	Number of Works <sup>†</sup> (works)	19.50 (12.00, 121.00)	10.50 (4.00, 52.00)	32.90 <sup>A</sup> (32.76)	17.60 <sup>B</sup> (15.83)
Exercise intensity	Days Between Events (days)	11.95 (7.83, 20.61)	17.54 (8.08, 41.85)	12.52 <sup>A</sup> (4.09)	19.90 <sup>A*</sup> (10.20)
	Days Between Events During Active Training <sup>†</sup> (days)	8.96 (7.83, 16.5)	11.34 (7.85, 13.78)	10.01 <sup>A</sup> (2.67)	10.87 <sup>A</sup> (2.34)
	Furlongs per Month (furlong/mo)	8.96 (2.99, 16.18)	4.57 (2.76, 10.69)	8.81 <sup>A</sup> (3.57)	5.89 <sup>A</sup> (2.78)
	Furlongs per Month of Active Training (furlong/mo)	11.15 (2.99, 16.18)	9.05 (4.54, 15.51)	10.68 <sup>A</sup> (3.49)	9.76 <sup>A</sup> (4.11)
Layup	Layup Time <sup>†</sup> (days)	87.5 (0.00, 698.00)	62.00 (0.00, 927.00)	136.6 <sup>A</sup> (211.02)	234 <sup>A</sup> (330.02)
	Average Layup Length <sup>†</sup> (days)	87.50 (0.00, 201.00)	55.25 (0, 323)	84.25 <sup>A</sup> (81.39)	106.75 <sup>A</sup> (130.74)
	Percent Career in Layup <sup>†</sup> (%)	19.43 (0.00, 42.41)	24.36 (0.00, 81.25)	16.99 <sup>A</sup> (16.05)	30.92 <sup>A</sup> (33.86)
	Time Since End of Last Layup (days)	256.00 (61, 461)	94.00 (0.00, 237.00)	259.90 <sup>A</sup> (139.86)	104.70 <sup>B</sup> (81.04)
	Events Since Last Layup (Events)	28.00 (8.00, 49.00)	10.00 (0.00, 26.00)	27.60 <sup>A</sup> (13.48)	10.40 <sup>B</sup> (8.64)

Variable Type	Variable (Unit)	Median (Minimum, Maximum)		Mean (Standard Deviation)	
		Case	Control	Case	Control
Exercise Before Death	Events 2 Months Before Death (events)	6.00 (3.00, 9.00)	4.00 (0.00, 7.00)	5.90 <sup>A</sup> (1.91)	3.50 <sup>B</sup> (2.32)
	Events 4 Months Before Death (events)	12.50 (8.00, 17.00)	8.00 (0.00, 14.00)	12.00 <sup>A</sup> (3.20)	7.20 <sup>B</sup> (5.12)
	Events 6 Months Before Death (events)	18.00 (11.00, 23.00)	10.00 (0.00, 22.00)	17.40 <sup>A</sup> (4.06)	9.90 <sup>B</sup> (6.67)
	Events 8 Months Before Death <sup>†</sup> (events)	22.00 (14.00, 29.00)	10.50 (1.00, 26.00)	21.40 <sup>A</sup> (6.33)	11.60 <sup>B</sup> (7.68)
	Events 10 Months Before Death <sup>†</sup> (events)	24.00 (14.00, 35.00)	11.00 (2.00, 26)	24.70 <sup>A</sup> (8.21)	11.80 <sup>B</sup> (7.51)
	Events 1 Year Before Death <sup>†</sup> (events)	24.50 (14.00, 41.00)	11.00 (4.00, 26)	27.10 <sup>A</sup> (10.40)	12.20 <sup>B</sup> (7.02)

### 3.3.4 Relationships between Exercise History, Microcracks and Densitometry

The directions of the regressions between BVF and AMD with exercise intensity, layup, and exercise intensity in the year prior to death in the CS ROIs differed from other regions and was most apparent between the CS and TB  $\mu$ ROIs (Figure 3.4). In the CS  $\mu$ ROI, BVF and AMD *decreased* with exercise intensity (e.g. *increasing* with days between activities;  $0.07 \leq R^2 \leq 0.12$ ), BVF *decreased* with Events and Works 2-12 months Before Death ( $0.09 \leq R^2 \leq 0.12$ ) and AMD *increased* with time in layup ( $R^2 = 0.10$ ). Conversely, in the TB  $\mu$ ROI, BVF *increased* with exercise intensity ( $R^2 = 0.17$ ), BVF *decreased* with time in layup ( $0.10 \leq R^2 \leq 0.15$ ), and BVF and AMD *decreased* with time elapsed between death and the previous event ( $R^2 = 0.34, 0.39$ ). When significant, BVF decreased with lifetime measures in both the CS and TB  $\mu$ ROIs (Table SA-3.7.3). CS  $\mu$ ROI AMD had no significant relationships to lifetime summary measures; AMD increased with horse age in the PS and CSB  $\mu$ ROIs ( $R^2 = 0.18, 0.13$ ) and with age at start of training in the TB  $\mu$ ROI ( $R^2 = 0.20$ ).

In the CS and TB  $\mu$ ROIs, TMD *decreased* with exercise intensity ( $0.14 \leq R^2 \leq 0.27$ ). TMD increased with lifetime summary variables in the CS, CSB, and PS  $\mu$ ROIs (Table SA-3.7.4). TMD was not associated with exercise in the year before death.

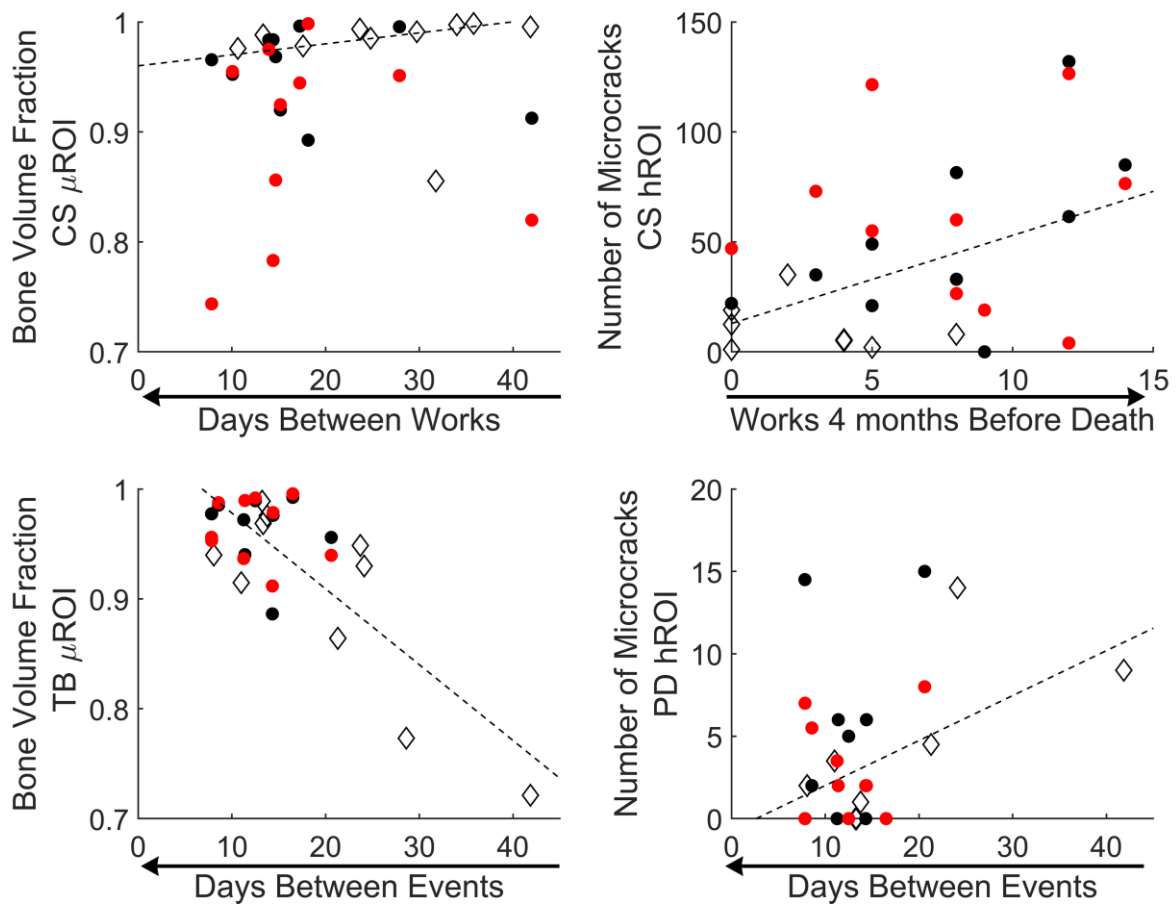


**Figure 3.4:** Selected exercise robust linear regressions for bone volume fraction (BVF) and number of subchondral microcracks (N.Cr). In all panels, the arrow below the x-axis title shows the direction of increasing exercise intensity. Data from Case Contralateral Limb Intact (CLI) PSBs are shown with the black filled circle, Case Fractured (FX) PSBs with the red filled circle, and Control with the open diamond; only CLI-PSB and CTRL-PSB data were used to build the robust linear regressions. In the Central Subchondral region of interest, BVF decreased with an increase in exercise intensity (or with *fewer* days between Works;  $R^2 = 0.10$ ) and N.Cr increased with exercise intensity ( $R^2 = 0.18$ ). In the trabecular  $\mu$ ROI, BVF decreased with a decrease in exercise intensity (or with *more* days between Events;  $R^2 = 0.17$ ). In the proximal deep hROI, N.Cr increased with the exercise intensity ( $R^2 = 0.17$ )

The relationships between microdamage and exercise in the CS hROI were different from those in the PS and PD hROIs, which had low, but detectable, amounts of microdamage. In the CS hROI, N.Cr, N.Cr/B.Ar and  $\Sigma$ Cr.Le/B.Ar *increased* with exercise frequency 2-4 months before death ( $0.19 \leq R^2 \leq 0.29$ ); *opposite* of the relationships observed between BVF, AMD, and exercise intensity in the overlapping CS  $\mu$ ROI. In the CS hROI,  $\Sigma$ Cr.Le/B.Ar increased with time spent in layup ( $R^2 = 0.18$ ). Events 1-2 months before death were the only predictors of presence of calcified cartilage cracks (Table SA-3.7.5).

Damage was not observed within the TB region; however, in the low damage PS and PD hROIs, N.Cr and N.Cr/B.Ar *decreased* with exercise intensity ( $0.15 \leq R^2 \leq 0.36$ ) and in the PD hROI  $\Sigma$ Cr.Le/B.Ar or  $\Sigma$ Cr.Le/N.Cr *decreased* with exercise intensity 1-10 months before death ( $0.15 \leq R^2 \leq 0.32$ ). In the PS and PD hROIs, N.Cr, N.Cr/B.Ar increased with time in layup ( $0.14 \leq R^2 \leq 0.28$ ). A summary of all regressions is in Tables SA-3.7.3 to SA-3.7.5.

### 3.5 Discussion

Medial PSBs from Thoroughbred racehorses that did (Case) and did not (Control) have a unilateral biaxial PSB fracture were evaluated for differences in tissue densitometric and microdamage measures at multiple locations, including the site of a radiolucent subchondral bone lesion.<sup>4</sup> In Case PSBs, the lesion site had higher N.Cr/B.Ar and lower bone volume fraction (BVF), apparent mineral density (AMD), and tissue mineral density (TMD) compared to surrounding tissue. The lesion observed in Case PSBs is believed to precede PSB fracture and tended to be bilaterally present, these findings are consistent with previous reports.<sup>4,25</sup>

We hypothesize that the calcified cartilage cracks developed after the osteopenic lesion. Likely, the lesion reduced tissue stiffness, allowing greater deformation of and cracking in the calcified cartilage. Three observations support this hypothesis. First, calcified cartilage cracks were primarily observed in PSBs with a lesion. Second, reduced bone volume fraction was associated with more calcified cartilage cracks at the lesion site. Third, the probability of calcified cartilage cracks increased with exercise 1-2 months prior to death while subchondral microcrack number and areal density increased with exercise 2-4 months prior to death. Similar observations have been associated with articular surface collapse of horses with palmar osteochondral disease.<sup>26</sup>



### 3.5.1 Relationship of Exercise to Densitometric & Microdamage Variables

The relationships between BVF, N.Cr, N.Cr/B.Ar and exercise intensity variables were different for the central subchondral and other ROIs. However, the relationships between tissue mineralization (TMD) and exercise intensity variables were similar among regions, providing an opportunity to infer how the rate terms in the conceptual model of bone remodeling (Figure 3.1) were related to exercise. Previous research indicates that osteoid formation rate ( $k_2$ ), damage formation rate ( $k_4$ ), undamaged mineralized bone resorption rate ( $k_1$ ), and damaged bone resorption rate ( $k_5$ ) likely depend on mechanical loading (i.e. strain magnitude and frequency) and, potentially, microdamage-induced inflammation.<sup>10,27-30</sup> Primary mineralization rate ( $k_3$ ) may be independent of mechanical loading.<sup>31,32</sup> The exact dependencies of the rate constants on mechanical parameters are unknown. However, inferences about how rate terms were affected by mechanical loadings (i.e., exercise) can be made from the regression findings.

Two location-specific contradictory relationships were observed between exercise intensity variables and bone volume fraction (BVF). In the central subchondral region, BVF *decreased* with exercise intensity and in the trabecular region BVF *increased* with lifetime exercise intensity (Figure 3.4). In the model, BVF is mineralized bone tissue per tissue volume (TV) ( $BVF = BV_M / TV = (BV_D + BV_{UD}) / TV$ ). Additionally, N.Cr/B.Ar (related to  $BV_D / TV$ ) was positively correlated to exercise intensity before death in the central subchondral region, but in the trabecular region no microdamage was observed. Also, in the examined low damage regions N.Cr/B.Ar was negatively correlated to exercise intensity (Figure 3.4). These contradictory relationships are explained if the rate constants depend on exercise intensity in a location-specific manner. Location dependence could result from differences in strain magnitude or rate among the sites.

We hypothesize that the contradictory relationships observed are caused by the central subchondral site unsuccessfully responding to microdamage induced by exercise in Case horses. Damage

and damage induced bone resorption resulted in increases in damaged bone ( $BV_D$ ) and marrow space (MV) and decrease of undamaged mineralized bone ( $BV_{UD}$ ). Other locations successfully responded to exercise by increasing/maintaining  $BV_{UD}$  and maintaining a “low-enough”  $BV_D$  to prevent a damage feedback loop. In Control PSBs, which had no lesions, all locations successfully adapted to exercise levels. The model predicts solutions consistent with this hypothesis if rate constants are allowed to vary among sites. Damage formation rate ( $k_4$ ) can be used to arrive at a consistent solution. The partial derivative of  $BV_D/TV$  with respect to damage formation rate ( $k_4$ ) is positive and the partial derivative of  $BV_M/TV$  with respect to  $k_4$  is negative if the damaged bone resorption rate ( $k_5$ ) is higher than the turnover rate ( $k_1$ ), a condition expected during normal *targeted* bone remodeling (Supplementary Material C).<sup>8,11</sup> At steady-state, the model predicts a site with a higher damage formation rate ( $k_4$ ) would have a higher  $BV_D/TV$  and lower  $BV_M/TV$  than a site with a lower  $k_4$ . That is, the model correctly predicts observed morphological differences in the central subchondral and trabecular sites if the mechanical damage rate is higher in the former compared to the latter site.

In the trabecular region bone damage was not detected, but the bone volume fraction (BVF) in horses with a lesion was higher than those without a lesion. In the model,  $BV_D/TV=0$  is predicted if the damage formation rate ( $k_4$ ) is zero and non-zero  $BV_{UD}/TV$  is predicted if the other rate constants are non-zero. Damage formation rate ( $k_4$ ) increases with tissue stress, and, therefore, would be different at the subchondral and trabecular tissue sites if respective stresses are different. In support of this hypothesis, previous research indicates that subchondral tissues experience a localized higher stress magnitude than deeper tissues,<sup>33</sup> that shear stresses resulting from the contact stress cause linear microcracks like those observed in the central subchondral site<sup>34</sup>, and that Young’s Modulus increases with BVF<sup>35</sup> and decreases with N.Cr/B.Ar.<sup>36</sup> So, there is likely a stress difference between the two regions that is exacerbated when the BVF at the central subchondral site is low. This low BVF central subchondral site may act as a stress riser, causing a further increase in the damage formation rate ( $k_4$ ). Regional dependencies on the other

rate constants may exist, but a full analysis is beyond the scope of this paper. To fully test this set of hypotheses a stress analysis model coupled with the proposed turnover model is needed.

Unlike bone volume fraction, tissue mineral density (TMD) decreased with event frequency regardless of location. TMD is the extent of mineralization of the mineralized bone ( $BV_M$ ) volume. In this model,  $k_3$  represents the rate of primary mineralization of bone, so  $BV_M$  is bone that had reached primary mineralization. Secondary mineralization is not explicitly included in the model but depends on elapsed time between initial mineralization and resorption of the mineralized tissue. In a steady-state model (as presented here) the rate at which tissue "cycles" through a compartment depends on the magnitudes of the rate constants, but not upon their ratios. The negative correlation of TMD with event frequency, therefore, suggests that *at all sites* the "cycle rate" is increased by event frequency. At a high cycle rate tissue remains in a mineralizing compartment (i.e.,  $BV_D$  or  $BV_{UD}$ ) for less time, so mineralization has less time to proceed, and TMD is reduced. The reduced TMD observed at the lesion site, compared to other regions, suggests a higher turnover rate at the lesion site. This hypothesis is consistent with the observation that TMD increases with tissue age and decreases with tissue turnover rate.<sup>37,38</sup>

Exercise intensity variables and layup variables were the best predictors of densitometric and microdamage measures. Rate of loading and the difference between applied and habitual loads affect bone formation, bone turnover, damage formation, and damage repair rates.<sup>27-29,32</sup> Exercise intensity variables reflect load application rate, whereas, layup variables reflect changes in load magnitude from a habitual condition; so, the observed relationships between these variable types and measured densitometric and microdamage variables are consistent with previous research.<sup>8</sup>

Exercise intensity variables were expressed as either activities per time or distance per time. These somewhat correlated measures may have different effects on bone biology and thus the rate constants. The response of bone cells to mechanical loading saturates rapidly after loading begins.<sup>29</sup>

Therefore, if saturation occurs early in an exercise event, event frequency variables may be better suited to drive osteoid formation rate ( $k_2$ ) than distance frequency. However, fatigue damage is related to the total number of applied load cycles. When combined with average stride length, distance frequency variables indicate number of load cycles, so distance frequency variables may be better suited to drive damage formation rate ( $k_4$ ). Study results neither support nor refute this hypothesis, as both event and distance frequency variables were strongly related to densitometric and microcrack data.

Limitations of this study include examination of only medial PSBs from a small sample of racehorses in one geographic population. Medial PSBs were selected because unilateral PSB fracture is more common in medial than lateral PSBs and subchondral lesions have previously been reported in medial PSBs.<sup>4,25</sup> Examination of PSBs from only California Thoroughbred racehorses limits the extent to which results can be generalized to other racehorses. However, similar changes have been reported or clinically observed (Figure 3.5) in other racing populations.<sup>25</sup>

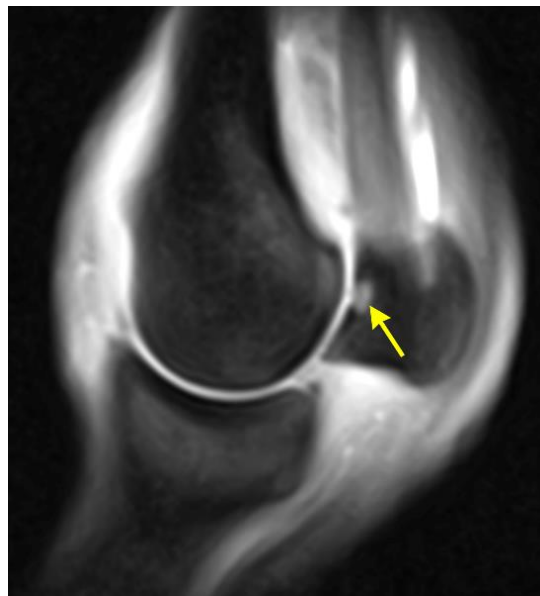


**Figure 3.5:** Magnetic Resonance Image (MRI) of the left fetlock joint of a living racehorse from a different racing population (outside USA) showing a bone bruise in the same location (yellow arrow) as the density lesions identified in this study. Increased signal indicates active bone remodeling at the lesion site. This horse suffered low-level intermittent lameness, but no other clinical symptoms. This image is used with permission of Drs. Weir, Riggs, and Stewart.

An abaxial region of focal osteopenia and high microdamage was observed in racehorses that were euthanized after incurring unilateral biaxial PSB fracture; these focal changes were not observed in racehorses euthanized during training from other injuries. The densitometric properties and microdamage measures within this bone lesion site had different relationships to exercise compared to other sites within the bone. A compartmental model of bone's tissue turnover cycle was introduced and used to understand the site-specific differences in densitometric and microdamage measures and in the relationships of those measures to exercise.

### **3.6 Acknowledgements**

This project was supported by the Grayson Jockey Club Research Foundation, Inc., the Maury Hull Fellowship (University of California Davis), the Louis R. Rowan Fellowship (California Thoroughbred Foundation), the University of California Davis Center for Equine Health (with funds provided by the State of California satellite wagering fund and contributions by private donors).

### 3.7 Supplemental Material A: Exercise history and relationship to densitometric and microdamage measures

Exercise history data from a commercial database included the date and distance of each race or official timed-work for all horses (InCompass, Jockey Club Information System). Sixty-seven racing-speed exercise variables were derived for each horse (Table SA-3.7.1) using previously reported methods (Anthenill, 2007). As described in Shaffer 2020, stratified sampling was used to select Case and Control horses based on a multivariate linear regression that contained a subset of these variables. A definition of all variables is given in Table SA-3.7.1.

**Table SA-3.7.1:** Exercise history variable definitions. Events include all official timed workouts (works) and races. Layup is defined as 60 or more days when a horse had no official events.<sup>13</sup> Furlongs are 1/8 mile (220 yards) and are a standard measurement unit used in horse racing.

Variable Type	Variable (Unit)	Definition
Lifetime Exercise	Active Days (days)	Total number of days the horse was in race-training, starting from the first timed event and ending at death, excluding layup days. It includes date of death and date of first training event day
	Age (years)	Horse age in years, not rounded to the Jan 1st birthday
	Career Days (days)	Total number of career days for horse; number of days between the horse's first timed event and date of death
	Age At Start of Training (days)	Days between date of birth and the first event in the horse's training history
	Number of Events (events)	Events in horse's career. Events include all races & timed works
	Number of Races (races)	Number of races during horse's lifetime
	Number of Works (works)	Number of timed-works during horse's lifetime
	Furlongs in Events (furlongs)	Total number of event furlongs
	Furlongs in Races (furlongs)	Total number of race furlongs
	Furlongs in Works (furlongs)	Total number of work furlongs
	Furlongs per Event (furlongs)	Furlongs in Events divided by Number of Events
	Furlongs per Race (furlongs)	Furlongs in Races divided by Number of Races

Variable Type	Variable (Unit)	Definition	
	Furlongs per Work (furlongs)	Furlongs in Works divided by Number of Works	
Exercise Intensity	Days Between Events (days)	Career Days divided by Number of Events – 1. Not calculated if horse had less than 2 events.	
	Days Between Events During Active Training (days)	Active Days divided by Number of Events – 1. Not calculated if horse had less than 2 events.	
	Events per Year (events/yr)	Number of Events divided by Career Days; converted to events per year	
	Events per Year during Active Training (events/yr)	Number of Events divided by Active Days; converted to events per year	
	Furlongs per Month (furlong/mo)	Furlongs in Races divided by Career Days; converted to furlongs per Month	
	Furlong per Month of Active Training (furlong/mo)	Furlongs in Events divided by Active Days; converted to furlongs per Month	
	Days Between Races (days)	Career Days divided by (Number of Races – 1). Not calculated if horse had less than 2 events.	
	Days Between Races During Active Training (days)	Active Days divided by (Number of Races– 1). Not calculated if horse had less than 2 events.	
	Races per year (races/yr)	Number of Events divided by Career Days; converted to races per year	
	Races per year of Active Training (races/yr)	Number of Races divided by Active Days; converted to races per year	
	Furlongs Raced per Month (furlong/mo)	Furlongs in Races divided by Career Days; converted to furlongs per Month	
	Furlongs Raced per Month of active raining (furlong/mo)	Furlongs in Races divided by Active Days; converted to furlongs per Month	
	Days Between Works (days)	Career Days divided by (Number of Works – 1). Not calculated if horse had less than 2 events.	
	Days Between Works During Active Training (days)	Active Days divided by (Number of Works – 1). Not calculated if horse had less than 2 events.	
Exercise Intensity	Works Per Year (works/yr)	Number of Works divided by Career Days; converted to works per year	
	Works Per Year of Active Training (works/yr)	Number of Works divided by Active Days; converted to works per year	
	Furlongs Worked per Month (furlong/mo)	Furlongs in Works divided by Career Days; converted to furlongs per Month	
	Furlongs Worked per Month of active Training (furlong/mo)	Furlongs in Works divided by Active Days; converted to furlongs per Month	
	Layup	Number of Layups (layup)	Total number of Number of Layups from start of training until death, where a layup is defined as 60+ days without an Event.
		Total Time in Layup (days)	Total number of days the horse was in a layup

Variable Type	Variable (Unit)	Definition
Layup	Average Layup Length (days)	Average number of days within individual layup periods; Total Time in Layup divided by Number of Layups
	Percent Career in Layup (%)	Percentage of horse's career spent in layup.
	Days Start of Last Layup (Days)	Number of days elapsed between when the horse died and the start of its previous layup period; if no layups occurred, this is Career Days – 1.
	Days End of Last Layup (days)	Number of days elapsed between when the horse died and the end of its previous layup period; If no layups occurred, this is Career Days – 1. If horse died during a layup, this value is 0.
	Events Since Last Layup (events)	Number of events that horse has participated in since the last layup period. If the horse died during a layup, this is 0. If the horse had no layups, this is the total number of events in the horse's lifetime.
Exercise Intensity Before Death	Events 1 Month Before Death (events)	Number events 1 month before death
	Events 2 Months Before Death (events)	Cumulative number events 2 months before death
	Events 4 Months Before Death (events)	Cumulative number events 4 months before death
	Events 6 Months Before Death (events)	Cumulative number events 6 months before death
	Events 8 Months Before Death (events)	Cumulative number events 8 months before death
	Events 10 Months Before Death (events)	Cumulative number events 10 months before death
	Events 1 Year Before Death (events)	Cumulative number of events 1 year before death
	Furlongs 1 Month Before Death (furlongs)	Number Furlongs 1 month before death
	Furlongs 2 Months Before Death (furlongs)	Cumulative number furlongs 2 months before death
	Furlongs 4 Months Before Death (furlongs)	Cumulative number furlongs 4 months before death
	Furlongs 6 Months Before Death (furlongs)	Cumulative number furlongs 6 months before death
	Furlongs 8 Months Before Death (furlongs)	Cumulative number furlongs 8 months before death
	Furlongs 10 Months Before Death (furlongs)	Cumulative number furlongs 10 months before death
	Furlongs 1 Year Before Death (furlongs)	Cumulative number of furlongs 1 year before death
	Races 1 Month Before Death (races)	Number races 1 month before death
	Races 2 Months Before Death (races)	Cumulative number races 2 months before death
	Races 4 Months Before Death (races)	Cumulative number races 4 months before death
	Races 6 Months Before Death	Cumulative number races 6 months before death



Variable Type	Variable (Unit)	Definition
Exercise Intensity Before Death	(races)	
	Races 8 Months Before Death (races)	Cumulative number races 8 months before death
	Races 10 Months Before Death (races)	Cumulative number races 10 months before death
	Races 1 Year Before Death (races)	Cumulative number of races 1 year before death
	Works 1 Month Before Death (works)	Number works 1 month before death
	Works 2 Months Before Death (works)	Cumulative number works 2 months before death
	Works 4 Months Before Death (works)	Cumulative number works 4 months before death
	Works 6 Months Before Death (works)	Cumulative number works 6 months before death
	Works 8 Months Before Death (works)	Cumulative number works 8 months before death
	Works 10 Months Before Death (works)	Cumulative number works 10 months before death
	Works 1 Year Before Death (works)	Cumulative number of works 1 year before death
	Days between Death and Previous Event (days)	Days between date of death and the previous event

The distributions of all exercise history variables were checked for normality using the Shapiro-Wilks statistic (W) and Group means were compared with a t-test ( $W > 0.90$ ) or Wilcoxon test ( $W \leq 0.90$ ).

A summary of exercise history variables is given in Table SA-3.7.2.

**Table SA-3.7.2:** Median (Minimum, Maximum) and Mean (Standard Deviation) of exercise history variables. Within each row, variables that share a superscript are not statistically different ( $p \leq 0.05$ ); Variables with a superscript \* were statistically different at  $p < 0.10$ . Variables with a non-normal distribution (Shapiro-Wilks Score  $> 0.90$ ) are indicated with superscript †.

Variable Type	Variable (Unit)	Median (Minimum, Maximum)		Mean (Standard Deviation)	
		Case	Control	Case	Control
Lifetime Exercise	Active Days <sup>†</sup> (days)	282.00 (102.00, 1479.00)	150.00 (40.00, 899.00)	419.50 <sup>A</sup> (398.55)	263.50 <sup>A</sup> (288.14)
	Age <sup>†</sup> (Years)	3.54 (2.34, 7.84)	3.38 (2.61, 7.37)	3.95 <sup>A</sup> (1.58)	3.81 <sup>A</sup> (1.53)
	Career Days <sup>†</sup> (days)	443.50 (102.00, 2177.00)	225.50 (40.00, 1826.00)	556.10 <sup>A</sup> (599.42)	497.50 <sup>A</sup> (594.98)
	Age when starting training <sup>†</sup> (days)	830.5 (684.00, 1451.00)	885.50 (704.00, 1135.00)	885.80 <sup>A</sup> (220.21)	894.70 <sup>A</sup> (147.20)

Variable Type	Variable (Unit)	Median (Minimum, Maximum)		Mean (Standard Deviation)		
		Case	Control	Case	Control	
Lifetime Exercise	Number of Events <sup>†</sup> (events)	28.0 (14.00, 153.00)	15.50 (4.00, 78.00)	43.60 <sup>A</sup> (41.19)	24.60 <sup>B</sup> (23.68)	
	Number of Races <sup>†</sup> (races)	8.00 (0.00, 32.00)	5.00 (0.00, 26.00)	10.70 <sup>A</sup> (9.92)	7.00 <sup>A</sup> (8.38)	
	Number of Works <sup>†</sup> (works)	19.50 (12.00, 121.00)	10.50 (4.00, 52.00)	32.90 <sup>A</sup> (32.76)	17.60 <sup>B</sup> (15.83)	
	Furlongs in Events <sup>†</sup> (furlongs)	136.50 (55.00, 743.00)	67.25 (13.00, 427.50)	209.85 <sup>A</sup> (204.78)	120.40 <sup>B</sup> (129.90)	
	Furlongs in Races <sup>†</sup> (furlongs)	53.75 (0.00, 210.00)	26.25 (0.00, 204.50)	67.55 <sup>A</sup> (64.17)	49.20 <sup>A</sup> (65.23)	
	Furlongs in Works <sup>†</sup> (furlongs)	84.50 (46.00, 533.00)	47.50 (13.00, 223.00)	142.30 <sup>A</sup> (147.07)	71.20 <sup>B</sup> (67.55)	
	Furlongs per Event (furlongs/event)	4.74 (3.84, 5.45)	4.50 (3.25, 5.89)	4.64 <sup>A</sup> (0.52)	4.49 <sup>A</sup> (0.84)	
	Furlongs per Race (furlongs/race)	6.38 (4.75, 7.65)	6.29 (4.5, 7.87)	6.22 <sup>A</sup> (0.92)	6.26 <sup>A</sup> (1.18)	
	Furlong per Work <sup>†</sup> (furlongs/work)	4.21 (3.60, 4.80)	4.03 (3.17, 4.6)	4.19 <sup>A</sup> (0.34)	3.92 <sup>A</sup> (0.50)	
	Exercise Intensity	Days Between Events (days)	11.95 (7.83, 20.61)	17.54 (8.08, 41.85)	12.52 <sup>A</sup> (4.09)	19.90 <sup>A*</sup> (10.20)
		Days Between Events During Active Training <sup>†</sup> (days)	8.96 (7.83, 16.5)	11.34 (7.85, 13.78)	10.01 <sup>A</sup> (2.67)	10.87 <sup>A</sup> (2.34)
Events per Year (events/yr)		31.33 (18.48, 50.1)	23.99 (9.39, 46.98)	33.28 <sup>A</sup> (11.03)	25.06 <sup>A</sup> (12.20)	
Events per Year during Active Training <sup>†</sup> (events/yr)		41.84 (22.91, 50.10)	35.88 (29.14, 50.10)	39.75 <sup>A</sup> (8.4)	38.15 <sup>A</sup> (8.35)	
Furlongs per Month (furlong/mo)		8.96 (2.99, 16.18)	4.57 (2.76, 10.69)	8.81 <sup>A</sup> (3.57)	5.89 <sup>A</sup> (2.78)	
Furlongs per Month of Active Training (furlong/mo)		11.15 (2.99, 16.18)	9.05 (4.54, 15.51)	10.68 <sup>A</sup> (3.49)	9.76 <sup>A</sup> (4.11)	
Days Between Races <sup>†</sup> (days)		49.79 (24.78, 94.80)	40.87 (26.44, 88.40)	54.84 <sup>A</sup> (26.09)	50.80 <sup>A</sup> (24.26)	
Days Between Races During Active Training (days)		43.21 (24.78, 58.20)	38.18 (26.44, 45.33)	41.20 <sup>A</sup> (12.63)	37.45 <sup>A</sup> (6.55)	
Races per year <sup>†</sup> (races/yr)		6.44 (0.00, 16.37)	4.80 (0.00, 15.34)	7.37 <sup>A</sup> (5.42)	6.30 <sup>A</sup> (5.78)	
Races per year of Active Training (races/yr)		9.03 (0.00, 16.37)	9.57 (0.00, 15.34)	8.69 <sup>A</sup> (5.38)	7.79 <sup>A</sup> (5.37)	
Furlongs Raced per Month (furlong/mo)		3.47 (0.00, 9.22)	2.91 (0.00, 9.58)	3.71 <sup>A</sup> (2.77)	3.28 <sup>A</sup> (3.17)	
Furlongs Raced per Month of Active Training (furlong/mo)		4.19 (0.00, 9.22)	4.57 (0.00, 9.58)	4.42 <sup>A</sup> (2.83)	4.11 <sup>A</sup> (3.12)	
Days Between Works <sup>†</sup> (days)		14.93 (7.85, 42.00)	27.28 (10.63, 41.85)	18.14 <sup>A</sup> (9.94)	26.32 <sup>A*</sup> (10.17)	

Variable Type	Variable (Unit)	Median (Minimum, Maximum)		Mean (Standard Deviation)	
		Case	Control	Case	Control
Exercise Intensity	Days Between Works During Active Training <sup>†</sup> (days)	11.86 (7.85, 42.00)	15.38 (7.85, 29.75)	14.92 <sup>A</sup> (9.80)	15.84 <sup>A</sup> (7.12)
	Works Per Year <sup>†</sup> (works/yr)	25.18 (9.48, 50.10)	15.47 (9.39, 36.50)	25.91 <sup>A</sup> (11.65)	18.76 <sup>A*</sup> (10.08)
	Works Per Year of Active Training (works/yr)	31.74 (9.48, 50.10)	29.48 (13.80, 50.10)	31.06 <sup>A</sup> (10.61)	30.35 <sup>A</sup> (12.42)
	Furlongs Worked per Month (furlong/mo)	12.21 (7.50, 18.63)	8.07 (2.76, 16.56)	12.52 <sup>A</sup> (3.68)	9.17 <sup>A*</sup> (4.49)
	Furlongs Worked per Month of active training (furlong/mo)	15.64 (8.73, 19.69)	14.25 (8.95, 17.19)	15.10 <sup>A</sup> (3.26)	13.86 <sup>A</sup> (2.86)
	Layup	Number of Layups <sup>†</sup> (layup)	1.00 (0.00, 4.00)	0.50 (0.00, 4.00)	0.90 <sup>A</sup> (1.2)
Layup Time <sup>†</sup> (days)		87.5 (0.00, 698.00)	62.00 (0.00, 927.00)	136.6 <sup>A</sup> (211.02)	234 <sup>A</sup> (330.02)
Average Layup Length <sup>†</sup> (days)		87.50 (0.00, 201.00)	55.25 (0, 323)	84.25 <sup>A</sup> (81.39)	106.75 <sup>A</sup> (130.74)
Percent Career in Layup <sup>†</sup> (%)		19.43 (0.00, 42.41)	24.36 (0.00, 81.25)	16.99 <sup>A</sup> (16.05)	30.92 <sup>A</sup> (33.86)
Time Since Start of Last Layup <sup>†</sup> (days)		400.00 (101.00, 571.00)	217.50 (39.00, 601.00)	343.30 <sup>A</sup> (180.71)	242.80 <sup>A</sup> (161.5)
Time Since End of Last Layup (days)		256.00 (61, 461)	94.00 (0.00, 237.00)	259.90 <sup>A</sup> (139.86)	104.70 <sup>B</sup> (81.04)
Events Since Last Layup (Events)		28.00 (8.00, 49.00)	10.00 (0.00, 26.00)	27.60 <sup>A</sup> (13.48)	10.40 <sup>B</sup> (8.64)
Exercise Intensity Before Death	Events 1 Month Before Death (events)	3.00 (2.00, 5.00)	2.00 (0.00, 4.00)	3.30 <sup>A</sup> (0.95)	1.90 <sup>B</sup> (1.29)
	Events 2 Months Before Death (events)	6.00 (3.00, 9.00)	4.00 (0.00, 7.00)	5.90 <sup>A</sup> (1.91)	3.50 <sup>B</sup> (2.32)
	Events 4 Months Before Death (events)	12.50 (8.00, 17.00)	8.00 (0.00, 14.00)	12.00 <sup>A</sup> (3.20)	7.20 <sup>B</sup> (5.12)
	Events 6 Months Before Death (events)	18.00 (11.00, 23.00)	10.00 (0.00, 22.00)	17.40 <sup>A</sup> (4.06)	9.90 <sup>B</sup> (6.67)
	Events 8 Months Before Death <sup>†</sup> (events)	22.00 (14.00, 29.00)	10.50 (1.00, 26.00)	21.40 <sup>A</sup> (6.33)	11.60 <sup>B</sup> (7.68)
	Events 10 Months Before Death <sup>†</sup> (events)	24.00 (14.00, 35.00)	11.00 (2.00, 26)	24.70 <sup>A</sup> (8.21)	11.80 <sup>B</sup> (7.51)
	Events 1 Year Before Death <sup>†</sup> (events)	24.50 (14.00, 41.00)	11.00 (4.00, 26)	27.10 <sup>A</sup> (10.40)	12.20 <sup>B</sup> (7.02)
	Furlongs 1 Month Before Death (furlongs)	19.00 (8.00, 28.00)	9.75 (0.00, 21.00)	17.65 <sup>A</sup> (5.79)	10.20 <sup>B</sup> (7.49)
	Furlongs 2 Months Before Death (furlongs)	30.75 (13.50, 54.00)	17.25 (0.00, 39.00)	30.35 <sup>A</sup> (11.04)	18.75 <sup>A*</sup> (13.85)
	Furlongs 4 Months Before Death (furlongs)	58.25 (36.00, 100.5)	39.00 (0.00, 77.00)	60.00 <sup>A</sup> (19.03)	36.70 <sup>B</sup> (28.51)
	Furlongs 6 Months Before Death (furlongs)	81.50 (49.50, 139.00)	40.50 (0.00, 101.50)	85.45 <sup>A</sup> (28.57)	48.70 <sup>B</sup> (35.33)

Variable Type	Variable (Unit)	Median (Minimum, Maximum)		Mean (Standard Deviation)	
		Case	Control	Case	Control
Exercise Intensity Before Death	Furlongs 8 Months Before Death <sup>†</sup> (furlongs)	100.50 (55.00, 176.00)	47.50 (3.00, 112.00)	105.65 <sup>A</sup> (40.87)	54.8 <sup>B</sup> (39.70)
	Furlongs 10 Months Before Death (furlongs)	115.00 (55.00, 208.50)	49.50 (6.00, 112.00)	120.55 <sup>A</sup> (49.94)	55.50 <sup>B</sup> (39.17)
	Furlongs 1 Year Before Death (furlongs)	123.5 (55.00, 238.50)	49.50 (13.00, 112.00)	132.20 <sup>A</sup> (61.39)	57.10 <sup>B</sup> (37.20)
	Races 1 Month Before Death <sup>†</sup> (races)	1.00 (0.00, 3.00)	1.00 (0.00, 2.00)	1.20 <sup>A</sup> (1.14)	1.1 <sup>A</sup> (0.88)
	Races 2 Months Before Death <sup>†</sup> (races)	2.00 (0.00, 4.00)	2.5 (0.00, 4.00)	1.90 <sup>A</sup> (1.29)	1.90 <sup>A</sup> (1.52)
	Races 4 Months Before Death <sup>†</sup> (races)	4.50 (0.00, 8.00)	3.00 (0.00, 7.00)	4.40 <sup>A</sup> (2.76)	3.10 <sup>A</sup> (2.81)
	Races 6 Months Before Death (races)	6.00 (0.00, 11.00)	3.00 (0.00, 10.00)	5.60 <sup>A</sup> (3.63)	3.50 <sup>A</sup> (3.27)
	Races 8 Months Before Death (races)	7.00 (0.00, 14.00)	3.00 (0.00, 10.00)	6.60 <sup>A</sup> (4.40)	3.50 <sup>A*</sup> (3.27)
	Races 10 Months Before Death (races)	8.00 (0.00, 16.00)	3.00 (0.00, 10.00)	7.40 <sup>A</sup> (5.15)	3.50 <sup>A*</sup> (3.27)
	Races 1 Year Before Death (races)	8.00 (0.00, 17.00)	3.00 (0.00, 10.00)	8.00 <sup>A</sup> (5.73)	3.5 <sup>B</sup> (3.27)
	Works 1 Month Before Death (works)	2.00 (0.00, 4.00)	0.00 (0.00, 3.00)	2.10 <sup>A</sup> (1.6)	0.80 <sup>A*</sup> (1.14)
	Works 2 Months Before Death <sup>†</sup> (works)	4.00 (0.00, 8.00)	0.50 (0.00, 6.00)	4.00 <sup>A</sup> (2.54)	1.60 <sup>B</sup> (2.12)
	Works 4 Months Before Death (works)	8.00 (0.00, 14.00)	4.00 (0.00, 9.00)	7.60 <sup>A</sup> (4.40)	4.10 <sup>A*</sup> (3.63)
	Works 6 Months Before Death <sup>†</sup> (works)	13.50 (0.00, 16)	5.50 (0.00, 16.00)	11.80 <sup>A</sup> (4.71)	6.40 <sup>B</sup> (4.88)
	Works 8 Months Before Death <sup>†</sup> (works)	16.00 (1.00, 22.00)	9.00 (1.00, 20.00)	14.80 <sup>A</sup> (6.00)	8.10 <sup>B</sup> (5.43)
	Works 10 Months Before Death <sup>†</sup> (works)	18.50 (2.00, 28.00)	9.00 (2.00, 20.00)	17.30 <sup>A</sup> (7.69)	8.30 <sup>B</sup> (5.31)
	Works 1 Year Before Death <sup>†</sup> (works)	19.00 (5.00, 28.00)	9.00 (2.00, 20.00)	19.10 <sup>A</sup> (8.40)	8.70 <sup>B</sup> (4.92)
	Days between death and previous event <sup>†</sup> (days)	12.50 (4.00, 22.00)	21.00 (5.00, 234.00)	11.90 <sup>A</sup> (5.76)	51.40 <sup>A</sup> (73.28)

Univariate robust linear regressions (mm method) were performed using Case Contralateral Intact PSB (CLI-PSB) and Control PSB (CTRL-PSB) data in microcomputed tomography regions of interest ( $\mu$ ROI) and histology regions of interest (hROI) to determine the relationship between each exercise history variable to measured parameters. Robust linear regressions were performed for morphometry variables in all four  $\mu$ ROIs (Table SA-3.7.3) and microdamage data in Central Subchondral, Proximal Subchondral,

Proximal Deep, and Whole Bone hROIs. For all regressions, exercise variable was the predictor. Robust linear regressions were used as an alternative to linear regressions because there were many leverage points in the data set.

**Table SA-3.7.3:** Robust univariate linear regressions between densitometric and exercise history variables [Model Slope (R<sup>2</sup>)]; reported regressions are significant at  $p \leq 0.05$ . Models were constructed in SAS 9.4 using Proc RobustReg, mm method.

$\mu$ CT Parameter	Exercise Variable Category	Exercise Variable	Central Subchondral $\mu$ ROI	Central Subchondral Border $\mu$ ROI	Proximal Subchondral $\mu$ ROI	Trabecular $\mu$ ROI
AMD (mgHA/cc)	Lifetime Summary	Active Days (days)	.	0.033 (0.11)	.	
		Age (years)	.	7.576 (0.18)	9.258 (0.13)	
		Number of Races (races)	.	0.994 (0.1)	.	
		Age When Starting Training (days)	.	.	.	0.126 (0.2)
	Exercise Intensity	Furlongs Per Event (furs/event)	.	.	16.200 (0.13)	
		Days Between Events (days)	.	.	.	-4.671 (0.29)
		Events Per Year (events/year)	.	-0.648 (0.08)	.	
		Days Between Works (works)	1.134 (0.11)	0.764 (0.11)	.	
		Days Between Works During Active Training (days)	.	.	.	2.348 (0.16)
		Furlongs Worked Per Month Active (days)	.	.	.	-6.761 (0.14)
		Works Per Year (works)	.	-0.737 (0.08)	.	-2.316 (0.1)
	Layup	Total Time in Layup (days)	0.042 (0.10)	.	.	-14.384 (0.09)
		Percent Career In Layup (%)	.	.	.	-1.539 (0.3)
	Exercise Intensity Before Death	Days Between Death and Previous Event (days)	.	.	.	-0.724 (0.35)
BVF	Lifetime Summary	Active Days (days)	-0.00004 (0.05)	.	.	-0.001 (0.13)
		Career Days (days)	.	.	.	-0.00003 (0.12)

$\mu$ CT Parameter	Exercise Variable Category	Exercise Variable	Central Subchondral $\mu$ ROI	Central Subchondral Border $\mu$ ROI	Proximal Subchondral $\mu$ ROI	Trabecular $\mu$ ROI
BVF		Number of Events (events)	-0.001 (0.08)	.	.	-0.001 (0.14)
		Number of Works (works)	-0.001 (0.11)	.	.	-0.001 (0.16)
		Furlongs in Events (furlongs)	-0.0001 (0.05)	.	.	-0.0001 (0.13)
		Furlongs in Works (furlongs)	-0.0001 (0.11)	.	.	-0.0001 (0.15)
	Exercise Intensity	Days Between Events (days)	.	.	.	-0.007 (0.17)
		Events Per Year (events/year)	-0.001 (0.11)	.	.	.
		Furlongs Per Month (furlongs/month)	-0.002 (0.07)	.	.	.
		Days Between Works (works)	0.001 (0.10)	.	.	.
		Works Per Year (works)	-0.001 (0.11)	.	.	.
		Furlongs Worked Per Month (furlongs/month)	-0.003 (0.12)	.	.	.
	Layup	Number of Layups (layups)	.	.	.	-0.017 (0.15)
		Total Time in Layup (days)	.	.	.	-0.0001 (0.10)
		Percent Career In Layup (%)	.	.	.	-0.001 (0.13)
		Days Since End of Last Layup (days)	-0.0001 (0.18)	.	.	.
		Events Since End of Last Layup (events)	-0.001 (0.12)	.	.	.
	Exercise Intensity Before Death	Events 2 Months Before Death (events)	-0.004 (0.10)	.	.	.
		Events 4 Months Before Death (events)	-0.002 (0.09)	.	.	.
		Events 10 Months Before Death (events)	-0.001 (0.11)	.	.	.
		Events 1 Year Before Death (events)	-0.001 (0.10)	.	.	.
		Works 4 Months Before Death (works)	-0.002 (0.12)	.	.	.

$\mu$ CT Parameter	Exercise Variable Category	Exercise Variable	Central Subchondral $\mu$ ROI	Central Subchondral Border $\mu$ ROI	Proximal Subchondral $\mu$ ROI	Trabecular $\mu$ ROI
BVF		Works 6 Months Before Death (works)	-0.002 (0.12)	.	.	.
		Works 8 Months Before Death (works)	-0.002 (0.10)	.	.	.
		Works 10 Months Before Death (works)	-0.002 (0.12)	.	.	.
		Works 1 Year Before Death (works)	-0.002 (0.10)	.	.	.
		Days Between Death and Previous Event (days)	.	.	.	-0.001 (0.39)
TMD (mgHA/cc)	Lifetime Summary	Active Days (days)	0.03 (0)	.	0.041 (0.07)	.
		Age (years)	.	.	7.979 (0.11)	.
		Number of Races (races)	.	0.78 (0.08)	1.266 (0.09)	.
		Furlongs in Events (furlongs)	0.316 (0)	.	.	.
		Furlongs in Races (furlongs)	.	.	0.175 (0.1)	.
		Furlongs in Events (furlongs)	0.060 (0)	.	.	.
	Exercise Intensity	Furlongs Per Event (furlongs/event)	.	.	15.768 (0.22)	.
		Days Between Races During Active Training (days)	.	-0.677 (0.26)	.	.
		Days Between Works (days)	0.591 (0.14)	0.661 (0.16)	.	.
		Days Between Works During Active Training (days)	.	.	.	1.672 (0.27)
		Furlongs Worked Per Month of Active Training (furlongs/month)	.	.	.	-2.346 (0.17)
		Works Per Year During Active Training (works/year)	.	.	.	-0.692 (0.14)
		Works Per Year (works)	.	.	.	.
Layup	Percent Career In Layup (%)	.	.	.	-0.239 (0.15)	

**Table SA-3.7.4:** Robust univariate linear regressions between microdamage and exercise history variables for selected regions of interest [Model Slope ( $R^2$ )]; reported parameters are significant at  $p \leq 0.05$ . Models were constructed in SAS using Proc RobustReg, mm method.

Damage Parameter	Exercise Variable Category	Exercise Variable	Central Subchondral hROI	Proximal Subchondral hROI	Proximal Deep hROI	Whole Bone
<b>N.Cr (#)</b>	Lifetime Summary	Career Days (days)	.	.	0.010 (0)	0.112 (0.04)
		Number of Events (events)	0.819 (0)	.	.	.
		Number of Works (works)	1.378 (0.01)	.	.	2.689 (0)
		Furlongs in Works (furlongs)	0.296 (0.01)	.	.	0.566 (0)
	Exercise Intensity	Days Between Events (days)	.	.	0.273 (0.17)	.
		Events Per Year (days)	.	.	-0.219 (0.15)	.
		Days Between Races (days)	.	0.677 (0.36)	0.146 (0.32)	1.751 (0.32)
		Days Between Races During Active Training (days)	.	1.475 (0.27)	.	.
	Layup	Total Time in Layup (days)	.	.	0.019 (0.21)	.
		Average Layup Length (days)	.	0.082 (0.14)	0.038 (0.28)	0.389 (0.26)
		Percent of Career In Layup (%)	.	.	0.106 (0.23)	.
	Exercise Intensity Before Death	Works 4 Months Before Death (works)	4.007 (0.18)	.	.	.
		Days Between Death and Previous Event (days)	.	.	0.031 (0.13)	.
	<b>N.Cr/ B.Ar (#/mm<sup>2</sup>)</b>	Lifetime Summary	Active Days (days)	.	.	.
Career Days (days)			.	.	0.001 (0)	0.002 (0)
Number of Events (events)			.	.	.	0.034 (0)
Furlongs in Events (furlongs)			.	.	.	0.006 (0)
Number of Works (works)			0.172 (0.03)	.	.	0.055 (0.09)
Furlongs in Works (furlongs)			0.039 (0.06)	.	.	0.012 (0)
Exercise Intensity		Days Between Races (days)	.	0.068 (0.32)	0.014 (0.33)	0.029 (0.25)
		Days Between Races During Active Training (days)	.	0.169 (0.32)	.	.



Damage Parameter	Exercise Variable Category	Exercise Variable	Central Subchondral hROI	Proximal Subchondral hROI	Proximal Deep hROI	Whole Bone
<b>N.Cr/ B.Ar</b> (#/mm <sup>2</sup> )	Layup	Total Time in Layup (days)	.	.	0.001 (0.12)	.
		Average Layup Length (days)	.	0.008 (0.12)	0.004 (0.27)	0.006 (0.23)
		Percent of Career In Layup (%)	.	.	0.01 (0.22)	.
		Days Since Start of Last Layup (days)	.	.	.	0.003 (0.14)
	Exercise Intensity Before Death	Events 2 Months Before Death (events)	0.742 (0.19)	.	.	.
		Events 4 Months Before Death (events)	0.401 (0.22)	.	.	.
		Furlongs 2 Months Before Death (furlongs)	0.13 (0.19)	.	.	.
		Works 2 Months Before Death (works)	0.681 (0.19)	.	.	.
		Works 4 Months Before Death (works)	0.541 (0.29)	.	.	.
	<b>ΣCr.Le/N.Cr</b> (mm)	Lifetime Summary	Career Days (days)	0.00003 (0.17)	.	.
Number of Events (events)			0.001 (0.19)	.	.	.
Number of Works (works)			0.001 (0.26)	0.002 (0)	.	0.001 (0.11)
Furlongs in Works (furlongs)			0.0002 (0.21)	0.0003 (0)	.	0.0002 (0.03)
Furlongs Per Race (furlongs/race)			.	.	-0.022 (0.33)	.
Layup		Number of Layups (layups)	0.009 (0.20)	.	.	.
		Total Time in Layup (days)	0.0001 (0.18)	.	.	.
		Average Layup Length (days)	.	0.0002 (0.22)	.	0.0001 (0.19)
Exercise Intensity Before Death		Events 1 Month Before Death (events)	.	.	-0.017 (0.31)	.
		Events 2 Months Before Death (events)	.	.	-0.009 (0.32)	.
		Furlongs 1 Month Before Death (furlongs)	.	.	-0.003 (0.28)	.
		Furlongs 2 Months Before Death (furlongs)	.	.	-0.002 (0.32)	.

Damage Parameter	Exercise Variable Category	Exercise Variable	Central Subchondral hROI	Proximal Subchondral hROI	Proximal Deep hROI	Whole Bone
$\Sigma$ Cr.Le/N.Cr (mm)	Exercise Intensity Before Death	Furlongs 4 Months Before Death (furlongs)	.	.	-0.001 (0.21)	.
		Races 6 Months Before Death (races)	.	.	-0.005 (0.17)	.
		Races 8 Months Before Death (races)	.	.	-0.006 (0.26)	.
		Races 10 Months Before Death (races)	.	.	-0.005 (0.24)	.
		Races 1 Year Before Death (races)	.	.	-0.004 (0.23)	.
		Works 2 Months Before Death (works)	.	.	-0.007 (0.16)	.
		Days Since End of Last Layup (days)	.	-0.0002 (0.19)	-0.0002 (0.33)	.
		Events Since End of Last Layup (events)	.	.	-0.001 (0.26)	.
		Days Between Death and Previous Event (days)	.	.	0.001 (0.08)	.
$\Sigma$ Cr.Le/B.Ar (mm/mm <sup>2</sup> )	Lifetime Summary	Career Days (days)	.	.	0.0001 (0)	0.0002 (0.11)
		Number of Events (events)	0.01 (0)	.	.	0.0035 (0.01)
		Number of Works (works)	0.017 (0.14)	0.006 (0)	.	0.006 (0.14)
		Furlongs in Events (furlongs)	0.002 (0)	.	.	0.001 (0)
		Furlongs in Works (furlongs)	0.004 (0.15)	0.001 (0)	.	0.001 (0.12)
	Exercise Intensity	Events Per Year (days)	.	.	-0.002 (0.20)	.
		Furlongs in Events Per Month (furlongs/month)	.	.	-0.004 (0.20)	.
	Layup	Total Time in Layup (days)	.	0.0003 (0.08)	0.0001 (0.12)	.
		Average Layup Length (days)	.	0.001 (0.32)	0.0002 (0.27)	0.001 (0.24)
		Percent of Career In Layup (%)	.	0.002 (0.12)	0.001 (0.27)	.
		Days Since End of Last Layup (days)	.	.	-0.0001 (0.21)	.
		Days Since Start of Last Layup (days)	.	0.0003 (0.12)	.	0.0003 (0.15)
	Exercise	Events 4 Months Before Death	0.034 (0.18)	.	.	.

Damage Parameter	Exercise Variable Category	Exercise Variable	Central Subchondral hROI	Proximal Subchondral hROI	Proximal Deep hROI	Whole Bone
	Intensity Before Death	(events)				
		Races 8 Months Before Death (races)	.	.	-0.004 (0.2)	.
		Works 4 Months Before Death (works)	0.045 (0.25)	.	.	.

Univariate logistic regressions were performed against each exercise history variable and the presence of calcified cartilage cracks in the Central Subchondral hROI and for the whole sample. Univariate logistic regressions, rather than robust linear regressions, were performed because 38% of CLI and CTRL-PSBs had no calcified cartilage cracks anywhere in the sample and 56% had no calcified cartilage cracks in the Central Subchondral ROI. All significant logistic regressions are reported in Table SA-3.5.7.

**Table SA-3.7.5:** Univariate logistic regressions (LR) predicting presence of calcified cartilage cracks in the Central Subchondral histology ROI based on exercise history variables. P-values before and after outlier removal are given, odds ratios [OR (95% Confidence Interval)] are given after outlier removal.

Exercise History Variable	Univariate LR P-Value prior to outlier removal	Univariate LR P-Value after outlier removal	Odds Ratio After Outlier Removal (95% CI)	Difference in Group Means (Case – Control)	Odds of having a calcified cartilage crack, based on difference in Group means
Events 2 Months Before Death (events)	0.103	0.036	2.8 (1.1, 7.4)	17	2.4
Furlongs 1 Month Before Death (furlongs)	0.142	0.050	1.3 (1, 1.6)	17	7.5
Furlongs 2 Months Before Death (furlongs)	0.132	0.058	1.2 (0.99, 1.4)	17	5.9
Works 2 Months Before Death (Works)	0.082	0.048	1.7 (1.0, 3.0)	17	2.4

### 3.8 Supplemental Material B: Densitometric and Microdamage Data

This contains the main effects of the ANOVAs presented in the body of the paper; all interaction effects are given in the main paper. It also contains results of ANOVA comparing apparent mineral density (AMD), tissue mineral density (TMD), and bone volume fraction (BVF) within the microcomputed tomography regions of interest ( $\mu$ ROI) for PSBs with and without a radiolucent subchondral bone lesion (BL) and ANOVA comparing microdamage variables for selected histology regions of interest (hROI) for PSBs with and without a radiolucent BL.

Region of interest had a significant effect on AMD, TMD, and BVF (Table SB-3.8.1). Apparent mineral density (AMD) was lowest in the Central Subchondral (CS) and Proximal Subchondral (PS)  $\mu$ ROIs, intermediate in the Trabecular (TB) ROI, and highest in the Central Subchondral Border (CSB)  $\mu$ ROIs (Table SB-3.8.1); BVF was lowest in the CS and TB  $\mu$ ROIs, and highest in the CSB  $\mu$ ROIs. There was no difference in AMD and BVF between the PS and CS ROI among all PSBs. Tissue mineral density (TMD) was lowest in the CS ROI, followed by the PS, CSB, and TB  $\mu$ ROIs; TMD in the CS ROI was significantly lower than all other ROIs among all PSBs (Table SB-3.8.1).

**Table SB-3.8.1** Least Square Means (Standard Error) from ANOVA or Raw Means (Standard Deviation) from ranked ANOVA<sup>¶</sup> for Bone Volume Fraction (BVF), Apparent Mineral Density (AMD), and Tissue Mineral Density (TMD) for all Groups and the four Regions of Interest (ROI). Within each column, for each effect (separated by dark lines), variables that do not share a superscript are significantly different ( $p < 0.05$ ). Results are from an ANOVA with Group (Control Group (CTRL), Case Contralateral Limb Intact (CLI), and Case Fractured (FX)), ROI, and Group\*ROI as fixed effects and horse as a random effect. Significant effects indicated by variable superscripts: <sup>†</sup>(ROI), <sup>§</sup>(Group), <sup>‡</sup>(Group\*ROI).

Effect Level (Group or Region of Interest)	BVF <sup>¶,†,‡</sup>	AMD <sup>†,‡</sup>	TMD <sup>†,§</sup>
<b>CTRL</b>	0.953 (0.07) <sup>A</sup>	796.28 (8.90) <sup>A</sup>	826.27 (4.00) <sup>A,B</sup>
<b>CLI</b>	0.965 (0.05) <sup>A</sup>	806.96 (8.90) <sup>A</sup>	830.12 (4.00) <sup>A</sup>
<b>FX</b>	0.95 (0.07) <sup>A</sup>	788.36 (9.01) <sup>A</sup>	819.05 (4.05) <sup>B</sup>
<b>Central Subchondral</b>	0.943 (0.07) <sup>A,B</sup>	770.44 (8.37) <sup>A</sup>	804.03 (3.66) <sup>A</sup>
<b>Central Subchondral Border</b>	0.977 (0.04) <sup>C</sup>	818.21 (8.37) <sup>C</sup>	835.57 (3.66) <sup>B</sup>
<b>Trabecular</b>	0.944 (0.06) <sup>A</sup>	808.87 (8.37) <sup>B,C</sup>	846.35 (3.66) <sup>C</sup>
<b>Proximal Subchondral</b>	0.963 (0.06) <sup>B,C</sup>	791.27 (8.61) <sup>A,B</sup>	814.64 (3.76) <sup>D</sup>

Group was a significant effect for TMD (Table SB-3.8.1), but not BVF or AMD. Mean FX-PSB TMD was significantly lower than in CLI-PSBs, but TMD in CTRL-PSBs was not different from either Case group.

Group and ROI had significant effects on calcified cartilage crack (Md.Cg.Cr) variables (Table SB-3.8.2).  $N.Md.Cg.Cr$ ,  $N.Md.Cg.Cr/Cg.Bd$ ,  $\Sigma Md.Cg.Cr.Le/N.Md.Cg.Cr$ , and  $\Sigma Md.Cg.Cr.Le/Cg.Bd$  were significantly higher in Case PSBs than in CTRLs; and they were all highest in FX-PSB, and intermediate in CLI-PSBs and lowest in CTRL-PSBs which were not statistically different from one another (Table SB-3.8.2).  $N.Md.Cg.Cr$ ,  $N.Md.Cg.Cr/Cg.Bd$ ,  $\Sigma Md.Cg.Cr.Le/N.Md.Cg.Cr$ , and  $\Sigma Md.Cg.Cr.Le/Cg.Bd$  were significantly higher in the Central Subchondral ROI than the Distal Subchondral ROI, with non-statistically different intermediate mean values in the Proximal Subchondral ROI (Table SB-3.8.2).

Region of Interest was a significant effect for  $N.Cr$ ,  $N.Cr/B.Ar$ , and  $\Sigma Cr.Le/B.Ar$ ; both ROI and Group were significant effects for  $\Sigma Cr.Le/N.Cr$  (Table SB-3.8.2).  $\Sigma Cr.Le/N.Cr$  was significantly higher in FX-PSBs, compared to the CTRL and CLI-PSBs, and was significantly higher in the Central Subchondral and Deep ROIs than in the Distal Subchondral and Deep ROIs (Table SB-3.8.2).  $\Sigma Cr.Le/N.Cr$  was highest in the two Central ROIs, intermediate in the two Proximal ROIs, and lowest in the two Distal ROIs (Table SB-3.8.2). No differences in  $N.Cr$ ,  $N.Cr/B.Ar$ , and  $\Sigma Cr.Le/B.Ar$  were present between Groups; however, these variables were significantly highest in the Central Subchondral ROI compared to all other ROIs (Table SB-3.8.2).  $N.Cr$ ,  $N.Cr/B.Ar$ , and  $\Sigma Cr.Le/B.Ar$  were highest in the Central Subchondral ROI, followed by the Proximal Subchondral, Central Deep, Distal Subchondral, Proximal Deep, and Distal Deep ROIs (Table SB-5.8.2).

**Table SB-3.8.2:** Raw Means (Standard Deviation) of microdamage variables for Group and Region of Interest (ROI). Significant effects indicated by variable superscripts: <sup>†</sup>(ROI), <sup>§</sup>(Group), <sup>‡</sup>(Group\*ROI). Within a column, for each main effect, variables that do not share a superscript are significantly different (p<0.05) based on an ANOVA with Group and ROI as fixed effects and horse as a random effect. Superscript NE indicates that pairwise comparisons could not be estimated. NA is not applicable.

Effect Level (Group or ROI)	N.Cr <sup>†</sup>	N.Cr/B.Ar <sup>†</sup>	ΣCr.Le/ N.Cr <sup>†,§</sup>	ΣCr.Le/ B.Ar <sup>†</sup>	N.Md.Cg.Cr <sup>†,§</sup>	N.Md.Cg.Cr/ Cg.Bd <sup>†,§</sup>	ΣMd.Cg.Cr.Le /N.Md.Cg.Cr <sup>†</sup> ,§	ΣMd.Cg.Cr.Le /Cg.Bd <sup>†,§</sup>	Md.Cg.Cr Average Angle <sup>†</sup>
CTRL	0.87 <sup>A</sup> (1.24)	8.38 <sup>A</sup> (12.59)	0.059 <sup>A</sup> (0.042)	0.07 <sup>A</sup> (0.12)	0.29 <sup>A</sup> (0.91)	0.04 <sup>A</sup> (0.13)	0.03 <sup>A</sup> (0.09)	0.012 <sup>A</sup> (0.05)	109.9 <sup>NE</sup> (6.3)
CLI	2.13 <sup>A</sup> (2.96)	18.93 <sup>A</sup> (27.51)	0.052 <sup>A</sup> (0.039)	0.17 <sup>A</sup> (0.26)	1.63 <sup>B</sup> (2.27)	0.29 <sup>B</sup> (0.40)	0.12 <sup>B</sup> (0.14)	0.07 <sup>B</sup> (0.11)	104.1 <sup>A</sup> (25.2)
FX	2.21 <sup>A</sup> (3.34)	17.41 <sup>A</sup> (26.81)	0.076 <sup>B</sup> (0.056)	0.23 <sup>A</sup> (0.39)	2.73 <sup>B</sup> (3.29)	0.49 <sup>B</sup> (0.55)	0.12 <sup>B</sup> (0.12)	0.10 <sup>B</sup> (0.13)	93.4 <sup>A</sup> (27.6)
Proximal Subchondral	18.41 <sup>B</sup> (23.52)	2.02 <sup>B</sup> (2.37)	0.068 <sup>A,B</sup> (0.031)	0.17 <sup>B,C</sup> (0.23)	1.45 <sup>A,B</sup> (1.98)	0.24 <sup>A,B</sup> (0.32)	0.09 <sup>A,B</sup> (0.12)	0.05 <sup>A,B</sup> (0.08)	112.0 <sup>NE</sup> (10.7)
Central Subchondral	45.98 <sup>A</sup> (38.44)	5.46 <sup>A</sup> (4.53)	0.091 <sup>A</sup> (0.044)	0.55 <sup>A</sup> (0.49)	2.79 <sup>A</sup> (3.42)	0.50 <sup>A</sup> (0.58)	0.13 <sup>A</sup> (0.14)	0.10 <sup>A</sup> (0.13)	102.7 <sup>NE</sup> (23.9)
Distal Subchondral	9.23 <sup>B,C</sup> (10.32)	1.12 <sup>B,C</sup> (1.19)	0.045 <sup>B</sup> (0.032)	0.07 <sup>C,D</sup> (0.08)	0.70 <sup>B</sup> (1.70)	0.13 <sup>B</sup> (0.33)	0.05 <sup>B</sup> (0.12)	0.04 <sup>B</sup> (0.10)	56.9 <sup>NE</sup> (8.3)
Proximal Deep	4.018 <sup>C,D</sup> (4.58)	0.47 <sup>C,D</sup> (0.52)	0.052 <sup>A,B</sup> (0.049)	0.04 <sup>D,E</sup> (0.05)	NA	NA	NA	NA	NA
Central Deep	12.70 <sup>B</sup> (10.33)	1.49 <sup>B</sup> (1.18)	0.082 <sup>A</sup> (0.05)	0.12 <sup>B</sup> (0.12)	NA	NA	NA	NA	NA
Distal Deep	1.88 <sup>D</sup> (2.88)	0.23 <sup>D</sup> (0.35)	0.038 <sup>B</sup> (0.053)	0.02 <sup>E</sup> (0.02)	NA	NA	NA	NA	NA

Total damage measures in each PSB (pooling all 6 hROIs) are summarized in Table SB-3.8.3. Case PSBs had higher N.Cr and N.Cr/B.Ar than Controls, however these differences were not significant. Case FX-PSBs had higher  $\Sigma$ Cr.Le/N.Cr and  $\Sigma$ Cr.Le/B.Ar than Controls. Case FX-PSBs had significantly higher N.Md.Cg.Cr and N.Md.Cg.Cr/Cg.Bd than Controls; Case CLI-PSBs had intermediate N.Md.Cg.Cr and N.Md.Cg.Cr/Cg.Bd levels that were not different from either the Case FX or Control PSBs.

**Table SB-3.8.3:** Least Square Means (Standard Error) of total damage found in Case fracture (FX), Case contralateral intact (CLI), and control (CTRL) proximal sesamoid bones. Within a column, variables that do not share a superscript are significantly different (pairwise comparisons,  $p \leq 0.05$  with tukey-kramer adjustment).

Group	N.Cr	N.Cr/B.Ar	$\Sigma$ Cr.Le/N.Cr	$\Sigma$ Cr.Le/B.Ar	N.Md.Cg.Cr	N.Md.Cg.Cr/Cg.Bd	$\Sigma$ Md.Cg.Cr.Le/N.Md.Cg.Cr	$\Sigma$ Md.Cg.Cr.Le/Cg.Bd
CTRL	50.25 <sup>A</sup> (25.51)	0.87 <sup>A</sup> (0.45)	0.07 <sup>A</sup> (0.01)	0.07 <sup>A</sup> (0.04)	0.88 <sup>A</sup> (1.44)	0.04 <sup>A</sup> (0.08)	0.07 <sup>A</sup> (0.04)	0.01 <sup>A</sup> (0.02)
CLI	113.55 <sup>A</sup> (22.82)	2.14 <sup>A</sup> (0.4)	0.08 <sup>A</sup> (0.01)	0.17 <sup>A,B</sup> (0.04)	4.90 <sup>A,B</sup> (1.29)	0.28 <sup>A,B</sup> (0.07)	0.20 <sup>A</sup> (0.03)	0.07 <sup>A</sup> (0.02)
FX	104.45 <sup>A</sup> (22.82)	2.23 <sup>A</sup> (0.40)	0.11 <sup>B</sup> (0.01)	0.23 <sup>B</sup> (0.04)	8.20 <sup>B</sup> (1.29)	0.49 <sup>B</sup> (0.07)	0.18 <sup>A</sup> (0.03)	0.09 <sup>A</sup> (0.02)

ANOVA comparing tissue properties for PSBs with and without a subchondral lesion indicated that BVF, AMD, and TMD were significantly lower at the Central Subchondral  $\mu$ ROI in PSBs with a subchondral lesion (Table SB-3.8.4). In the Central Subchondral  $\mu$ ROI of PSBs with a subchondral lesion, BVF is 7.5% lower, AMD is 7.8% lower, and TMD is 2.8% lower compared to PSBs with no subchondral lesion. When FX-PSB results were excluded, BVF in the Central Subchondral  $\mu$ ROI of PSBs with a subchondral lesion remained significantly lower than in the same  $\mu$ ROI of those with no lesion. Proximal subchondral and internal trabecular BVF and AMD were higher for bones with a subchondral lesion than those without, and proximal subchondral was higher for TMD for a PSBs with a subchondral lesion than those without.

**Table SB-3.8.4:** Raw Means (Standard Deviation) of tissue morphometry variables for region of interest (ROI) and presence or absence of a subchondral lesion on the microcomputed tomography scan; using data from all PSBs and from just non-fractured PSBs (Case CLI and CTRL). Significant ranked ANOVA effects indicated by variable superscripts: <sup>†</sup>(ROI), <sup>§</sup>(subchondral Lesion), <sup>‡</sup>(Subchondral Lesion\*ROI). Pairwise comparisons of ROIs for PSBs with/without a subchondral lesion are indicated by letter superscripts (down column; A,B,C,D). Pairwise comparisons within each ROI are indicated by subscripts (across row; $\alpha,\beta$ ). For all comparisons, significant differences are indicated by \* and variables that do not share a superscript are significantly different at  $p \leq 0.05$ .

ANOVA Results using Case FX, Case CLI, and Control Data			ANOVA Results using Case CLI and Control Data		
	BVF			BVF	
	No Lesion*	Lesion*		No Lesion*	Lesion*
Central Subchondral*	0.97 (0.0) $\alpha^A$	0.91 (0.1) $\beta^C$	Central Subchondral*	0.97 (0.0) $\alpha^A$	0.96 (0.0) $\beta^C$
Central Subchondral Border	0.96 (0.1) $\alpha^{A,B}$	0.99 (0.0) $\alpha^A$	Central Subchondral Border*	0.96 (0.1) $\alpha^A$	0.99 (0.0) $\beta^A$
Proximal Subchondral*	0.94 (0.1) $\alpha^B$	0.98 (0.0) $\beta^{A,B}$	Proximal Subchondral*	0.95 (0.1) $\alpha^A$	0.99 (0.0) $\beta^{A,B}$
Internal Trabecular*	0.91 (0.1) $\alpha^C$	0.97 (0.0) $\beta^B$	Internal Trabecular*	0.91 (0.1) $\alpha^B$	0.98 (0.0) $\beta^{B,C}$
	AMD			AMD	
	No Lesion*	Lesion*		No Lesion*	Lesion*
Central Subchondral*	797.14 (37.2) $\alpha^{A,B}$	747.08 (48.1) $\beta^A$	Central Subchondral	795.22 (38.0) $\alpha^B$	777.8 (22.3) $\alpha^A$
Central Subchondral Border	815.42 (41.5) $\alpha^A$	820.65 (16.7) $\alpha^B$	Central Subchondral Border	812.07 (41.1) $\alpha^A$	831.26 (17.5) $\alpha^B$
Proximal Subchondral	773.81 (56.4) $\alpha^B$	808.55 (21.3) $\alpha^B$	Proximal Subchondral*	781.16 (51.2) $\alpha^B$	816.64 (20) $\beta^B$
Internal Trabecular	789.62 (55.7) $\alpha^{A,B}$	825.72 (31.0) $\alpha^B$	Internal Trabecular*	786.62 (56.8) $\alpha^B$	839.1 (28.7) $\beta^B$
	TMD			TMD	
	No Lesion*	Lesion*		No Lesion*	Lesion*
Central Subchondral*	814.01 (16.7) $\alpha^B$	795.29 (16.1) $\beta^C$	Central Subchondral	813.04 (17.0) $\alpha^B$	806.53 (13.4) $\alpha^C$
Central Subchondral Border*	839.94 (13.2) $\alpha^A$	831.75 (14.1) $\beta^{A,B}$	Central Subchondral Border	837.97 (11.4) $\alpha^A$	838.7 (16.6) $\alpha^A$
Proximal Subchondral	808.18 (20.5) $\alpha^B$	821.52 (19.9) $\alpha^B$	Proximal Subchondral*	810.03 (20.1) $\alpha^B$	825.88 (20.0) $\beta^B$
Internal Trabecular	847.89 (17.6) $\alpha^A$	845 (22.6) $\alpha^A$	Internal Trabecular	844.63 (13.1) $\alpha^A$	854.85 (24.8) $\alpha^A$



ANOVA comparing microdamage among bones with and without a lesion indicates that there was more microdamage and calcified cartilage cracks in the Central Subchondral hROI of PSBs with a lesion, compared to those without a lesion (Tables SB-5.8.5 & SB-5.8.6). This trend held when the ANOVA was run excluding data from FX-PSBs, indicating that the greater damage in the Central Subchondral hROIs of was not exclusively due to the fracture event (Tables SB-5.8.5 & SB-5.8.6). N.Cr, N.Cr/B.Ar, and  $\Sigma$ Cr.Le/B.Ar were higher in the Central Deep hROI of PSBs with a subchondral lesion; this finding only held for N.Cr/B.Ar when FX-PSB data was removed, so the increased damage levels in this region of PSBs with a subchondral lesion may or may not have been due to the fracture event. When comparing hROIs among PSBs without a lesion, the Central Subchondral hROI did not have more damage than other regions. When comparing hROIs among all PSBs with a subchondral lesion, the Central Subchondral hROI had significantly more internal microdamage and calcified cartilage microdamage than other subchondral regions.

**Table SB-3.8.5:** Raw Means (Standard Deviation) of microdamage variables for region of interest (ROI) depending on lesion presence (Yes, No) on the microcomputed tomography scan; using data from all PSBs and from only non-fractured PSBs (Case CLI and CTRL). Significant ranked ANOVA effects indicated by variable superscripts: <sup>†</sup>(ROI), <sup>§</sup>(Subchondral Lesion), <sup>‡</sup>(Subchondral Lesion\*ROI). Pairwise comparisons of ROIs for PSBs with or without a subchondral lesion are indicated by letter superscripts (down column; <sup>A,B,C,D</sup>). Pairwise comparisons within each ROI are indicated by Greek letter subscripts (across row; <sub>α,β</sub>). For all comparisons, significance is indicated by \* and variables that do not share a super- or sub-script are significantly different at  $p \leq 0.05$  down the column or across the row, respectively.

ANOVA Results using Case CLI, Case FX, and Control PSB Data (n = 28 PSBs)			ANOVA Results using Case CLI and Control Data (n = 18 PSBs)		
	N.Cr <sup>†‡</sup>			N.Cr <sup>†‡</sup>	
	No Lesion*	Lesion*		No Lesion	Lesion*
Proximal Subchondral	13.917 (17.973) <sub>α<sup>A,B</sup></sub>	21.781 (27.028) <sub>α<sup>B</sup></sub>	Proximal Subchondral	15.182 (18.282) <sub>α<sup>A,B</sup></sub>	30.286 (37.047) <sub>α<sup>B</sup></sub>
Central Subchondral*	19.458 (19.102) <sub>α<sup>A</sup></sub>	65.875 (37.517) <sub>β<sup>A</sup></sub>	Central Subchondral*	19.5 (20.034) <sub>α<sup>A</sup></sub>	66.286 (37.173) <sub>β<sup>A</sup></sub>
Distal Subchondral	5.375 (7.929) <sub>α<sup>B,C</sup></sub>	12.125 (11.177) <sub>α<sup>B</sup></sub>	Distal Subchondral	5.591 (8.279) <sub>α<sup>D,C</sup></sub>	14.714 (15.055) <sub>α<sup>B,C</sup></sub>
Proximal Deep	4.75 (5.298) <sub>α<sup>B,C</sup></sub>	3.469 (4.052) <sub>α<sup>C</sup></sub>	Proximal Deep	5 (5.482) <sub>α<sup>B,C,D</sup></sub>	3.929 (5.279) <sub>α<sup>C,D</sup></sub>
Central Deep*	7.583 (9.197) <sub>α<sup>A,B</sup></sub>	16.531 (9.674) <sub>β<sup>B</sup></sub>	Central Deep	7.909 (9.573) <sub>α<sup>A,B,C</sup></sub>	16.143 (11.213) <sub>α<sup>A,B</sup></sub>
Distal Deep	1.542 (2.742) <sub>α<sup>C</sup></sub>	2.125 (3.047) <sub>α<sup>C</sup></sub>	Distal Deep	1.682 (2.831) <sub>α<sup>D</sup></sub>	2.071 (3.878) <sub>α<sup>D</sup></sub>
	N.Cr/B.Ar <sup>†§‡</sup>			N.Cr/B.Ar <sup>†‡</sup>	
	No Lesion*	Lesion*		No Lesion	Lesion*
Proximal Subchondral	1.423 (1.787) <sub>α<sup>A,B</sup></sub>	2.474 (2.693) <sub>α<sup>B</sup></sub>	Proximal Subchondral	1.552 (1.814) <sub>α<sup>A,B</sup></sub>	3.328 (3.679) <sub>α<sup>A,B</sup></sub>
Central Subchondral*	2.059 (1.864) <sub>α<sup>A</sup></sub>	8.013 (4.268) <sub>β<sup>A</sup></sub>	Central Subchondral*	2.06 (1.955) <sub>α<sup>A</sup></sub>	7.706 (3.544) <sub>β<sup>A</sup></sub>
Distal Subchondral*	0.573 (0.816) <sub>α<sup>B,C</sup></sub>	1.529 (1.278) <sub>β<sup>B</sup></sub>	Distal Subchondral*	0.595 (0.852) <sub>α<sup>B,C</sup></sub>	1.699 (1.506) <sub>β<sup>B</sup></sub>
Proximal Deep	0.488 (0.516) <sub>α<sup>B,C</sup></sub>	0.456 (0.538) <sub>α<sup>C</sup></sub>	Proximal Deep	0.513 (0.533) <sub>α<sup>B,C</sup></sub>	0.436 (0.532) <sub>α<sup>C</sup></sub>
Central Deep*	0.788 (0.906) <sub>α<sup>A,B</sup></sub>	2.009 (1.114) <sub>β<sup>B</sup></sub>	Central Deep*	0.823 (0.942) <sub>α<sup>A,B</sup></sub>	1.845 (1.029) <sub>β<sup>A,B</sup></sub>
Distal Deep	0.162 (0.29) <sub>α<sup>C</sup></sub>	0.273 (0.395) <sub>α<sup>C</sup></sub>	Distal Deep	0.176 (0.299) <sub>α<sup>C</sup></sub>	0.238 (0.462) <sub>α<sup>C</sup></sub>
	ΣCr.Le/N.Cr <sup>†‡</sup>			ΣCr.Le/N.Cr <sup>†‡</sup>	
	No Lesion	Lesion*		No Lesion	Lesion*
Proximal Subchondral	0.066 (0.029) <sub>α<sup>A</sup></sub>	0.07 (0.034) <sub>α<sup>A,B,C</sup></sub>	Proximal Subchondral	0.072 (0.021) <sub>α<sup>A</sup></sub>	0.07 (0.046) <sub>α<sup>A,B</sup></sub>
Central Subchondral*	0.067 (0.028) <sub>α<sup>A</sup></sub>	0.108 (0.046) <sub>β<sup>A</sup></sub>	Central Subchondral	0.067 (0.03) <sub>α<sup>A,B</sup></sub>	0.082 (0.014) <sub>α<sup>A</sup></sub>
Distal Subchondral	0.046 (0.037) <sub>α<sup>A</sup></sub>	0.044 (0.029) <sub>α<sup>C</sup></sub>	Distal Subchondral	0.047 (0.039) <sub>α<sup>A,B</sup></sub>	0.045 (0.027) <sub>α<sup>B,C</sup></sub>
Proximal Deep	0.057 (0.05) <sub>α<sup>A</sup></sub>	0.049 (0.049) <sub>α<sup>B,C</sup></sub>	Proximal Deep	0.047 (0.036) <sub>α<sup>A,B</sup></sub>	0.031 (0.034) <sub>α<sup>B,C</sup></sub>
Central Deep	0.076 (0.052) <sub>α<sup>A</sup></sub>	0.086 (0.05) <sub>α<sup>A,B</sup></sub>	Central Deep	0.077 (0.054) <sub>α<sup>A,B</sup></sub>	0.059 (0.015) <sub>α<sup>A,B</sup></sub>
Distal Deep	0.039 (0.06) <sub>α<sup>A</sup></sub>	0.037 (0.049) <sub>α<sup>C</sup></sub>	Distal Deep	0.043 (0.061) <sub>α<sup>B</sup></sub>	0.013 (0.023) <sub>α<sup>C</sup></sub>
	ΣCr.Le/B.Ar <sup>†§‡</sup>			ΣCr.Le/B.Ar <sup>†‡</sup>	
	No Lesion*	Lesion*		No Lesion	Lesion*
Proximal Subchondral	0.106 (0.128) <sub>α<sup>A,B</sup></sub>	0.212 (0.285) <sub>α<sup>B</sup></sub>	Proximal Subchondral	0.116 (0.13) <sub>α<sup>A</sup></sub>	0.309 (0.395) <sub>α<sup>B</sup></sub>
Central Subchondral*	0.163 (0.183) <sub>α<sup>A</sup></sub>	0.842 (0.45) <sub>β<sup>A</sup></sub>	Central Subchondral*	0.166 (0.192) <sub>α<sup>A</sup></sub>	0.644 (0.318) <sub>β<sup>A</sup></sub>
Distal Subchondral	0.049 (0.093) <sub>α<sup>B,C</sup></sub>	0.089 (0.085) <sub>α<sup>B,C</sup></sub>	Distal Subchondral	0.052 (0.097) <sub>α<sup>B,C</sup></sub>	0.094 (0.094) <sub>α<sup>B,C</sup></sub>
Proximal Deep	0.033 (0.031) <sub>α<sup>B,C</sup></sub>	0.041 (0.065) <sub>α<sup>C,D</sup></sub>	Proximal Deep	0.032 (0.032) <sub>α<sup>B,C</sup></sub>	0.026 (0.036) <sub>α<sup>C,D</sup></sub>
Central Deep*	0.066 (0.082) <sub>α<sup>A,B</sup></sub>	0.168 (0.121) <sub>β<sup>B</sup></sub>	Central Deep	0.07 (0.084) <sub>α<sup>A,B</sup></sub>	0.112 (0.073) <sub>α<sup>A,B</sup></sub>
Distal Deep	0.014 (0.025) <sub>α<sup>C</sup></sub>	0.017 (0.024) <sub>α<sup>D</sup></sub>	Distal Deep	0.015 (0.026) <sub>α<sup>C</sup></sub>	0.01 (0.019) <sub>α<sup>D</sup></sub>

**Table SB-3.8.6:** Raw Means (Standard Deviation) of calcified cartilage microdamage variables for region of interest (ROI) depending on lesion presence (Yes, No) on the micrcomputed tomography scan; using data from all PSBs and from just non-fractured PSBs (Case CLI and CTRL). Significant ranked ANOVA effects indicated by variable superscripts: †(ROI), §(Subchondral Lesion), ‡(Subchondral Lesion\*ROI). Pairwise comparisons of ROIs for PSBs with/without a subchondral lesion are indicated by letters (down column; A,B,C,D). Pairwise comparisons within each ROI are indicated by greek letters (across row; $\alpha,\beta$ ). For all comparisons, significance is indicated by \* and variables that do not share a super- or sub-script are significantly different at  $p \leq 0.05$  down the column or across the row, respectively.

ANOVA Results using Case CLI, Case FX, and Control PSB Data (84 hROI fields)			ANOVA Results using Case CLI and Control Data (54 hROI fields)		
	N.Md.Cg.Cr <sup>†§‡</sup>			N.Md.Cg.Cr <sup>†§‡</sup>	
	No Lesion	Lesion*		No Lesion*	Lesion*
Proximal Subchondral	1 (1.537) $\alpha^A$	1.781 (2.243) $\alpha^A$	Proximal Subchondral	1.091 (1.578) $\alpha^A$	2 (3.109) $\alpha^A$
Central Subchondral*	0.333 (0.888) $\alpha^A$	4.625 (3.467) $\beta^B$	Central Subchondral*	0.091 (0.302) $\alpha^A\beta$	3.714 (1.976) $\beta^B$
Distal Subchondral*	0 (0) $\alpha^A$	1.219 (2.121) $\beta^A$	Distal Subchondral	0 (0) $\alpha^B$	0.429 (0.787) $\alpha^A$
	N.Md.Cg.Cr/Cg.Bd <sup>†§‡</sup>			N.Md.Cg.Cr/Cg.Bd <sup>†§‡</sup>	
	No Lesion	Lesion*		No Lesion*	Lesion*
Proximal Subchondral	0.147 (0.227) $\alpha^A$	0.313 (0.365) $\alpha^A$	Proximal Subchondral	0.161 (0.233) $\alpha^A$	0.331 (0.508) $\alpha^A$
Central Subchondral*	0.052 (0.143) $\alpha^A$	0.827 (0.553) $\beta^B$	Central Subchondral*	0.013 (0.042) $\alpha^A$	0.681 (0.388) $\beta^B$
Distal Subchondral*	0 (0) $\alpha^A$	0.23 (0.416) $\beta^A$	Distal Subchondral	0 (0) $\alpha^A$	0.078 (0.142) $\alpha^A$
	$\Sigma$ Md.Cg.Cr.Le/N.Cr <sup>†§‡</sup>			$\Sigma$ Md.Cg.Cr.Le/N.Cr <sup>†§‡</sup>	
	No Lesion	Lesion*		No Lesion*	Lesion*
Proximal Subchondral	0.04 (0.072) $\alpha^A$	0.055 (0.086) $\alpha^A$	Proximal Subchondral	0.091 (0.14) $\alpha^A$	0.109 (0.136) $\alpha^A$
Central Subchondral*	0.009 (0.029) $\alpha^A$	0.174 (0.125) $\beta^B$	Central Subchondral*	0.009 (0.031) $\alpha^A$	0.252 (0.117) $\beta^B$
Distal Subchondral*	0 (0) $\alpha^A$	0.062 (0.128) $\beta^A$	Distal Subchondral	0 (0) $\alpha^A$	0.081 (0.152) $\alpha^A$
	$\Sigma$ Md.Cg.Cr.Le/Cg.Bd <sup>†§‡</sup>			$\Sigma$ Md.Cg.Cr.Le/Cg.Bd <sup>†§‡</sup>	
	No Lesion	Lesion*		No Lesion*	Lesion*
Proximal Subchondral	0.084 (0.136) $\alpha^A$	0.098 (0.104) $\alpha^A$	Proximal Subchondral	0.044 (0.075) $\alpha^A$	0.082 (0.125) $\alpha^A$
Central Subchondral*	0.025 (0.063) $\alpha^A$	0.209 (0.12) $\beta^B$	Central Subchondral*	0.001 (0.004) $\alpha^A\beta$	0.17 (0.125) $\beta^B$
Distal Subchondral*	0 (0) $\alpha^A$	0.094 (0.147) $\beta^A$	Distal Subchondral	0 (0) $\alpha^B$	0.020.034) $\alpha^A$

### 3.9 Supplemental Material C: Equilibrium Solution for Bone Compartment

#### Model

This supplemental presents the equations for the compartment model of bone remodeling given in Figure 3.1. In this model, the 4 tissue types are: undamaged mineralized bone ( $BV_{UD}$ ), damaged mineralized bone ( $BV_D$ ), osteoid ( $OV$ ), and marrow ( $MV$ ). The time derivatives of these 4 tissue types can be expressed using the rate constants ( $k_i$ ) and are given in Equations 3.9.1-4. The summation of the 4 tissue types is equal to the total tissue volume ( $TV$ ).

$$\frac{d(BV_{UD})}{dt} = k_3 OV - (k_1 + k_4) BV_{UD} \quad (\text{Eqn. 3.9.1})$$

$$\frac{d(BV_D)}{dt} = k_4 BV_{UD} - k_5 BV_D \quad (\text{Eqn. 3.9.2})$$

$$\frac{d(OV)}{dt} = k_2 MV - k_3 OV \quad (\text{Eqn. 3.9.3})$$

$$\frac{d(MV)}{dt} = k_5 DV + k_1 BV_{UD} - k_2 OV \quad (\text{Eqn. 3.9.4})$$

At steady-state, the summation of the 4 tissue types is constant within a given tissue volume; therefore, the time derivatives are all equal to zero. While the rate terms cannot be determined from this set of equations, the steady-state solution for the 4 volume fractions are Equations 3.9.5-8.

$$\frac{BV_{UD}}{TV} = \frac{k_2 k_3 k_5}{k_1 k_2 k_5 + k_1 k_3 k_5 + k_2 k_3 k_4 + k_2 k_3 k_5 + k_2 k_4 k_5 + k_3 k_4 k_5} \quad (\text{Eqn. 3.9.5})$$

$$\frac{BV_D}{TV} = \frac{k_2 k_3 k_4}{k_1 k_2 k_5 + k_1 k_3 k_5 + k_2 k_3 k_4 + k_2 k_3 k_5 + k_2 k_4 k_5 + k_3 k_4 k_5} \quad (\text{Eqn. 3.9.6})$$

$$\frac{OV}{TV} = \frac{k_2 k_5 (k_1 + k_4)}{k_1 k_2 k_5 + k_1 k_3 k_5 + k_2 k_3 k_4 + k_2 k_3 k_5 + k_2 k_4 k_5 + k_3 k_4 k_5} \quad (\text{Eqn. 3.9.7})$$

$$\frac{MV}{TV} = \frac{k_3 k_5 (k_1 + k_4)}{k_1 k_2 k_5 + k_1 k_3 k_5 + k_2 k_3 k_4 + k_2 k_3 k_5 + k_2 k_4 k_5 + k_3 k_4 k_5} \quad (\text{Eqn. 3.9.8})$$

The partial derivatives of the equilibrium volume fractions with respect to damage formation rate ( $k_4$ ) are given in Equations 3.9.9-12.

$$\frac{\delta\left(\frac{BV_{UD}}{TV}\right)}{\delta k_4} = - \frac{k_2 k_3 k_5 (k_2 k_3 + k_2 k_5 + k_3 k_5)}{(k_1 k_2 k_5 + k_1 k_3 k_5 + k_2 k_3 k_4 + k_2 k_3 k_5 + k_2 k_4 k_5 + k_3 k_4 k_5)^2} \quad (\text{Eqn. 3.9.9})$$

$$\frac{\delta\left(\frac{MV}{TV}\right)}{\delta k_4} = - \frac{k_2 k_3^2 k_5 (k_1 - k_5)}{(k_1 k_2 k_5 + k_1 k_3 k_5 + k_2 k_3 k_4 + k_2 k_3 k_5 + k_2 k_4 k_5 + k_3 k_4 k_5)^2} \quad (\text{Eqn. 3.9.10})$$

$$\frac{\delta\left(\frac{OV}{TV}\right)}{\delta k_4} = - \frac{k_2^2 k_3 k_5 (k_1 - k_5)}{(k_1 k_2 k_5 + k_1 k_3 k_5 + k_2 k_3 k_4 + k_2 k_3 k_5 + k_2 k_4 k_5 + k_3 k_4 k_5)^2} \quad (\text{Eqn. 3.9.11})$$

$$\frac{\delta\left(\frac{BV_D}{TV}\right)}{\delta k_4} = \frac{k_2 k_3 k_5 (k_1 k_2 + k_1 k_3 + k_2 k_3)}{(k_1 k_2 k_5 + k_1 k_3 k_5 + k_2 k_3 k_4 + k_2 k_3 k_5 + k_2 k_4 k_5 + k_3 k_4 k_5)^2} \quad (\text{Eqn. 3.9.12})$$

### 3.10 References

1. Ferry AT, Graves T, Theodore GH, Gill TJ. 2010. Stress fractures in athletes. *Phys. Sportsmed.* 38(2):109–116.
2. Martig S, Chen W, Lee PVS, Whitton RC. 2014. Bone fatigue and its implications for injuries in racehorses. *Equine Vet. J.* 46(4):408–415.
3. Stover SM. 2003. The Epidemiology of Thoroughbred Racehorse Injuries. *Clin. Tech. Equine Pract.* 2(4):312–322.
4. Shaffer SK, To C, Garcia TC, et al. 2021. Subchondral focal osteopenia associated with proximal sesamoid bone fracture in Thoroughbred racehorses. *Equine Vet. J.* 53(2):294–305 Available from: <https://onlinelibrary.wiley.com/doi/abs/10.1111/evj.13291>.
5. Anthenill LA, Stover SM, Gardner IA, et al. 2006. Association between findings on palmarodorsal radiographic images and detection of a fracture in the proximal sesamoid bones of forelimbs obtained from cadavers of racing Thoroughbreds. *Am. J. Vet. Res.* 67(5):858–868 Available from: <http://avmajournals.avma.org/doi/abs/10.2460/ajvr.67.5.858>.
6. Riggs CM. 2002. Fractures - A preventable hazard of racing thoroughbreds? *Vet. J.* 163(1):19–29.
7. Anthenill LA, Stover SM, Gardner IA, Hill AE. 2007. Risk factors for proximal sesamoid bone fractures associated with exercise history and horseshoe characteristics in Thoroughbred racehorses. *Am. J. Vet. Res.* 68(7):760–771 Available from: <http://avmajournals.avma.org/doi/abs/10.2460/ajvr.68.7.760>.
8. Robling AG, Fuchs RK, Burr DB. 2014. Mechanical Adaptation. In: *Basic and Applied Bone Biology*. Elsevier. p 175–204 Available from: <https://linkinghub.elsevier.com/retrieve/pii/B9780124160156000095>.
9. Martin RB. 2001. The Role of Bone Remodeling in Preventing or Promoting Stress Fractures. In: Burr DD, Milgrom C, editors. *Musculoskeletal Fatigue and Stress Fractures*. CRC Press, Inc. p 183–203.
10. Martin RB, Burr DB, Sharkey NA, Fyhrie DP. 2015. *Mechanical Adaptability of the Skeleton*, 2nd ed. New York, NY: Springer New York. 275–343 p. Available from: <http://link.springer.com/10.1007/978-1-4939-3002-9>.
11. Robling AG, Castillo AB, Turner CH. 2006. Biomechanical and Molecular Regulation of Bone Remodeling. *Annu. Rev. Biomed. Eng.* 8(1):455–498 Available from: <http://www.annualreviews.org/doi/10.1146/annurev.bioeng.8.061505.095721>.
12. Murshed M. 2018. Mechanism of Bone Mineralization. *Cold Spring Harb. Perspect. Med.* 8(12):1–12.
13. Hernandez CJ, Gupta A, Keaveny TM. 2006. A Biomechanical Analysis of the Effects of Resorption Cavities on Cancellous Bone Strength. *J. Bone Miner. Res.* 21(8):1248–1255 Available from: <http://doi.wiley.com/10.1359/jbmr.060514>.

14. Hughes JM, Popp KL, Yanovich R, et al. 2017. The role of adaptive bone formation in the etiology of stress fracture. *Exp. Biol. Med.* 242(9):897–906.
15. van Oers RFM, van Rietbergen B, Ito K, et al. 2011. Simulations of trabecular remodeling and fatigue: Is remodeling helpful or harmful? *Bone* 48(5):1210–1215 Available from: <http://dx.doi.org/10.1016/j.bone.2011.01.011>.
16. Hodsman A., Kisiel M, Adachi J., et al. 2000. Histomorphometric evidence for increased bone turnover without change in cortical thickness or porosity after 2 years of cyclical hPTH(1-34) therapy in women with severe osteoporosis. *Bone* 27(2):311–318 Available from: <https://linkinghub.elsevier.com/retrieve/pii/S8756328200003161>.
17. Bradbeer JN, Arlot ME, Meunier PJ, Reeve J. 1992. Treatment of osteoporosis with parathyroid peptide (hPTH 1–34) and oestrogen: increase in volumetric density of iliac cancellous bone may depend on reduced trabecular spacing as well as increased thickness of packets of newly formed bone. *Clin. Endocrinol. (Oxf)*. 37(3):282–289.
18. Dempster DW, Compston JE, Drezner MK, et al. 2013. Standardized nomenclature, symbols, and units for bone histomorphometry: A 2012 update of the report of the ASBMR Histomorphometry Nomenclature Committee. *J. Bone Miner. Res.* 28(1):2–17.
19. Whitton RC, Ayodele BA, Hitchens PL, Mackie EJ. 2018. Subchondral bone microdamage accumulation in distal metacarpus of Thoroughbred racehorses. *Equine Vet. J.* 50(6):766–773.
20. Kristoffersen M, Hetzel U, Parkin TDH, Singer ER. 2010. Are bi-axial proximal sesamoid bone fractures in the british thoroughbred racehorse a bone fatigue related fracture?: A histological study. *Vet. Comp. Orthop. Traumatol.* 23(5):336–342.
21. Burr DB, Hooser M. 1995. Alterations to the en bloc basic fuchsin staining protocol for the demonstration of microdamage produced in vivo. *Bone* 17(4):431–433.
22. Schneider CA, Rasband WS, Eliceiri KW. 2012. NIH Image to ImageJ: 25 years of image analysis. *Nat. Methods* 9(7):671–675.
23. Lee TC, Mohsin S, Taylor D, et al. 2003. Detecting microdamage in bone. *J. Anat.* 203(2):161–172.
24. Greco L, Luta G, Krzywinski M, Altman N. 2019. Analyzing outliers: robust methods to the rescue. *Nat. Methods* 16(4):275–276.
25. Ayodele BA, Hitchens PL, Wong ASM, et al. 2020. Microstructural properties of the proximal sesamoid bones of Thoroughbred racehorses in training. *Equine Vet. J.* (November):1–9.
26. Bani Hassan E, Mirams M, Ghasem-Zadeh A, et al. 2016. Role of subchondral bone remodelling in collapse of the articular surface of Thoroughbred racehorses with palmar osteochondral disease. *Equine Vet. J.* 48(2):228–233 Available from: <https://onlinelibrary.wiley.com/doi/10.1111/evj.12415>.
27. Rubin C, Lanyon L. 1984. Bone remodeling in response to applied dynamic loads. *J. Bone Jt. Surg.* 66-A(3):397–402.

28. Lanyon LE. 1984. Functional strain as a determinant for bone remodeling. *Calcif. Tissue Int.* 36(1 Supplement):56–61.
29. Turner CH. 1998. Three rules for bone adaptation to mechanical stimuli. *Bone* 23(5):399–407.
30. Loi F, Córdova LA, Pajarinen J, et al. 2016. Inflammation, fracture and bone repair. *Bone* 86:119–130.
31. Suniaga S, Rolvien T, vom Scheidt A, et al. 2018. Increased mechanical loading through controlled swimming exercise induces bone formation and mineralization in adult zebrafish. *Sci. Rep.* 8(1):3646 Available from: <http://www.nature.com/articles/s41598-018-21776-1>.
32. Robling AG, Burr DB, Turner CH. 2001. Recovery periods restore mechanosensitivity to dynamically loaded bone. *J. Exp. Biol.* 204(19):3389–3399.
33. Eberhardt AW, Keer LM, Lewis JL, Vithoontien V. 1990. An analytical model of joint contact. *J. Biomech. Eng.* 112(4):407–413.
34. Boyce TM, Fyhrie DP, Glotkowski MC, et al. 1998. Damage type and strain mode associations in human compact bone bending fatigue. *J. Orthop. Res.* 16(3):322–329.
35. Hodgskinson R, Currey JD. 1992. Young's modulus, density and material properties in cancellous bone over a large density range. *J. Mater. Sci. Mater. Med.* 3(5):377–381.
36. Hernandez CJ, Lambers FM, Widjaja J, et al. 2014. Quantitative relationships between microdamage and cancellous bone strength and stiffness. *Bone* 66:205–213 Available from: <http://dx.doi.org/10.1016/j.bone.2014.05.023>.
37. Donnelly E, Boskey AL, Baker SP, van der Meulen MCH. 2009. Effects of tissue age on bone tissue material composition and nanomechanical properties in the rat cortex. *J. Biomed. Mater. Res. Part A* 9999A(3):NA-NA Available from: <https://onlinelibrary.wiley.com/doi/10.1002/jbm.a.32442>.
38. Grynpas M. 1993. Age and disease-related changes in the mineral of bone. *Calcif. Tissue Int.* 53(1 Supplement).



## **Chapter 4: Training Drives Turnover Rates in Racehorse Proximal Sesamoid**

### **Bones**

#### **4.1 Abstract**

Stress-reactions develop in bone tissue before a full stress fracture. In subchondral bone, stress-reactions are characterized as focal regions of low bone volume fraction, low mineral density, and high levels of microdamage and are hypothesized to develop when bone tissue is unable to adapt to damaging loading. However, in athletes it is difficult to determine how training drives the formation of stress reactions because bone biologically responds to both mechanical loading and damage. In this study, we derive steady-state rate constants for a compartment model of bone's tissue turnover cycle using morphometric data from Case and Control racehorse proximal sesamoid bones (PSBs) and then relate the rate constants to exercise data. The Case bones had a naturally occurring subchondral stress-reaction. We determined steady-state model rate constants in the stress-reaction region (Damaged ROI) and in an internal region with no microdamage (Non-Damaged ROI). Steady-state rate constants were determined using bone volume fraction, tissue mineral density, and microdamage area fraction measurements from the PSBs. These rate constants were then related to training history. We found the derived undamaged bone resorption rate, damage formation rate, and osteoid formation rate had significant robust regression relationships to exercise intensity (rate) variables, layup (time out of exercise), and exercise 2-10 months before death. However, the direction of these relationships varied between the Damaged and Non-Damaged region, indicating that some aspect of the mechanical loading (likely strain) is different between the two regions.

## 4.2 Introduction

Physiologic strain rates and magnitudes are known to cause fatigue damage in bone tissue. The number of loading cycles at physiologic strain magnitudes required to cause fatigue (stress) fracture during mechanical testing are much higher than those that cause fractures *in vivo*. Generally, the lower cycle number required to cause a stress fracture *in vivo* is attributed to bone's innate damage repair process.<sup>1</sup> During damage repair, osteoclasts remove damaged tissue and form a porosity, called a resorption bay, then osteoblasts deposit unmineralized tissue, called osteoid, to refill the resorption bay. The osteoid mineralizes in a two-stage process that is, at least partially, controlled by osteocytes.<sup>2-4</sup> First, a rapid primary mineralization period brings the osteoid to 45-80% of the interstitial mineral content; this initial rapid mineralization completes within a few days.<sup>2-5</sup> Second, a slow secondary mineralization period brings the tissue to a mineral density comparable to the surrounding tissue; secondary mineralization occurs at a decreasing rate for several years.<sup>2-5</sup> Consequently, damage repair temporarily increases porosity and reduces tissue mineralization at the location where damage occurred; these tissue changes transiently reduce tissue stiffness. These transient changes are believed to accelerate the progression to a stress fracture when damaging loading is continued since the reduced modulus can elevate strain and promote the formation of more microdamage, leading to more damage repair in a vicious cycle. Supporting this idea, microdamage preferentially forms near resorption bays and computer modeling indicates that resorption bays are stress risers.<sup>6,7</sup> Additionally, stress fractures occur through sites with evidence of damage repair and occur in consistent configurations.<sup>8-11</sup> Further, stress fracture risk increases with exercise intensity.<sup>10,12</sup>

Further complicating the link between exercise and stress fractures *in vivo* is bone's response to mechanical loading. Generally, two cellular processes are used by bone tissue to respond to damage and load: modeling and remodeling. These processes are distinguished based on the spatial and temporal coupling of cellular activity. During modeling, bone formation by osteoclasts and bone resorption by

osteoblasts are not spatially or temporally linked. Therefore, modeling is associated with shape changes (e.g., altering trabecular width or bone curvature) and may or may not be associated with a change in bone density. During remodeling, bone resorption is followed, at the same location, by bone formation. In healthy adults, the amount of tissue removed is approximately equal to the amount added and remodeling is considered balanced. However, unbalanced remodeling does occur and will change the amount of bone tissue at a specific site. Unbalanced remodeling can be caused by disease states, endocrine changes, and many other factors. For example, osteopetrosis can cause positive balance remodeling by making osteoclasts less effective at resorbing bone and vitamin-D deficiency causes a negative remodeling balance by inhibiting osteoid mineralization.<sup>13</sup> Loading history, strain rate and magnitude, general health status, anatomic location within the bone, and many other factors affect bone formation or resorption in response to loading (or lack of loading) through both modeling and remodeling.<sup>14</sup>

Racehorses, like many high-performance athletes, are subject to repetitive high-strain, high-cycle number, training activities. At racing speeds, strains of up to nearly 5000  $\mu\epsilon$  have been reported in racehorse third metacarpal bones (a long bone in the distal forelimb); this peak strain is much higher than peak periosteal strains typically observed in other species (2000-3000  $\mu\epsilon$ ).<sup>15,16</sup> Stress fractures are the most common cause of fatalities associated with horse racing and stress fracture risk is associated with exercise (training).<sup>10,12</sup> Focal differences in bone tissue, compared to surrounding regions, called stress-reactions are often found at the stress fracture site in a fractured bone and at the same anatomic location in the contralateral (opposite) side of the body. Stress-reactions are believed to precede a complete stress fracture and have characteristics of a focal region undergoing damage repair. Stress-reactions are characterized by osteopenia, low mineral density, microdamage, and (if location permits) a periosteal or endosteal bone callus.<sup>18-20</sup> One method commonly used to determine if an athlete is at risk of a stress fracture (regardless of species) is to look for a stress-reaction.<sup>18,20</sup> Many stress fracture configurations and

focal stress reactions observed in racehorses are not found in horses that do not habitually train at gallop-speeds; this further implies a link between training and stress fractures.<sup>21</sup> However, the interactions between bone formation (or resorption) due to exercise and the repair of tissue damage makes it difficult to determine specific exercise patterns that cause (or protect against) stress fractures. For example, horses that have a higher-rate of training 2-12 months prior to death and those in training for longer periods without a rest (colloquially called a layup) have an increased stress-fracture risk.<sup>12,22</sup> However, the 1-2 months after returning to work from a rest period are also a period of high stress-fracture risk.<sup>10</sup> Therefore, it would be advantageous to determine what specific aspects of a training program are protective against stress-reactions and stress-fractures.

Previously, we introduced a compartment model of bone's "tissue turnover cycle" (Figure 4.1)<sup>23</sup> and used the model to organize observed relationships between racehorse proximal sesamoid bone (PSB) morphometric data and training data. PSBs were used because PSB fracture is the most common fatal injury in many racing populations.<sup>24-27</sup> Consistent fracture configurations, a subchondral stress-reaction, and association with training indicates that PSB fractures are stress fractures.<sup>10,12,28</sup> We reported a focal subchondral osteopenic and microdamaged stress-reaction (lesion) in fractured and contralateral limb intact PSBs of Thoroughbred racehorses; this lesion was not found in racehorses that did not experience PSB fracture.<sup>19</sup> The observed differences from Control PSB bone volume fraction, tissue mineral density, and microdamage were site-specific and correlated with training history. Figure 4.1 shows the compartment model we developed to relate changes in bone tissue histological measures to rates of bone turnover. This model accounts for changes in bone volume fractions caused by both modeling and remodeling. The aims of this manuscript are to: 1) calculate the steady-state rate constants for the compartmental model (Figure 4.1) based on previously collected histological and microcomputed tomography ( $\mu$ CT) data from racehorse PSBs and 2) determine the relationships between model rate constants and lifetime exercise data.

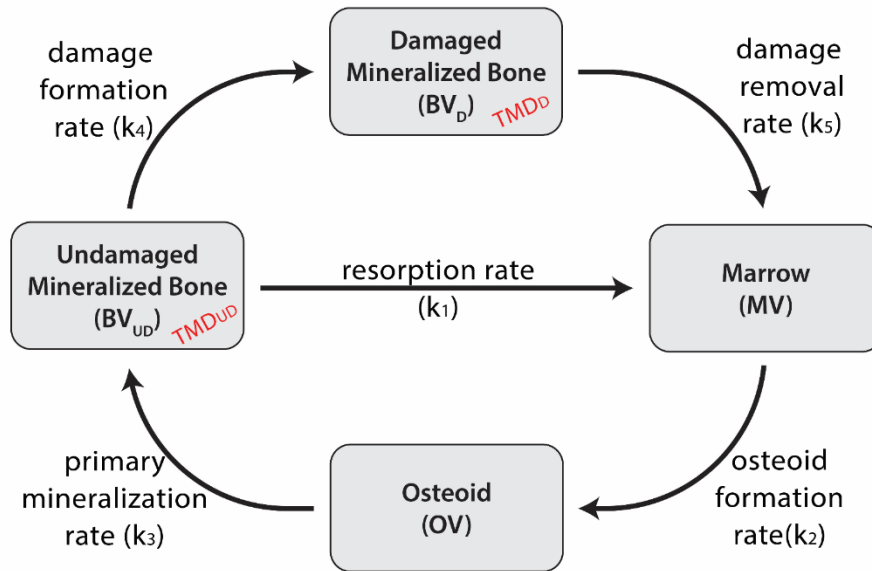


**Figure 4.1:** Compartment model of the bone “tissue turnover cycle.” There are four tissue volumes: damaged mineralized bone, undamaged mineralized bone, marrow, and osteoid. Tissue volumes can transform following the paths indicated by the arrows at the specified rates ( $k_i$ ). Tissue mineral density (TMD) is defined for the undamaged and damaged mineralized bone volumes.

## 4.3 Methods

### 4.3.1 Study Design

The compartment model (Figure 4.1) was designed to allow the tissue types to be defined either histologically or using x-ray imaging. We will derive the relationships between observable morphometric data and the compartment model values in the following sections. Then, we will calculate steady-state rate constants using morphometric data collected in two regions of interest (ROIs) from racehorse PSBs. Data were measured within 10 fractured medial PSBs (FX-PSB) from Case racehorses euthanized due to unilateral biaxial PSB fracture, 10 contralateral limb intact medial PSBs (CLI-PSBs) from the same Case racehorses, and 10 medial PSBs from Control racehorses (CTRL-PSBs) euthanized for injuries unrelated to PSB fracture.<sup>19,23</sup> The steady-state rate constants were determined in a Damaged ROI and in a Non-Damaged ROI in all PSBs (Figure 4.2). The Damaged ROI contains the identified subchondral bone stress-reaction (lesion) or was constructed at a comparable location in samples without a lesion. The Damaged ROI was previously identified as “central subchondral ROI” in Chapter 3.<sup>23</sup> The Non-damaged ROI was

constructed in a standardized internal trabecular region and was previously identified as the “trabecular ROI” in Chapter 3.<sup>23</sup> The steady-state rate constants in each ROI were then compared among the three Groups. Additionally, the steady-state rate constants for the CTRL and CLI PSBs were related to Case and Control exercise history. Case FX and Case CLI PSBs are from the same horses and, therefore, have the same exercise history. The model, relationships to morphometric data, and solving procedures are expanded upon in the following sections.

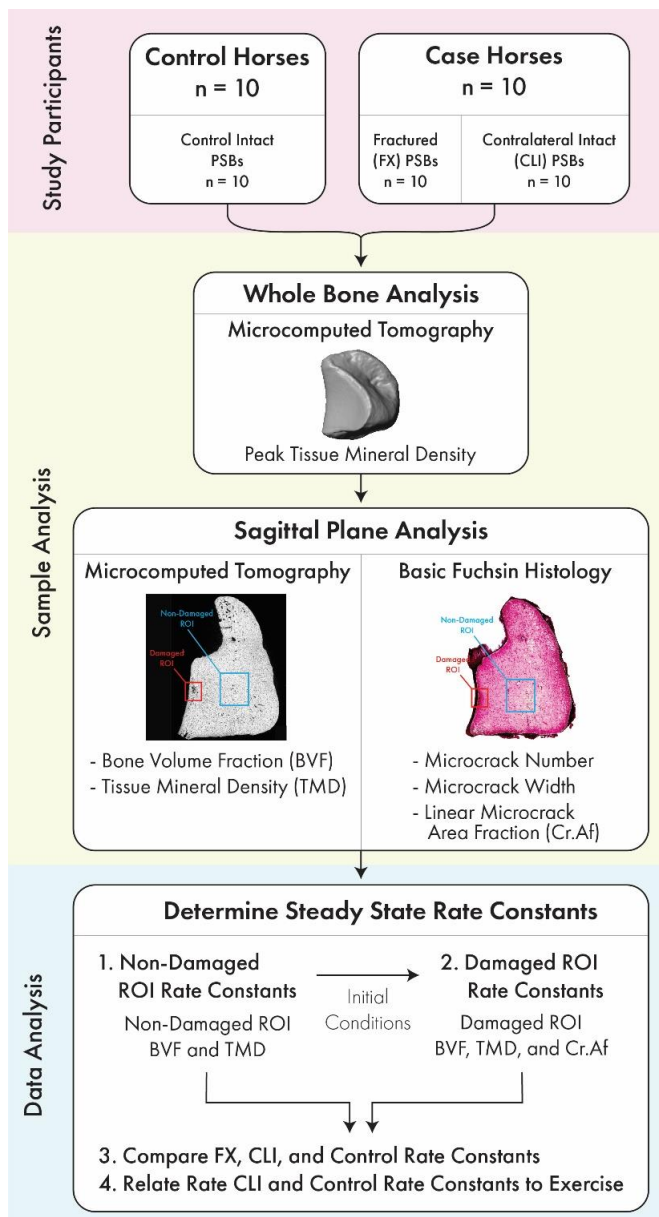


**Figure 4.2:** Flowchart of study methods. Data were collected from 30 PSBs, provided by 10 Case and 10 Control racehorses. The whole PSB was used to determine the peak tissue mineral density of the sample. Then data was collected in two sagittal plane regions of interest (ROIs): a Non-Damaged ROI (blue) and Damaged ROI (red). Steady-state rate constants were determined using the collected data. First, steady-state rate constants were determined in the Non-Damaged ROI (1). Second, steady-state rate constants were determined within the Damaged ROI (2), using the rate constants for the Non-Damaged ROI (1) as initial conditions. Finally, the rate constants were compared among groups (3) and related to exercise (4).

### 4.3.2 Model Description

A compartment model for the “bone tissue turnover cycle” is presented in Figure 4.1. This model separates bone tissue into four types that fill a tissue volume (TV): undamaged mineralized bone ( $BV_{UD}$ ), damaged mineralized bone ( $BV_D$ ), osteoid (OV), and marrow or void space (MV; Figure 4.1). Each tissue type is a portion of the tissue volume (TV) and is defined using histological features. The summation of the four volume compartments (TV) is constant, as this compartment model is closed and has no inflows or outflows (Eqn. 4.1a). The tissue types can transform between compartments in the directions indicated by the arrows at the given transfer rates ( $k_1 - k_5$ ; Figure 4.1). As is typical of compartment models, we require the transfer rates to be non-negative.<sup>29,30</sup> This convention prevents negative compartment volumes, which would be physiologically nonsensical. Further, non-negative transfer rates bound the total volume flow out of a compartment within a time increment by the volume added to the compartment during that time increment plus the original volume present.

$$BV_{UD} + BV_D + OV + MV = TV \quad \text{Eqn. 4.1a}$$

The model is constructed based on well-known aspects of bone modeling and remodeling. Each compartment histologically defines a tissue volume within the TV, therefore, internal surfaces are not defined and volume changes due to modeling and remodeling cannot be distinguished. For example, in this model it cannot be determined whether a reduction in  $BV_{UD}$  was due to internal modeling (e.g., reducing trabecular width), negatively balanced remodeling (e.g., incomplete refilling of a resorption bay), or some combination of the processes. The model can quantify the net reduction in  $BV_{UD}$ , but not attribute the change as being due to a specific cell process. Regardless, the tissue “transformations” between compartments that occur during modeling and remodeling have the same volume-averaged effect on the TV.

The tissue transformations are captured by the compartment model. Removal of mineralized bone by osteoclasts creates a resorption cavity (e.g., a void space with no osteoid or mineralized tissue).

In this model, resorption is represented by the transition of a volume of damaged mineralized bone ( $BV_D$ ) or undamaged mineralized bone ( $BV_{UD}$ ) into the marrow (MV) compartment. These processes occur at the resorption rate ( $k_1$ ) and damage removal rate ( $k_5$ ). Formation of new bone tissue occurs through deposition of osteoid by osteoblasts; bone formation is represented by the transition of marrow volume (MV) into osteoid volume (OV) at the osteoid formation rate ( $k_2$ ). After deposition, osteoid then undergoes a period of maturation, followed by rapid primary, and a slower secondary mineralization. We will assume that tissue within the osteoid compartment (OV) is undergoing osteoid maturation or primary mineralization. Therefore, tissue in the mineralized bone compartments ( $BV_{UD}$  &  $BV_D$ ) is undergoing secondary mineralization and has a mineral density that changes with time. Tissue mineral density (TMD) is another observable quantity of bone separate from the histological division of the tissue into four types. TMD changes with time (i.e., bone mineralization is time dependent) and is often considered an index for tissue age.<sup>5,31</sup> In this study, we will represent TMD as the volumetric average of the TMD within the two mineralized compartments ( $BV_D$  &  $BV_{UD}$ ). An auxiliary relationship (presented later) governs how secondary mineralization proceeds while tissue resides in the mineralized bone compartments. The transition of osteoid volume (OV) to undamaged mineralized bone ( $BV_{UD}$ ) occurs at the primary mineralization rate ( $k_3$ ). Damage in bone tissue occurs within mineralized bone tissue; this transition is represented by the conversion of undamaged mineralized bone volume ( $BV_{UD}$ ) to damaged mineralized bone ( $BV_D$ ) at the damage formation rate ( $k_4$ ).

The main aim of this manuscript is to solve for the steady-state rate constants based on experimental morphometric data from Case racehorses with PSB stress fracture and Controls without. The time derivatives of the four tissue types can be expressed as a function of the rate constants (Section 4.7; Equation 4.7.1-4). At steady-state, these time derivatives are equal to zero. The general steady-state volume solutions (i.e., solutions not considering TMD) are underdetermined to a constant (derivation in Section 4.7; Eqns. 4.7.1 – 7). This is consistent with the solutions of outflow closed compartment systems



which inherently have a singular rate transfer matrix (coefficient matrix).<sup>29,30</sup> However, the constant can be eliminated if the system is written in terms of volume fractions (Section 4.7; Eqns. 4.7.8-11).

For the rest of this manuscript, the steady-state volume fractions equations (Eqns. 4.7.8-11) will be used instead of the steady-state volumes. Note that when Eqn. 4.1a is written in terms of the volume fractions, the summation of the volume fraction is always equal to one (Eqn. 4.1b). However, without the addition of the TMD to the compartment model, the system is underdetermined when solving for the five rate constants in terms of 4 volume fractions. The addition of TMD will allow us to solve the system for the five rate constants using observed morphometric data. Note that the steady-state volume fractions depend on the ratios of the rate constants (Eqns. 4.7.8-11) and TMD depends on the magnitude of the rate constants (derivation below).

$$\frac{BV_{UD}}{TV} + \frac{BV_D}{TV} + \frac{OV}{TV} + \frac{MV}{TV} = 1 \quad (\text{Eqn. 4.1b})$$

### 4.3.3 Derivation of the Dependence of TMD on Remodeling Rates

Tissue mineral density (TMD), as defined by microcomputed tomography ( $\mu$ CT), is the equivalent density of hydroxyapatite within a volume of mineralized tissue and TMD is known to change with tissue age.<sup>31-33</sup> Therefore, an expression can be developed for TMD using population statistics and the model rate constants if a formula expresses mineralization as a function of tissue age.<sup>34</sup> In stochastic compartment models, the reciprocal sum of outflow coefficients ( $1/\Sigma k_{i,out}$ ) is the average retention time of a "particle" in the compartment during a single visit to that compartment.<sup>35</sup> Additionally, the expected (average) value of a continuous variable,  $m(t)$ , is determined as the integral of  $m(t)$  multiplied by the probability distribution function of the population that has the property  $m(t)$ .<sup>34</sup> Equation 4.2 defines the expected value of TMD (or average TMD) where  $m(t)$  is a continuous function defining TMD during secondary mineralization and  $P(t)$  is the probability distribution function describing the chances of mineralized bone resorption at time  $t$ .

$$TMD = \int_0^{\infty} m(t)P(t)dt \quad (\text{Eqn. 4.2})$$

#### 4.3.4 Mineralization Law

To use Eqn. 4.2, we require a mineralization law,  $m(t)$ , for the two mineralized bone compartments. We only require an  $m(t)$  for secondary mineralization, and not also primary mineralization, because we use primary mineralization to *define* the difference between osteoid (OV) and mineralized undamaged bone ( $BV_{UD}$ ).

For simplicity, we will model  $m(t)$  as bounded exponential growth (Eqn. 4.3), and demonstrate below that this is a reasonable form. In Eqn. 4.3,  $TMD_{max}$  and  $TMD_o$  are the maximum and minimum bounds for TMD, respectively. To relate Eqn. 4.3 to collected x-ray measurements,  $TMD_o$  is the mineralization threshold used by  $\mu$ CT to distinguish mineralized bone from non-mineralized tissue. Due to the assumption that mineralized bone tissue ( $BV_M$ ) has completed primary mineralization,  $TMD_o$  is also the cut-off value distinguishing primary and secondary mineralization. Similarly,  $TMD_{max}$  is the peak empirically observed mineral density.

$$m(t) = (TMD_o - TMD_{max})e^{-k_m t} + TMD_{max} \quad (\text{Eqn. 4.3})$$

The secondary mineralization rate constant ( $k_m$ ) may vary among species (Figure 4.3).<sup>2,3,5,36</sup> However, the differences in mineralization rates among species are not well established and, to our knowledge, mineralization rate studies have not been performed in horses. Consequently, we cannot directly estimate  $k_m$  for our horses from equine data. Limited evidence suggests exercise increases the mineralization rate, however this dependence is also not well described.<sup>37</sup> Therefore, we will assume a constant  $k_m$  that is unaffected by exercise. The value we select ( $k_m = 0.00505 \text{ days}^{-1}$ ; Table 4.1) is the average  $k_m$  from cortical and cancellous data from ewes estimated via root-mean-square error curve-fitting to data from Bala, et. al, 2010 to Eqn. 4.3.<sup>2</sup> We also assume that the same mineralization law (Eqn. 4.3) holds in both the damaged and undamaged volume compartments. There is evidence that damaged

tissue can reach a higher peak mineral density than undamaged tissue;<sup>38</sup> however, the relationship between mineral peaks in damaged and undamaged tissue is not well established.

Previous work indicates that using the sum of two exponentials to define  $m(t)$ , rather than a single exponential better reproduces the calcium concentration distribution (BMDD) observed in bone tissue.<sup>39</sup> However, since we are only using Eqn. 4.3 to determine average TMD, and not BMDD, we will use the simpler, single-exponential model. Additionally, when fitting mineralization time course data (Figure 4.3), we found a single exponential for  $m(t)$  has comparable  $r^2$  values to the sum of two exponentials.

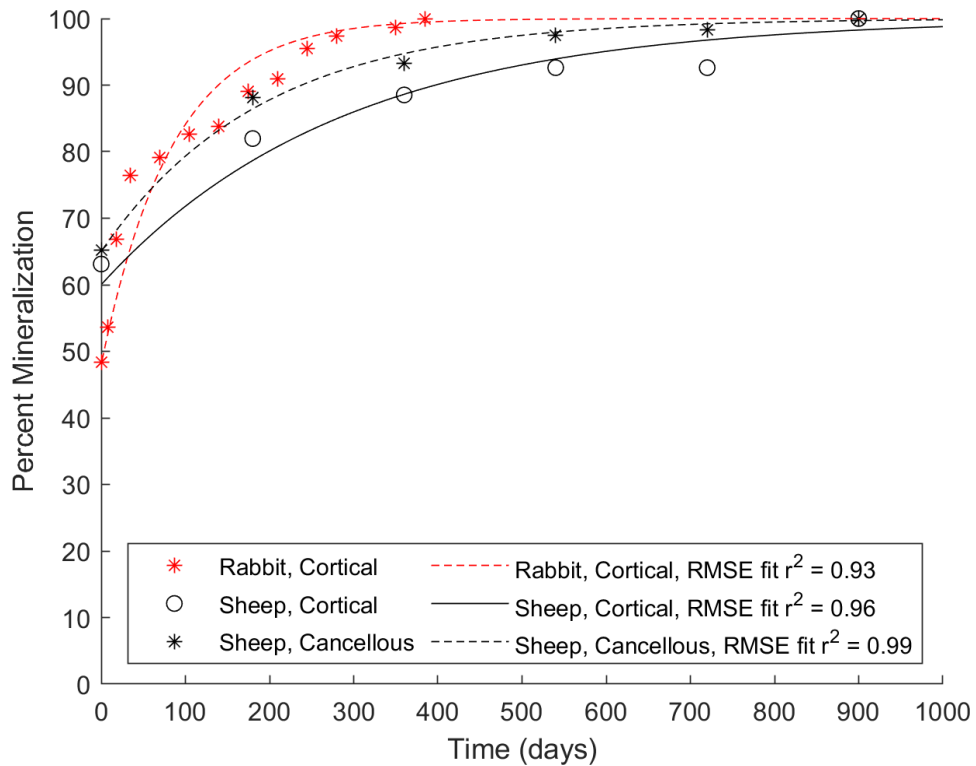


**Figure 4.3:** RMSE curve-fits of Equation 4.3 from rabbit and sheep bones. Data used for curve fits were digitized from Fuchs, et. al., 2008 (rabbit) and Bala, et. al., 2010 (sheep). Mineral content data was normalized to peak measured mineralization to create this figure;  $TMD_0$  was the normalized measurement at the first time point and  $TMD_{max}$  was the normalized peak measurement (i.e., 100%). When data was not normalized, the  $r^2$  values were similar and  $\leq 0.93$ . Curve-fits were performed in MATLAB's non-linear least-square's solver using the Levenberg-Marquardt option.

### 4.3.5 Average Mineralization

To use Eqn. 4.2, the probability of resorption at a given time must be determined to create the probability distribution function,  $P(t)$ . We assume that resorption of mineralized bone is independent of the amount of time spent in its compartment. Physically, this models resorption as independent of the mineral content accumulated during secondary mineralization (i.e., the only requirement for resorption is for  $TMD > TMD_0$ ). An exponential probability distribution (Eqn. 4.4) is the unique solution for a probability distribution with these properties as it is a memoryless distribution.<sup>40</sup> The average time to an event governed by an exponential probability distribution is  $1/\lambda$ .<sup>41</sup> Therefore, in Eqn. 4.4,  $1/\lambda$  is the average time to resorption. This is convenient, because the average residence time in a compartment is the reciprocal of the sum of all outflow rates ( $1/\sum k_{i,out}$ ).<sup>35</sup> Therefore, we will define  $\lambda = k_i$ . For undamaged mineralized bone,  $\lambda = k_1 + k_4$  (which represents tissue leaving the compartment due to resorption ( $k_1$ ) or by being damaged ( $k_4$ )) and for damaged mineralized bone  $\lambda = k_5$ . Notice if  $k_5 > k_1$ , resorption of  $BV_D/TV$  occurs (on average) faster than  $BV_{UD}/TV$  bone. This means that  $k_5 > k_1$  is targeted remodeling, which is important to note because targeted remodeling of damaged tissue is well established in bone turnover.<sup>42</sup>

$$P(t) = \lambda e^{-\lambda t} \quad (\text{Eqn. 4.4})$$

The average TMD within a mineralized compartment can now be defined using Eqn. 4.2, using  $m(t)$  and  $P(t)$  defined by Eqns. 4.3 and 4.4. Equation 4.5 defines the average TMD within the undamaged mineralized bone volume fraction ( $BV_{UD}/TV$ ) and Equation 4.6 describes the average TMD within the damaged mineralized bone volume fraction ( $BV_D/TV$ ). In Equation. 4.6, the  $m(t)$  profile starts at  $t = 1/k_4$  rather than at  $t = 0$ ;  $1/k_4$  is the average time tissue spends in the undamaged compartment before transferring to the damaged compartment. This time shift sets the starting TMD of tissue in the damaged compartment to the average TMD accumulated after  $1/k_4$  days in the undamaged compartment.

$$TMD_{BV_{UD}} = \int_0^{\infty} m(t)(k_1 + k_4)e^{-(k_1+k_4)t} dt = \frac{k_1+k_4}{k_1+k_4+k_m} TMD_0 + \frac{k_m}{k_1+k_4+k_m} TMD_{max} \quad (\text{Eqn. 4.5})$$

$$\text{TMD}_{\text{BV}_D} = \int_0^{\infty} m \left( t + \frac{1}{k_4} \right) k_5 e^{-k_5 t} dt = \text{TMD}_{\text{max}} + \frac{k_m e^{-\frac{k_m}{k_4}} (\text{TMD}_0 - \text{TMD}_{\text{max}})}{k_5 + k_m} \quad (\text{Eqn. 4.6})$$

Microcomputed tomography measurements of TMD do not distinguish between damaged and undamaged mineralized bone TMD values. Therefore, we need an equation to represent the average TMD within the total mineralized bone volume ( $\text{BV}_M/\text{TV}$ ; Eqn. 4.7). We calculate the average TMD of  $\text{BV}_M/\text{TV}$  as the weighted average of the TMD in the two mineralizing compartments (Eqn. 4.8;  $\text{TMD}_{\text{BV}_M}$ ).

$$\frac{\text{BV}_M}{\text{TV}} = \frac{\text{BV}_{\text{UD}}}{\text{TV}} + \frac{\text{BV}_D}{\text{TV}} \quad (\text{Eqn. 4.7})$$

$$\text{TMD}_{\text{BV}_M} = \frac{\frac{\text{BV}_{\text{UD}}}{\text{TV}}}{\frac{\text{BV}_M}{\text{TV}}} \text{TMD}_{\text{BV}_{\text{UD}}} + \frac{\frac{\text{BV}_D}{\text{TV}}}{\frac{\text{BV}_M}{\text{TV}}} \text{TMD}_{\text{BV}_D} \quad (\text{Eqn. 4.8})$$

#### 4.3.6 Relating Morphometric Data to Volume Fractions and Tissue Mineral Density

In this study, bone volume fraction (BVF), void volume fraction ( $1 - \text{BVF}$ ), and tissue mineral density (TMD) were measured via  $\mu\text{CT}$ . Bone volume fraction (BVF) defined by  $\mu\text{CT}$  distinguishes mineralized bone from void using a set mineralization threshold. The threshold selected for our data was 540 mgHA/ccm. We will assume that mineralized bone volume fraction ( $\text{BV}_M/\text{TV}$ ; Eqn. 4.7) is equal to the measured BVF (i.e.,  $\text{BV}_M/\text{TV} = \text{BVF}$ ) and that the unmineralized bone volume fraction ( $\text{BV}_{\text{UM}}/\text{TV}$ ; Eqn. 4.9) is the measured void volume fraction (i.e.,  $\text{BV}_{\text{UM}}/\text{TV} = 1 - \text{BVF}$ ). Note that in the Non-Damaged ROI,  $\text{BV}_D/\text{TV} = 0$ , so  $\text{BVF} = \text{BV}_{\text{UD}}/\text{TV}$ . The steady-state expressions for  $\text{BV}_{\text{UM}}/\text{TV}$  and  $\text{BV}_M/\text{TV}$ , in terms of the rate constants are given in Section 4.7 (Eqns. 4.7.11-12).

$$\frac{\text{BV}_{\text{UM}}}{\text{TV}} = \frac{\text{MV}}{\text{TV}} + \frac{\text{OV}}{\text{TV}} \quad (\text{Eqn. 4.9})$$

The tissue mineral density (TMD) measured via  $\mu\text{CT}$  also defines  $\text{TMD}_0$ ,  $\text{TMD}_{\text{max}}$  and each ROI's  $\text{TMD}_{\text{BV}_M}$ . The mineralization threshold sets  $\text{TMD}_0 = 540 \text{ mgHA/ccm}$  (Table 4.1) and indicates that we will consider primary mineralization complete once TMD reaches 540 mgHA/ccm. The maximum TMD

achieved during secondary mineralization ( $TMD_{max}$ ) was defined as the average peak mineralization measured in all samples (Figure 4.2). The peak TMD of each PSB was determined from the TMD histogram for the entire PSB sample, after thresholding at 540 mgHA/ccm, and was defined as 3.115 standard deviations from the histogram's mean TMD.<sup>43</sup> In our samples,  $TMD_{max} = 1163.7$  mgHA/ccm (Table 4.2). In both the Non-Damaged and Damaged ROIs (Figure 4.2), we set  $TMD_{BVM}$  (Eqn. 4.8) to the value measured by  $\mu$ CT in each ROI.

The  $\mu$ CT measure of mineralized volume fraction ( $BV_M/TV$ ) cannot distinguish between damaged and undamaged mineralized volume fractions. Therefore, we used basic fuchsin stained histology sections to define the damaged volume fraction ( $BV_D/TV$ ). Specifically, we define  $BV_D/TV$  as the area fraction of stained microcracks (Cr.Af) observed in our ROIs (Figure 4.4). Note that setting a volume fraction equal to an area fraction is consistent with stereology applied to histologic samples.<sup>44</sup> The area diffusely stained with basic fuchsin was not included in  $BV_D/TV$ , as we did not determine if the diffuse staining was due to diffuse microdamage or tissue with a low mineral density. The undamaged bone volume fraction ( $BV_{UD}/TV$ ) was then determined by subtracting the damaged bone area fraction (Cr.Af) from the measured BVF (i.e.,  $BV_{UD}/TV = BVF - Cr.Af$ ).

In this study, Cr.Af was defined as the area fraction of basic fuchsin stained linear microcracks within an ROI (i.e.,  $Cr.Af = \Sigma Crack Area / ROI Area$ ). For each microcrack, stained crack area was defined as crack length multiplied by crack width. Crack length was previously determined using standard methods (see Chapter 3).<sup>23</sup> Crack width was defined as the width of the basic fuchsin halo at the midpoint of each microcrack, measured perpendicular to the crack at the midpoint. The width measurement was made using Image J.<sup>45</sup> This stain halo was identifiable on all microcracks and is a common criteria for the detection of microcracks stained with basic fuchsin.<sup>46</sup> Figure 4.4 shows the damage area fraction measured on a CLI PSB.

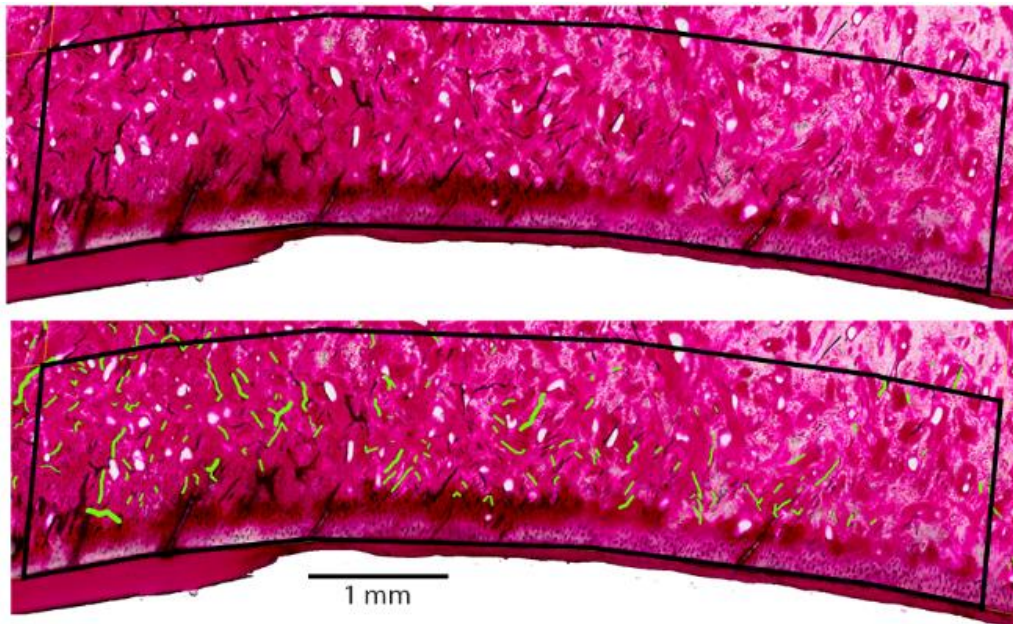


**Figure 4.4:** Top) Damaged ROI is outlined in black on a Case Contralateral Intact PSB. This region has a high microcrack density in Case PSBs, but not in Controls. Bottom) Measured microcracks are shown in green, their widths vary based on the width of the basic fuchsin halo at the crack midpoint. The damage area fraction in the area fraction of the green overlay within the Damaged ROI.

The BVF data allows us to estimate the unmineralized bone volume fraction (i.e.,  $BV_{UM}/TV = 1 - BVF$ ). However, we lacked data that could distinguish  $OV/TV$  and  $MV/TV$ . Therefore, one rate constant must be fixed among samples to solve for the remaining steady-state rate constants. We chose to select the osteoid formation rate ( $k_3$ ) to remain constant across samples.

#### 4.3.7 Selection of a Fixed Primary Mineralization Rate ( $k_3$ )

As previously described, mineralized bone tissue ( $BV_D$  or  $BV_{UD}$ ) was assumed to have completed primary mineralization. This assumption requires two processes to occur before tissue transfers out of the osteoid volume ( $OV$ ) compartment into the mineralized bone compartment ( $BV_{UD}$ ): osteoid maturation and primary mineralization. Osteoid maturation time depends on the time needed to complete the aspects of osteoid maturation (e.g., collagen crosslinking), which can depend upon animal health. For example, Vitamin D-deficiencies slow the osteoid maturation process.<sup>47</sup> Primary mineralization is assumed to occur within hours or days;<sup>4</sup> however, the exact time to complete the process is unknown.

Histologically, two terms are commonly used to define the time that osteoid remains un-mineralized: mineralization lag time (MLT) and osteoid maturation time (OMT). By definition  $OMT \leq MLT$ , but assuming that all horses in our population are healthy and that matrix maturation is the main determinant for the onset of mineralization,  $OMT = MLT$ .<sup>4,48</sup> The effects of exercise on OMT or MLT are not described in the literature. Additionally, exercise does not appear to affect the overall primary mineralization rate.<sup>37</sup> Therefore, we will assume that both osteoid maturation and primary mineralization are unaffected by mechanical loading (exercise) and that  $k_3$  was the same for all study horses.

Osteoid mineralization rate is not defined on standard lists of bone histology variables.<sup>49</sup> However, Parfitt defined osteoid mineralization rate as the inverse of MLT, so we could assume that the average time required to complete primary mineralization ( $1/k_3$ ) is included in MLT measurements (i.e.,  $k_3 = 1/MLT$ ).<sup>50</sup> To our knowledge, there are no estimates for either OMT or MLT for horses and it is unknown if this rate varies among species. However, previous work reports MLT of 26-58 days in women,<sup>50</sup> 9.5-10.7 days in female dogs,<sup>51</sup> and 1.2-1.4 days in rat.<sup>47</sup> In context of the compartment model, using  $k_3 = 1/MLT$  with these values indicates the average residence time in the osteoid volume compartment is between 1.2-58 days and  $k_3$  is between 0.03-0.83 days<sup>-1</sup>. Since we do not have a direct estimate for MLT, and therefore  $k_3$ , in horses we must make an assumption for  $k_3$  to solve for model rate constants. We will determine the minimum  $k_3$  that allows acceptable solutions (i.e., non-negative rate constants) for each Non-Damaged ROI (this need not be done in the Damaged ROI because of the solving method, outlined below). We also will test whether different assumptions of  $k_3$  (Table 4.1) change the significant correlations between the rate constants and measurements of exercise intensity.

#### **4.3.8 Determining Steady-State Rate Constants**

Steady-state rate constants were determined first in the Non-Damaged ROI and second in the Damaged ROI (Figure 4.2). Appendix A gives the two sets of steady-state volume fraction equations,



written in terms of the rate constants that will be solved in the two ROIs. These steady-state equations are different in the two ROIs, because the Non-Damaged ROI has  $BV_D/TV = 0$  which requires setting  $k_4 = k_5 = 0$  and the Damaged ROI has  $BV_D/TV > 0$ , requiring  $k_4, k_5 > 0$ . Table 4.1 summarizes the constants used to solve for steady-state rate constants in the two ROIs.

**Table 4.1:** Parameter values used to solve for rate constants.

Variable	Value (Unit)
TMD <sub>o</sub>	540 mgHA/ccm
TMD <sub>max</sub>	1163.7 mgHA/ccm
$k_M$	0.00505 days <sup>-1</sup>
$k_3$	1.024, 10, or 100 days <sup>-1</sup>

In the Non-Damaged ROI,  $TMD_{BVM}$  (Eqn. 4.8) was solved for  $k_1$  using the Non-Damaged ROI's TMD; note that this solution for  $k_1$  is independent of  $k_3$ . Then, the determined  $k_1$  value and a selected  $k_3$  were used in the steady state  $BV_{UD}/TV$  equation (Eqn 4.7.19) to determine  $k_2$ . Figure 4.5 shows the surfaces of the possible values of  $BV_{UD}/TV$ ,  $MV/TV$ , and  $OV/TV$  for the Non-Damaged region, as functions of the ratios of  $k_1/k_3$  and  $k_2/k_3$ . Since these surfaces depend *only* on the ratios  $k_1/k_3$  and  $k_2/k_3$  the exact numerical value of  $k_3$  won't change their shapes.

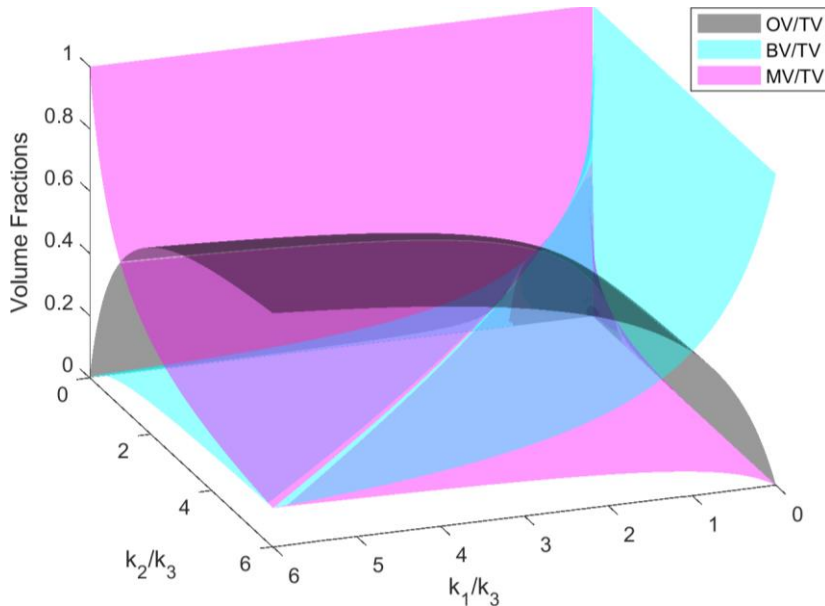


**Figure 4.5:** Volume fraction surfaces for the Non-Damaged ROI are shown in terms of rate constant ratios. The bone volume fraction (BVF) measured in the Non-Damaged ROI (Table 2) was less than 0.80 for all samples. In the Non-Damaged ROI,  $BV_D/TV = 0$  so  $BVF \equiv BV_M/TV = BV_{UD}/TV$ . So, for  $BVF < 0.80$ , this surface indicates that we must have  $k_1/k_3 < 0.50$ .

Because the direct effect of  $k_3$  magnitude on exercise regressions was unknown,  $k_2$  was solved using multiple values of  $k_3$ . First, the smallest feasible  $k_3$  (e.g., the minimum  $k_3$  that allowed for  $k_2 > 0$ ) was determined in each Non-Damaged ROI. The smallest feasible  $k_3$ s were compared among Groups (see Statistical Analysis) to check if our assumption of a fixed  $k_3$  among all horses was reasonable given our data. Second,  $k_2$  was determined for each Non-Damaged ROI using the minimum feasible value of  $k_3$  that allowed for a  $k_2 > 0$  in all Non-Damaged ROIs (this value was  $1.024 \text{ days}^{-1}$ ). Third,  $k_2$  also was determined using  $k_3 = 10$  and  $100$ . These two larger numbers were chosen because  $k_1$  was smaller than 1 for all samples and large values of  $k_3$  would guarantee that  $k_1/k_3$  solutions were within the  $BV_M/TV$  range observed in the Non-Damaged ROI (Table 4.2; Figure 4.5).

For each sample's Damaged ROI, MATLAB's non-linear least squares solver (lsqnonlin; central finite difference method) was used to solve the steady-state  $BV_{UD}/TV$  (Eqn 4.7.8),  $BV_D/TV$  (Eqn 4.7.9),  $BV_{UM}/TV$  (Eqn 4.7.12) and TMD (Eqn. 4.8) equations for  $k_1$ ,  $k_2$ ,  $k_4$ , and  $k_5$ . The lower bound for the solutions vector was set to 0, to prevent the solver from returning negative rate constants. The solver was run with 500 starting points, with  $k_4$  and  $k_5$  randomly varied between 0-100 and  $k_1$  and  $k_2$  set to the values found in the Non-Damaged ROI (MATLAB, MultiStart algorithm, 0.001 function tolerance and xtolerance). After running the multi-start optimization, the set of constants ( $k_1$ ,  $k_2$ ,  $k_4$ , and  $k_5$ ) returning the smallest root-mean-square error was selected. This solution process was performed with  $k_3 = 1.024$ , 10, or  $100 \text{ days}^{-1}$ . One CLI PSB contained zero  $BV_D/TV$  in the Damaged ROI, for this bone  $k_4 = k_5 = 0$  in the Damaged ROI and the steady-state solution for  $k_1$  and  $k_3$  from the Non-Damaged Region were used for the Damaged Region.

#### **4.3.9 Racehorse exercise data**

The date and distance for all official lifetime high-speed activities were known (Jockey Club Information Systems) for all study horses. Individual exercise Events are either considered a Race or Work (a high-speed training activity). A layup (time out of work) was defined as  $\geq 60$  days without an Event.

Exercise was characterized for the entire career and during active training periods, which excluded time periods when horses were in a layup. Sixty-seven derived variables represented four categories: lifetime exercise, exercise intensity, layup, and cumulative exercise in the year before death (see Section 3.7).<sup>12</sup>

#### **4.3.10 Statistical Analysis**

The relationships between rate constants ( $k_1$ ,  $k_2$ ,  $k_4$ ,  $k_5$ ) and calibration data (BVF, TMD, Cr.Af) from Control, Case CLI, and Case FX PSBs were determined using partial Spearman correlation coefficients ( $r$ ) with horse identity as the controlled variable. The relationships between rate constants ( $k_1$ ,  $k_2$ ,  $k_4$ ,  $k_5$ ) and exercise variables were determined using robust linear regressions (mm-method; SAS 9.4) using data from Control and Case CLI PSBs.<sup>52</sup> FX-PSB data were excluded because both the CLI and FX PSBs were from the same horses, and therefore, had the same exercise history. Additionally, a ranked analysis of variance (ANOVA) with horse set as a random variable was performed to determine the effects of Group (FX, CLI, and CTRL) and ROI (Damaged, Non-Damaged) on steady-state rate constants. Ranked ANOVA was used because the ANOVA residuals were not normally distributed ( $W < 0.90$ ). Correlation, regressions, and ANOVA were calculated separately for the Damaged and Non-Damaged ROI. For all analyses,  $p \leq 0.05$  was considered statistically significant.

Additional analyses were performed to check model assumptions. ANOVA, with horse as a random variable, was performed to determine if the smallest feasible  $k_3$  was different among Groups within the Non-Damaged region. Additionally, the Borgonovo sensitivity of  $k_1$  to  $k_m$ ,  $TMD_{ROI}$ , and  $TMD_{max}$  was determined for the Non-Damage region to assess the effects of model assumptions (Section 4.9).<sup>53,54</sup>

## 4.4 Results

The mean BVF, TMD, and Cr.Af for the Damaged and Non-Damaged ROIs are summarized in Table 4.2.<sup>23</sup>

**Table 4.2:** Least Square Means  $\pm$  Standard Error from ANOVA or Raw Means  $\pm$  Standard Deviation from ranked ANOVA<sup>†</sup> for bone volume fraction (BVF), tissue mineral density (TMD), and stained crack area fraction (Cr.Af) in each region of interest in all three study groups.<sup>23</sup>

Region of Interest	CTRL	CLI	FX
	<b>BVF<sup>†</sup></b>		
Damaged	0.98 (0.04)	0.96 (0.04)	0.90 (0.09)
Non-Damaged	0.90 (0.09)	0.97 (0.03)	0.96 (0.03)
	<b>TMD (mgHA/ccm)</b>		
Damaged	812.37 (5.79)	809.15 (5.79)	790.55 (5.79)
Non-Damaged	843.47 (5.79)	852.94 (5.79)	842.63 (5.79)
	<b>Cr.Af<sup>†</sup> (mm<sup>2</sup>/mm<sup>2</sup>)</b>		
Damaged	.003 (0.004)	.008 (0.005)	.020 (.017)
Non-Damaged	NA	NA	NA

### 4.4.1 Effect of $k_3$

Group did not have a significant effect on the smallest feasible  $k_3$  observed in the Non-Damaged ROI. In the Non-Damaged ROI, the least squares mean and standard error of the smallest feasible  $k_3$  was  $0.11 \pm 0.07 \text{ days}^{-1}$ ,  $0.24 \pm 0.07 \text{ days}^{-1}$ , and  $0.33 \pm 0.07 \text{ days}^{-1}$  for the Control, Case CLI, and Case FX groups. There was a significant pairwise difference in the smallest feasible  $k_3$  between the FXs and CTRLs. The smallest feasible  $k_3$  that allowed for  $k_2 > 0$  in all samples was  $1.024 \text{ days}^{-1}$ .

The choice of  $k_3 = 1.024, 10,$  and  $100$  did not affect the correlations between  $k_1$  and  $k_2$  with BVF and TMD in the Non-Damaged ROI. The choice of  $k_3 = 1.024, 10,$  or  $100$  did not alter the exercise variables that were significantly related to  $k_1$  (which was expected because  $k_1$  did not depend on  $k_3$ ) or  $k_2$  in the Non-Damaged ROI. However, the regressions performed with  $k_3 = 100$  tended to have higher  $r^2$  compared to those performed with  $k_3 = 1.024$  or  $10$ .

In the Damaged ROI, using  $k_3 = 1.024 \text{ days}^{-1}$  resulted in higher root-mean-square error for the predicted volume fractions compared to  $k_3$  set to  $10$  or  $100 \text{ days}^{-1}$ . Additionally,  $k_3 = 1.024$  or  $10$  resulted in one sample with  $k_5 < k_1$ ; this was undesirable as we require  $k_5 > k_1$  for targeted remodeling. With  $k_3 =$

100,  $k_5 > k_1$  for all samples. The choice of  $k_3$  did not affect the correlations among  $k_1$ ,  $k_2$ , and BVF,  $BV_D/TV$ ,  $BV_{UD}/TV$  and TMD in the Damaged ROI. However, setting  $k_3 = 1.024 \text{ days}^{-1}$  gave significant correlations between  $k_5$  and BVF, and TMD that were not present with  $k_3 = 10$  or 100 and removed a significant correlation between  $k_4$  and Cr.Af that was observed with  $k_3 = 10$  and 100. Because  $k_3 = 100$  allowed for targeted remodeling in the Damaged ROI, and  $k_3$  had a limited effect on correlations to morphologic variables in both ROIs, all remaining results use  $k_3 = 100 \text{ days}^{-1}$ .

#### 4.4.2 Group Differences among Rate Constants

The mean and standard deviation of the steady-state rate constants for both ROIs are given in Table 4.3. Group did not have a significant effect on  $k_1$ ,  $k_2$ ,  $k_4$ , or  $k_5$ . However, ROI had a significant effect on  $k_1$ ,  $k_4$ , and  $k_5$  and a marginally significant effect on  $k_2$  ( $p = 0.06$ );  $k_1$ ,  $k_2$ ,  $k_4$  and  $k_5$  were higher in the Damaged ROI compared to the Non-Damaged ROI (Table 4.3). The interaction of Group and ROI was significant for  $k_2$ . In the Damaged ROI,  $k_1 < k_5$  for all samples.

Based on the mean steady-state rate constants (Table 4.3) and  $k_3 = 100 \text{ days}^{-1}$ , the average time for one “particle” to complete the lower (non-damaging) loop (i.e.,  $\sum k_i$ ) was 5-6 months or 149 days<sup>-1</sup> for FX PSBs, 174 days<sup>-1</sup> for CLI PSBs, and 159 days<sup>-1</sup> for CTRL PSBs. Similarly, the mean time for a particle to cycle through the upper (damaging) loop is 934 days<sup>-1</sup> for FX PSBs, 1006 days<sup>-1</sup> for CLI PSBs, and 5000 days<sup>-1</sup> for CTRL PSBs.

**Table 4.3:** Summary [Mean (Standard Deviation)] of derived steady-state rate constants. A + indicates ROI was a significant effect and \* indicates the interaction of Group and ROI was significant in a ranked ANOVA. For each steady-state rate constant, values share a superscript are not statistically different at  $p < 0.05$ . These calculations were performed with  $k_3 = 100 \text{ days}^{-1}$  and other constants as defined in Table 4.1. Note that  $\text{day}^{-1}$  indicates the rate constants are measured on a “per day” basis, i.e.  $0.006 \text{ days}^{-1}$  is 0.006 per day.

		CTRL	CLI	FX
$k_1^+$ ( $\text{days}^{-1}$ )	Damaged ROI	0.0063(0.0005) <sup>A</sup>	0.0058(0.0021) <sup>A</sup>	0.0068(0.0017) <sup>A</sup>
	Non-Damaged ROI	0.0053(0.0005) <sup>B</sup>	0.0051(0.0006) <sup>B</sup>	0.005(0.001) <sup>B</sup>
$k_2^*$ ( $\text{days}^{-1}$ )	Damaged ROI	0.8872(0.7220) <sup>A</sup>	0.4534(0.5563) <sup>B</sup>	0.4816(1.189) <sup>B,C</sup>
	Non-Damaged ROI	0.1150(0.102) <sup>C</sup>	0.2380(0.1508) <sup>B</sup>	0.3360(0.3220) <sup>B</sup>
$k_4^+$ ( $\text{days}^{-1}$ )	Damaged ROI	0.0002(0.0003) <sup>B</sup>	0.001(0.0018) <sup>A</sup>	0.0011(0.0015) <sup>A</sup>
	Non-Damaged ROI	0 (0) <sup>C</sup>	0 (0) <sup>C</sup>	0 (0) <sup>C</sup>
$k_5^+$ ( $\text{days}^{-1}$ )	Damaged ROI	0.1658(0.246) <sup>A</sup>	0.2222(0.5747) <sup>A</sup>	0.0422(0.0213) <sup>A</sup>
	Non-Damaged ROI	0 (0) <sup>B</sup>	0 (0) <sup>B</sup>	0 (0) <sup>B</sup>

#### 4.4.3 Correlations among Steady-State Rate Constants and morphometric Data

In the Non-Damaged ROI,  $k_1$  was correlated to BVF ( $r = -0.42$ ) and TMD ( $r = -1$ ; Figure 4.6). However,  $k_2$  was correlated to BVF ( $r = 0.98$ ), but not TMD ( $r = 0.30$  at  $p = 0.11$ ; Figure 4.6). Further,  $k_1$  and  $k_2$  were not correlated to one another.

In the Damaged ROI,  $k_1$ , and  $k_2$ , were correlated to BVF ( $r = -0.73, 0.99$ ) and TMD ( $r = -0.84, 0.80$ ), but not to Cr.Af (Figure 4.6). In the Damaged ROI,  $k_4$  was correlated to Cr.Af ( $r = 0.83$ ; Figure 4.7) but not to BVF or TMD and  $k_5$  was not correlated to BVF, TMD, or Cr.Af. Also,  $k_1$  was negatively correlated to  $k_2$  ( $r = -0.72$ ) and  $k_5$  ( $r = -0.59$ ), but not correlated to  $k_4$ . And,  $k_4$  was positively correlated to  $k_5$  ( $r = 0.52$ ), but not correlated to either  $k_1$  or  $k_2$ .

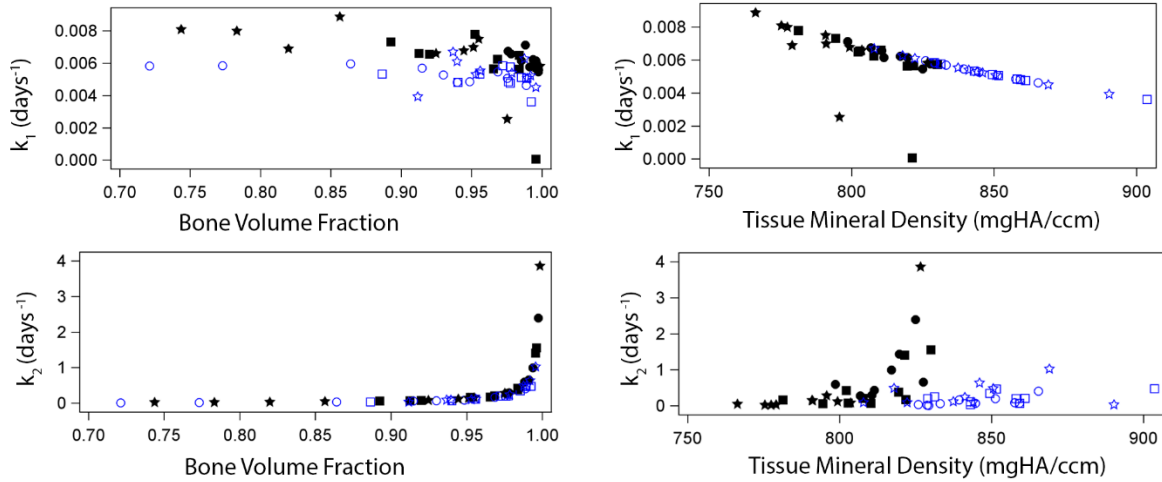


**Figure 4.6:** Non-Damaged ROI (open blue symbols) and Damaged ROI (filled black symbols) solutions for resorption rate ( $k_1$ ) and osteoid formation rate ( $k_2$ ) plotted against measured bone volume fraction and tissue mineral density. Data from FX PSB (star) CLI PSBs (square) and CTRL PSBs (circles).

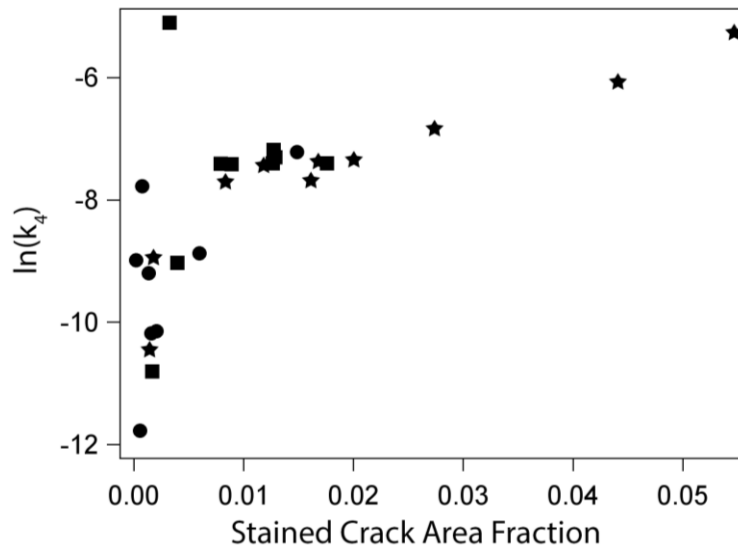


**Figure 4.7:** Damaged ROI solutions for damage formation rate ( $k_4$ ) plotted against the stained microcrack area fraction (Cr.Af). In the model,  $BV_0/TV \equiv Cr.Af$ . Data from FX PSB (star), CLI PSBs (square) and CTRL PSBs (circle) is shown. Solutions for the Non-Damaged ROI are not shown, as Cr.Af and  $k_4$  were zero in the Non-Damaged ROI.

#### 4.4.4 Regressions between Morphometric Data and Steady-State Rate Constants

The resorption rate ( $k_1$ ) tended to increase with exercise intensity in the Non-Damaged region. For example,  $k_1$  increased with exercise intensity during active training periods ( $r^2 = 0.14-0.23$ ). However, we did  $k_1$  decreased with the number of races 10 months before death ( $r^2 = 0.11$ ). In the Damaged ROI,

there were no significant relationships between exercise and  $k_1$ . We found that  $k_1$ , rather than  $\ln(k_1)$ , had larger  $r^2$  values in significant relationships to exercise variables in the Non-Damaged ROI (Table SB-4.8.1).

The relationships between osteoid formation rate ( $k_2$ ) and exercise history had different directions in the Damaged and Non-Damaged ROI (Figure 4.8 and 9; Table SB-4.8.2). In the Non-Damaged ROI,  $k_2$  increased with cumulative races 1-10 months before to death ( $r^2 = 0.17-0.23$ ), increased with career exercise intensity variables ( $r^2 = 0.17-0.20$ ), and decreased with time in layup ( $r^2 = 0.17-0.27$ ). Note that  $k_2$  did decrease in the Non-Damaged ROI with one exercise intensity variable (days between works during active training). In the Damaged ROI,  $k_2$  decreased with cumulative high-speed exercise 1-12 months before death ( $r^2 = 0.11-0.28$ ), decreased with career exercise intensity ( $r^2 = 0.15-0.22$ ), increased with time in layup ( $r^2 = 0.23$ ), and decreased with the number of days and exercise events since the last layup period ( $r^2 = 0.12-0.15$ ). In both regions, the relationships between  $\ln(k_2)$  and exercise tended to have higher  $r^2$  values than those between  $k_2$  and exercise (Table SB-4.7.2).

In the Damaged ROI, the damage formation rate ( $k_4$ ) increased with the high-speed workouts 4 months before death ( $r^2 = 0.20$ ; Figure 4.10) and  $\ln(k_4)$  increased with time between races during active training periods ( $r^2 = 0.19$ ) and with average layup length ( $r^2 = 0.13$ ; Table SB-4.8.3). No regression relationships were observed between damage resorption rate ( $k_5$ ) or  $\ln(k_5)$  and exercise.



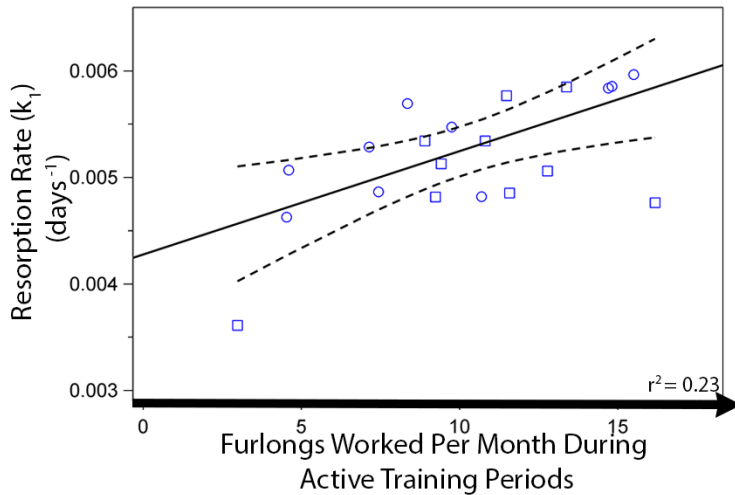


**Figure 4.8:** Robust regressions among  $k_1$  and  $k_2$  in the Non-Damaged ROI and selected exercise intensity variables, significant at  $p \leq 0.05$ ; the 95% confidence interval is shown on regressions as dashed line. The direction of increasing exercise intensity is shown by the arrow along the exercise axis. Data from CTRL PSBs (open square) and CLI PSBs (open circle) were used to construct the robust regressions. When CTRL & FX data was used to construct the regressions, the directions of the relationships shown stayed the same.

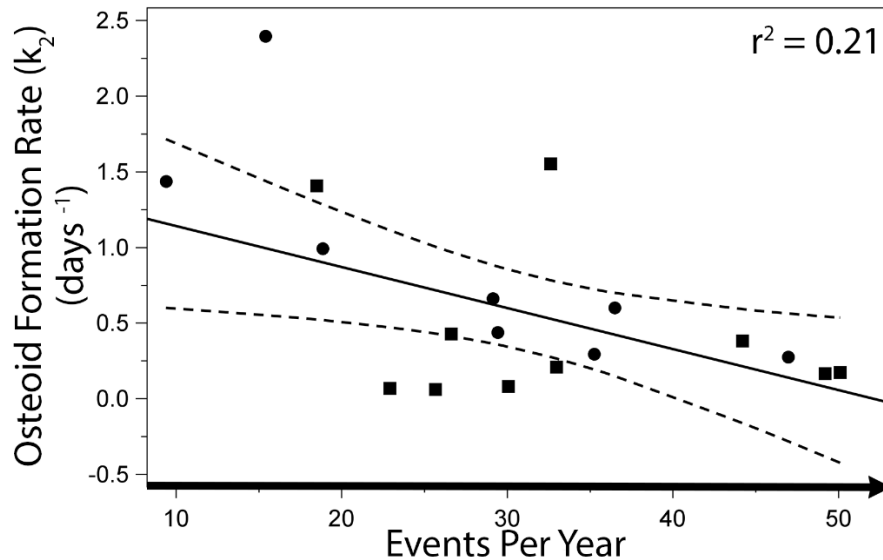
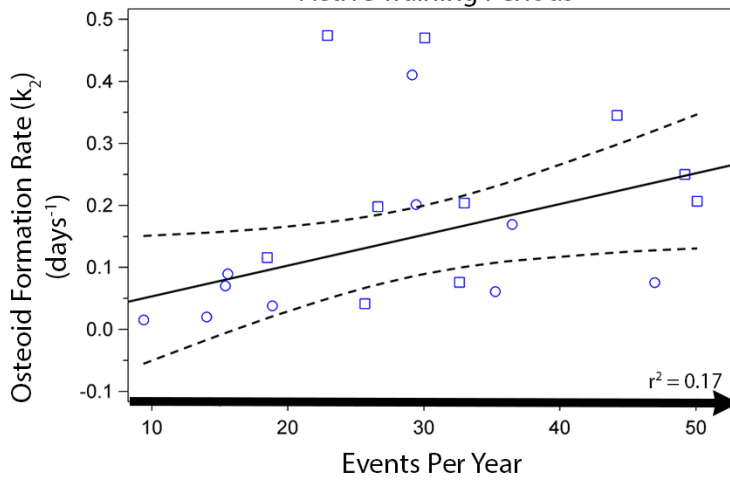


**Figure 4.9:** Robust regressions between  $k_2$  and Events Per Year in the Damaged ROI, significant at  $p \leq 0.05$ ; the 95% confidence interval is shown as dashed lines. The direction of increasing exercise intensity is shown by the arrow along the exercise axis. Data from CTRL PSBs (square) and CLI PSBs (circle) PSBs were used to construct the robust regressions. When CTRL & FX data was used to construct the regressions, the directions of the relationships shown stayed the same.

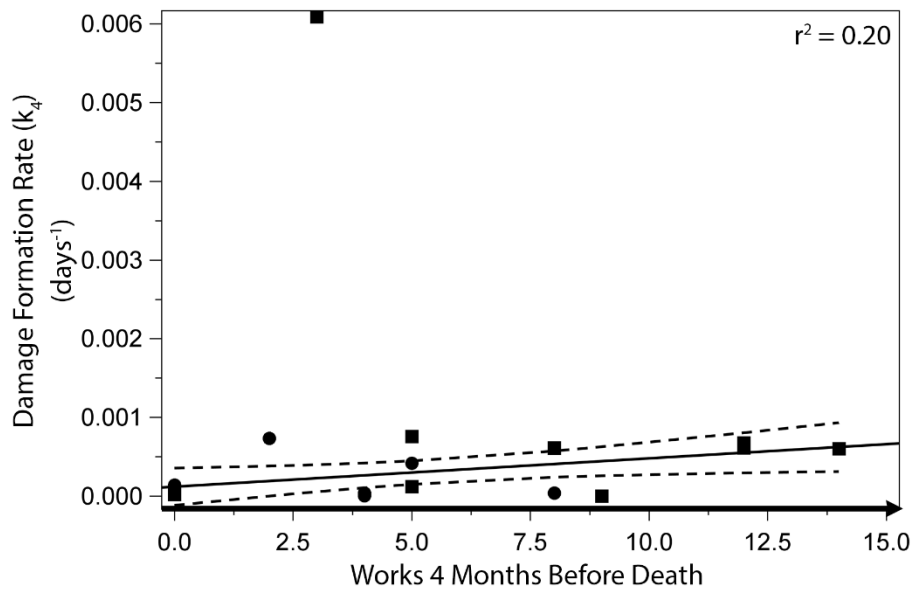


**Figure 4.10:** Significant robust regression between damage formation rate ( $k_4$ ) and cumulative works 4 months before death ( $r^2 = 0.20$ ). The 95% confidence interval is shown as dashed lines. Data from CTRL PSBs (circle) and CLI PSBs (square) were used to construct the robust regressions. The direction of increasing exercise intensity is shown by the arrow along the exercise axis. The CLI data point with a  $k_4 = 0.006$  was identified as an outlier by the robust regression procedure and was one of 3 CLIs without a subchondral lesion. When this outlier was removed from the data set, a significant regular linear regression also shows that  $k_4$  increases with works 4 months before death ( $r^2 = 0.20$ ;  $p < 0.05$ ).

## 4.5 Discussion

The primary goal of this study was to derive steady-state rates constants for the compartment model (Figure 4.1) using morphometric data from racehorse proximal sesamoid bones (PSBs). Rate constants were determined for two regions of interest within the PSBs, first in a subchondral lesion location with focal osteopenia and high levels of microdamage (Damaged ROI) and in an internal region with no microdamage (Non-Damaged ROI). We solved steady-state rate constants using bone volume fraction, tissue mineral density, and microdamage area fraction measurements from the PSBs after making assumptions about tissue mineral density and the primary mineralization rate ( $k_3$ ).

The correlations between BVF and TMD with resorption rate ( $k_1$ ) and osteoid formation rate ( $k_2$ ) indicate the solving procedure predicted steady-state rate constants from morphometric data that are consistent with model equations. The significant negative correlations observed between  $k_1$  and BVF

(remember,  $BV_M/TV \equiv BVF$ ) in both ROIs is consistent with the partial derivative of  $BV_M/TV$  taken with respect to  $k_1$ , which is always less than zero (Eqn. 4.7.14). Similarly, significant positive correlations between  $k_2$  and  $BVF$  in both ROIs is consistent with the partial derivative of  $BV_M/TV$  taken with respect to  $k_2$ , which is always greater than zero (Eqn. 4.7.14). The steady-state damage removal rates ( $k_5$ ) were greater than the resorption rate ( $k_1$ ) within the Damaged ROI. This observation is consistent with targeted removal of damaged tissue (e.g., targeted remodeling) because the average time to resorb damaged tissue ( $1/k_5$ ) is faster than for undamaged tissue ( $1/k_1$ ) when  $k_5 > k_1$ . If  $k_5 > k_1$ , an increase in  $k_4$  would cause a decrease in  $BV_M/TV$  (Eqn. 4.7.17). We did not observe a correlation between  $k_4$  and  $k_5$  with  $BVF$ .

The compartment model was constructed based on the effects that remodeling and modeling have within a volume of bone tissue. Decades of research indicate that bone's adaptation to loading is affected by strain magnitude, strain rate, changes in loading conditions from a habitual condition, and many other factors, and that bone cells target the removal of damaged tissue.<sup>14</sup> Therefore, we expected to find relationships between model rate constants and exercise (e.g., applied load). We did not find many relationships between lifetime exercise and model rate constants, however exercise intensity, layups, and exercise before death had significant relationships to resorption rate ( $k_1$ ), osteoid formation rate ( $k_2$ ) and damage removal rate ( $k_4$ ). Exercise intensity, layups, and exercise before death probably represent recent strain rate (or changes in strain rate) better than lifetime exercise variables. Therefore, in retrospect, it is not surprising that these variable types had stronger relationships to  $k_1$ ,  $k_2$ , and  $k_4$  compared to lifetime exercise. In bone, damage removal is targeted, and we could hypothesize that damage removal depends primarily on the presence of tissue damage rather than directly on exercise. This idea is consistent with our finding that the steady-state damage removal rate ( $k_5$ ) was not related to exercise, but was related to the damage formation rate ( $k_4$ ). In a dynamic model,  $k_5$  could be modeled as a constant or as an increasing function of the amount of tissue damage. A repair rate that increases with the amount of damage is consistent with increased physiological inflammation caused by greater amounts of damage. This is an

observed phenomenon in the repair of whole bone fractures and is implicated in studies of osteocyte apoptosis in laboratory microdamage studies.<sup>55</sup>

The relationships between resorption rate ( $k_1$ ) and osteoid formation rate ( $k_2$ ) with exercise history had different directions in the Damaged and Non-Damaged regions. These regional differences in the relationships to exercise are consistent with a stress-reaction to damaging loading (i.e., high strain), causing increased bone turnover and reduced bone volume fraction ( $BVF \equiv BV_M/TV$ ) within the subchondral tissue (Damaged ROI) but not within the deeper tissue (Non-Damaged ROI; Table 4.2). In the Damaged ROI we observed  $k_2$  *decreased* with exercise intensity. Conversely, in the Non-Damaged region, both  $k_1$  and  $k_2$  *increased* with exercise intensity. Previously we observed that that in the Damaged ROI,  $BVF$  *decreased* with exercise intensity and in the Non-Damaged ROI,  $BVF$  *increased* with lifetime exercise intensity.<sup>23</sup> The directions of these changes are shown in Table 4.4. Model equations predict that a decrease in  $BV_M/TV$  is associated with a decrease in  $k_2$  and an increase in  $k_1$  (Eqns. 4.7.15-16 & 4.7.19) and, if  $k_5 > k_1$ , an increase in  $k_4$  (Eqn. 4.7.17). These predictions are consistent with the relationships between observed between the model rate constants,  $BVF$  and exercise if a factor directly related to exercise had affected  $k_2$  and  $k_4$  differently in the two regions. However, the observed increase in  $k_1$  with exercise intensity is not consistent with a common exercise-related factor unless the exercise-related factor affects  $k_2$  more strongly than  $k_1$  in the Non-Damaged Region (Eqns. 4.7.15-16, 4.7.19) or that the cycle rate increases with exercise in the Non-Damaged ROI. However, we previously observed that tissue mineral density decreased with exercise intensity and that the TMD in the Non-Damaged ROI was similar among Case and Controls. Therefore, we expect that the common-exercise related factor affects  $k_2$  more strongly than  $k_1$  – however, a dynamic simulation calibrated against this data would be useful in testing this hypothesis.

**Table 4.4:** Summary of how the rate constants, mineralized bone volume fraction, and tissue mineral density changed with exercise intensity. NS indicates no significant relationships were observed.

	Resorption Rate ( $k_1$ )	Osteoid Formation Rate ( $k_2$ )	Damage Formation Rate ( $k_4$ )	BVF	TMD
Damaged ROI	NS	↓ exercise	↑ exercise	↓ exercise	↓ exercise
Non-Damaged ROI	↑ exercise	↑ exercise	N/A	↑ exercise	↓ exercise

We can hypothesize that the exercise related factor that drives the rate constants in different directions in the two regions is strain. Both ROIs experienced the same exercise intensity (because they were in the same bone of the same horse), however, there will be a mechanical strain difference between subchondral tissue (Damaged ROI) and tissue deeper to a joint surface (Non-Damaged ROI). Strain is a known driver of damage formation and bone's response to load.<sup>14</sup> So, a strain difference between the two regions is consistent with an exercise-related factor driving  $BV_M/TV$ ,  $k_1$ ,  $k_2$  in opposite directions in the two regions.

The different direction relationships between osteoid formation rate ( $k_2$ ) in the Damaged and Non-Damaged ROI could alternatively be explained by suppression of bone turnover in the subchondral tissue (i.e., reduced  $k_2$ ) with increased exercise intensity, rather than a difference in the strain states. Suppressed turnover has been proposed in the subchondral racehorse bone in high-intensity training<sup>56</sup>; however, we do not believe this is the case in our samples for multiple reasons. First, the TMD in the Damaged ROI was lower than in the Non-Damaged (Table 4.2)<sup>23</sup> implying that the tissue in the Damaged ROI is younger than in the Non-Damaged ROI.<sup>31</sup> While we were unable to track TMD changes over time in these samples, the low TMD in the Damaged ROI combined with high microdamage and low BVF is typical of a stress-reaction with active bone turnover. If bone turnover was suppressed, we would expect the tissue in the two regions to have a similar TMD (similar age). Second, if there was suppressed turnover in the subchondral region (Damaged ROI) we would expect the mean time for one sub-unit to complete the turnover cycle to be longer in Cases than in Controls as Case horses had, on average, higher intensity

training schedules. This was not observed. Instead, the mean time for any sub-unit to complete one cycle around the outer (damaged tissue) model loop was longer for Controls compared to Cases. The mean time to complete the inner loop (with no damaged tissue) was similar among Case and Control PSBs.

Damage formation rate ( $k_4$ ) increased with the number of high-speed gallop workouts 4 months before death and lifetime works (Table 4.4). Previous observations that microdamage in the subchondral tissue (Damaged ROI) is related to *4 months* of exercise before death implicates the typical time required to replace damaged tissue with new, unmineralized osteoid. Creation of a new osteon takes 4-6 months in humans, but unknown in horses. So, we tentatively conclude that damage formation rate is more strongly related to recent loading history (< 6 months) rather than to lifetime exercise. This hypothesis is consistent with our results,  $k_4$  was more strongly related to exercise 4 months before death ( $r^2 = 0.20$ ) than to lifetime works ( $r^2 = 0$ ). Further, this hypothesis is consistent with our previous work that indicates microcrack number and areal density increased with workouts 4 months prior to death ( $r^2 = 0.18, 0.29$ ) in the subchondral tissue (Damaged ROI).<sup>23</sup> Additionally, BVF was observed to decrease with cumulative exercise 2-10 months prior to death in the Damaged ROI.<sup>23</sup> An important conclusion from this work is that exercise 4-6 months prior to death is a good candidate for management by trainers to prevent formation of the subchondral stress-reaction and also to drive damage formation in a predictive dynamic simulation.

In fatigue-testing and computational stress-analysis, damage is often defined as a reduction in material modulus. Many types of damage are observed in bone tissue, including linear microcracks, diffuse damage, and microfracture of trabeculae. These damage types are associated with modulus reduction and reduced modulus.<sup>57</sup> We chose to define the damaged mineralized volume fraction ( $BV_D/TV$ ) as the stained linear microcrack area fraction. Nearly all histology sections contained bone tissue diffusely stained with basic fuchsin (Figure 4), which diffusely stains low mineral density tissue and diffuse microdamage.<sup>58,59</sup> We do not know what the diffuse stain represents in these samples, however, both low TMD and diffuse damage imply a reduced modulus in an area with diffuse stain compared to unstained

tissue.<sup>57,60</sup> Additionally, the width of the basic fuchsin halo to define crack width ( $\sim 14\mu\text{m}$ ) is larger than reported cracks widths in literature ( $\sim 4\mu\text{m}$ ).<sup>61</sup> Therefore, while our crack width definition does reflect a physical microcrack width, the crack area fraction estimate still represents a region with reduced modulus compared to undamaged tissue in a consistent manner. Further, cracks in the calcified cartilage layer that often extended into the subchondral tissue were identified in Case bones.<sup>23</sup> These cracks would also reduce subchondral tissue modulus; however, calcified cartilage cracks were not included when estimating the  $BV_D/TV$  because calcified cartilage cracks do not appear to be repaired by remodeling.<sup>62</sup> Therefore, our  $BV_D/TV$  estimate may underestimate the total amount of bone damaged bone in our samples. Regardless, a different definition of damage would have altered the estimated  $BV_D/TV$ . We expect that alternate assumptions would change the numerical values of the solutions, but not the important conclusions from the regression relationships.

In our model, we assumed bone exiting the osteoid volume (OV) compartment had completed primary mineralization. Primary mineralization is assumed to occur rapidly because many more high mineral density osteons are observed than low density osteons,<sup>4,63</sup> mineralization rate studies observe newly mineralized tissue at early time points,<sup>3,5</sup> and newly formed bone has been found to mineralize faster than quiescent bone by a factor of two.<sup>37</sup> Generally, primary mineralization is considered the accumulation of 0-70% of maximum possible mineral density and secondary mineralization accounts for 70-95% of maximum possible mineral density.<sup>4</sup> Original estimates for the percentage of mineralization completed during primary mineralization were defined with microchemical analysis of phosphorous-nitrogen ratios of whole osteons, which do not track changes over time and have a lower resolution compared to  $\mu\text{CT}$ .<sup>4,64</sup> For example, one of the original estimates reported the least dense osteons had phosphorous-nitrogen ratios  $\sim 70\%$  of the most dense osteons (i.e.,  $P/N = 2.03$  vs  $2.65$ )<sup>64</sup> and was later used to define primary mineralization to be 70% of the maximum observed  $P/N$  ratio.<sup>65</sup> The percent threshold distinguishing primary and secondary mineralization phases appears to be sensitive to both

resolution of the measurement technique and the definition of mineral content. A wider range of minimum-to-maximum mineralization density (~30-70%) is reported in studies performed at a higher resolution using radiodensity referenced to hydroxyapatite to define mineral content.<sup>66-70</sup> The average minimum-to-maximum TMD ratio for our samples was 46.4%, which is within the range reported in these studies. Additionally, bone mineral is not purely hydroxyapatite ( $\text{Ca}_{10}(\text{PO}_4)_6(\text{OH})_2$ ), but instead contains a wide variety of anionic (i.e.  $\text{CO}_3^{2-}$ ) and cationic (i.e.  $\text{Na}^+$ ) substitutions in the hydroxyapatite lattice and the mineralization rate of chemical species occurs at different rates in bone tissue.<sup>36,71</sup> So, it is entirely possible that the traditional radiodensity and histochemical reference measurements do not fully capture the primary and secondary mineralization processes. Therefore, while our threshold distinguishing primary and secondary mineralization is not at the typically stated ~70% value, we think using the observable threshold from  $\mu\text{CT}$  is appropriate to separate the two mineralization regimes.

Our compartment model could be easily integrated into dynamic finite element simulation. Finite element methods are frequently used to predict bone's response to damage and applied loads. The finite element approach allows strain distributions in bone tissue to be coupled with a mathematical theory of bone modeling and/or remodeling to predict the effect of loading and damage on bone structure. Continuum mechanics is the mathematical underpinning of the finite element method. However, bone tissue, which is filled with numerous pores, is not a continuum. To avoid violating the continuum assumptions, volumetric averages for morphologic and material properties (e.g., apparent-level modulus) are often used in finite element models of bone.<sup>72</sup> The size required for the averaging volume varies with location in the bone and is a function of the structural features of bone tissue and of the unknown stress field.<sup>73</sup> Because our compartment model is designed using volume fractions, it could easily be incorporated into a volume-averaged finite element model. Further, the exercise variables in this study could be converted into load inputs (e.g., daily applied loads) within a finite element model. Our results indicate that resorption rate ( $k_1$ ), osteoid formation rate ( $k_2$ ), and damage formation rate ( $k_4$ ) were related



to exercise. This finding implies these three rate constants should be driven by mechanical loading if the compartment model was coupled to a finite element model. Importantly, this work outlines a solving procedure that can be used to define the initial rate constants and/or volume fractions if this model were incorporated with a finite element model.

The primary study limitation was the small sample set (20 horses) and the lack of osteoid data. Because we did not measure osteoid data, we defined (rather than solved for) the osteoid formation rate ( $k_3$ ). Because osteoid formation rate is unknown (to our knowledge) in horses and there is limited evidence it is affected by mechanical loading (unlike the other rate constants in the model), it was a good candidate to assume fixed among horses. Further, our results indicate that the choice of  $k_3$  did not have a substantial effect on the correlations observed with morphometric measures or the significant relationships between  $k_1$ ,  $k_2$ , and  $k_4$  with exercise. Future research will include quantitation of osteoid content of the PSB.

In summary, we developed a compartment model of bone's tissue turnover cycle and were able to determine steady-state rate constants with observed morphological data. This solving procedure could be repeated in any bone where bone volume fraction, tissue mineral density, and an estimate for damage area (or volume) fraction is known. Additionally, we found significant relationships between the resulting steady-state model rate constants and measured exercise. These relationships were consistent with bone biology and could be used to dynamically drive the rate constants with strain (or another parameter derived from exercise) in a finite element model.

## **4.6 Acknowledgements**

This project was supported by the Grayson Jockey Club Research Foundation, Inc., the Maury Hull Fellowship (University of California Davis), the Louis R. Rowan Fellowship (California Thoroughbred Foundation), the University of California Davis Center for Equine Health (with funds provided by the State of California satellite wagering fund and contributions by private donors).

## 4.7 Supplemental Material A: Steady-State Solution for Bone Compartment

### Model

This supplemental material presents the equations for the compartment model of bone turnover given in Figure 4.1. In this model, the 4 tissue types are: undamaged mineralized bone ( $BV_{UD}$ ), damaged mineralized bone ( $BV_D$ ), osteoid ( $OV$ ), and marrow ( $MV$ ). The time derivatives of these 4 tissue types can be expressed using the rate constants ( $k_i$ ) and are given in Equations 4.7.1-4. The summation of the 4 tissue types is equal to the total tissue volume ( $TV$ ). To prevent negative volume components, all rates terms ( $k$ ) are non-negative.

$$\frac{d(BV_{UD})}{dt} = k_3 OV - (k_1 + k_4) BV_{UD} \quad (\text{Eqn. 4.7.1})$$

$$\frac{d(BV_D)}{dt} = k_4 BV_{UD} - k_5 BV_D \quad (\text{Eqn. 4.7.2})$$

$$\frac{d(OV)}{dt} = k_2 MV - k_3 OV \quad (\text{Eqn. 4.7.3})$$

$$\frac{d(MV)}{dt} = k_5 DV + k_1 BV_{UD} - k_2 OV \quad (\text{Eqn. 4.7.4})$$

At steady-state, these time derivatives are equal to zero. In matrix form, the steady-state equations are represented as:

$$\begin{bmatrix} dBV/dt \\ dMV/dt \\ dOV/dt \\ dDV/dt \end{bmatrix} = \underline{M} * \underline{X} = \begin{bmatrix} -k_1 - k_4 & 0 & k_3 & 0 \\ k_1 & -k_2 & 0 & k_5 \\ 0 & k_2 & -k_3 & 0 \\ k_4 & 0 & 0 & -k_5 \end{bmatrix} * \begin{bmatrix} BV \\ MV \\ OV \\ DV \end{bmatrix} = \begin{bmatrix} 0 \\ 0 \\ 0 \\ 0 \end{bmatrix} \quad (\text{Eqn. 4.7.5})$$

The general solution for the four tissue types is found using the null space of  $\underline{M}$ . The basis vector for this null space is  $\underline{X}'$  (Eqn. 4.7.6). The general solution is, therefore, any constant ( $B$ ) multiplied by  $\underline{X}'$ .

$$\underline{X}' = \begin{bmatrix} \frac{k_5}{k_4} \\ \frac{k_5(k_1+k_4)}{k_2 k_4} \\ \frac{k_5(k_1+k_4)}{k_3 k_4} \\ 1 \end{bmatrix} \quad (\text{Eqn. 4.7.6})$$

However, the general solution to the system of equations (Eqn. 4.7.5) is subjected to the constraints that:  $k_i \geq 0$  and  $BV_{UD} + BV_D + OV + MV = TV$  (Eqn. 4.1a). This limits the general solution to Eqn. 4.7.7a, where B is a constant that is greater than or equal to zero, and requires that  $B \cdot TV > 0$  (Eqn. 4.7.7b). This solution indicates that 1) the volumes are related to ratios of the rate constants and 2) the total tissue volume. However, the solution is indeterminate to the constant B.

$$\underline{X} = \begin{bmatrix} BV \\ MV \\ OV \\ DV \end{bmatrix} = B * \begin{bmatrix} \frac{k_5}{k_4} \\ \frac{k_5(k_1+k_4)}{k_2 k_4} \\ \frac{k_5(k_1+k_4)}{k_3 k_4} \\ 1 \end{bmatrix} \quad \text{where } B > 0, k_i \geq 0 \quad (\text{Eqn. 4.7.7a})$$

$$B * (BV_{UD} + BV_D + OV + MV) = TV > 0 \quad (\text{Eqn. 4.7.7b})$$

To eliminate the unknown constant, B, from the equations, we will divide the general solution for the volumes (Eqn. 4.7.7a) by the tissue volume (Eqn. 4.7.7b). This results in four volume fractions (Eqn. 4.7.8 –11) that are independent of the constant B and that only depend on the *ratios* of the rate constants.

$$\frac{BV_{UD}}{TV} = \frac{k_2 k_3 k_5}{k_1 k_2 k_5 + k_1 k_3 k_5 + k_2 k_3 k_4 + k_2 k_3 k_5 + k_2 k_4 k_5 + k_3 k_4 k_5} \quad (\text{Eqn. 4.7.8})$$

$$\frac{BV_D}{TV} = \frac{k_2 k_3 k_4}{k_1 k_2 k_5 + k_1 k_3 k_5 + k_2 k_3 k_4 + k_2 k_3 k_5 + k_2 k_4 k_5 + k_3 k_4 k_5} \quad (\text{Eqn. 4.7.9})$$

$$\frac{OV}{TV} = \frac{k_2 k_5 (k_1 + k_4)}{k_1 k_2 k_5 + k_1 k_3 k_5 + k_2 k_3 k_4 + k_2 k_3 k_5 + k_2 k_4 k_5 + k_3 k_4 k_5} \quad (\text{Eqn. 4.7.10})$$

$$\frac{MV}{TV} = \frac{k_3 k_5 (k_1 + k_4)}{k_1 k_2 k_5 + k_1 k_3 k_5 + k_2 k_3 k_4 + k_2 k_3 k_5 + k_2 k_4 k_5 + k_3 k_4 k_5} \quad (\text{Eqn. 4.7.11})$$

The steady-state mineralized bone volume fraction (Eqn. 4.7.12) and unmineralized volume fraction (Eqn. 4.7.13) are also shown.

$$\frac{BV_{UM}}{TV} = \frac{k_5(k_2+k_3)(k_1+k_4)}{k_1k_2k_5+k_1k_3k_5+k_2k_3k_4+k_2k_3k_5+k_2k_4k_5+k_3k_4k_5} \quad (\text{Eqn. 4.7.12})$$

$$\frac{BV_M}{TV} = \frac{k_2k_3(k_5+k_4)}{k_1k_2k_5+k_1k_3k_5+k_2k_3k_4+k_2k_3k_5+k_2k_4k_5+k_3k_4k_5} \quad (\text{Eqn. 4.7.13})$$

The partial derivatives of the mineralized bone volume fraction (Eqn. 4.7.13) with respect to the rate constants are given below (Eqn. 4.7.14-18).

$$\frac{\partial(\frac{BV_M}{TV})}{\partial k_1} = -\frac{k_2k_3k_5(k_2+k_3)(k_4+k_5)}{(k_1k_2k_5+k_1k_3k_5+k_2k_3k_4+k_2k_3k_5+k_2k_4k_5+k_3k_4k_5)^2} \quad (\text{Eqn. 4.7.14})$$

$$\frac{\partial(\frac{BV_M}{TV})}{\partial k_2} = \frac{k_3^2k_5(k_1+k_4)(k_4+k_5)}{(k_1k_2k_5+k_1k_3k_5+k_2k_3k_4+k_2k_3k_5+k_2k_4k_5+k_3k_4k_5)^2} \quad (\text{Eqn. 4.7.15})$$

$$\frac{\partial(\frac{BV_M}{TV})}{\partial k_3} = \frac{k_2^2k_5(k_1+k_4)(k_4+k_5)}{(k_1k_2k_5+k_1k_3k_5+k_2k_3k_4+k_2k_3k_5+k_2k_4k_5+k_3k_4k_5)^2} \quad (\text{Eqn. 4.7.16})$$

$$\frac{\partial(\frac{BV_M}{TV})}{\partial k_4} = \frac{k_2k_3k_5(k_2+k_3)(k_1-k_5)}{(k_1k_2k_5+k_1k_3k_5+k_2k_3k_4+k_2k_3k_5+k_2k_4k_5+k_3k_4k_5)^2} \quad (\text{Eqn. 4.7.17})$$

$$\frac{\partial(\frac{BV_M}{TV})}{\partial k_5} = -\frac{k_2k_3k_4(k_1+k_4)(k_2+k_3)}{(k_1k_2k_5+k_1k_3k_5+k_2k_3k_4+k_2k_3k_5+k_2k_4k_5+k_3k_4k_5)^2} \quad (\text{Eqn. 4.7.18})$$

If no damage is present in a region, then the damaged mineralized bone compartment contains no tissue. At steady state, this indicates that both  $k_4$  and  $k_5$  are equal to zero. The steady-state solution for the volume fractions is then Equations 4.7.19-21. The steady-state equation for unmineralized bone volume fraction in a region without damage is shown in Eqn. 4.7.22.

$$\frac{BV_{UD}}{TV} = \frac{k_2k_3}{k_1k_2+k_1k_3+k_2k_3} \quad (\text{Eqn. 4.7.19})$$

$$\frac{OV}{TV} = \frac{k_1k_3}{k_1k_2+k_1k_3+k_2k_3} \quad (\text{Eqn. 4.7.20})$$

$$\frac{MV}{TV} = \frac{k_1 k_2}{k_1 k_2 + k_1 k_3 + k_2 k_3} \quad (\text{Eqn. 4.7.21})$$

$$\frac{BV_{UM}}{TV} = \frac{k_1 k_2 + k_1 k_3}{k_1 k_2 + k_1 k_3 + k_2 k_3} \quad (\text{Eqn. 4.7.22})$$

The partial derivatives of the mineralized bone volume fraction in a region without damaged (Eqn. 4.7.19) with respect to the steady state rate constants are shown in Equations 4.7.23-25.

$$\frac{\partial BV_{UD}}{\partial k_1} = -\frac{k_2 k_3 (k_2 + k_3)}{(k_1 k_2 + k_1 k_3 + k_2 k_3)^2} \quad (\text{Eqn. 4.7.23})$$

$$\frac{\partial BV_{UD}}{\partial k_2} = \frac{k_1 k_3^2}{(k_1 k_2 + k_1 k_3 + k_2 k_3)^2} \quad (\text{Eqn. 4.7.24})$$

$$\frac{\partial BV_{UD}}{\partial k_3} = \frac{k_1 k_2^2}{(k_1 k_2 + k_1 k_3 + k_2 k_3)^2} \quad (\text{Eqn. 4.7.25})$$

## 4.8 Supplementary Material B: Exercise History Regressions

**Table SB-4.8.1:** Robust linear regressions results [Slope ( $R^2$ )] between  $k_1$  or  $\ln(k_1)$  and exercise variables. Regressions were performed separately in the Damaged and Non-Damaged regions of interest (ROI). All reported results were significant at  $p \leq 0.05$ . Note that: Events include all official timed workouts (works) and races. Layup is defined as 60 or more days when a horse had no official events and active periods exclude times when a horse was in layup.<sup>12</sup> Furlongs are 1/8 mile (220 yards) and are a standard measurement unit used in horse racing.

Exercise Variable		Damaged ROI		Non-Damaged ROI	
Type	Variable (Units)	$k_1$	$\ln(k_1)$	$k_1$	$\ln(k_1)$
Before Death	Races 10 Months Before Death (races)	.	.	-0.0001 (0.11)	.
Exercise Intensity	Days Between Events During Active Training (days)	.	.	-0.0001 (0.14)	.
	Days Between Works During Active Training (days)	.	.	-0.0001 (0.31)	.
	Events per Year during Active Training (events/yr)	.	.	0.000036 (0.16)	.
	Furlongs Worked per Month of Active Training (furlong/mo)	.	.	0.0001 (0.23)	0.0065 (0.17)
	Works Per Year of Active Training (works/yr)	.	.	0.000029 (0.18)	0.0019 (0.14)
Layup	Percent Career in Layup (%)	.	.	0.000009 (0.17)	0.0007 (0.15)

**Table SB-4.8.2:** Robust linear regressions results [Slope ( $R^2$ )] between  $k_2$  or  $\ln(k_2)$  and exercise variables. Regressions were performed in both the Damaged and Non-Damaged regions of interest (ROI). All reported results were significant at  $p \leq 0.05$ . Note that: Events include all official timed workouts (works) and races. Layup is defined as 60 or more days when a horse had no official events and active periods exclude times when a horse was in layup.<sup>12</sup> Furlongs are 1/8 mile (220 yards) and are a standard measurement unit used in horse racing.

Type	Exercise Variables Variable Name	Damaged ROI		Non-Damaged ROI	
		K2	Ln(K2)	K2	Ln(K2)
Before Death	Days between death and previous event (days)	.	.	.	-0.0049 (0.32)
	Races 1 Month Before Death (races)	.	.	0.0684 (0.17)	
	Races 6 Month Before Death (races)	.	.	0.022 (0.23)	0.0607 (0.19)
	Races 8 Month Before Death(races)	.	.	0.0189 (0.21)	.
	Races 10 Month Before Death(races)	.	.	0.0152 (0.17)	.
	Events 1 Month Before Death (events)	-0.216 (0.23)	-0.482 (0.32)	.	.
	Events 2 Months Before Death (events)	-0.131 (0.3)	-0.29 (0.41)	.	.
	Events 4 Months Before Death (events)	-0.06 (0.28)	-0.134 (0.38)	.	.
	Events 6 Months Before Death (events)	-0.042 (0.2)	-0.093 (0.31)	.	.
	Events 8 Months Before Death (events)	-0.031 (0.15)	-0.074 (0.28)	.	.
	Events 10 Months Before Death (events)	-0.026 (0.15)	-0.068 (0.31)	.	.
	Events 1 Year Before Death (events)	-0.022 (0.11)	-0.067 (0.29)	.	.
	Furlongs 1 Month Before Death (furlongs)	-0.035 (0.17)	-0.07 (0.22)	.	.
	Furlongs 2 Months Before Death (furlongs)	-0.021 (0.22)	-0.046 (0.31)	.	.
	Furlongs 4 Months Before Death (furlongs)	-0.009 (0.17)	-0.021 (0.25)	.	.
	Furlongs 10 Months Before Death (furlongs)	.	-0.01 (0.22)	.	.
	Furlongs 1 Year Before Death (furlongs)	.	-0.009 (0.19)	.	.
	Works 2 Months Before Death (works)	.	-0.207 (0.21)	.	.
	Works 4 Months Before Death (works)	-0.061 (0.2)	-0.165 (0.37)	.	.
	Works 6 Months Before Death (works)	-0.049 (0.16)	.	.	.
Works 8 Months Before Death (works)	.	-0.116 (0.32)	.	.	
Works 10 Months Before Death (furlongs)	.	-0.094 (0.32)	.	.	
Works 1 Year Before Death (furlongs)	.	-0.083 (0.26)	.	.	
Exercise Intensity	Days Between Events (days)	.	0.069 (0.26)	-0.0071 (0.19)	-0.0356 (0.38)
	Days Between Works During Active Training (days)	.	.	0.0108 (0.26)	
	Days Between Works (days)	0.035 (0.15)	0.073 (0.29)		
	Events per Year during Active Training (events/yr)				
	Events per Year (events/yr)	-0.027 (0.22)	-0.051 (0.26)	0.0047 (0.17)	0.0189 (0.21)
	Furlong per Month (furlong/mo)	-0.07 (0.19)	-0.125 (0.21)	0.0149 (0.2)	0.058 (0.25)
	Furlongs Raced per Month (furlong/mo)			0.0239 (0.19)	
	Furlongs Worked per Month (furlong/mo)	.	-0.182 (0.24)		
	Races per year (races/yr)			0.0129 (0.19)	
	Works per year (works/yr)	.	-0.049 (0.19)		
Layup	Days since last layup (days)	-0.002 (0.12)	-0.005 (0.3)		
	Events Since Last Layup (events)	-0.018 (0.15)	-0.055 (0.32)		
	Number of Layups (layup)	.	.	-0.0498 (0.21)	-0.2095 (0.32)
	Total Time in Layup (days)	.	0.003 (0.19)		
	Average Layup Length (days)	.	0.006 (0.18)	-0.0006 (0.17)	
Lifetime	Percent Career in Layup (%)	0.012 (0.23)	0.022 (0.22)	-0.0028 (0.27)	-0.0128 (0.45)
	Age (years)	.	0.749 (0.04)		

**Table SB-4.8.3:** Robust linear regressions results [Slope ( $R^2$ )] between  $k_4$  and  $\ln(k_4)$  and exercise variables. All reported results were significant at  $p \leq 0.05$ . Note that: Events include all official timed workouts (works) and races. Layup is defined as 60 or more days when a horse had no official events and active periods exclude times when a horse was in layup.<sup>12</sup> Furlongs are 1/8 mile (220 yards) and are a standard measurement unit used in horse racing.

Exercise Variables		Damaged ROI	
Type	Variable Name	$k_4$	$\ln(k_4)$
Lifetime	Active Days (days)	.	.
	Career Days (days)	.	.
	Number of Works (works)	0.000012 (0)	.
	Number of Events (events)	.	.
Layup	Average Layup Length (days)	.	0.008 (0.13)
Exercise Intensity	Days Between Races During Active Training (days)	.	0.088 (0.19)
	Events Per Year of Active Training (events/yr)	.	.
	Furlongs Per Work (furs/work)	.	.
	Furlongs Per Event (furs/event)	.	.
Exercise Before Death	Works 4 Months Before Death (works)	0.000036 (0.20)	.



## 4.9 Supplementary Material C: Sensitivity of $k_1$ to Input Distributions in Non-Damaged ROI

Borgonovo sensitivity analysis indicated that the output distribution of  $k_1$  in the Non-Damaged ROI (from Eqn. 4.8) was most sensitive to  $k_m$ , followed by  $TMD_{ROI}$ , and then  $TMD_{max}$ . For these calculations,  $TMD_o$  was fixed to 540 mgHA/ccm because we did not have a distribution for the value.  $TMD_{ROI}$  modeled as a Gaussian distribution with mean and standard deviation of the TMD measured in the Non-Damaged Region in all PSBs:  $846.34 \pm 20.14$  mgHA/ccm.  $TMD_{max}$  was modeled as a Gaussian distribution with mean and standard deviation of the maximum TMD measured in all PSBs:  $1163.70 \pm 21.27$  mgHA/ccm. Mineralization rate ( $k_m$ ) was modeled as a Gaussian distribution using curve-fits of Eqn.4 data from cortical and cancellous sheep bone with a mean and standard deviation of  $0.00505 \pm 0.0009$  days<sup>-1</sup>.<sup>2</sup> Mineralization rate was also modeled as a Gaussian or uniform random distribution using curve-fits of Eqn.4 data from young rats,<sup>36</sup> rabbits,<sup>3</sup> and sheep<sup>2</sup> (mean: 0.31 days<sup>-1</sup>, standard deviation: 0.61 days<sup>-1</sup>). Regardless of the  $k_m$  distribution, the output distribution of  $k_1$  was most affected by the distribution of  $k_m$ , and less affected by the distributions of  $TMD_{ROI}$  and  $TMD_{max}$ .

## 4.10 References

1. Martin RB, Gibson VA, Stover SM, et al. 1997. Residual strength of equine bone is not reduced by intense fatigue loading: Implications for stress fracture. *J. Biomech.* 30(2):109–114.
2. Bala Y, Farlay D, Delmas PD, et al. 2010. Time sequence of secondary mineralization and microhardness in cortical and cancellous bone from ewes. *Bone* 46(4):1204–1212 Available from: <http://dx.doi.org/10.1016/j.bone.2009.11.032>.
3. Fuchs RK, Allen MR, Ruppel ME, et al. 2008. In situ examination of the time-course for secondary mineralization of Haversian bone using synchrotron Fourier transform infrared microspectroscopy. *Matrix Biol.* 27(1):34–41 Available from: <https://linkinghub.elsevier.com/retrieve/pii/S0945053X07001060>.
4. Parfitt AM. 1983. The Physiologic and Clinical Significance of Bone Histomorphometric Data. In: Recker RR, editor. *Bone histomorphometry : techniques and interpretation.* p 143–224.
5. Marotti G, Favia A, Zallone AZ. 1972. Quantitative analysis on the rate of secondary bone mineralization. *Calcif. Tissue Res.* 10(1):67–81 Available from: <http://link.springer.com/10.1007/BF02012537>.
6. Hernandez CJ, Gupta A, Keaveny TM. 2006. A Biomechanical Analysis of the Effects of Resorption Cavities on Cancellous Bone Strength. *J. Bone Miner. Res.* 21(8):1248–1255 Available from: <http://doi.wiley.com/10.1359/jbmr.060514>.
7. Slyfield CR, Tkachenko EV, Fischer SE, et al. 2012. Mechanical failure begins preferentially near resorption cavities in human vertebral cancellous bone under compression. *Bone* 50(6):1281–1287 Available from: <https://linkinghub.elsevier.com/retrieve/pii/S8756328212007156>.
8. Riggs CM. 2002. Fractures - A preventable hazard of racing thoroughbreds? *Vet. J.* 163(1):19–29.
9. Stover SM, Johnson BJ, Daft BM, et al. 1992. An association between complete and incomplete stress fractures of the humerus in race horses. *Equine Vet. J.* 24:260–263.
10. Stover SM. 2003. The Epidemiology of Thoroughbred Racehorse Injuries. *Clin. Tech. Equine Pract.* 2(4):312–322.
11. Riggs CM, Whitehouse GH, Boyde A. 1999. Pathology of the distal condyles of the third metacarpal and third metatarsal bones of the horse. *Equine Vet. J.* 31(2):140–148 Available from: <http://doi.wiley.com/10.1111/j.2042-3306.1999.tb03803.x>.
12. Anthenill LA, Stover SM, Gardner IA, Hill AE. 2007. Risk factors for proximal sesamoid bone fractures associated with exercise history and horseshoe characteristics in Thoroughbred racehorses. *Am. J. Vet. Res.* 68(7):760–771 Available from: <http://avmajournals.avma.org/doi/abs/10.2460/ajvr.68.7.760>.
13. Thompson K. 2007. Bones and Joints. In: Maxie MG, editor. *Jubb, Kennedy, and Palmer's Pathology of Domestic Animals; Volume 1, 5th ed.* Elsevier. p 1–185.
14. Robling AG, Castillo AB, Turner CH. 2006. Biomechanical and Molecular Regulation of Bone Remodeling. *Annu. Rev. Biomed. Eng.* 8(1):455–498 Available from:

<http://www.annualreviews.org/doi/10.1146/annurev.bioeng.8.061505.095721>.

15. Nunamaker DM, Butterweck DM, Provost MT. 1990. Fatigue fractures in thoroughbred racehorses: Relationships with age, peak bone strain, and training. *J. Orthop. Res.* 8(4):604–611 Available from: <https://onlinelibrary.wiley.com/doi/10.1002/jor.1100080417>.
16. Rubin BYCT, Lanyon LE, Rubin CT, Lanyon LE. 1982. Limb Mechanics As a Function of Speed and Gait: a Study of Functional Strains in the Radius and Tibia of Horse and Dog. *J. Exp. Biol.* 101:187–211.
17. Martin RB, Stover SM, Gibson VA, et al. 1996. In vitro fatigue behavior of the equine third metacarpus: Remodeling and microcrack damage analysis. *J. Orthop. Res.* 14(5):794–801.
18. Stover SM. 2013. Diagnostic Workup of Upper-Limb Stress Fractures and Proximal Sesamoid Bone Stress Remodeling. In: *AAEP Proceedings; In-Depth: Racing-Related Lameness*. p 427–435.
19. Shaffer SK, To C, Garcia TC, et al. 2021. Subchondral focal osteopenia associated with proximal sesamoid bone fracture in Thoroughbred racehorses. *Equine Vet. J.* 53(2):294–305 Available from: <https://onlinelibrary.wiley.com/doi/abs/10.1111/evj.13291>.
20. Matcuk GR, Mahanty SR, Skalski MR, et al. 2016. Stress fractures: pathophysiology, clinical presentation, imaging features, and treatment options. *Emerg. Radiol.* 23(4):365–375. Available from: <http://dx.doi.org/10.1007/s10140-016-1390-5>.
21. Martig S, Chen W, Lee PVS, Whitton RC. 2014. Bone fatigue and its implications for injuries in racehorses. *Equine Vet. J.* 46(4):408–415.
22. Hill AE, Gardner IA, Carpenter TE, Stover SM. 2004. Effects of injury to the suspensory apparatus, exercise, and horseshoe characteristics on the risk of lateral condylar fracture and suspensory apparatus failure in forelimbs of Thoroughbred racehorses. *Am. J. Vet. Res.* 65(11):1508–1517.
23. Shaffer, SK., Chapter 3 of Dissertation, “High-speed exercise and fetlock kinematics affect the development of stress reactions in racehorse proximal sesamoid bones.” 2021
24. Stover SM. 2015. Personal Communication.
25. Johnson BJ, Stover SM, Daft BM, et al. 1994. Causes of death in racehorses over a 2 year period. *Equine Vet. J.* 26(4):327–330 Available from: <http://doi.wiley.com/10.1111/j.2042-3306.1994.tb04395.x>.
26. Spargo KE, Rubio-Martinez LM, Wheeler DP, et al. 2019. Catastrophic musculoskeletal injuries in Thoroughbred racehorses on racetracks in Gauteng, South Africa. *J. S. Afr. Vet. Assoc.* 90:1019–9128 Available from: <https://journals.jsava.aosis.co.za/index.php/jsava/article/view/1640>.
27. Sun TC, Riggs CM, Cogger N, et al. 2019. Noncatastrophic and catastrophic fractures in racing Thoroughbreds at the Hong Kong Jockey Club. *Equine Vet. J.* 51(1):77–82 Available from: <https://onlinelibrary.wiley.com/doi/10.1111/evj.12953>.
28. Anthenill LA, Stover SM, Gardner IA, et al. 2006. Association between findings on palmarodorsal radiographic images and detection of a fracture in the proximal sesamoid bones of forelimbs obtained from cadavers of racing Thoroughbreds. *Am. J. Vet. Res.* 67(5):858–868 Available from: <http://avmajournals.avma.org/doi/abs/10.2460/ajvr.67.5.858>.
29. Jacquez JA, Simon CP. 1993. Qualitative theory of compartmental systems. *SIAM Rev.* 35(1):43–

- 79.
30. Hearon JZ. 1963. THEOREMS ON LINEAR SYSTEMS\*. *Ann. N. Y. Acad. Sci.* 108(1):36–68 Available from: <https://onlinelibrary.wiley.com/doi/10.1111/j.1749-6632.1963.tb13364.x>.
  31. Grynblas M. 1993. Age and disease-related changes in the mineral of bone. *Calcif. Tissue Int.* 53(1 Supplement).
  32. Boivin G, Farlay D, Bala Y, et al. 2009. Influence of remodeling on the mineralization of bone tissue. *Osteoporos. Int.* 20(6):1023–1026 Available from: <http://link.springer.com/10.1007/s00198-009-0861-x>.
  33. Donnelly E, Boskey AL, Baker SP, van der Meulen MCH. 2009. Effects of tissue age on bone tissue material composition and nanomechanical properties in the rat cortex. *J. Biomed. Mater. Res. Part A* 9999A(3):NA-NA Available from: <https://onlinelibrary.wiley.com/doi/10.1002/jbm.a.32442>.
  34. Goodson DZ. 2011. Probability Distribution Functions. In: *Mathematical Methods for Physical and Analytical Chemistry*. Hoboken, NJ: Wiley. p 111–121.
  35. Yu J, Wehrly TE. 2004. An approach to the residence time distribution for stochastic multi-compartment models. *Math. Biosci.* 191(2):185–205.
  36. Wergedal J, Baylink D. 1974. Electron microprobe measurements of bone mineralization rate in vivo. *Am. J. Physiol.* Content 226(2):345–352 Available from: <https://www.physiology.org/doi/10.1152/ajplegacy.1974.226.2.345>.
  37. Lukas C, Ruffoni D, Lambers FM, et al. 2013. Mineralization kinetics in murine trabecular bone quantified by time-lapsed in vivo micro-computed tomography. *Bone* 56(1):55–60 Available from: <http://dx.doi.org/10.1016/j.bone.2013.05.005>.
  38. Aruwajoye OO, Patel MK, Allen MR, et al. 2013. Microcrack density and nanomechanical properties in the subchondral region of the immature piglet femoral head following ischemic osteonecrosis. *Bone* 52(2):632–639 Available from: <http://dx.doi.org/10.1016/j.bone.2012.07.028>.
  39. Ruffoni D, Fratzl P, Roschger P, et al. 2007. The bone mineralization density distribution as a fingerprint of the mineralization process. *Bone* 40(5):1308–1319 Available from: <https://linkinghub.elsevier.com/retrieve/pii/S8756328207000373>.
  40. Leemis LM, Mcqueston JT. 2008. Univariate Distribution Relationships. *Am. Stat.* 62(1):45–53 Available from: <https://www.jstor.org/stable/10.2307/2986561?origin=crossref>.
  41. Jowett GH. 1958. The Exponential Distribution and Its Applications. *Inc. Stat.* 8(2):89 Available from: <https://www.jstor.org/stable/10.2307/2986561?origin=crossref>.
  42. Bentolila V, Boyce TM, Fyhrie DP, et al. 1998. Intracortical remodeling in adult rat long bones after fatigue loading. *Bone* 23(3):275–281.
  43. Hansen A. 2020. The Three Extreme Value Distributions: An Introductory Review. *Front. Phys.* 8(December):1–8 Available from: <https://www.frontiersin.org/articles/10.3389/fphy.2020.604053/full>.
  44. Russ JC. 1986. *Practical Stereology*. Boston, MA: Springer US. Available from:

- <http://link.springer.com/10.1007/978-1-4899-3533-5>.
45. Schneider CA, Rasband WS, Eliceiri KW. 2012. NIH Image to ImageJ: 25 years of image analysis. *Nat. Methods* 9(7):671–675.
  46. Lee TC, Mohsin S, Taylor D, et al. 2003. Detecting microdamage in bone. *J. Anat.* 203(2):161–172.
  47. Baylink D, Stauffer M, Wergedal J, Rich C. 1970. Formation, mineralization, and resorption of bone in vitamin D—deficient rats. *J. Clin. Invest.* 49(6):1122–1134 Available from: <http://www.jci.org/articles/view/106328>.
  48. Parfitt MA, Drezner MK, Glorieux FH, et al. 1987. Bone Histomorphometry : Standardization of Nomenclature, Symbols, and Units. *J. Bone Miner. Res.* 2(6):595–610.
  49. Dempster DW, Compston JE, Drezner MK, et al. 2013. Standardized nomenclature, symbols, and units for bone histomorphometry: A 2012 update of the report of the ASBMR Histomorphometry Nomenclature Committee. *J. Bone Miner. Res.* 28(1):2–17.
  50. Parfitt AM, Han Z-H, Palnitkar S, et al. 1997. Effects of Ethnicity and Age or Menopause on the Remodeling and Turnover of Iliac Bone: Implications for Mechanisms of Bone Loss. *J. Bone Miner. Res.* 12(4):498–508 Available from: <http://doi.wiley.com/10.1359/jbmr.1997.12.4.498>.
  51. High WB, Capen CC, Black HE. 1981. The effects of 1,25-dihydroxycholecalciferol, parathyroid hormone, and thyroxine on trabecular bone remodeling in adult dogs. A histomorphometric study. *Am. J. Pathol.* 105(3):279–87 Available from: <http://www.ncbi.nlm.nih.gov/pubmed/1903892>.
  52. Greco L, Luta G, Krzywinski M, Altman N. 2019. Analyzing outliers: robust methods to the rescue. *Nat. Methods* 16(4):275–276.
  53. Borgonovo E. 2007. A new uncertainty importance measure. *Reliab. Eng. Syst. Saf.* 92(6):771–784 Available from: <https://linkinghub.elsevier.com/retrieve/pii/S0951832006000883>.
  54. Marelli S, Sudret B. 2014. UQLab: A Framework for Uncertainty Quantification in Matlab. In: *Vulnerability, Uncertainty, and Risk*. Reston, VA: American Society of Civil Engineers. p 2554–2563 Available from: <http://ascelibrary.org/doi/10.1061/9780784413609.257>.
  55. Loi F, Córdova LA, Pajarinen J, et al. 2016. Inflammation, fracture and bone repair. *Bone* 86:119–130.
  56. Whitton RC, Trope GD, Ghasem-Zadeh A, et al. 2010. Third metacarpal condylar fatigue fractures in equine athletes occur within previously modelled subchondral bone. *Bone* 47(4):826–831 Available from: <http://dx.doi.org/10.1016/j.bone.2010.07.019>.
  57. Hernandez CJ, Lambers FM, Widjaja J, et al. 2014. Quantitative relationships between microdamage and cancellous bone strength and stiffness. *Bone* 66:205–213 Available from: <http://dx.doi.org/10.1016/j.bone.2014.05.023>.
  58. Boyce TM, Fyhrie DP, Glotkowski MC, et al. 1998. Damage type and strain mode associations in human compact bone bending fatigue. *J. Orthop. Res.* 16(3):322–329.
  59. Burr DB, Hooser M. 1995. Alterations to the en bloc basic fuchsin staining protocol for the demonstration of microdamage produced in vivo. *Bone* 17(4):431–433.

60. Keller TS, Carter DR, Hernandez CJ, Beaupre GS. 2001. The Influence of Bone Volume Fraction and Ash Fraction on Bone Strength and Modulus. *J Biomech*. 29(1):74–78.
61. Larrue A, Rattner A, Peter Z-A, et al. 2011. Synchrotron Radiation Micro-CT at the Micrometer Scale for the Analysis of the Three-Dimensional Morphology of Microcracks in Human Trabecular Bone. *PLoS One* 6(7):e21297 Available from: <https://dx.plos.org/10.1371/journal.pone.0021297>.
62. Oegema TR, Carpenter RJ, Hofmeister F, Thompson RC. 1997. The interaction of the zone of calcified cartilage and subchondral bone in osteoarthritis. *Microsc. Res. Tech.* 37(4):324–332 Available from: [https://onlinelibrary.wiley.com/doi/10.1002/\(SICI\)1097-0029\(19970515\)37:4%3C324::AID-JEMT7%3E3.O.CO;2-K](https://onlinelibrary.wiley.com/doi/10.1002/(SICI)1097-0029(19970515)37:4%3C324::AID-JEMT7%3E3.O.CO;2-K).
63. Amprino R, Engström A. 1952. STUDIES ON X RAY ABSORPTION AND DIFFRACTION OF BONE TISSUE. *Cells Tissues Organs* 15(1–2):1–22 Available from: <https://www.karger.com/Article/FullText/140734>.
64. Strandh J. 1960. Microchemical studies on single Haversian systems. *Exp. Cell Res.* 21(2):406–413 Available from: <https://linkinghub.elsevier.com/retrieve/pii/001448276090272X>.
65. Parfitt AM. 1976. The actions of parathyroid hormone on bone: Relation to bone remodeling and turnover, calcium homeostasis, and metabolic bone disease. *Metabolism* 25(7):809–844 Available from: <https://linkinghub.elsevier.com/retrieve/pii/0026049576901517>.
66. Boivin G, Meunier PJ. 2002. The Degree of Mineralization of Bone Tissue Measured by Computerized Quantitative Contact Microradiography. *Calcif. Tissue Int.* 70(6):503–511 Available from: <http://link.springer.com/10.1007/s00223-001-2048-0>.
67. Rowland RE, Jowsey J, Marshall JH. 1959. Microscopic Metabolism of Calcium in Bone: III. Microradiographic Measurements of Mineral Density. *Radiat. Res.* 10(2):234 Available from: <https://www.jstor.org/stable/3570762>.
68. Renders GAP, Mulder L, Van Ruijven LJ, Van Eijden TMGJ. 2006. Degree and distribution of mineralization in the human mandibular condyle. *Calcif. Tissue Int.* 79(3):190–196.
69. Nuzzo S, Peyrin F, Cloetens P, et al. 2002. Quantification of the degree of mineralization of bone in three dimensions using synchrotron radiation microtomography. *Med. Phys.* 29(11):2672–2681.
70. Boivin G, Meunier PJ. 2003. Methodological considerations in measurement of bone mineral content. *Osteoporos. Int.* 14:22–28 Available from: <http://link.springer.com/10.1007/s00198-003-1469-1>.
71. Von Euw S, Wang Y, Laurent G, et al. 2019. Bone mineral: new insights into its chemical composition. *Sci. Rep.* 9(1):8456 Available from: <http://www.nature.com/articles/s41598-019-44620-6>.
72. Fyhrie DP, Schaffler MB. 1995. The Adaptation of Bone Apparent Density to Applied Load. *J. Biomech.* 28(2):135–146.
73. Harrigan TP, Jasty M, Mann RW, Harris WH. 1988. Limitations of the continuum assumption in cancellous bone. *J. Biomech.* 21(4):269–275.

## **Chapter 5: In Vitro Assessment of the Motion of Equine Proximal Sesamoid Bones Relative To The Third Metacarpal Bone Under Physiologic Midstance Loads**

### **Loads**

This chapter has been published as:

Shaffer, S.K., Sachs, N., Garcia, T.C., Fyhrie, D.P., Stover, S.M., 2021. In Vitro Assessment of the Motion of the Equine Proximal Sesamoid Bones Relative To The Third Metacarpal Bone Under Physiologic Midstance Loads. 2021. *American Journal of Veterinary Research*, 3, 198-206. DOI: 10.2460/ajvr.82.3.198

#### **5.1 Abstract**

**OBJECTIVE:** To assess the motion of the proximal sesamoid bones (PSBs) relative to the third metacarpal bone (MC3) of equine forelimbs during physiologic midstance loads.

**SAMPLE:** 8 musculoskeletally normal forelimbs (7 right and 1 left) from 8 adult equine cadavers.

**PROCEDURES:** Each forelimb was harvested at the mid-radius level and mounted in a material testing system so the hoof could be moved in a dorsal direction while the radius and MC3 remained vertical. The PSBs were instrumented with 2 linear variable differential transformers to record movement between the 2 bones. The limb was sequentially loaded at a displacement rate of 5 mm/s from 500 N to each of 4 loads (1.8 [standing], 3.6 [walking], 4.5 [trotting], and 10.5 [galloping] kN), held at the designated load for 30 seconds while lateromedial radiographs were obtained, and then unloaded back to 500 N. The position of the PSBs relative to the transverse ridge of the MC3 condyle and angle of the metacarpophalangeal (fetlock) joint were measured on each radiograph.

**RESULTS:** The distal edge of the PSBs moved distal to the transverse ridge of the MC3 condyle at 10.5 kN

(gallop) but not at lower loads. The palmar surfaces of the PSBs rotated away from each other during fetlock joint extension, and the amount of rotation increased with load.

**CONCLUSIONS AND CLINICAL RELEVANCE:** At loads consistent with a high-speed gallop, PSB translations may create an articular incongruity and abnormal bone stress distribution that contribute to focal subchondral bone lesions and PSB fracture in racehorses.

## 5.2 Introduction

Proximal sesamoid bone fracture is the leading reason for euthanasia of Thoroughbred racehorses in the United States.<sup>1,2</sup> In racehorses, PSB fracture is believed to be the result of an interaction between fatigue damage and stress remodeling.<sup>3</sup> Subchondral bone lesions consistent with fatigue-induced stress-remodeling are associated with transverse midbody fracture of the medial PSB. Palmar lesions have also been described in association with midbody fracture of the PSBs.<sup>4</sup> A subchondral lesion is often associated with the fracture line in the midbody of a fractured PSB. In horses with unilateral biaxial PSB fracture, a similar subchondral lesion has also been observed at the same midbody location of the nonfractured contralateral medial PSB. The focal subchondral lesion is generally located toward the medial (abaxial) aspect of a medial PSB; lateral PSBs have not been examined.<sup>5,6,a,b</sup> The characteristic focal, abaxial, subchondral lesions found at the midbody of medial PSBs with transverse fractures and described in association with some abaxial avulsion fractures of lateral PSBs suggest that an anatomic mechanism may cause high subchondral bone and transverse stresses that promote lesion development and fracture in Thoroughbred racehorses.<sup>4,6</sup>

In the forelimbs of horses, the PSBs, MC3, and P1 articulate in the metacarpophalangeal (fetlock) joint. The distal AS of the MC3 condyle has two distinct aspects: a dorsal articulation with P1 and a palmar articulation with the PSBs. The dorsal and palmar portions of the distal AS of MC3 have



different curvatures and are separated by the TR.<sup>7-9</sup> The dorsal portion of the distal AS of the MC3 condyle appears rounder (ie, has a greater curvature) than the palmar portion.<sup>8</sup> The motion of the MC3 relative to P1 is well documented at a walk, trot, canter, and gallop<sup>10-14</sup>; however, the motion of the PSBs relative to the MC3 condyle is not well documented at any gait. At low angles of fetlock joint extension, the PSBs do not appear to move distally past the TR and articulate with their congruent ASs.<sup>15</sup> However, when a horse gallops, the fetlock joint is extended to large angles,<sup>16</sup> and motion of the PSBs during extreme extension of the fetlock joint is not well understood. During high-speed galloping, the proximodorsal aspect of P1 can impinge against the dorsal aspect of MC3 proximal to the condylar AS, and that movement is beyond the articulation of P1 on the MC3.<sup>17</sup> Therefore, the PSBs are likewise expected to move beyond their normal AS with MC3 at high angles of fetlock joint extension (ie, when a horse is at a high-speed gallop). Movement of the PSBs beyond the opposing congruent AS of MC3 may alter stresses on the PSBs and cause an articular incongruity, which could contribute to the subchondral bone lesions and fracture patterns typically observed in the PSBs of Thoroughbred racehorses.

The axial borders of the medial and lateral PSBs are connected by the intersesamoidean ligament, but the 2 bones are kept separate by the wedge-shaped SR. Although not quantitatively documented, subjectively, the distal aspect of the SR appears to be wider than the proximal aspect on the palmar surface of the MC3 condyle. During extension of the fetlock joint, the asymmetry of the SR may induce relative motion (ie, distraction) between the medial and lateral PSBs. At extreme angles of fetlock joint extension, distraction between the medial and lateral PSBs might alter the stress distribution within the bones and contribute to the subchondral bone lesions observed with PSB fractures.

The purpose of the study reported here was to assess the motion of the PSBs relative to the MC3 condyle by means of in vitro biomechanical testing of cadaveric forelimbs of horses. Our goal was

to elucidate a possible mechanism for the formation of subchondral bone lesions at the abaxial portion of the midbody of medial PSBs in Thoroughbred racehorses. We hypothesized that during simulation of a high-speed gallop, the midstance load sustained by the forelimb would cause the medial and lateral PSBs to move distally beyond the TR and induce mediolateral separation of those 2 bones during extension of the fetlock joint.

## **5.3 Materials and Methods**

### **5.3.1 Sample**

Eight cadaveric forelimbs (7 left and 1 right) were obtained from 8 horses (ie, 1 forelimb was harvested from each horse) that were euthanized for reasons unrelated to forelimb dysfunction and unrelated to the study. The horses included 5 Thoroughbreds, 1 Quarter Horse, 1 Pinto, and 1 Hanoverian that ranged in age from 2 to 21 years and body weight from 373 to 564 kg. The 5 Thoroughbreds ranged in age from 2 to 7 years and body weight from 430 to 535 kg and were euthanized while in race training. The forelimbs from those horses were collected as part of the California Horse Racing Board Racing Safety Program.

Each forelimb was transected and removed from the body at the mid-radius level to ensure that the accessory (check) ligaments of the superficial and deep digital flexor tendons and the stay apparatus of the fetlock joint remained intact. The limbs were wrapped in towels soaked with saline (0.9% NaCl) solution and stored frozen at  $-20^{\circ}\text{C}$  until preparation for biomechanical testing. Each forelimb was removed from the freezer and allowed to thaw at room temperature (approx  $22^{\circ}\text{C}$ ) for 24 hours prior to biomechanical testing.

### 5.3.2 Biomechanical testing

All biomechanical tests were performed with a servohydraulic material testing system<sup>c</sup> equipped with an axial-torsional load transducer.<sup>d</sup> A translation table (405 X 400 X 40 mm) on a linear-bearing system<sup>e</sup> was mounted on the actuator so that, when the forelimb specimen was mounted in the machine and exposed to a mechanical load, the hoof could be moved in a dorsal direction while the radius and MC3 remained approximately vertical to simulate midstance conditions.<sup>17</sup>

The proximal end of each forelimb specimen was fixed (potted) in a cylinder with polymethyl methacrylate while the limb was in a standing position.<sup>17,f</sup> After potting, the PSBs were instrumented with 2 LVDTs spaced 20 mm apart.<sup>g</sup> The LVDTs were rigidly attached between the medial and lateral PSBs by means of 2 threaded rods, each of which was inserted to a standard depth into the palmar aspect of a PSB abaxial to the flexor tendons and palmar to the insertion of the suspensory ligament (Figure 5.1). The fixed ends of the LVDTs were attached to the rod in the lateral PSB, and the spring-loaded ends of the LVDTs were free to move against a smooth plate that was attached to the rod inserted in the medial PSB. Three 3-mm-diameter lead markers were inserted into the medial cortex of MC3, P1, middle phalanx, and medial PSB to assist with radiographic measurements. A 20-gauge 1-inch needle was inserted through the palmar aspect of the limb at the base of the lateral PSB to facilitate identification of that PSB on radiographic images.

The cylinder was then secured to the material testing machine, and the hoof was secured to the translation table such that the radius and MC3 were aligned parallel to the axis of loading under 500 N of axial compression.<sup>17</sup> For testing, each limb was loaded from 500 N to the target load with a 5 mm/s displacement control, held at that load for 30 seconds while lateromedial radiographs<sup>h,i</sup> were obtained, and then unloaded back to 500 N. The displacement of the LVDTs was recorded at 20 Hz for the entire loading profile. This process was sequentially repeated for target loads of 1.8, 3.6, 4.5, and 10.5 kN,

which were selected to represent the physiologic loads when a horse was standing, walking, trotting, and galloping at a high speed, respectively, as estimated on the basis of known in vivo peak vertical ground reaction forces for equine forelimbs at those postures or mid-stance of those gaits.<sup>16–20</sup>

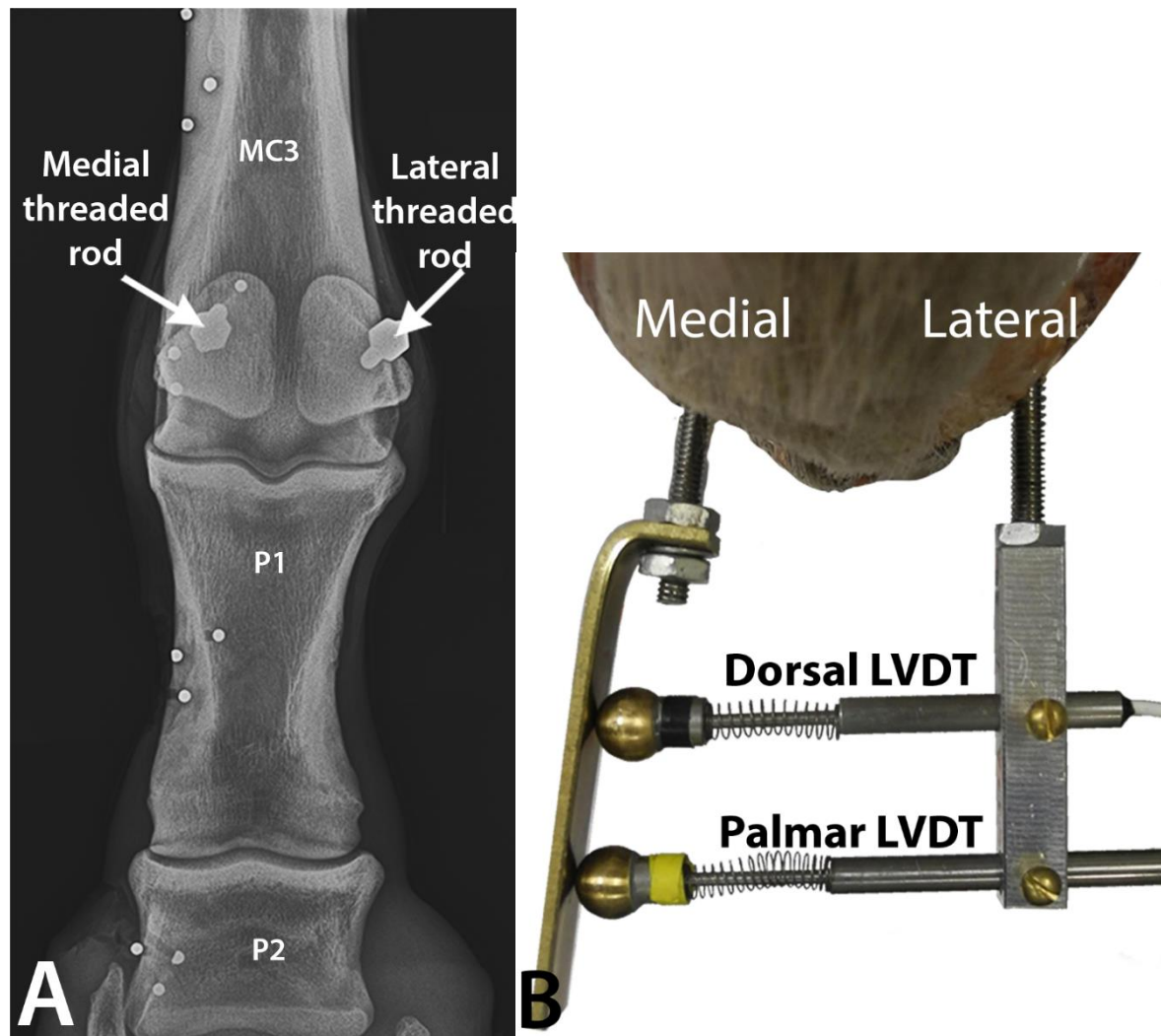


**Figure 5.1:** Dorsopalmar radiographic image (A) and photograph (B) of the metacarpophalangeal (fetlock) region of an equine cadaveric forelimb that depict placement of lead markers and instrumentation of the PSBs to facilitate data collection during biomechanical testing in an in vitro study conducted to assess the motion of the PSBs relative to the MC3 condyle under physiologic loads consistent with standing (1.8 kN) and midstance walking (3.6 kN), trotting (4.5 kN), and galloping (10.5 kN). A—Three 3-mm-diameter lead markers (small white dots) were inserted into the medial cortex of the MC3, P1, middle phalanx (P2), and medial PSB to assist with radiographic measurements. Two threaded rods that were inserted to a standard depth into the palmar aspect of the medial and lateral PSBs abaxial to the flexor tendons and palmar to the insertion of the suspensory ligament as means to instrument those bones with 2 LVDTs are also evident. B—Photograph, proximal view of the palmar aspect of the fetlock region, to depict instrumentation of the PSBs with 2 LVDTs to record movement between the 2 bones during biomechanical testing. The fixed ends of the LVDTs were attached to the rod in the lateral PSB, and the spring-loaded ends of the LVDTs were free to move against a smooth plate that was attached to the rod inserted in the medial PSB. The lateral side of the limb is to the right in both images.

### 5.3.3 Radiographic measurements

All radiographic measurements were obtained by the same investigator (NS) who was unaware of (blinded to) the load condition and horse identification. Before performing the measurements for this study, the investigator trained on 2 complete sets of radiographs. That training consisted of the investigator performing each measurement on 3 consecutive days. The coefficient of variation was less than 5% for all measurements. All radiographic measurements recorded for the study were obtained once within a 2-week period.

The fetlock angle was the palmar angle at the junction of a line through the proximodistal axis of MC3 and a line through the proximodistal axis of P1 (Figure 5.2). The MC3 and P1 axes were determined by a standard method on all radiographs.

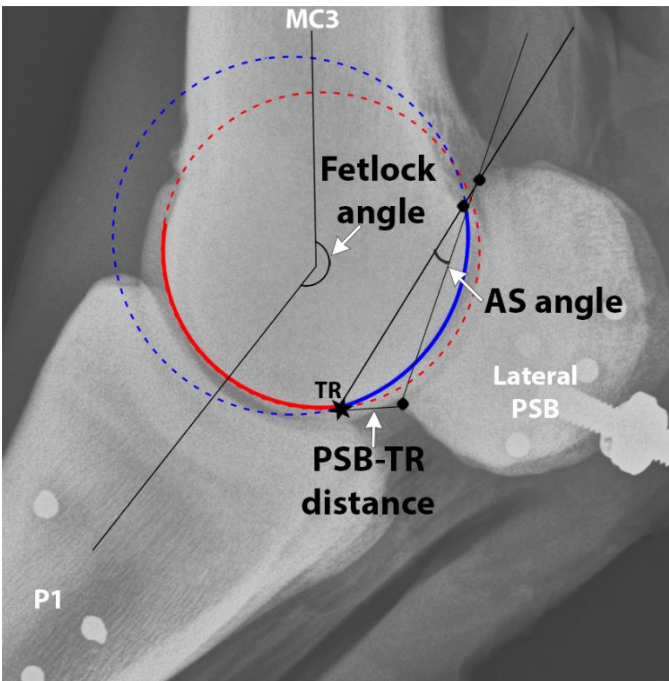


**Figure 5.2:** Lateromedial radiographic image of the fetlock region of an equine forelimb under 1.8 kN of axial compression (i.e., physiologic load consistent with standing) with annotations depicting the measurements obtained during the study described in Figure 5.1. The fetlock angle was the palmar angle at the junction of a line through the proximodistal axis of MC3 and a line through the proximodistal axis of the P1. The AS angle was the angle at the intersection of a line through the TR (star) and proximal edge of the palmar AS of the MC3 and a line through the proximal and distal edges of the AS of the lateral PSB. The PSB-TR distance was the distance between the TR and distal edge of the AS of the lateral PSB. For both AS angle and PSB-TR distance, a positive value indicated that the distal edge of the lateral PSB was proximal to the TR and a negative value indicated that the distal edge of the lateral PSB was distal to the TR. The dorsal and palmar portions of the AS of the MC3 condyle are demarcated by solid red and blue lines, respectively. The dashed red and blue circles depict the difference in curvature between the dorsal and palmar portions of the AS of the MC3 condyle.

Two measurements (angle at the intersection of a line through the proximal edge of the palmar AS of the MC3 and TR and a line through the proximal and distal edges of the AS of the lateral PSB [AS angle] and distance between the TR and distal edge of the AS of the lateral PSB [PSB-TR distance]) were used to evaluate the position of the PSBs relative to the TR in the sagittal plane (Figure 5.2). For both of those measurements, the sign (positive or negative) was determined on the basis of the location of the distal edge of the lateral PSB in relation to the TR; a positive value indicated that the distal edge of the lateral PSB was proximal to the TR and a negative value indicated that the distal edge of the lateral PSB was distal to the TR.

The PSBs did not undergo pure mediolateral distraction as was hypothesized, but instead underwent rotation in the transverse plane. Specifically, the palmar aspects of the PSBs rotated away from each other during extension of the fetlock joint. Recorded data could not distinguish pure PSB rotation from PSB rotation coupled with mediolateral translation because of mathematical coupling between rotation and translation inherent in use of 1-dimensional displacement sensors. So, the full three-dimensional nature of the rotation cannot be determined from the given data. However, assuming PSB rotation is confined to a transverse plane, and both PSBs rotate the same amount, rotation ( $\alpha$ ) could be extracted because the palmar LVDT always displaced further than the dorsal LVDT (Figure 5.3). Given this assumption, LVDT displacements were used to calculate the rotation angle ( $\alpha$ ) for 1 PSB using the following formula:  $\tan(\alpha) = [(0.5 * \text{Palmar LVDT displacement} - 0.5 * \text{Dorsal LVDT displacement}) / (\text{spacing between LVDTs})]$ . Thus,  $\alpha$  was used as a proxy for true PSB rotation under the given assumption.

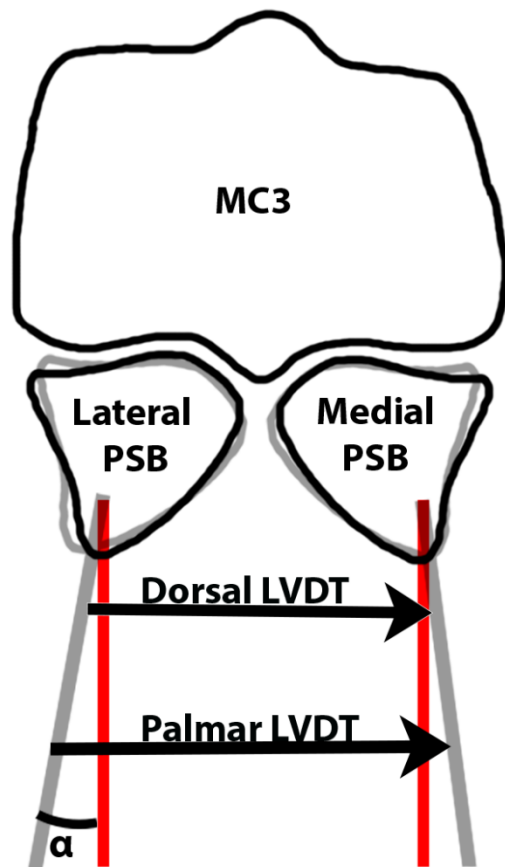


**Figure 5.3:** Schematic of the transverse plane of the distal aspect of MC3 for an equine forelimb of the study described in Figure 5.1 that depicts the positions of the PSBs relative to MC3 and apparent movement of the 2 LVDTs when the limb was unloaded and loaded during biomechanical testing. The black lines indicate the positions of the bones and the red lines indicate the positions of the 2 rods securing the LVDTs (LVDT rods) when the limb was unloaded. The gray lines indicate the positions of the PSBs and LVDT rods when the limb was loaded. In this study, the displacement of the palmar LVDT was always greater than the displacement of the dorsal LVDT. The known distance between the LVDTs and their relative displacements between unloading and loading of the limb were used to calculate the  $\alpha$  for a single PSB, which was used as a proxy for the rotation angle of the PSB assuming that rotation was confined to a transverse plane and that both PSBs rotated the same amount. It is possible that the PSBs also underwent mediolateral translation, but pure PSB rotation could not be distinguished from PSB rotation coupled with mediolateral translation owing to the mathematical coupling between rotation and translation inherent in the 1-dimensional LVDT data.

#### 5.3.4 Statistical analysis

Outcome variables of interest were fetlock angle, AS angle, PSB-TR distance, and  $\alpha$ . A repeated-measures ANOVA was used to determine the effect of target load (mid-stance vertical ground reaction force [stand, walk, trot, or gallop]) on each outcome variable. Each model included a fixed effect for target load and random effect to account for repeated measures within limb specimens. Body weight and age were considered as potential fixed effects in the models but were found to have no significant effect on any outcome variable; therefore, they were excluded from the final models. Post hoc pairwise comparisons were compared using the Tukey adjustment to control for type I error inflation. The normality assumption of the ANOVA was assessed by means of a Shapiro-Wilks test on model residuals; all model residuals were confirmed to be normally distributed (Shapiro-Wilks  $P > 0.9$ ). The partial

Spearman correlation coefficient (*partial r<sub>s</sub>*, while controlling for cadaver limb) were used to determine the extent of correlation between outcome variables. Simple linear regression analysis was used to assess the nature of the respective relationships (coefficient of determination, *R*<sup>2</sup>) between target load and other variables. Values of *P* < 0.05 were considered significant. All analyses were performed by use of a commercially available statistical software program.<sup>†</sup>

## 5.4 Results

Target load had a significant (*P* < 0.001) effect on fetlock angle, and the mean fetlock angle differed significantly among the 4 target loads (Table 5.1). There was a strong positive correlation (*partial r<sub>s</sub>* = 0.98) and a strong linear relationship (*R*<sup>2</sup> = 0.90) between fetlock angle and target load (Figure 5.4).

**Table 5.1:** Least squares mean ± SE values for measurements obtained during biomechanical testing of 8 equine cadaveric forelimbs in an in vitro study conducted to assess the motion of the PSBs relative to the MC3 condyle under physiologic midstance loads consistent with standing (1.8 kN), walking (3.6 kN), trotting (4.5 kN), and galloping (10.5 kN).

Variable	Posture or gait (target load)			
	Standing (1.8 kN)	Walking (3.6 kN)	Trotting (4.5 kN)	Galloping (10.5 kN)
Fetlock angle (°)	217.3 ± 2.1	227.9 ± 2.1	234.2 ± 2.1	262.2 ± 2.1
AS angle (°)	13.3 ± 1.7	6.1 ± 1.7	2.8 ± 1.7	-15.1 ± 1.7
PSB-TR distance (mm)(mm)	8.0 ± 0.6	5.5 ± 0.6	3.6 ± 0.6	-4.3 ± 0.6
α (°)	1.0 ± 0.2	2.2 ± 0.2	2.8 ± 0.2	6.2 ± 0.3
Half of dorsal LVDT displacement (mm)	0.3 ± 0.1	0.9 ± 0.1	1.3 ± 0.1	2.8 ± 0.1
Half of palmar LVDT displacement (mm)	0.7 ± 0.2	1.7 ± 0.2	2.3 ± 0.2	4.9 ± 0.2

For all variables, target load had a significant effect on all variables (*P* < 0.001) and the least squares mean values differed significantly (*P* < 0.05) among the 4 applied loads.



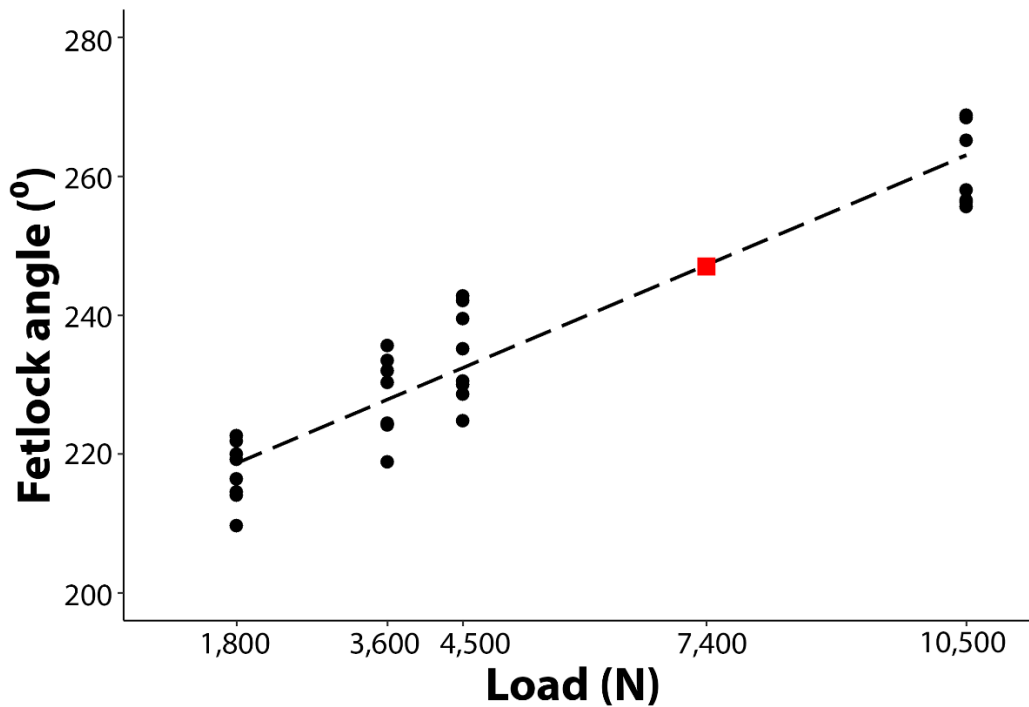


**Figure 5.4:** Plot of fetlock angle versus load for 8 equine forelimbs that underwent biomechanical testing as described in Figure 5.1. Each dot represents the fetlock angle for 1 limb at the given load. The linear regression line (dashed line) had the following equation: fetlock angle = (0.0051 X load) + 209.5. The coefficient of determination ( $R^2$ ) was 0.90; the partial spearman correlation between fetlock load and angle also indicated strong positive correlation (*partial*  $r_s = 0.98$ ). The red square indicates the point at which the distal edge of the lateral PSB moved distodorsally beyond the TR as estimated from the PSB-TR distance data.

The AS angle data indicated that the PSBs move distally then distodorsally then dorsally around the palmar portion of the MC3 condyle during extension of the fetlock joint. The AS angle decreased as the target load increased from 1.8 (stand) to 4.5 (trot) kN and became negative at 10.5 kN (gallop; Table 5.1). Target load had a significant ( $P < 0.001$ ) effect on AS angle, and the mean AS angle differed significantly among the 4 target loads. There was a strong negative correlation and negative linear relationship between AS angle and target load (*partial*  $r_s = -0.96$ ,  $R^2 = 0.85$ ) and AS angle and fetlock angle (*partial*  $r_s = -0.98$ ,  $R^2 = 0.88$ ; Figure 5.5).

The PSB-TR distance data indicated that the distal edge of the lateral PSBs moved dorsally past the TR at a target load consistent with a gallop. The distal edge of the lateral PSB approached the TR as

the target load increased from 1.8 to 4.5 kN, which was reflected by a decrease in the PSB-TR distance. The distal edge of the lateral PSB moved distal to the TR as the target load increased from 4.5 to 10.5 kN, resulting in a negative value for PSB-TR distance at a target load consistent with a gallop (Table 5.1). The distal edge of the lateral PSB was closest to the TR at a target load of 4.5 kN. Target load had a significant ( $P < 0.001$ ) effect on PSB-TR distance, and the mean PSB-TR distance differed significantly among the 4 target loads. There was a strong negative correlation between PSB-TR distance and target load ( $partial r_s = -0.96$ ) and between PSB-TR distance and fetlock angle ( $partial r_s = -0.98$ ; Figure 5.5) and a positive correlation between PSB-TR distance and AS angle ( $partial r_s = 0.97$ ).

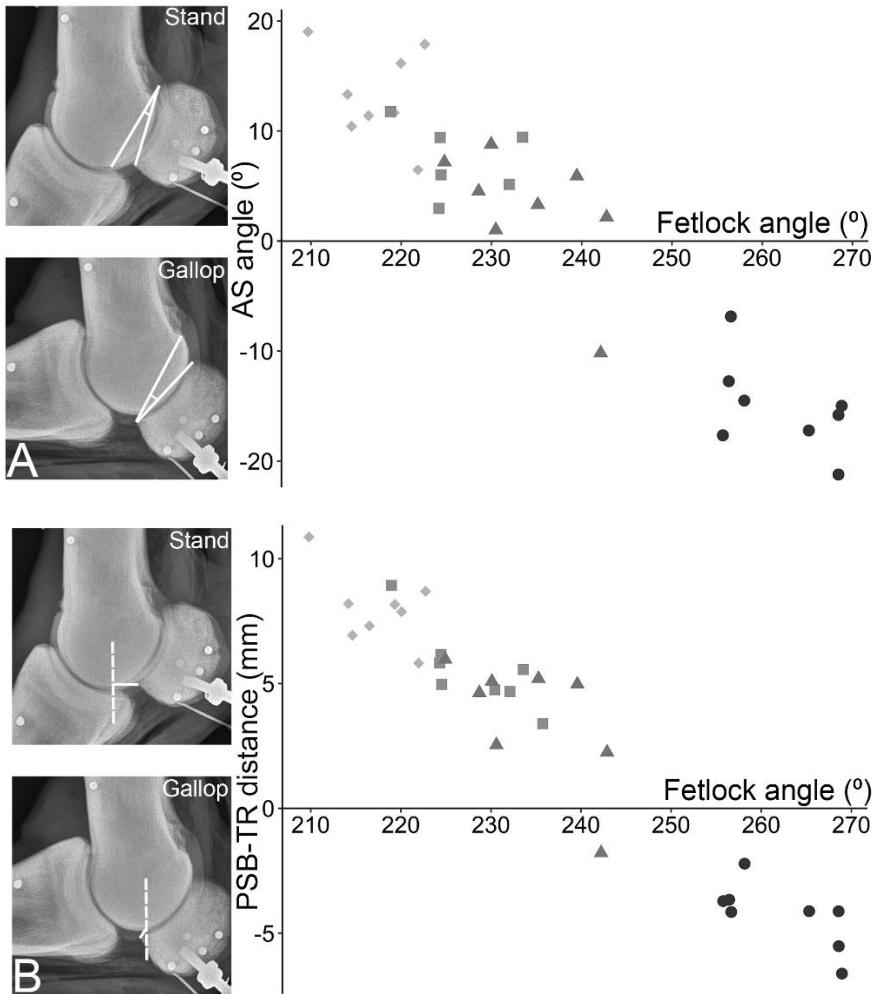


**Figure 5.5:** Scatterplots of AS angle (A) and PSB-TR distance (B) versus fetlock angle for 8 equine forelimbs when biomechanically tested at loads consistent with standing (diamonds), walking (square), trotting (triangle), and galloping (circle) as described in Figure 5.1. Each panel is accompanied by representative lateromedial radiographs of the fetlock region of a forelimb obtained when the limb was loaded with 1.8 (standing) and 10.5 (galloping) kN of axial compression to demonstrate the difference between the 2 loads in regard to the position of the PSBs relative to the MC3 condyle. The radiographs have been annotated to depict measurement of the AS angle (A) and PSB-TR distance (B), respectively. For both AS angle and PSB-TR distance, negative values indicate that the distal edge of the lateral PSB had moved distal to TR.

Radiographic and load data were used to construct linear regression equations to estimate the fetlock angle and load at which the distal margin of the lateral PSB moved distal to the TR. The regression equations and model  $R^2$  are as follows: PSB-TR distance =  $(-0.2692 \times \text{fetlock angle}) + 66.568$  with  $R^2 = 0.93$  and PSB-TR distance =  $(-0.0014 \times \text{load}) + 10.365$  with  $R^2 = 0.88$ . From these equations, it was estimated that the distal edge of the lateral PSB moved distal to the TR at a fetlock angle of  $247^\circ$  or a load of 7.4 kN.

Target load had a significant ( $P < 0.001$ ) effect on the displacement of both the dorsal and palmar LVDTs and  $\alpha$  (rotational angle). For each of those 3 variables, the mean value increased as target load increased and differed significantly among the 4 target loads (Table 5.1). Also, the displacement of the palmar LVDT was significantly greater than that of the dorsal LVDT by 46% to 56% at each target load. That finding indicated that the palmar aspect of the PSBs rotated away from each other as the limb was loaded (Figure 5.3). There was strong positive correlation and positive linear relationships between load and dorsal LVDT displacement (*partial*  $r_s = 0.97$ ,  $R^2 = 0.86$ ), palmar LVDT displacement (*partial*  $r_s = 0.96$ ,  $R^2 = 0.91$ ), and  $\alpha$  (*partial*  $r_s = 0.97$ ,  $R^2 = 0.90$ ).

## 5.5 Discussion

The TR demarcates the separation of the dorsal and palmar portions of the MC3 condyle, which articulate with the P1 and PSBs, respectively. The arc of curvature differs between the dorsal and palmar portions of the MC3 condyle to correspond with the curvature of the opposing ASs of the P1 and PSBs. The present in vitro study determined the position of the PSBs relative to the MC3 condyle at biomechanical loads selected to simulate those on the forelimb when a horse is standing and at midstance when the horse is walking, trotting, or galloping at a high speed. Results indicated that the distal margin of the PSBs moved distal to the TR, and thus beyond the congruent AS of MC3, when a

horse is at a high-speed gallop. Findings also indicated that the palmar surfaces of the PSBs rotate away from each other when the fetlock joint is extended, and that rotation is greatest when a horse is at a gallop.

As expected, results of the present study indicated that extension of the fetlock joint increases as the axial load applied to the forelimb increases. Importantly, the mean fetlock angles measured in the present study for target loads consistent with a walk (228°), trot (234°), and gallop (264°) were similar to those reported for those gaits in in vivo kinematic studies.<sup>10-14</sup> Those findings suggested that the target loads evaluated in the present study accurately simulated the anatomic alignment of and physiologic loads applied to equine forelimbs during the midstance phase of the stride at the selected gaits. Therefore, the motion of the PSBs observed in this study should closely mimic that in vivo. The target load selected to represent a trot (4.5 kN) in this study was lower than that used to simulate a trot in other studies.<sup>17,20</sup> It is estimated that the peak load sustained by a forelimb during a trot is 90% of the horse's body weight<sup>19</sup>; thus, for an average Thoroughbred racehorse (mean body weight, 483 kg<sup>k</sup>), the estimated peak forelimb load during a trot would be 4.3 kN. Additionally, the least squares mean  $\pm$  SE fetlock angle (234°  $\pm$  2.1°) at the target load for a trot measured in the present study was consistent with the fetlock angles (range, 225° to 241°) reported during a trot for horses of in vivo kinematic studies,<sup>14,21</sup> which further supported our supposition that the in vitro conditions of the present study accurately simulate in vivo kinematics of the equine forelimb.

The AS angle data obtained during the present study indicated that, as expected, the PSBs moved distodorsally around the palmar portion of the MC3 condyle during extension of the fetlock joint. The extent of the distodorsal movement of the PSBs increased as load increased and was greatest at the target load (10.5 kN) representative of a gallop. In the present study, the AS angle was assigned a negative value when the distal edge of the PSBs moved distal to the TR or the proximal edge of the PSBs

became distracted from MC3. Distodorsal movement of the PSBs was apparent, but distraction of the proximal edges of the PSBs from MC3 was not evident during visual examination of the radiographic images obtained during this study.

The PSB-TR distance measurements obtained during the present study indicated that the distal margins of the lateral PSB moved distal to the TR, and thus beyond its congruent articulation with the palmar aspect of the MC3 condyle, at a load consistent with a high-speed gallop. The data suggested that the distal margin of the lateral PSB moves distal to the TR at approximately 7.4 kN (a load consistent with a fast trot or canter<sup>18</sup>) and that distal movement continued until a target load of 10.5 kN (a load consistent with peak high-speed gallop<sup>16,18</sup>) was achieved. The proximodorsal motion of P1 is limited by contact of P1 with the dorsal aspect of MC3; however, distodorsal movement of the PSBs is limited by the extent to which the suspensory ligament can lengthen before rupture. Any movement of the PSBs distodorsal to the TR implies an articular incongruity exists between the PSBs and MC3. Joint incongruities affect the stress distribution in subchondral bone, since subchondral bone stress patterns are directly related to the load applied to the AS.<sup>22</sup> Joint incongruity could be a factor in the formation of stress remodeling induced subchondral bone lesions that precede biaxial midbody PSB fracture in racehorses.<sup>5,6,a,b</sup> Additionally, joint incongruity might induce a bending moment about a transverse axis located at the location where the PSBs moves distal to the TR. Because the distance the PSBs move distally beyond the TR appears to approximately correspond to the midbody to basilar aspect of the PSBs, it supports development of microdamage (leading to lesion formation) at a basilar to midbody PSB location. Thus, movement of the PSBs distal to the TR may contribute to the high prevalence of midbody and basilar PSB fractures reported in Thoroughbred racehorses.<sup>23,24</sup> Alternatively, extreme extension of the fetlock joint may lead to supraphysiologic stresses in subchondral bone on opposing ASs.

MC3-PSB contact areas under physiological loads have yet to be fully elucidated for horses. Results of an in vitro study<sup>25</sup> of cadaveric forelimbs indicate that the distal portion of the PSBs do not come into contact with MC3 when exposed to loads consistent with a gallop, which implies articular incongruity at those loads. However, the forelimbs evaluated in that study<sup>25</sup> were harvested distal to the carpometacarpal joint; therefore, the proximal and distal accessory (check) ligaments and their respective contributions to the superficial and deep digital flexor tendons did not remain intact to provide support to the fetlock region. In another in vitro study<sup>15</sup> of equine forelimbs in which the supporting structures of the fetlock region remained intact, it was reported that the PSBs did not move distal to the TR when the fetlock joint was maximally extended. However, the loading conditions were not specified for the limbs of that study,<sup>15</sup> and it is unknown whether loads consistent with a high-speed gallop were simulated. In the present study, known physiologic loads were applied to equine forelimbs in which the passive support structures of the fetlock region remained intact, and results indicated that the PSBs moved beyond their congruent ASs at loads consistent with a high-speed gallop.

In horses, the digital flexor tendons, ligamentous suspensory apparatus, and geometry of the MC3 and P1 limit motion of the fetlock joint primarily to the sagittal plane. Bone-fixed in-vivo and in vitro kinematic markers indicate only small amounts of internal-external rotation and adduction-abduction exist between MC3 and P1.<sup>12,17</sup> Results of the present study indicated that rotation between the lateral and medial PSBs occurs as the limb is loaded. The cause of that rotation is unknown and could be related to the geometry of the interdigitating ASs or tension from soft tissue attachments (eg, branches of the suspensory or extensor ligaments) during load application. In Thoroughbred racehorses, subchondral bone lesions are frequently identified on the abaxial portion of the AS of the medial PSB and are believed to contribute to biaxial midbody PSB fracture.<sup>5,6,a,b</sup> Rotation of the PSBs relative to each other likely changes the joint contact pattern and enhances stresses on the abaxial side of the PSBs. That

rotation may contribute to the formation of subchondral bone lesions that are commonly observed abaxial to the median sagittal plane of the PSBs.<sup>5,6,a,b</sup>

In the present study, the relative rotation of the PSBs was determined under the assumption that the rotation was confined to the transverse plane. One-dimensional kinematic measures (eg, LVDT displacements) cannot distinguish between rotation and rotation combined with distraction. If medial-to-lateral distraction of the PSBs occurs in combination with the observed rotation of the palmar surfaces of those bones away from one another, it may be a factor in axial avulsion fractures of the PSBs. An axial avulsion fracture of the lateral PSB in combination with a transverse fracture of the medial PSB is a commonly observed fetlock breakdown pattern for Thoroughbred racehorses.<sup>24</sup>

Finite element analysis indicates that the SR angle affects stress distribution on MC3 and P1. Specifically, more shallow SR angles resulted in higher stress at the condylar groove of P1, which is believed to contribute to MC3 and P1 fractures in racehorses.<sup>26</sup> Because MC3 articulates with the PSBs, it is likely the SR angle also affects stresses on the PSBs. Further investigation of the relationship between SR angle and PSB rotation is necessary and may help elucidate the specific cause of subchondral bone lesions on the abaxial surface of the PSBs.

The primary limitation of the present study was the fact that it was performed in vitro rather than in vivo. However, tracking PSB location with kinematic skin or embedded bone markers is not practical in live horses. Skin markers would likely have become dislodged during extension of the fetlock joint because the palmar aspect of the joint commonly impacts the ground surface at a high-speed gallop. Additionally, the amount of PSB movement beneath the skin would severely limit the accuracy of skin makers. Implants embedded in the PSBs would weaken the bone and increase the risk of PSB fracture during a high-speed gallop. Another limitation associated with the in vitro nature of the study was the fact that the forelimb muscles were not active during biomechanical testing, however the

passive support structures of the forelimb remained intact. The passive support structures are considered the main stabilizers of the forelimb during midstance,<sup>27</sup> so the lack of muscle activation was unlikely to have any clinically relevant effect on our results. Also, fetlock suspensory apparatus strains and translations should be directly related to fetlock angle independent of digital flexor muscle activation, and the fetlock angles observed in this study were consistent with those reported in in vivo kinematic studies.<sup>10-14, 21</sup> The in vitro nature of the present study also resulted in the loading rates for the forelimbs to be slower than the physiologic loading rates of forelimbs in vivo. This may have allowed stress relaxation of the limb's passive support structures. However, given that the observed fetlock angles were consistent with those observed during in vivo kinematic studies,<sup>10-14,21</sup> it appeared that any error associated with nonphysiologic loading rates was minimal. Finally, the position of the PSBs relative to the condyle of MC3 was measured on lateromedial radiographic images by use of the lateral PSB as a landmark. It is possible that the distance of movement beyond the TR differs between the lateral and medial PSBs, although that seems unlikely given the extent of binding between the lateral and medial PSBs provided by the intersesamoidean ligament.<sup>23</sup>

Results of the present in vitro study indicated that distal translation of the PSBs beyond their congruent AS with the condyle of MC3 and PSB rotation occurred during biomechanical testing at loads consistent with a high-speed gallop. Preexisting lesions of the subchondral bone of PSBs have been identified in Thoroughbred racehorses with PSB fracture.<sup>4,5,6</sup> The findings of this study suggested a potential anatomic cause for the observed abaxial midbody location of subchondral bone lesions and midbody-to-basilar location of most transverse PSB fractures. Additionally, rotation of the PSBs away from each other during extension of the fetlock joint at loads consistent with a high-speed gallop might contribute to intersesamoidean ligament rupture and axial avulsion fracture of the lateral PSB.



## 5.6 Acknowledgments

Supported by the University of California-Davis School of Veterinary Medicine Students Training in Advanced Research Program, Grayson Jockey Club Research Foundation, Center for Equine Health (with funds provided by the State of California satellite wagering fund and contributions from private donors), Maury Hull Fellowship, Louis R. Rowan Fellowship, and the Le Maitre Wild Oak Farm Endowment.

Presented, in part, at the Veterinary Orthopedics Society Conference, Sun Valley, Idaho, February 2020. The authors declare that there were no conflicts of interest.

## 5.7 Footnotes

- a. Shaffer SK, To C, Stover SM, et al. Evidence of subchondral lesions preceding proximal sesamoid bone fracture in Thoroughbred racehorses (abstr), in *Proceedings*. Veterinary Orthopedics Society Conference, 2019
- b. Shaffer, SK, Stover SM, Fyhrie DP. Morphological changes in the proximal sesamoid bones of racehorses as a model for overuse joint injuries (abstr), in *Proceedings*. Orthopaedic Research Society Conference, 2020
- c. Model 809, MTS Systems Corp, Eden Prairie, Minn.
- d. Model 662.10A-08, MTS Systems Corp, Eden Prairie, Minn.
- e. Super Pillow Block (SPB 32 OPN), Thomson Industries Inc, Port Washington, NY.
- f. Co Tray Plastics, GC America Inc. Alsip, Ill.
- g. Lord Microstrain, Williston Vt.
- h. Next Equine Digital X-ray, Sound Technologies, Carlsbad, Calif.
- i. Smart DR Software, version 3.6.6180.15264, Sound Technologies, Carlsbad, Calif.
- j. SAS, version 9.4, SAS Institute, Cary, NC.
- k. Uzal FA. California Animal Health and Food Safety Laboratory, San Bernardino, Calif: Personal communication, 2019.

## 5.8 References

1. Johnson BJ, Stover SM, Daft BM, et al. Causes of death in racehorses over a 2 year period. *Equine Vet* 1994;26:327–330.
2. California Horse Racing Board Postmortem Examination Program 2017-2018 annual report. Davis, Calif;2019.
3. Stover SM. The epidemiology of Thoroughbred racehorse injuries. *Clin Tech Equine Pract* 2003;2:312–322.
4. Anthenill LA, Gardner IA, Pool RR, et al. Comparison of macrostructural and microstructural bone features in Thoroughbred racehorses with and without midbody fracture of the proximal sesamoid bone. *Am J Vet Res* 2010;71:755–765.
5. Stover SM. Diagnostic workup of upper-limb stress fractures and proximal sesamoid bone stress remodeling, in *Proceedings*. Am Assoc Equine Pract 2013;59:427–435.
6. Shaffer SK, To C, Garcia TC, et al. Subchondral focal osteopenia associated with proximal sesamoid bone fracture in Thoroughbred racehorses. *Equine Vet J* 2020:evj.13291.
7. Janes JG, Kennedy LA, Garrett KS, et al. Common lesions of the distal end of the third metacarpal/metatarsal bone in racehorse catastrophic breakdown injuries. *J Vet Diagnostic Invest* 2017;29:431–436.
8. Pool RR, Meagher DM. Pathologic findings and pathogenesis of racetrack injuries. *Vet Clin North Am Equine Pract* 1990;6:1–30.
9. Park RD. Equine diagnostic imaging—part 1: radiology. In: Stashak TS, ed. *Adams' lameness in horses*. 5th Ed. Philadelphia: Lippincott Williams and Wilkins, 2002;228–231.
10. Butcher MT, Ashley-Ross MA. Fetlock joint kinematics differ with age in Thoroughbred racehorses. *J Biomech* 2002;35:563–571.
11. Setterbo J, Garcia T, Campbell I, et al. Forelimb kinematics of galloping Thoroughbred racehorses measured on dirt, synthetic, and turf track surfaces (P235). In: *The engineering of sport 7*. Paris: Springer Paris, 2009;437–446.
12. Clayton HM, Sha D, Stick J, et al. 3D kinematics of the equine metacarpophalangeal joint at walk and trot. *Vet Comp Orthop Traumatol* 2007;20:86–91.
13. Hodson E, Clayton HM, Lanovaz JL. The forelimb in walking horses: 1. Kinematics and ground reaction forces. *Equine Vet J* 2000;32:287–294.
14. Harrison SM, Whitton RC, Kawcak CE, et al. Relationship between muscle forces, joint loading and utilization of elastic strain energy in equine locomotion. *J Exp Biol* 2010;213:3998–4009.

15. Colahan P, Piotrowski G, Poulos P. Kinematic analysis of the instant centers of rotation of the equine metacarpophalangeal joint. *Am J Vet Res* 1988;49:1560–1565.
16. Swanstrom MD, Zarucco L, Hubbard M, et al. Musculoskeletal modeling and dynamic simulation of the Thoroughbred equine forelimb during stance phase of the gallop. *J Biomech Eng* 2005;127:318–328.
17. Singer E, Garcia T, Stover S. How do metacarpophalangeal joint extension, collateromotion and axial rotation influence dorsal surface strains of the equine proximal phalanx at different loads in vitro? *J Biomech* 2013;46:738–744.
18. Setterbo JJ, Garcia TC, Campbell IP, et al. Hoof accelerations and ground reaction forces of Thoroughbred racehorses measured on dirt, synthetic, and turf track surfaces. *Am J Vet Res* 2009;70:1220–1229.
19. Schryver HF, Bartel DL, Langrana N, et al. Locomotion in the horse: kinematics and external and internal forces in the normal equine digit in the walk and trot. *Am J Vet Res* 1978;39:1728–1733.
20. Brama PA, Karszenberg D, Barneveld A, et al. Contact areas and pressure distribution on the proximal articular surface of the proximal phalanx under sagittal plane loading. *Equine Vet J* 2001;33:26–32.
21. Hjertén G, Drevemo S. Semi-quantitative analysis of hoof-strike in the horse. *J Biomech* 1994;27:997–1004.
22. Eckstein F, Jacobs CR, Merz BR. Mechanobiological adaptation of subchondral bone as a function of joint incongruity and loading. *Med Eng Phys* 1997;19:720–728.
23. Schnabel LV, Redding WR. Diagnosis and management of proximal sesamoid bone fractures in the horse. *Equine Vet Educ* 2018;30:450–455.
24. Anthenill LA, Stover SM, Gardner IA, et al. Association between findings on palmarodorsal radiographic images and detection of a fracture in the proximal sesamoid bones of forelimbs obtained from cadavers of racing Thoroughbreds. *Am J Vet Res* 2006;67:858–868.
25. Vilar JM, Pinedo M, De Mier J, et al. Equine metacarpophalangeal joint surface contact changes during walk, trot and gallop. *J Equine Vet Sci* 1995;15:315–319.
26. Liley H, Davies H, Firth E, et al. The effect of the sagittal ridge angle on cartilage stress in the equine metacarpo-phalangeal (fetlock) joint. *Comput Methods Biomech Biomed Engin* 2017;20:1140–1149.
27. Harrison SM, Whitton RC, King M, et al. Forelimb muscle activity during equine locomotion. *J Exp Biol* 2012;215:2980–2991.

## **Chapter 6: In Vitro Motions of the Medial and Lateral Proximal Sesamoid Bones** **under Mid-Stance Load Conditions are Consistent with Racehorse Fracture**

### **Configurations**

This chapter has been accepted, pending revisions, as:

Shaffer, S.K., Shelly, K., Garcia, T.C., Samol, M.A., Hill, A.E., Fyhrie, D.P., Stover, S.M., 2021. In Vitro

Motions of the Medial and Lateral Proximal Sesamoid Bones Under Mid-Stance Load Conditions Are Consistent With Racehorse Fracture Configurations. *Journal of Biomechanics*.

### **6.1 Abstract**

Proximal sesamoid bone (PSB) fractures in racehorses are likely fatigue fractures that occur due to repetitive loads and stress remodeling. The loading circumstances that may induce damage in the PSBs are not well understood. The goal of this study was to determine in three-dimensions, PSB motions relative to the opposing metacarpal condyle during simulated mid-stance loads. Seven equine cadaveric forelimbs were axially loaded in a material testing system to simulate standing and mid-stance walk, trot, and gallop load conditions (1.8-10.5 kN). Joint angles were determined by tracking the positions of bone-fixed kinematic markers. Internal-external rotation, abduction-adduction, and flexion-extension of each PSB relative to the third metacarpal condyle were compared between loads and between PSBs using an ANOVA with Tukey-Kramer post hoc tests for pairwise comparisons. The medial PSB rotated externally and the lateral PSB apex abducted during limb loading. Medial PSB external rotation was significantly greater at the gallop load condition than at the walk or trot load conditions. The medial and lateral PSB motions observed in this study are consistent with location of fatigue damage and fracture configurations frequently seen in medial and lateral PSBs from Thoroughbred racehorses. Specifically, medial PSB external rotation is consistent with the development of an abaxial subchondral medial PSB lesion that is

reported in association with medial PSB transverse fracture and lateral PSB abduction is consistent with axial longitudinal fracture of the lateral PSB.

## 6.2 Introduction

Proximal sesamoid bone (PSB) fracture is a leading cause of death for Thoroughbred racehorses.<sup>1-3</sup> Catastrophic PSB fracture is typically biaxial, meaning both the medial and lateral PSBs fracture. Biaxially fractured PSBs typically have different fracture configurations.<sup>4,5</sup> Medial PSBs fracture transversely through the midbody to basilar portions of the bone, while the lateral PSBs fracture obliquely or transversely through the midbody to basilar portion of the bone or longitudinally along the axial border (Figure 6.1).<sup>4</sup> In California Thoroughbred racehorses, transverse midbody medial PSB fracture coupled with lateral PSB axial longitudinal fracture or intersesamoidean ligament rupture (Figure 6.1) accounts for 5.4% of fatal fetlock injuries; a majority (73%) of these occur with a lateral condylar fracture of the third metacarpal bone (MC3).<sup>6</sup> Biaxial PSB fractures (excluding axial longitudinal lateral PSB fractures) account for 50.4% of fatal fetlock injuries, generally in this fracture configuration the medial PSB fractures transversely and the lateral PSB fractures obliquely. Most biaxial PSB fractures (92%) occur without involvement of the MC3.<sup>6</sup>

Evidence indicates that PSB fractures are repetitive, overuse injuries.<sup>7,8</sup> Subchondral bone lesions found in the medial PSB have been associated with transverse fracture (Figure 6.1).<sup>5,9-11</sup> Lesion characteristics are consistent with damage induced bone remodeling,<sup>10-12</sup> suggesting that there is a biomechanical mechanism that repeatedly causes high subchondral bone stress at the lesion location prior to fracture. While lateral PSB axial longitudinal fractures have not been thoroughly investigated, the consistency of this fracture configuration also implies a potential biomechanical etiology.

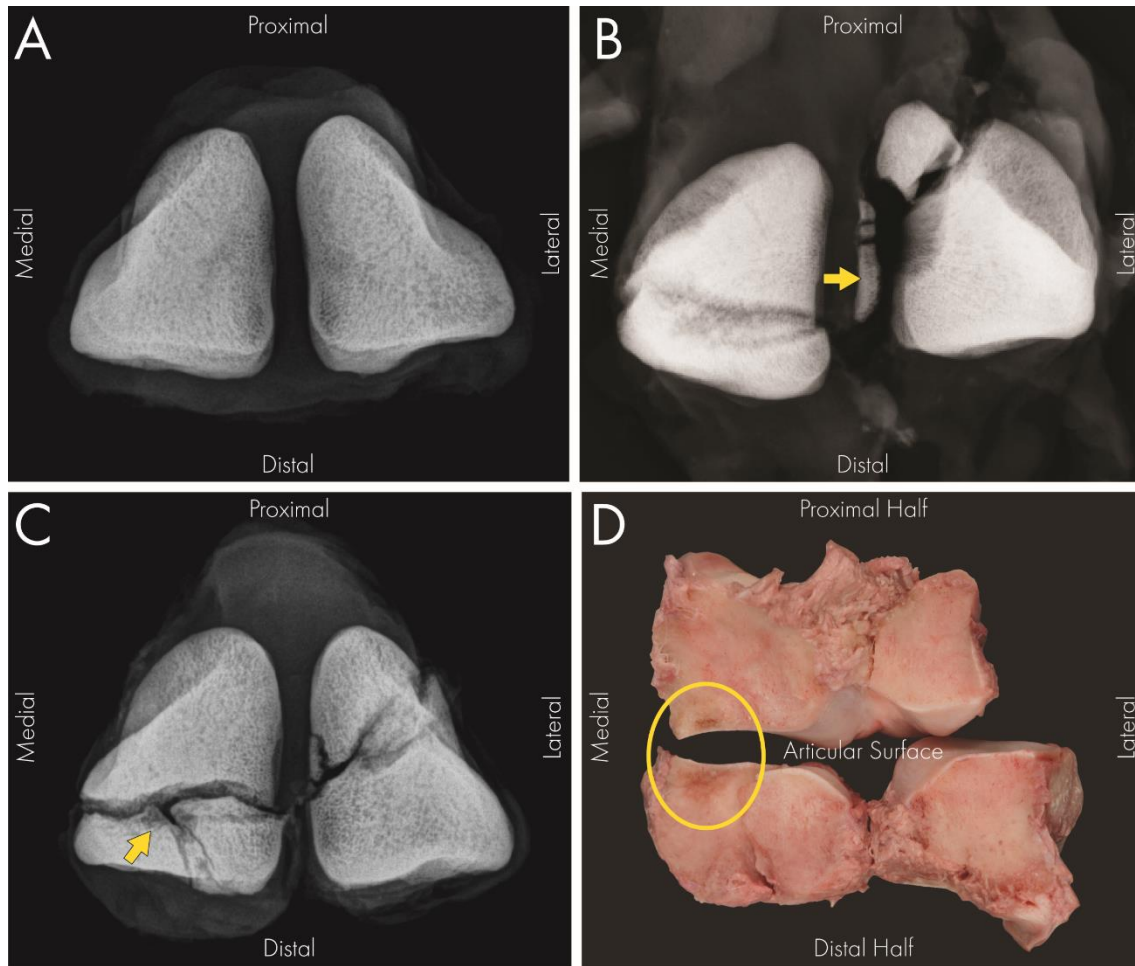


**Figure 6.1:** Dorsopalmar radiographic projection of intact Proximal Sesamoid Bones (PSBs; Panel A) and examples of common bilateral PSB fracture configurations in Panels B and C. Panel B) Medial mid-body PSB fracture with a lateral axial longitudinal PSB fracture; the yellow arrow shows where the intersesamoidean ligament avulsed lateral PSB fragments. Panel C) Medial mid-body PSB fracture with a lateral oblique apical fracture; the yellow arrow indicates the site of a subchondral bone lesion illustrated on the fracture faces (yellow circle) of the medial PSB in Panel D.

The medial and lateral PSBs are embedded in the suspensory apparatus of the distal portion of the forelimb and support the metacarpophalangeal joint (MCPJ) during locomotion. Four bones constitute the MCPJ: the third metacarpal bone (MC3), medial PSB, lateral PSB, and proximal phalanx (P1). The MC3 has two distinct portions of its distal articular surface, one congruent with the PSBs and the other with the P1; the PSBs do not articulate with P1. Previously, the authors reported that PSBs extend beyond their congruent articular surface on the MC3 at racing-speed loads and that some external rotation of the PSBs occurs during limb loading.<sup>13</sup> However, the full nature of PSB motion was not determined.

The purpose of the present study was to assess the full three-dimensional movements of the PSBs relative to the MC3 during in vitro limb loading. Our goal is to determine if PSB motions are consistent with the reported location of fatigue damage and fracture configurations for the medial and lateral PSBs. We hypothesize that during simulation of mid-stance racing-speed gallop, the PSBs would rotate externally and the lateral PSB would abduct relative to the long-axis of the MC3.

## **6.3 Materials and Methods**

Cadaveric forelimbs were loaded in vitro to simulate walk, trot, and gallop mid-stance loads. MCPJ joint angles were determined from bone-fixed kinematic markers, calibrated to a reference frame.

### **6.3.1 Sample Selection**

Seven cadaveric unilateral forelimbs (5 left, 2 right) were a convenience sample from horses euthanized for reasons unrelated to forelimb pathology (4 mares, 3 geldings; 4 Thoroughbreds in race training (2-4 years; 380-493 kg), 1 Paint (5 years; weight unknown), 1 Quarter Horse (14 years; 537.5 kg), and 1 Warmblood (21 years; 570 kg)). Owners provided informed consent for unrestricted or research use of cadavers. Limbs were harvested during clinical necropsy, wrapped in saline soaked towels, and stored frozen (-20°C; up to 16 months) until thawed at room temperature (21°C) for 24 hours prior to biomechanical testing.

Forelimbs were transected at mid-radius to retain the accessory ligaments of the superficial and deep digital flexor tendons and the fetlock stay apparatus. Horseshoes, when present, were removed prior to biomechanical testing.

### 6.3.2 Limb Instrumentation

The proximal end of each forelimb was fixed in a cylinder with polymethylmethacrylate (Coe Tray Plastic, GC America, Alsip IL) while the limb was in a standing position.<sup>13,14</sup> Fixation pins (3.2 mm diameter; Smooth Fixation Pin, IMEX Veterinary Inc.) were inserted perpendicularly to the median plane of the MC3 and P1 (Figure 6.2). In each PSB, one 5 mm long 3.2 mm diameter fixation pin (Duraface, IMEX Veterinary Inc.) was inserted palmarly, abaxial to the flexor tendons and palmar to the insertion of the suspensory ligament (Figure 6.2).

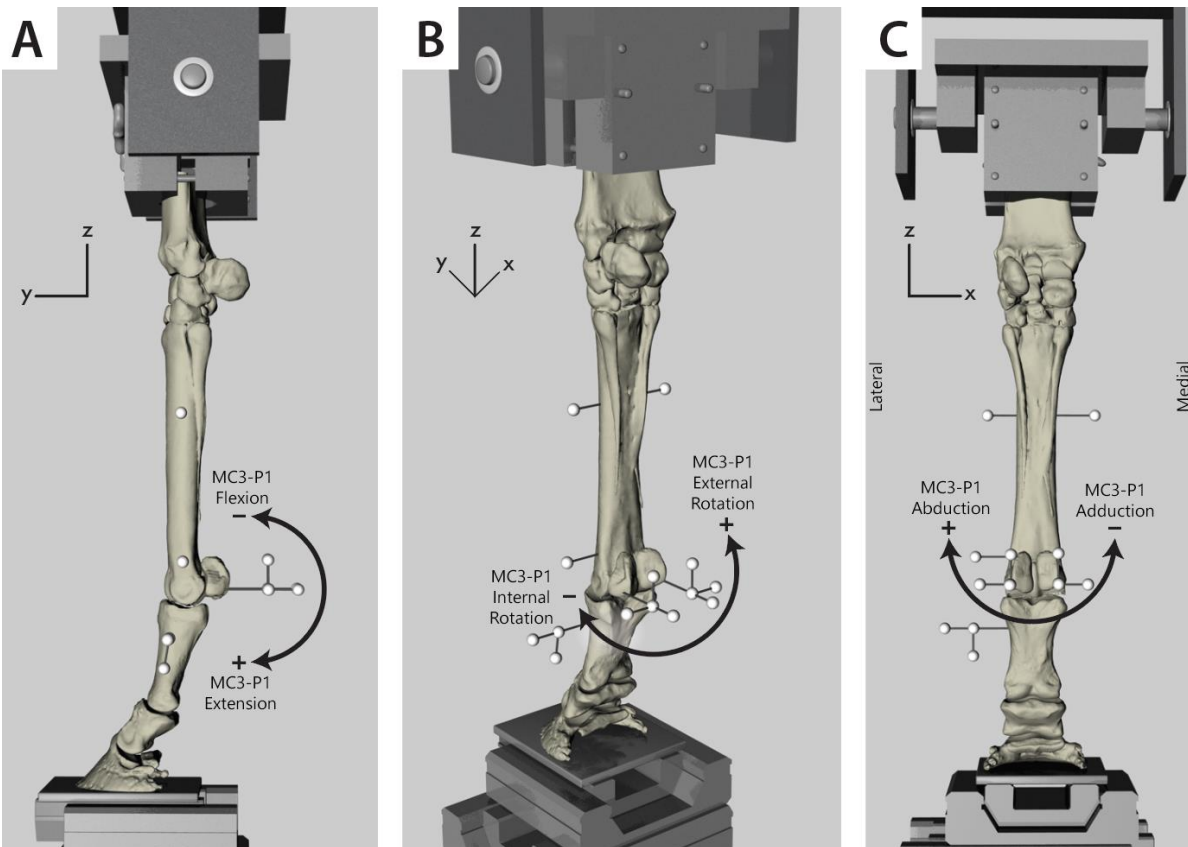


**Figure 6.2:** Lateral (A), lateropalmar (B), and palmar (C) views illustrating instrumentation of a left forelimb in the material testing system showing MC3-P1 sign conventions for the flexion-extension, internal-external rotation, and abduction-adduction joint angles. The upper left corner of each panel indicates the positive direction of the coordinate axes (X, Y, Z) used for all bones. Note that all supporting soft tissues were maintained during tests, but are not shown in figures.



Spherical markers covered by reflective tape (3M Scotchlite 3710) were attached to these pins to track bone movements. Single spherical markers (9.53 mm diameter) were attached to the MC3 pins. Orthogonal kinematic marker sets (30mm height/width/depth with 8mm diameter spheres, 3D printed Onyx, Mark2 Markforged) were attached to the PSB pins (Figure 6.3). Planar kinematic marker sets were attached to the P1 pins (30mm height/width with 8mm diameter spheres, 3D printed, Onyx, Mark2 Markforged; Figure 6.2).

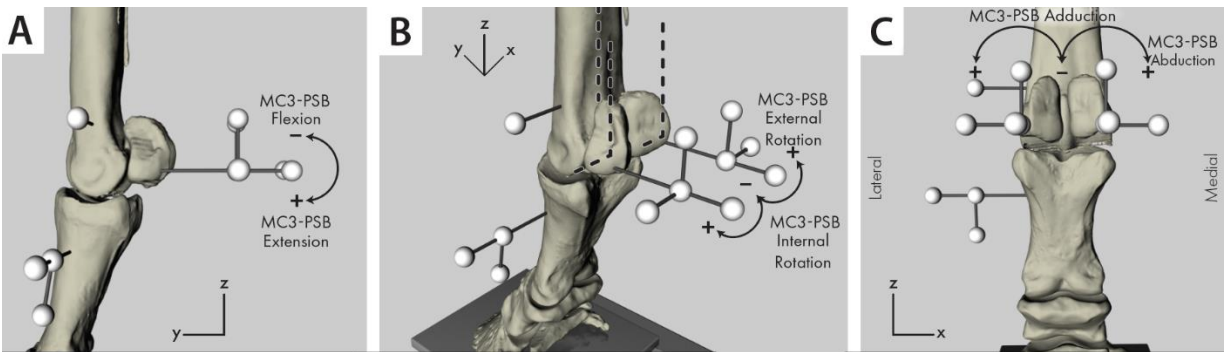


**Figure 6.3:** Lateral (A), lateropalmar (B), and palmar (C) views illustrating instrumentation and sign conventions for the MC3-PSB flexion-extension, internal-external rotation, and abduction-adduction joint angles are shown on a left forelimb. The positive direction of the coordinate axes (X, Y, Z) are illustrated for all bones. Note that all supporting soft tissues were maintained during tests, but are not shown in figures.

### 6.3.3 Biomechanical Testing

In vitro biomechanical testing was performed with a servohydraulic material testing system equipped with an axial-torsional load transducer (Model 809 and Model 662.10A-08; MTS Systems Corp., Minneapolis, MN). The radius was secured to the material testing system via the polymethylmethacrylate cylinder. The hoof was placed on a linear bearing translation table attached to the material testing system actuator, so that the radius and MC3 were parallel to the load axis under ~700N compression (Figure 6.2)<sup>13,14</sup> During loading the hoof moved dorsally and the MC3 remained parallel to the load axis.<sup>13,14</sup> Dorsopalmar radiographs were taken to convert marker positions to bone reference frames (Next DR, Sound Carlsbad, CA; HF100/30 +, MinXray, Inc., Northbrook, IL; 70 kVp, 2.0 mAs). The limb was preconditioned for 200 cycles of 700-1,800N compression at 0.25Hz, then loaded once from 700 to

10,500N, and unloaded prior to testing. Limbs were tested from 700 to 10,500N under displacement control at 5mm/s while marker positions were recorded at 60 Hz with 2 high-speed video cameras (S-PRI, AOS Technologies AB, Dattwil Switzerland) in a calibrated field of view (Motion Analysis Calibration Cube, CF-20, Santa Rosa, CA).

#### **6.3.4 Data Reduction**

Radiographic distances from kinematic markers to bone longitudinal axes were used to transform MC3 and P1 marker positions to bone-fixed virtual markers along the proximo-distal axes of MC3 and P1;<sup>14</sup> these defined the bone-fixed coordinate systems for MC3 and P1 in kinematic software (Motus 10.0, Contemplas GmbH, Kempten Germany). Kinematic triads were used to define the bone fixed axes for the PSBs. For all bones, the Z-axis was positive proximally and Y-axis positive dorsally, and the X-axis completed a right-handed coordinate system (positive medially in left limb, laterally in right limb; Figure 6.3).<sup>15</sup> A joint coordinate system was then established for the MC3-P1, MC3-medial PSB, and MC3-lateral PSB articulations of the MCPJ in the kinematic analysis program. Flexion-extension angles occur about the MC3's X-axis, internal-external rotation occurs about the P1's Z-axis for the MC3-P1 or the PSB's Z-axis for MC3-PSB rotation, and abduction-adduction angles about the joint coordinate system's mutual perpendicular axis.<sup>15</sup> Custom equations, based on Grood (1983), were applied in kinematic analysis software to determine MC3-P1 angles (defined as movement of the P1 relative to MC3; Figure 6.2) and PSB-MC3 joint angles (defined as movement of PSBs relative to MC3; Figure 6.3).<sup>15</sup>

The MC3-P1 flexion-extension angle is the palmar angle between P1 and MC3; it increases with MCPJ extension (Figure 6.2).<sup>14</sup> The MC3-P1 internal-external rotation angle increases with external rotation of P1 relative to MC3 (i.e., the dorsal aspect of P1 moves laterally relative to MC3; Figure 6.2); MC3-P1 abduction-adduction angle increases with abduction (i.e., rotation of the proximal end of MC3 or distal end of P1 away from the body midline; Figure 6.2). MC3-PSB angles were determined individually

for the medial and lateral PSB. For all MC3-PSB angles, the flexion-extension angle increases as the PSB moves distally around the MC3 condyle during MCPJ extension, internal-external rotation angle increases with external rotation of the PSB relative to the midline of the MC3 (e.g. abaxial aspect of the PSB would move dorsally relative to the axial aspect of the PSB, or the axial aspect of the PSB would move palmarly relative to the abaxial aspect of the PSB), and abduction-adduction angle increases as the apex of the PSB moves away from the midline of the MC3 (Figure 6.3).

Angle data were filtered with a low-pass filter (5Hz cutoff; MATLAB R2020a, The MathWorks Inc., Natick, MA) followed with a robust linear regression smoothing filter (sampling window 45 units; MATLAB 2020a).

### **6.3.5 Data Analysis**

Metacarpophalangeal joint angles (MC3-P1, MC3-medial PSB, and MC3-lateral PSB) at Stand (1800 N) and mid-stance Walk (3600 N), Trot (4500 N), and Gallop (10500 N) load conditions were extracted from angle-load curves. Loads are consistent with in vivo peak vertical ground reaction forces during mid-stance and with previous in vitro studies.<sup>13,14,16-19</sup> The gallop load condition is consistent with estimates from simulation of 18 m/s gallop for a 500 kg horse.<sup>19</sup>

The effect of load condition (Walk, Trot, Gallop) and PSB side (Medial, Lateral) on the changes in MC3-PSB joint angles from the Stand load condition were assessed using ANOVA. The effects of load condition on MC3-P1 angle and on the change of MC3-P1 angle from Stand were also assessed using an ANOVA. Repeated measures within limbs were accounted for by incorporating horse as a random effect; Tukey-Kramer corrections were made for the post-hoc pairwise comparisons. A p-value  $\leq 0.05$  was statistically significant. Normality of model residuals were assessed via a Shapiro-Wilks score ( $W$ ;  $W > 0.90$  for all models). For analyses with non-normally distributed residuals, a ranked ANOVA was used. The

effects of horse age, breed (Thoroughbred or non-Thoroughbred), limb side (left or right) and the load-limb side interaction were examined but were not significant.

The relationships between load and MC3-P1 and MC3-PSB joint angle differences from Stand sampled every 1050N (10% of peak load) starting at 2100N, were determined using linear regressions. Coefficient of determination ( $R^2$ ) values are reported for statistically significant ( $p \leq 0.05$ ) relationships. Partial Spearman correlation coefficients, controlling for horse, were determined for MC3-P1 flexion-extension and MC3-PSB joint angles; significant correlation coefficients ( $r$ ;  $p \leq 0.05$ ) are reported.

## 6.4 Results

Limb loading caused MCPJ extension and external rotation of P1 about MC3 (Table 6.1). The change in MC3-P1 extension from Stand increased linearly with load ( $R^2 = 0.89$ ) and was significantly different among all load conditions (Table 6.1). The MC3-P1 extended  $36^\circ$  between the Stand and Gallop conditions. The change in MC3-P1 external rotation from Stand had a weak linear relationship with load ( $R^2 = 0.31$ ) and  $3.8^\circ$  of MC3-P1 external rotation occurred between the Stand and Gallop conditions. The MC3-P1 did not experience statistically significant amounts of abduction or adduction.

**Table 6.1:** Least Square Mean  $\pm$  Standard Error of MC3-P1 angles at Stand, Walk, Trot, and Gallop load conditions and the Change in MCPJ angles from the Stand load condition.

	Flexion (-)/Extension(+)		Internal (-)/External (+) Rotation		Adduction(-)/Abduction(+)	
	Angle <sup>†</sup>	Angle Change from Stand <sup>†</sup>	Angle <sup>§</sup>	Angle Change from Stand <sup>§</sup>	Angle <sup>§</sup>	Angle Change from Stand <sup>§</sup>
<b>Stand</b>	222.27 $\pm$ 2.24 <sup>A</sup>	NA	1.93 $\pm$ 2.32 <sup>A</sup>	NA	4.98 $\pm$ 1.79 <sup>A</sup>	NA
<b>Walk</b>	231.71 $\pm$ 2.24 <sup>B</sup>	9.44 $\pm$ 1.50 <sup>A</sup>	2.50 $\pm$ 2.32 <sup>A</sup>	0.57 $\pm$ 0.94 <sup>A</sup>	4.84 $\pm$ 1.79 <sup>A</sup>	-0.14 $\pm$ 0.82 <sup>A</sup>
<b>Trot</b>	236.82 $\pm$ 2.24 <sup>C</sup>	14.55 $\pm$ 1.50 <sup>B</sup>	3.04 $\pm$ 2.32 <sup>A</sup>	1.11 $\pm$ 0.93 <sup>A</sup>	5.13 $\pm$ 1.79 <sup>A</sup>	0.15 $\pm$ 1.15 <sup>A</sup>
<b>Gallop</b>	258.48 $\pm$ 2.24 <sup>D</sup>	36.21 $\pm$ 1.50 <sup>C</sup>	5.75 $\pm$ 2.32 <sup>B</sup>	3.82 $\pm$ 3.83 <sup>B</sup>	5.49 $\pm$ 1.79 <sup>A</sup>	0.51 $\pm$ 3.42 <sup>A</sup>

Note: MC3 (third metacarpal bone); P1 (proximal phalanx)

Significant effects: <sup>†</sup>ANOVA, <sup>§</sup> ranked ANOVA

<sup>A,B,C,D</sup>: pairwise comparisons among load conditions; values within a column that do not share a superscript are statistically different at  $p \leq 0.05$  with Tukey-Kramer adjustment

Limb loading caused extension (distal motion) of both PSBs relative to the MC3. There were no significant differences in MC3-PSB flexion-extension angle between medial and lateral PSBs at any load condition. PSB extension changed 26° between Stand and Gallop; which was greater than the changes from Stand to Walk and Trot (Table 6.2). The change in PSB-MC3 extension from Stand increased linearly with load (Figure 6.4A).

**Table 6.2:** Least Square Mean ± Standard Error of MC3-PSB angles from the Stand load condition for the Walk, Trot, and Gallop load conditions. Within a column, for each effect (separated by bold lines), values that share a superscript are not statistically different.

Load Condition	PSB Side	Flexion(-)/ Extension(+) Angle Change from Stand †	Internal (-)/External (+) Rotation Angle Change from Stand †,‡,¶	Adduction(-)/ Abduction(+) Angle Change from Stand ‡
Walk	.	5.87+1.24 <sup>A</sup>	0.82+0.44 <sup>A</sup>	0.18+0.41 <sup>A</sup>
Trot	.	9.09+1.24 <sup>B</sup>	1.11+0.44 <sup>A</sup>	0.33+0.41 <sup>A</sup>
Gallop	.	26.02+1.24 <sup>C</sup>	3.67+0.44 <sup>B</sup>	0.98+0.41 <sup>A</sup>
.	Lateral	13.71+1.19 <sup>α</sup>	1.04+0.38 <sup>α</sup>	1.01+0.34 <sup>α</sup>
.	Medial	13.61+1.19 <sup>α</sup>	2.69+0.38 <sup>β</sup>	-0.01+0.34 <sup>β</sup>
Walk	Lateral	5.87+1.39 <sup>1</sup>	0.8+0.59 <sup>1</sup>	0.38+0.58 <sup>1</sup>
Walk	Medial	5.86+1.39 <sup>1</sup>	0.84+0.59 <sup>1</sup>	-0.02+0.58 <sup>1</sup>
Trot	Lateral	9.06+1.39 <sup>1</sup>	0.64+0.59 <sup>1</sup>	0.6+0.58 <sup>1</sup>
Trot	Medial	9.12+1.39 <sup>1</sup>	1.58+0.59 <sup>1</sup>	0.06+0.58 <sup>1</sup>
Gallop	Lateral	26.19+1.39 <sup>2</sup>	1.67+0.59 <sup>1</sup>	2.04+0.58 <sup>1</sup>
Gallop	Medial	25.84+1.39 <sup>2</sup>	5.67+0.59 <sup>2</sup>	-0.07+0.58 <sup>1</sup>

Note: MC3 (third metacarpal bone), PSB (proximal sesamoid bone)

Significant ANOVA effects: † Load condition, ‡ PSB side, ¶ Load Condition and PSB Side interaction

<sup>A,B,C,D</sup>: pairwise comparisons among load conditions,  $p \leq 0.05$  with Tukey-Kramer adjustment

<sup>α,β</sup>: pairwise comparisons among PSB Side,  $p \leq 0.05$  with Tukey-Kramer adjustment

<sup>1,2</sup>: pairwise comparisons load condition and PSB side interaction,  $p \leq 0.05$  with Tukey-Kramer adjustment

Both PSBs rotated externally as the limb was loaded; however, the medial PSB experienced more external rotation than the lateral PSB (Table 6.2; Figure 6.4B). Between Stand and Gallop, the medial PSB externally rotated 5.7° and the lateral PSB externally rotated 1.7° (Table 6.2; Figure 6.4B); the difference between Stand and Gallop was significant only for the medial PSB. The change in external rotation of the medial and lateral PSBs had strong and weak linear relationships with load, respectively (Figure 6.4B).

The apex of the lateral PSB experienced significantly more abduction than the medial PSB; however, load condition did not have a significant effect on PSB abduction. Averaged over all load

conditions, the abduction change from Stand was higher for the lateral PSB than medial PSB. The change in lateral PSB abduction from Stand had a weak linear relationship with load and the lateral PSB abducted 2° between the Stand and Gallop loads (Table 6.2; Figure 6.4C). There was no similar significant relationship for the medial PSB.

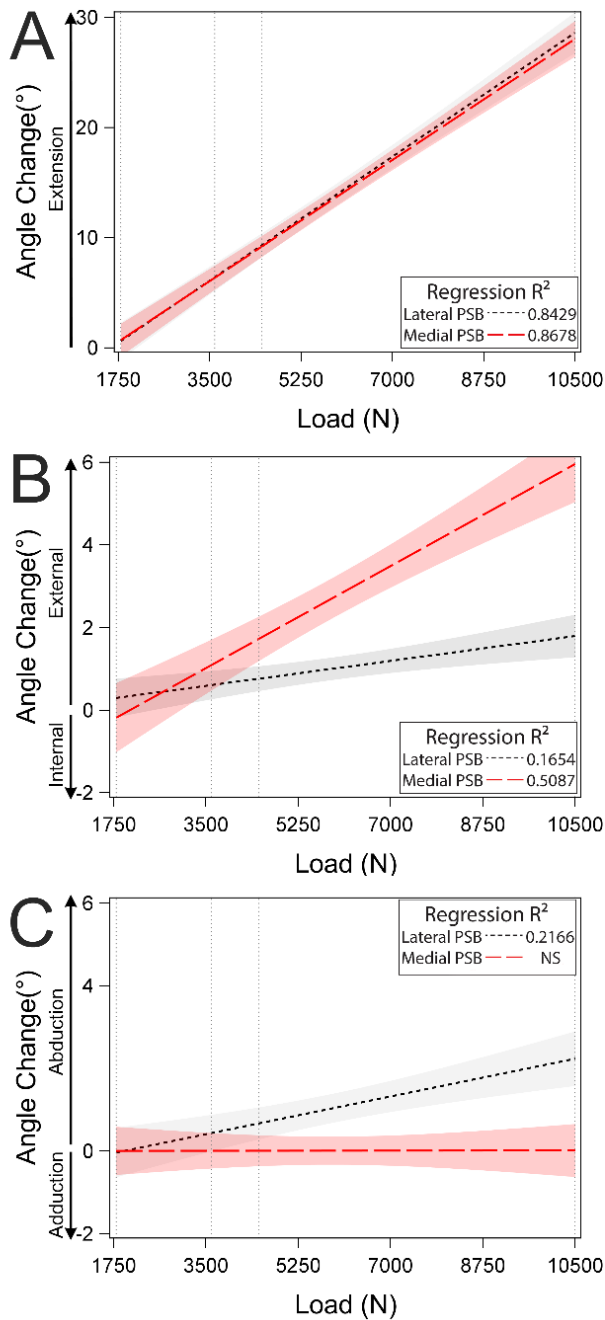


**Figure 6.4:** Linear regressions and 95% confidence intervals for the change in medial MC3-PSB (red long-dashed line) and lateral MC3-PSB (black short-dashed line) angles from the Stand load condition for MC3-PSB flexion-extension angle (A), internal-external rotation angle (B), and abduction-adduction angle (C). Stand, Walk, Trot, and Gallop loads are indicated by vertical dashed lines. NS=non-significant

The MC3-medial PSB external rotation increased with abduction of the MC3-lateral PSB ( $r = 0.52$ ; Table 6.3). The MC3-medial PSB adduction increased as the MC3-lateral PSB externally rotated ( $r = -0.55$ ) and abducted ( $r = -0.65$ ). Additionally, lateral PSB external rotation increased with lateral PSB abduction ( $r = 0.55$ ).

**Table 6.3:** Partial Spearman correlation coefficients (r values) for the change of MC3-P1 angle and MC3-PSB angles from the Stance load condition for the Walk, Trot, and Gallop load conditions. Correlations are partial with respect to horse and all reported correlations are significant at  $p \leq 0.05$ .

		MC3-P1 Extension (+)	Medial PSB Joint Angle Change			Lateral PSB Joint Angle Change	
			Internal (-)/ External (+) Rotation	Adduction(-)/ Abduction(+)	Flexion (-)/ Extension(+)	Internal (-)/ External (+) Rotation	Adduction(-)/ Abduction(+)
Medial PSB Joint Angle Change	Internal (-)/ External (+) Rotation	0.92	.	.	.	.	.
	Adduction(-)/ Abduction(+)	NS	NS	.	.	.	.
	Flexion (-)/ Extension(+)	0.98	0.91	NS	.	.	.
Lateral PSB Joint Angle Change	Internal (-)/ External (+) Rotation	NS	NS	-0.55	NS	.	.
	Adduction(-)/ Abduction(+)	0.64	0.52	-0.65	0.68	0.55	.
	Flexion (-)/ Extension(+)	0.98	0.92	NS	0.99	NS	0.71

Note: MC3 (third metacarpal bone); P1 (proximal phalanx), PSB (proximal sesamoid bone), NS (non-significant interaction;  $p < 0.05$ ).

## 6.5 Discussion

The primary movement of both PSBs during axial limb loading is extension relative to MC3, which occurs as the PSBs wrap distodorsally around the MC3 condyle to support the limb during stance. The current study indicates that the medial and lateral PSBs have similar sagittal plane motion but differing non-sagittal plane motions during axial limb loading that are exaggerated at high-speed gallop loads. The medial PSB rotated externally more than the lateral PSB throughout loading and medial PSB external

rotation was greatest for Gallop loads. The lateral PSB abducted more than the medial PSB during limb loading; however, abduction was not significantly different among load conditions.

Study results showing large amounts of flexion-extension compared to small out-of-plane rotations for MC3-P1, MC3-medial PSB, and MC3-lateral PSBs were expected since bone and soft tissue structures in the MCPJ confine its motion primarily to flexion-extension within the sagittal plane (Figure 1.3). The sagittal ridge of the MC3 condyle interdigitates with both the sagittal groove on the proximal articular surface of P1 and the intersesamoidean ligament between the two PSBs, and in conjunction with the collateral ligaments, confines MCPJ motion to the sagittal plane. The suspensory apparatus (SA) supports the palmar aspect of the equine MCPJ, restricting excessive MCPJ extension. The SA consists of 3 structures in series, the suspensory ligament and its medial and lateral branches, the medial and lateral PSBs, and the distal ligaments of the PSBs (distal sesamoidean ligaments or DSLs). The SA originates from the proximal end of MC3 and inserts on P1 and the middle phalanx (P2). Within the SA, the suspensory ligament branches insert on the apices of the PSBs. The bases of the PSBs are bound tightly to P1 and P2 by four sets of DSLs, of which the straight and oblique DSLs are the most substantive. The PSBs are tightly bound to each other along their axial borders, on their respective sides of the sagittal ridge, by the intersesamoidean ligament.

Motion of the PSBs outside of the sagittal plane (i.e., outside of flexion-extension) may be related to PSB fracture configurations (Figure 6.1). Within the same limb the medial and lateral PSBs often fracture in different configurations, and in this study, were shown to have different non-sagittal plane motions during limb loading. Medial PSBs often fracture transversely through the midbody to basilar portion of the bone<sup>4</sup> and a focal midbody abaxial subchondral bone lesion is believed to precede fracture and increase fracture risk (Figure 6.1).<sup>12,13</sup> The observed external rotation of the medial PSB against the medial MC3 condyle could increase stresses on the abaxial portion of the PSBs articular surface and contribute to the formation of abaxial subchondral bone lesions. However, lateral PSB oblique, transverse, or axial



longitudinal fracture often accompanies medial PSB transverse fracture (Figure 6.1).<sup>4,6</sup> In the current study, abduction of the apex of the lateral PSB was observed. PSB abduction may increase tension in the intersesamoidean ligament, which tightly binds the medial and lateral PSBs.<sup>20</sup> Increased stress along the axial border of the PSBs is consistent with axial longitudinal fracture and intersesamoidean ligament rupture.

Although the non-sagittal plane MC3-PSB rotations observed in this study were consistent with commonly observed pathologies in Thoroughbred racehorses, the cause of these movements is unknown. External rotation of P1 about MC3 as observed in this study and previously,<sup>21,22</sup> may be responsible for the non-sagittal plane movement of the PSBs. External rotation of P1 relative to MC3 could facilitate external rotation of the medial PSB, since the medial PSB is tightly bound to P1 via the medial collateral sesamoidean ligament (Figure 1.2). If this interaction occurs, the higher MC3-P1 external rotations observed in vivo indicates that MC3-PSB external rotation is greater in live horses.<sup>23</sup> External rotation of the medial PSB and constraint of the lateral PSB by the MC3 sagittal ridge may increase stress on the intersesamoidean ligament and axial border of the lateral PSB. External rotation of P1 relative to MC3 may increase stress on the base of the lateral PSB by the lateral oblique distal sesamoidean ligament (OSL) and contribute to abduction of the apex of the lateral PSB (Figure 6.5). Lateral OSL lesions are more prevalent than medial OSL lesions in Thoroughbred racehorses, and lesions within the suspensory apparatus were associated with 4.6 times increased odds of having suffered a suspensory apparatus failure (e.g. PSB fracture, suspensory ligament rupture, or distal sesamoidean ligament rupture).<sup>24</sup> Collectively, these factors could promote lateral PSB axial longitudinal fracture or intersesamoidean ligament rupture.

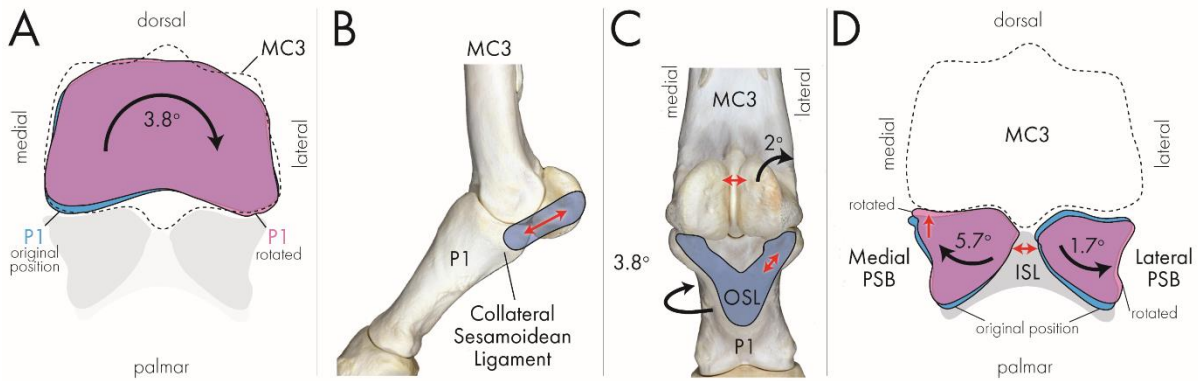


**Figure 6.5:** Non-sagittal plane rotations of the proximal phalanx (P1) and the proximal sesamoid bones (PSBs) relative to the third metacarpal bone (MC3) and the potential interaction between these rotations and metacarpophalangeal joint ligaments at gallop equivalent load. External rotation of P1 about MC3 (Panel A) may increase tension in the medial collateral sesamoidean ligament (Panel B) and in the lateral branch of the lateral oblique sesamoidean ligament (OSL; Panel C). Increased tension in the medial collateral sesamoidean ligament may cause the observed external rotation of the medial PSB (Panel D) and increase contact between the medial PSB's abaxial surface and the MC3 condyle, promoting subchondral bone lesion formation. The non-sagittal plane PSB rotations likely increase tension in the intersesamoidean ligament (ISL; Panel D). Increased tension in the lateral OSL may cause the abduction and slight-internal rotation observed to occur on the lateral PSB; this may promote lateral PSB fracture.

Horse- and training-specific factors may influence MC3-PSB rotations. Individual MCPJ conformation and shoeing may impact the direction of MC3-P1 internal-external rotation and abduction-adduction,<sup>21,23</sup> so conformation may impact PSB-MC3 rotations. Additionally, in Thoroughbreds, medial PSBs are shorter and wider than lateral PSBs and the medial MC3 condyle tends to be larger than the lateral condyle;<sup>4,25,26</sup> the size differences combined with specific articular surface geometries may contribute to the amount of non-sagittal motion. However, geometries of PSB and MC3 articular surfaces are not known in enough detail to support or refute this idea. Finally, horseshoe (e.g., mediolateral geometry) and race-surface characteristics (e.g. uneven footing) affect forelimb kinetics and kinematics,<sup>21,27,28</sup> so may also affect MC3-PSB rotations. This study indicates that medial PSB external rotation and lateral PSB abduction increases with MC3-P1 extension; so, horses with conformation, horseshoes, or other characteristics that increase MC3-P1 extension may experience greater non-sagittal plane MC3-PSB rotations.

The MC3-P1 angles observed in this study were consistent with previous work.<sup>14,18,21,23,29</sup> Mean MC3-P1 extension at Walk, Trot, and Gallop are consistent with in vivo.<sup>14,18,29</sup> Mean MC3-P1 external rotation and abduction between Stand and Gallop is consistent with an in vitro study, but less than the external rotation and abduction observed in vivo.<sup>14,23</sup>

MC3-P1 abduction was not observed in the current or other in vitro studies that restricted mediolateral hoof movement and/or kept the hoof at a neutral position.<sup>14,21</sup> However, there is evidence that P1 abduction occurs in vivo during limb loading ( $18 \pm 7$  degrees at trot)<sup>23</sup> and in vitro during asymmetric hoof placement.<sup>21</sup> MC3-P1 abduction would induce bending about the fetlock joint, increasing compression on the lateral side of the joint and tension on the medial side. This hypothesis is supported by higher density tissue observed in the lateral MC3 condyle, compared to the medial condyle (Riggs, et. al., 1999).<sup>30</sup> Mediolateral bending during fetlock extension may also contribute to characteristic racehorse fetlock fracture patterns (Figure 6.6). Transverse fracture is more common in the medial PSB (70%) than in the lateral PSB (30%, Anthenill, et. al., 2006) which is consistent with medial PSB failure under tension.<sup>39</sup> Since bone is generally weaker in tension than compression, and lesions that predispose to fracture are common in the medial PSB, fetlock failure may be initiated by tension in the medial PSB.<sup>11</sup> Oblique and axial longitudinal fractures are more common in the lateral PSB than the medial PSB,<sup>4</sup> which is consistent with compression contributing to lateral PSB failure. Further, 73% of biaxial PSB fractures involving medial PSB fracture and lateral PSB axial longitudinal fracture or axial intersesamoidean ligament rupture also involve lateral MC3 condylar fracture (a complex fetlock breakdown).<sup>6</sup> These complex fetlock breakdowns can similarly be attributed to excessive compressive loading of the lateral MC3 condyle. Variations in lateral PSB abduction may affect risk for complex breakdowns, by altering loading along the axial aspect of the lateral PSB. However, 92% of biaxial PSB fractures, involving medial PSB transverse and lateral PSB oblique fractures, are not associated with MC3 condylar fracture. Lateral compartment compression, due to MC3-P1 abduction, also offers a possible explanation for the higher prevalence of lateral MC3 condylar

fractures (76-85%)<sup>1,31</sup> compared to medial condylar fractures (8-15%), despite the larger geometry and surface area of the medial condyle.<sup>25,32</sup> Speculating further, a common P1 fracture configuration originates in or near the sagittal groove and courses obliquely distally to exit the lateral cortex.<sup>33</sup> This fracture configuration is consistent with P1 abduction and excessive compressive loading of the lateral aspect of the bone column. Importantly, in vitro evidence indicates MC3-P1 kinematics are influenced by hoof asymmetry,<sup>21,34,35</sup> therefore hoof conformation, shoeing, and racetrack surface topography could affect risk or protection for fetlock failure.

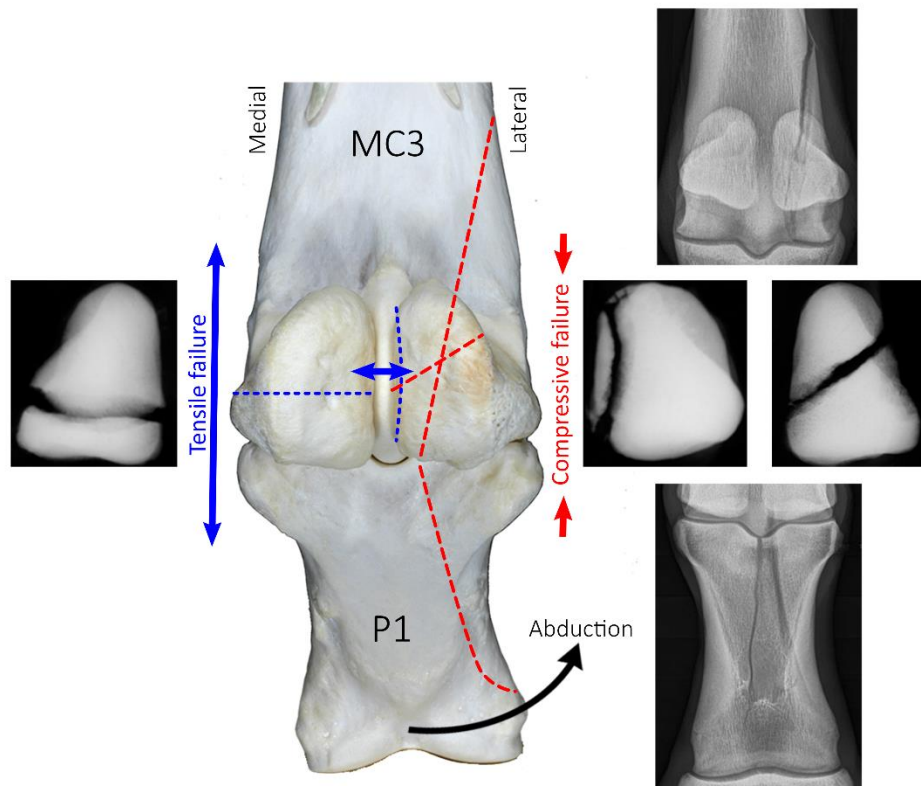


**Figure 6.6:** Dorsopalmar radiographs illustrate characteristic fractures in the proximal sesamoid bones (PSBs), third metacarpal bone (MC3), and proximal phalanx (P1). Abduction of P1 relative to the MC3 during limb loading would induce bending about the fetlock joint with tension on the medial side of the joint and compression on the lateral side of the joint. The characteristic fracture patterns that occur in MC3, PSBs, and P1 are consistent with this loading condition. The medial PSB typically has a transverse fracture, consistent with tensile failure. The axial avulsion fracture of the lateral PSB is consistent with abduction of the apex of the lateral PSB and tension from the intersesamoidean ligament. The typical oblique fracture in the lateral PSB that commonly occurs with biaxial PSB fracture and the fractures in the lateral condyle of the MC3 and lateral oblique component common to some P1 fractures would be promoted by excessive compression on the lateral aspect of the fetlock.

The primary study limitation is that the study was performed in vitro instead of in vivo; however, in vivo PSB markers are impractical in live horses. In addition to presenting a significant welfare issue due to increased fracture risk, bone-fixed kinematic markers would be difficult to maintain during high-speed gallop as the fetlock can impact the ground. The slow, non-physiologic loading rates used in this study may have allowed for soft tissue stress relaxation during loading. However, the limbs were preconditioned and reported MC3-P1 extension angles are consistent with those from in vivo studies.<sup>14,18,29</sup> Also, applied loads are consistent with the ranges for Stand (1.5-1.8 kN)<sup>16</sup>, Walk (3.9 – 3.5 kN),<sup>17</sup> Trot (4.4-8.1kN),<sup>17,36,37</sup> and Gallop (8.3-12.3kN)<sup>19,38</sup> midstance (peak load) in previous studies estimated for a 500-600kg horse. The sample size was adequate. Post hoc study power was > 0.9 for all significant study variables except for lateral PSB abduction using  $\alpha=0.05$ ; lateral PSB abduction had a power of 0.4. Although not all limbs were sourced from racehorses (4 Thoroughbred racehorses, 3 other breeds) and there was a wide age range for study horses (2 to 21 years), breed and age did not have statistically significant effects on study outcomes.

In summary, the medial and lateral PSBs experience different non-sagittal plane motions during biomechanical testing at loads consistent with a racing-speed gallop. External rotation of the medial PSB is consistent with midbody fractures commonly reported in medial PSBs and abduction of the lateral PSB is consistent with axial longitudinal fracture frequently seen in lateral PSBs.

## **6.6 Acknowledgements**

The authors thank Dr. Ellen Singer for her insightful comments on metacarpophalangeal anatomy and function. This work was supported by the University of California-Davis School of Veterinary Medicine Students Training in Advanced Research Program, Grayson Jockey Club Research Foundation, Center for Equine Health (with funds provided by the State of California satellite wagering fund and contributions

from private donors), Maury Hull Fellowship, Louis R. Rowan Fellowship, and the Le Maitre Wild Oak Farm Endowment.

## 6.7 References

1. Johnson BJ, Stover SM, Daft BM, et al. 1994. Causes of death in racehorses over a 2 year period. *Equine Vet. J.* 26(4):327–330 Available from: <http://doi.wiley.com/10.1111/j.2042-3306.1994.tb04395.x>.
2. Sun TC, Riggs CM, Cogger N, et al. 2019. Noncatastrophic and catastrophic fractures in racing Thoroughbreds at the Hong Kong Jockey Club. *Equine Vet. J.* 51(1):77–82 Available from: <https://onlinelibrary.wiley.com/doi/10.1111/evj.12953>.
3. Wylie CE, McManus P, McDonald C, et al. 2017. Thoroughbred fatality and associated jockey falls and injuries in races in New South Wales and the Australian Capital Territory, Australia: 2009–2014. *Vet. J.* 227:1–7 Available from: <https://doi.org/10.1016/j.tvjl.2017.06.008>.
4. Anthenill LA, Stover SM, Gardner IA, et al. 2006. Association between findings on palmarodorsal radiographic images and detection of a fracture in the proximal sesamoid bones of forelimbs obtained from cadavers of racing Thoroughbreds. *Am. J. Vet. Res.* 67(5):858–868 Available from: <http://avmajournals.avma.org/doi/abs/10.2460/ajvr.67.5.858>.
5. Stover SM. 2013. Diagnostic Workup of Upper-Limb Stress Fractures and Proximal Sesamoid Bone Stress Remodeling. In: *AAEP Proceedings; In-Depth: Racing-Related Lameness*. p 427–435.
6. Hill AE. 2020. Unpublished Data.
7. Stover SM. 2003. The Epidemiology of Thoroughbred Racehorse Injuries. *Clin. Tech. Equine Pract.* 2(4):312–322.
8. Riggs CM. 2002. Fractures - A preventable hazard of racing thoroughbreds? *Vet. J.* 163(1):19–29.
9. Anthenill LA, Gardner IA, Pool RR, et al. 2010. Comparison of macrostructural and microstructural bone features in Thoroughbred racehorses with and without midbody fracture of the proximal sesamoid bone. *Am. J. Vet. Res.* 71(7):755–765 Available from: <http://avmajournals.avma.org/doi/abs/10.2460/ajvr.71.7.755>.
10. Shaffer SK, Stover SM, Fyhrie DP. 2020. Morphological Changes in Proximal Sesamoid Bones from Racehorses as a Model for Overuse Joint Injuries. In: *ORS 2020 Annual Meeting*. p Paper No. 2312.
11. Shaffer SK, To C, Garcia TC, et al. 2021. Subchondral focal osteopenia associated with proximal sesamoid bone fracture in Thoroughbred racehorses. *Equine Vet. J.* 53(2):294–305 Available from: <https://onlinelibrary.wiley.com/doi/abs/10.1111/evj.13291>.
12. Ayodele BA, Hitchens PL, Wong ASM, et al. 2020. Microstructural properties of the proximal sesamoid bones of Thoroughbred racehorses in training. *Equine Vet. J.* (November):1–9.
13. Shaffer SK, Sachs N, Garcia TC, et al. 2021. In vitro assessment of the motion of equine proximal sesamoid bones relative to the third metacarpal bone under physiologic midstance loads. *Am. J.*

- Vet. Res. 82(3):198–206 Available from:  
<https://avmajournals.avma.org/doi/10.2460/ajvr.82.3.198>.
14. Singer E, Garcia T, Stover S. 2013. How do metacarpophalangeal joint extension, collateromotion and axial rotation influence dorsal surface strains of the equine proximal phalanx at different loads in vitro? *J. Biomech.* 46(4):738–744 Available from:  
<http://dx.doi.org/10.1016/j.jbiomech.2012.11.028>.
  15. Grood ES, Suntay WJ. 1983. A joint coordinate system for the clinical description of three-dimensional motions: Application to the knee. *J. Biomech. Eng.* 105(2):136–144.
  16. BRAMA PAAJ, Karssenber D, Barneveld A, Weeren PR. 2001. Contact areas and pressure distribution on the proximal articular surface of the proximal phalanx under sagittal plane loading. *Equine Vet. J.* 33(1):26–32.
  17. Schryver HF, Bartel DL, Langrana N, Lowe JE. 1978. Locomotion in the horse: kinematics and external and internal forces in the normal equine digit in the walk and trot. *Am. J. Vet. Res.* 39(11):1728–1733.
  18. Setterbo J, Garcia T, Campbell I, et al. 2009. Forelimb Kinematics of Galloping Thoroughbred Racehorses Measured on Dirt, Synthetic, and Turf Track Surfaces (P235). In: *The Engineering of Sport 7*. Paris: Springer Paris. p 437–446 Available from: [http://link.springer.com/10.1007/978-2-287-99056-4\\_54](http://link.springer.com/10.1007/978-2-287-99056-4_54).
  19. Swanstrom MD, Zarucco L, Hubbard M, et al. 2005. Musculoskeletal Modeling and Dynamic Simulation of the Thoroughbred Equine Forelimb During Stance Phase of the Gallop. *J. Biomech. Eng.* 127(2):318–328 Available from:  
<https://asmedigitalcollection.asme.org/biomechanical/article/127/2/318/469840/Musculoskeletal-Modeling-and-Dynamic-Simulation-of>.
  20. Weaver JCB, Stover SM, O'Brien TR. 1992. Radiographic anatomy of soft tissue attachments in the equine metacarpophalangeal and proximal phalangeal region. *Equine Vet. J.* 24(4):310–315.
  21. CHATEAU H, DEGUEURCE C, JERBI H, et al. 2001. Normal three-dimensional behaviour of the metacarpophalangeal joint and the effect of uneven foot bearing. *Equine Vet. J.* 33(S33):84–88 Available from: <https://onlinelibrary.wiley.com/doi/10.1111/j.2042-3306.2001.tb05366.x>.
  22. Merritt JS, Pandy MG, Brown NAT, et al. 2010. Mechanical loading of the distal end of the third metacarpal bone in horses during walking and trotting. *Am. J. Vet. Res.* 71(5):508–514 Available from: <http://avmajournals.avma.org/doi/abs/10.2460/ajvr.71.5.508>.
  23. Clayton HM, Sha D, Stick J, Elvin N. 2007. 3D Kinematics of the equine metacarpophalangeal joint at walk and trot. *Vet. Comp. Orthop. Traumatol.* (20):86–91.
  24. Hill AE, Gardner IA, Carpenter TE, et al. 2016. Prevalence, location and symmetry of noncatastrophic ligamentous suspensory apparatus lesions in California Thoroughbred racehorses, and association of these lesions with catastrophic injuries. *Equine Vet. J.* 48(1):27–32 Available from: <http://doi.wiley.com/10.1111/evj.12367>.
  25. Alrtib AM, Philip CJ, Abdunnabi AH, Davies HMS. 2013. Morphometrical study of bony elements of the forelimb fetlock joints in horses. *J. Vet. Med. Ser. C Anat. Histol. Embryol.* 42(1):9–20.
  26. Beccati F, Gialletti R, Giontella A, et al. 2014. Morphologic radiographic study of the proximal

- sesamoid bones of the forelimb in thoroughbred racehorses in training. *J. Vet. Med. Ser. C Anat. Histol. Embryol.* 43(5):403–407.
27. Harvey AM, Williams SB, Singer ER. 2012. The effect of lateral heel studs on the kinematics of the equine digit while cantering on grass. *Vet. J.* 192(2):217–221 Available from: <https://linkinghub.elsevier.com/retrieve/pii/S1090023311002176>.
  28. Roepstorff L, Johnston C, Drevemo S. 1999. The effect of shoeing on kinetics and kinematics during the stance phase. *Equine Exerc. Physiol.* 5(S30):279–285 Available from: <http://doi.wiley.com/10.1111/j.2042-3306.1999.tb05235.x>.
  29. Butcher MT, Ashley-Ross MA. 2002. Fetlock joint kinematics differ with age in thoroughbred racehorses. *J. Biomech.* 35(5):563–571 Available from: <https://linkinghub.elsevier.com/retrieve/pii/S0021929001002238>.
  30. Riggs CM, Whitehouse GH, Boyde A. 1999. Structural variation of the distal condyles of the third metacarpal and third metatarsal bones in the horse. *Equine Vet. J.* 31(2):130–139 Available from: <https://onlinelibrary.wiley.com/doi/10.1111/j.2042-3306.1999.tb03806.x>.
  31. Zekas LJ, Bramlage LR, Embertson RM, Hance SR. 1999. Characterisation of the type and location of fractures of the third metacarpal/metatarsal condyles in 135 horses in central Kentucky (1986–1994). *Equine Vet. J.* 31(4):304–308 Available from: <https://onlinelibrary.wiley.com/doi/10.1111/j.2042-3306.1999.tb03821.x>.
  32. Singh B. 2017. The Forelimb of the Horse. In: Dyce, Sack, and Wensing's Textbook of Veterinary Anatomy, 5th ed. Saunders.
  33. Smith MRW, Wright IM. 2014. Radiographic configuration and healing of 121 fractures of the proximal phalanx in 120 Thoroughbred racehorses (2007–2011). *Equine Vet. J.* 46(1):81–87 Available from: <https://onlinelibrary.wiley.com/doi/10.1111/evj.12094>.
  34. Denoix J-M. 1999. Functional Anatomy of the Equine Interphalangeal Joints. *AAEP Proc.* 45:174–177.
  35. Chateau H, Degueurce C, Denoix J-M. 2010. Three-dimensional kinematics of the distal forelimb in horses trotting on a treadmill and effects of elevation of heel and toe. *Equine Vet. J.* 38(2):164–169 Available from: <http://doi.wiley.com/10.2746/042516406776563260>.
  36. Hjertén G, Drevemo S. 1994. Semi-quantitative analysis of hoof-strike in the horse. *J. Biomech.* 27(8):997–1004 Available from: <https://linkinghub.elsevier.com/retrieve/pii/002192909490216X>.
  37. Setterbo JJ, Garcia TC, Campbell IP, et al. 2009. Hoof accelerations and ground reaction forces of Thoroughbred racehorses measured on dirt, synthetic, and turf track surfaces. *Am. J. Vet. Res.* 70(10):1220–1229 Available from: <http://avmajournals.avma.org/doi/abs/10.2460/ajvr.70.10.1220>.
  38. Kingsbury HBB, Quddus MA, Rooney JR, Geary JE. 1978. A laboratory system for production of flexion rates and forces in the forelimb of the horse. *Am. J. Vet. Res.* 39(3):365–369.
  39. Markel MD. Fracture Biology and Mechanics. In: *Equine Surgery*, JA Auer Editor. WB Saunders Co, Philadelphia, 1992 Pgs 798–807



## **Chapter 7: Conclusion**

The research presented in this dissertation is related to understanding 1) densitometric and histomorphologic features associated with subchondral bone stress-reactions (tissue changes) that precede stress fractures; 2) unique features of a stress-reactions that promote a complete stress fracture; 3) loading circumstances associated with stress-reactions and complete fracture development; and 4) the interaction of bone's biological turnover and repair processes with microdamage accumulation involved in stress fracture development.

The Thoroughbred racehorse provides an opportunity to investigate subchondral bone stress-reactions. Specifically, the proximal sesamoid bones (PSBs) of the distal forelimb were used for this research. As discussed in Section 1.5, PSB fractures are the most common cause of death for racehorses worldwide. Besides providing supporting evidence that PSB fractures are related to exercise – and thus emphasizing that training programs could be modified to prevent PSB fractures and subsequent death – this research is generally applicable to stress fractures in other species.

Three specific Aims were provided in Section 1.6. A summary of the research presented in this dissertation, in response to the three Aims, follows.

### **7.1 Summary: Aim 1**

As outlined in Section 1.6, the first specific Aim of this research was:

*To compare microstructural and macrostructural features of PSBs from Thoroughbred racehorses with and without unilateral biaxial PSB fractures to identify bone abnormalities that precede fracture.*

This Aim was addressed in Chapters 2 and 3. In these chapters, fractured PSBs from racehorses that experienced a PSB fracture were compared to the intact PSB in the opposite (contralateral) forelimb and to intact PSBs from Control horses. In Chapter 2, two sample sets of racehorse PSBs were examined. In the first set, morphological differences observable with the naked eye (Sections 2.4.1) were characterized. In the second set, morphological differences observable via microcomputed tomography ( $\mu$ CT; Sections 2.4.2) were characterized. In Chapter 3, the same set of PSBs examined for morphological differences observable with the naked eye were examined for differences via  $\mu$ CT and microscopy. We observed 1) a focal bone lesion in Case PSBs that was not present in Controls and 2) higher density tissue in the center of Case PSBs compared to Controls. The lesion was consistently found in the subchondral tissue (directly below the articular surface) near the midbody on the abaxial aspect of the Case medial PSBs. Upon gross examination, this lesion appeared as a focal discoloration. Further examination revealed that, this region of focal discoloration also had a low bone volume fraction (low density), a low tissue mineral density, and high levels of microdamage compared to surrounding tissue (i.e., was a bone lesion). A focal lesion with the described characteristics is consistent with a bone's biological damage-repair response occurring beneath a joint surface (see Section 1.3.1). Further, since both forelimbs experience similar loads at racing-speeds, the bilateral presence of the lesion indicates exercise programs are related to its development; this idea is explored in Aim 2. The consistent location of the lesion indicates bone anatomy may lead to its development at that site; this concept is explored in Aim 3. The bone immediately surrounding the lesion and in another region of the subchondral tissue had high density and less microdamage and was similar in Case and Controls. Additionally, we found that tissue in the center of the PSB was denser in Case PSBs, compared to controls. More loading in Case bones could cause the higher internal density (see Section 1.3.2), which also implies that specific exercise programs are associated with Case PSB. Overall, these findings indicate that at the osteopenic lesion site, repair of microdamage by remodeling was not successful (e.g., lower bone mass, increased damage, lower mineralization) but that

in regions away from the lesion remodeling successfully controlled damage (e.g., higher bone mass, less microdamage, lower mineralization). These findings support the hypothesis that PSB fractures are stress fractures

This work is novel in that it systematically characterized changes associated with PSB fracture within the subchondral tissue of racehorse PSBs. Anecdotally, many of the differences observed with the naked eye (like a focal bruise) had been observed at necropsy. This work is (to our knowledge) the first time microdamage was characterized within the subchondral tissue of the PSBs. A previous study looked for microdamage within the central trabecular tissue— but only observed a very low damage density in the center of the PSB.<sup>1</sup> This observation is consistent with our findings; stained microdamage was not found in the internal trabecular region histology samples. Additionally, previous work characterized changes on the palmar aspect of the PSBs and reported a lesion may develop at this location; the palmar lesion was rarely seen in our samples.<sup>2</sup> However, in the report showing palmar lesions (which was conducted in our laboratory) the subchondral surface was not examined.

The current work is clinically relevant because it indicates specific regions within the PSB that should be examined to determine if a horse is at an immediate fracture risk. Current clinical tools cannot determine bone volume fraction, tissue mineral density, and microdamage density at the resolution required to detect relevant, focal, differences in these variables. Simply, the distal forelimb of a horse will not fit in common  $\mu$ CT machines (designed for small research samples) and both radiographs and only emerging clinical veterinary (standing) computed tomography (CT) technology with enhanced resolution may detect the lesion.

One method that can be used to detect the biological activity in these lesions is positron emission tomography (PET). PET visualizes radiotracer uptake; while many different radiotracers can be used, increased uptake of  $^{18}\text{F}$ -NaF is a marker of bone formation.<sup>3</sup> Recent advancements have allowed clinicians

to use PET to identify focal uptake in a subchondral location that appears to be the same as the lesion described in this Aim.<sup>4,5</sup> In the future, if a horse with a recent PET scan showing this focal uptake dies, the PSBs could be examined with  $\mu$ CT to determine if the PET-identified region is the same as the focal subchondral lesion identified in this Aim.

### **7.3 Summary Aim 2**

As outlined in Section 1.6, the second specific Aim of this research was:

*To determine if the structural measures identified in Aim 1 are linked to horse exercise and to determine if a compartment model of bone tissue turnover cycle can be used to explain and predict the observed changes.*

This Aim was addressed in Chapters 3 & 4. We observed that exercise intensity was negatively related to bone volume fraction (BVF) and positively related to microcrack areal density in within the subchondral lesion; however, in the undamaged, central trabecular site, the relationships were opposite in direction (Chapter 3). Using the compartment model, these contradictory relationships are explained if model rate constants depend on exercise intensity in a location-specific manner (Chapter 3 & 4). We hypothesize that these relationships are due to differing strain distributions in the subchondral and internal tissues. Regardless of location where tissue mineral density (TMD) was measured, TMD decreased with event frequency in both Case and Control PSBs, suggesting bone turnover increased with exercise.

The compartment model for bone's tissue turnover cycle introduced for this Aim is novel. We were able to show, in Chapter 4, that the compartment model could be solved at steady-state using observed densitometric and histomorphologic data. Additionally, the relationships found in this Aim between observable bone tissue properties and horse exercise add to the body of evidence indicating that PSB fractures in racehorses are stress-fractures associated with the formation of a subchondral lesion.

## 7.2 Summary Aim 3

As outlined in Section 1.6, the third specific Aim of this research was:

*To determine the motion of the proximal sesamoid bones at racing-speed load conditions and if their motions may contribute to the formation of the abnormalities observed in Aim 1.*

This Aim was addressed in Chapters 5 & 6. In both studies, equine cadaveric forelimbs were axially loaded to simulate standing and peak mid-stance walk, trot, and gallop load conditions (1.8-10.5 kN). The first study (Chapter 5) used radiographic images to determine the sagittal-plane position of the PSBs and linear variable differential transformers to determine if the PSBs separated during axial limb loading. The second study (Chapter 6), use kinematic markers to track three-dimensional motion of the metacarpophalangeal (fetlock) joint bones. Section 1.5.1 contains a review of fetlock anatomy. In brief, the PSBs articulate only with the third metacarpal bone (MC3) and not the proximal phalanx (P1). The MC3 has a continuous articular surface that changes its curvature at the transverse ridge (TR); the PSBs are congruent with the surface proximal to the TR and the P1 is congruent with the surface distal to the TR. This work is novel because it specifically describes the PSBs motion during axial loading. In existing literature, the kinematics reported for the fetlock joint only describe the articulation of the MC3 relative to P1 (see Section 1.5.2).

Our first finding was that the distal edge of the PSBs moved distal to the TR of the MC3 at a gallop-equivalent load (10.5 kN) but not at lower load conditions (Chapter 5). This observation indicates that the distal end of the PSBs moved beyond the congruent articular surface at racing-speed loads; this motion likely leads to an articular incongruity. Two previous studies have looked at fetlock joint congruity and if the distal edge of the PSB moves beyond the TR during axial loading; one study was consistent with our results<sup>6</sup> and one was not.<sup>7</sup> However, it is unclear if racing-speed loads were simulated in the study with contradicting results.<sup>7</sup> Our second finding was that the PSBs experience movement outside of the sagittal

plane during axial loading. The linear variable differential transformers indicated that palmar surfaces of the PSBs rotated away from each other during fetlock joint extension and the amount of rotation increased with load. The full kinematic analysis (Chapter 6), showed that the medial and lateral PSBs had different non-sagittal plane motions. Specifically, the medial PSB rotated externally and the lateral PSB apex abducted during limb loading. Motion outside of the sagittal plane was unexpected, as fetlock anatomy confines MC3-P1 motion primarily to the sagittal plane (see Section 1.5.2).

These findings are likely related to the formation of the abaxial subchondral lesion found in medial PSBs (see Aim 1). First, movement of the PSBs beyond its congruent articular surface on the MC3 imply that an articular incongruity (a mismatch between the opposing joint surfaces) could occur near the distal aspect of the PSB. Second, external rotation of the medial PSB may increase the contact stress on the abaxial aspect of the medial PSBs. The (potential) incongruity was only observed at gallop loads and medial PSB external rotation was maximal at gallop loads. These observations suggest PSB motion at the gallop might cause an increased tissue strain on the abaxial aspect of the PSB – at the location where the lesion develops – compared to the tissue strain at lower gaits. We attempted to inject dye into the joint capsule to determine if the articular incongruity occurs at the gallop-equivalent load (as an additional step in Chapter 5); however, we abandoned this procedure because we were unable to consistently get dye into (and flushed from) the joint capsule at maximal fetlock extension. In the future, pressure film could be placed inside the joint capsule to determine joint contact (and pressure changes) at the varying load levels.

## **7.4 Study Strengths & Limitations**

It is important to keep in mind the sample size, fracture characteristics, and population of racehorses the examined PSBs were drawn from when interpreting the results of Aims 1 & 2. The choice of which

bones to examine were made so that a sample set could be examined in detail. However, the sample selection also imposes some limitations for interpretation of results.

Case horses experienced unilateral biaxial fracture where the medial and lateral PSB fractures were transverse, oblique, or comminuted (see Section 1.5.3); biaxial PSB fractures involving axial longitudinal fracture of the lateral PSB and uniaxial (single) PSB fractures were not included. These two fracture configurations were excluded because they occur much less frequently than the examined biaxial PSB fracture configurations.<sup>8,9</sup> Therefore, we do not know if the observed lesion is related to these other PSB fracture configurations. Based on the results of Aim 3, we can hypothesize that the other fracture configurations are caused by fatigue processes occurring in different locations within the PSBs or within the third metacarpal bone (see Section 4.5). Second, the subchondral lesion was described in only medial PSBs and lateral PSBs were not examined. Therefore, we do not know if the lateral PSB would contain a similarly abaxial, subchondral lesion. However, because we observed less external rotation of the lateral PSB compared to the medial PSB (see Chapter 6), we predict that an abaxial lesion would not be observed in lateral PSBs. Third, only a small sample set (30 PSBs from 20 horses) of California Thoroughbred racehorses were used to describe lesion characteristics. Horses in other racing populations, which may have different training programs, racetrack surfaces, medication rules, veterinary inspection regulations, etc., may or may not develop these lesions. However, PSB fracture is the leading cause of death of racehorses worldwide; and the biaxial configuration we examined is (when fracture configurations specifics are reported) also the most common worldwide. Additionally, we did report that the lesion was observed in a second, independent set of California racehorses (36 PSBs from 18 horses; see Section 2.3.2); this indicates that the lesion is broadly found in the Californian population. Since the publication of Chapter 2, this lesion has been observed clinically in other Thoroughbred populations using magnetic resonance imaging (see Figure 5.5) and in Australian racehorses using microcomputed tomography.<sup>10</sup> Therefore, we can reasonably expect that it is present in the general racehorse population – and not

exclusive to California. Anecdotally, PSB fractures are rare in the general performance horse population (e.g., in jumping horses, reining horses, etc.).<sup>11</sup> The observation that this lesion develops consistently in multiple racing populations supports the idea that high-intensity (frequent) gallop-speed work, rather than lower-speed activity, is linked to its development. However, it is possible that Thoroughbred racehorse conformation (specific anatomy), genetics, or other factors are involved in its formation.

One advantage to our sample selection, especially relevant to Aim 2, is that all examined PSBs were from horses that died due to musculoskeletal injuries sustained during race-training. Often, in bone Case-Control studies, a non-exercising control group is used to determine exercise-related differences from an exercising case group. However, we wanted to know which aspects of race-training were related to PSB fractures (and, as stress fractures, would be causal to these fractures) rather than if any exercise increased fracture risk. The use of Case and Controls that were both in race-training adds, perhaps, more confidence in our findings that greater exercise in the 6-8 months prior to death and training after an extended absence (layup) have a greater effect on lesion formation than other exercise parameters (for example, total distance accumulated over the horse's life). Further, the use of Controls that fractured a different bone (not the PSB) is important as stress fractures occur in other racehorse bones besides the PSBs. These other stress fractures tend to occur in a different (typically younger) subset of racehorses that are in training. So, the observations made from the sample set used in this work highlight which aspects of a training program lead specifically to PSB stress fractures, rather than to stress fractures in other bones.

The primary limitations of Aim 3 are that it was performed on a convenience sample of a small number of limbs (less than 10 per study) and it was performed in vitro. Not all limbs were sourced from racehorses and the age range (2-21 years) was larger than is typical in racehorses; however, horse breed and age did not statistically affect results. If this work is repeated in the future, it may be advantageous to either increase the sample size (to ensure breed or age-related changes could be detected) or to only source



limbs from racehorses. As discussed in Chapters 5 & 6, the observed motion of the MC3 relative to the P1 matched previous in vivo work. Therefore, we expect that our in vitro studies also replicate in vivo PSB motion. However, an in vivo study could account for the effect of muscle activation on PSB motion, hoof surface interactions, and other factors. Additionally, the kinematic markers were only approximately aligned with bone axes; consequently, cross-talk could have occurred. However, data from the 1-dimensional linear variable differential transformers did show that non-sagittal plane movement of the PSBs occurred. Therefore, we have confidence in the results reported in Chapter 6.

## **7.5 Future Opportunities**

### **7.5.1 In Vivo Assessment of Morphological Changes within the PSBs**

One of the most obvious opportunities to expand upon this work is to collect morphometric changes in racehorse PSBs in vivo. This would permit observations to be made at multiple time points, instead of at time of death. The observations made in Aim 1 required destruction of the PSBs in ways inconsistent with life; so, we could only report differences (not changes) between Case and Control PSBs and among regressions for morphometric measures from multiple regions taken at time of death and exercise. However, the observations made in Aim 1 could guide an in vivo study. These observations show that the abaxial region of medial PSBs should be closely examined for a lesion and that densification of the central trabecular tissue may be an indicator that a horse has a lesion or is at risk of developing a lesion. The observed morphometric differences (Aim 1) and exercise regressions (Aim 2) reported in this dissertation support the hypothesis that PSB fractures are stress fractures, when they are interpreted through our current understanding of bone's biological response to damage and load (Section 1.3). However, tracking how PSB morphology changes with concurrent knowledge of the training program in vivo would allow for 1) better estimation of the rate constants derived in Aim 2, 2) a more direct indication of which exercise variables drive the changes in PSB morphology, and 3) confirmation that the processes are causal and not

just correlated. Our work indicates that recent exercise frequency (e.g., workouts/month) and changes in exercise frequency (e.g., days after a return from layup) are good candidates for what aspects of the race-training programs drive lesion formation.

In vivo study could incorporate the effect of medication on fracture development. We do not know the medication history of the horses studied in this dissertation. However, bone pain may be an early indicator of lesions formation and it would be interesting to correlate NSAID and/or corticosteroid use with morphology changes in vivo. Previous survey-work is mixed as to whether these medications are associated with catastrophic injury in racehorses.<sup>12</sup> Additionally, bisphosphonates are often given to racehorses (despite regulations prohibiting their use) and they are suspected of increasing stress fracture risk.<sup>13</sup> Among other effects, bisphosphonates limit bone resorption and alter the normal tissue turnover cycle. Previous work indicates risedronate (a bisphosphonate) does not alter clinically diagnosed stress fractures in military recruits when given for 12 weeks;<sup>14</sup> however, bisphosphonates can be found in the body years after their administration.<sup>13,15</sup> Additionally, when high doses of bisphosphonates were given to beagle dogs for 1 year, multiple skeletal sites in treated dogs had more microdamage and reduced fracture toughness compared to controls.<sup>16</sup> Studying the effect of bisphosphonates on a naturally occurring stress fracture in racehorses may be a model for their effect in humans.

An in vivo study would probably need to be performed by a combination of PET scanning and clinical CT. Currently, veterinary clinical CT does not have the resolution required to detect morphologic changes occurring early in lesion development. Lesions also cannot be observed with standard radiographs due to the overlying bone in the fetlock joint. As previously discussed, recent advancements, have allowed clinicians to use PET to identify focal radiotracer uptake in a subchondral location that coincides with the osteopenic lesion described in Aim 1.<sup>4</sup> Therefore, an in vivo study performed by PET scanning cannot detect changes in bone volume fraction or tissue mineral density. However, because the lesion was

associated with an increased density of central trabecular bone (in a comparatively large, 5mm wide, region), CT machines could be used to track bone volume fraction changes in this larger region as opposed to at the lesion site. The first step in such a study would be to determine if internal density changes were associated with radiotracer uptake at the lesion site. This relationship is likely: 1) the lesion was associated with increased internal trabecular bone density at death and 2) the region of high radiotracer uptake identified by PET is in the same location as what we have observed. However, we would need to confirm that the region identified by PET has the same microstructural properties as the lesion observed in Aim 1. Depending on the radiotracer, increased uptake visible with PET can be hypothesized to occur before morphologic changes can be detected by clinical CT. If this is the case, PET scanning could be used as an early screening mechanism to recommend which horses should be temporarily removed from high-intensity work until the lesion is able to heal. Further, an in vivo study could correlate PET or clinical CT results with exercise history; this would allow for more accurate determination of the rate constants (developed for Aim 2). Additionally, if enough horses were screened to determine appropriate clinical time-points, an in vivo study could recommend how and when to screen horses via PET or clinical CT before being allowed to compete to mitigate fracture risk. My work indicates clinical time-points of interest are likely 1-8 months after an increase in exercise intensity.

### **7.5.2 PSB Motion Studies**

Two opportunities for future study of PSB motion are readily apparent. First, PSB motion should be tracked in live horses (in vivo) rather than during a mechanical test. An in vivo study could confirm that the in vitro PSB motion results do mimic the in vivo motion. As discussed in Chapters 5 & 6, in vitro tests performed with the methods used are known to replicate in vivo motion of the third metacarpal bone relative to the proximal phalanx, so we expect the in vitro tests also replicate in vivo PSB motion. Second, it would be good to determine how PSB motion is affected by manageable external factors, such as shoeing, uneven footing, surface type (stiffness), and protective legwear. This type of study could be

performed in vivo or in vitro. As discussed at length in Sections 1.5.2, many of these manageable external factors affect both sagittal plane and non-sagittal plane motion of the third metacarpal bone relative to the proximal phalanx, so we to expect PSB motion would also be affected. Also, as discussed in Section 4.5, non-sagittal plane motion is likely consistent with both the PSB fractures described in this dissertation and to other commonly observed distal limb stress fractures. Clearly, exercise (another management decision) also affects fracture risk. So, it would be good to know how other management choices (like running on a banked track, which is very common in the US) affect risk. This would allow for a holistic approach for fracture prevention in racehorses that incorporates exercise programming and other manageable factors.

If an in vivo study were to be performed, x-ray reconstruction of moving morphology (XROMM) with markers embedded within the fetlock bones should be considered as a potential methodology. Kinematic markers, like those used in Chapter 6, are impractical for measuring PSB motion in live horses. Kinematic markers can be attached to the bones (bone-fixed; see Section 4.3) or attached to the skin. Both marker types would be difficult to maintain during high-speed gallop as the fetlock can impact the ground and bone-fixed markers would likely increase PSB fracture risk. XROMM uses biplanar videoradiography to capture bone motion and track embedded markers.<sup>17</sup> A recent study has shown that XROMM can be used to track fetlock motion at the walk, trot, and landing a jump;<sup>18</sup> therefore, it would likely also work at the gallop on a treadmill. XROMM would also reduce kinematic crosstalk error that can occur if kinematic markers are not well aligned with anatomic axes.<sup>19</sup>

### **7.5.3 Finite Element Modeling**

The next step for the compartment model introduced in Chapters 3 & 5 is to use the model within a finite element simulation. Because we have the experimental data from racehorse PSBs, we plan to build a finite element model for volume fraction changes as a function of exercise for racehorse PSBs. However,

the modeling approach will be valid for other species. The results of Chapters 3 & 4 indicate that several rates ( $k_1$ ,  $k_2$ , and  $k_4$ ) should be driven by exercise. Using the compartment model to predict the development of the subchondral lesion in racehorse PSBs will allow us to perform a sensitivity analysis on the specific aspects of the training program – for example, how many furlongs per month, or an activity threshold – that would predict lesion development. We predict that training programs that increase lesion development in the model would increase the fracture risk in actual racehorses. Figure 7.1 shows a diagram outlining how the compartment model could be incorporated within a larger finite element scheme. Our laboratory has a validated racehorse forelimb model that can estimate load magnitudes caused by galloping upon various race-track surfaces.<sup>20</sup> The 2D finite element mesh (shown in Figure 7.1) has been constructed based on sagittal plane uCT scans. If necessary, steady-state model rate constant estimations could be improved via an in vivo PET/clinical CT study (as previously discussed) or by counting osteoid volume on appropriately stained histologic slides.

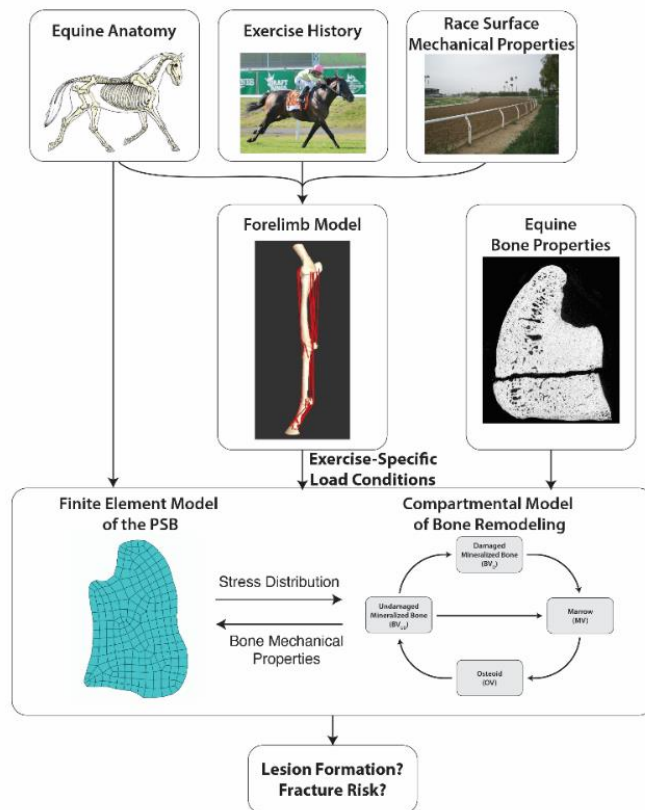


**Figure 7.1:** Flowchart of how the compartment model could be linked within a larger finite element modeling scheme.

A simple “proof-of-concept” finite element model indicates that the compartment model can be linked within a finite element scheme. This simple model uses two linear elements in series; to represent subchondral and deep tissue. The subchondral element (first in series) is loaded, and the second element (deep tissue) has its motion constrained. In this model, damage formation rate ( $k_4$ ) is linearly proportional to applied strain and the other rate constants are kept constant. Despite its simplicity, this “proof-of-concept” model is encouraging that our approach will allow us to predict changes in volume fractions with the compartment model (Figure 7.2).

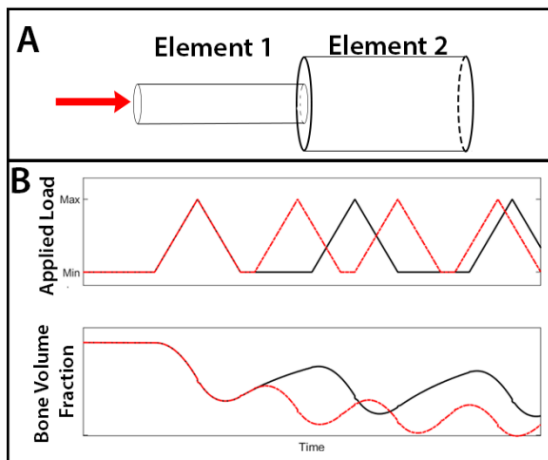


**Figure 7.2:** Two-element finite element model. **A)** A compressive load is applied to Element 1, which represents subchondral bone tissue. Element 2 represents the deeper subchondral tissue. The two elements have different areas and Young’s modulus. In each element, the Young’s modulus is set to change with bone volume fraction, following a power law ( $E = C \cdot BVF^A$  where  $C$  and  $A$  are constants). **B)** Predicted bone volume fraction (BVF) for two hypothetical load cases within Element 1 of the simple, two-element, model shown in A. In red, the load is applied more often, and the solution diverges from the black case, which is loaded less frequently.

## 7.6 Summary

Thoroughbred racehorse proximal sesamoid bones (PSBs) were used to investigate the association between subchondral stress-reactions and exercise. We documented a low bone density, low tissue mineral density, high microdamage density subchondral bone lesion that we hypothesize precedes a biaxial transverse (or oblique) PSB stress-fracture. The lesion’s densitometric and morphometric measures were significantly related to high-intensity exercise, especially 1-8 months prior to death. Additionally, we determined that the medial and lateral PSB motion during fetlock extension may be related to the consistent, abaxial location of the lesion. Finally, a compartment model of bone’s turnover cycle was introduced, and we derived steady-state values for model rate constants based on

densitometric and morphologic measures of the racehorse PSBs. Besides providing supporting evidence that the subchondral stress reaction and PSB stress fractures are related to exercise – and thus emphasizing that training programs could be modified to prevent PSB fractures and subsequent death – this research is generally applicable to stress fractures in other species.

## 7.7 References

1. Kristoffersen M, Hetzel U, Parkin TDH, Singer ER. 2010. Are bi-axial proximal sesamoid bone fractures in the british thoroughbred racehorse a bone fatigue related fracture?: A histological study. *Vet. Comp. Orthop. Traumatol.* 23(5):336–342.
2. Anthenill LA, Gardner IA, Pool RR, et al. 2010. Comparison of macrostructural and microstructural bone features in Thoroughbred racehorses with and without midbody fracture of the proximal sesamoid bone. *Am. J. Vet. Res.* 71(7):755–765 Available from: <http://avmajournals.avma.org/doi/abs/10.2460/ajvr.71.7.755>.
3. Jadvar H, Desai B, Conti PS. 2015. Sodium 18F-Fluoride PET/CT of Bone, Joint, and Other Disorders. *Semin. Nucl. Med.* 45(1):58–65 Available from: <https://linkinghub.elsevier.com/retrieve/pii/S0001299814000683>.
4. Spriet M, Espinosa P, Kyme AZ, et al. 2018. 18F-sodium fluoride positron emission tomography of the equine distal limb: Exploratory study in three horses. *Equine Vet. J.* 50(1):125–132.
5. Warren R. 2020. First Year of Equine PET Scans at Santa Anita is Success. Davis, CA. Available from: <https://www.vetmed.ucdavis.edu/news/first-year-equine-pet-scans-santa-anita-success>.
6. Vilar JM, Pinedo M, De Mier J, et al. 1995. Equine metacarpophalangeal joint surface contact changes during walk, trot and gallop. *J. Equine Vet. Sci.* 15(7):315–319 Available from: <https://linkinghub.elsevier.com/retrieve/pii/S0737080606817375>.
7. Colahan P, Piotrowski G, Poulos P. 1988. Kinematic analysis of the instant centers of rotation of the equine metacarpophalangeal joint. *Am. J. Vet. Res.* 49(9):1560–1565.
8. Anthenill LA, Stover SM, Gardner IA, et al. 2006. Association between findings on palmarodorsal radiographic images and detection of a fracture in the proximal sesamoid bones of forelimbs obtained from cadavers of racing Thoroughbreds. *Am. J. Vet. Res.* 67(5):858–868 Available from: <http://avmajournals.avma.org/doi/abs/10.2460/ajvr.67.5.858>.
9. Hill AE. 2020. Unpublished Data.
10. Ayodele BA, Hitchens PL, Wong ASM, et al. 2020. Microstructural properties of the proximal sesamoid bones of Thoroughbred racehorses in training. *Equine Vet. J.* (November):1–9.
11. Stover SM. 2015. Personal Communication.
12. Hitchens PL, Hill AE, Stover SM. 2018. Relationship between historical lameness, medication usage, surgery, and exercise with catastrophic musculoskeletal injury in racehorses. *Front. Vet. Sci.* 5(SEP):1–10.

13. McLellan J. 2017. Science-in-brief: Bisphosphonate use in the racehorse: Safe or unsafe? *Equine Vet. J.* 49(4):404–407.
14. Milgrom C, Finestone A, Novack V, et al. 2004. The effect of prophylactic treatment with risedronate on stress fracture incidence among infantry recruits. *Bone* 35(2):418–424 Available from: <https://linkinghub.elsevier.com/retrieve/pii/S8756328204001759>.
15. Riggs CM, Thompson SL, So YM, et al. 2021. Tiludronic acid can be detected in blood and urine samples from Thoroughbred racehorses over 3 years after last administration. *Equine Vet. J.* 53(6):1287–1295.
16. Mashiba T, Turner C., Hirano T, et al. 2001. Effects of suppressed bone turnover by bisphosphonates on microdamage accumulation and biomechanical properties in clinically relevant skeletal sites in beagles. *Bone* 28(5):524–531 Available from: <https://linkinghub.elsevier.com/retrieve/pii/S8756328201004148>.
17. Brainerd E. [date unknown]. X-Ray Reconstruction of Moving Morphology. Brown Univ. Available from: <https://www.xromm.org/>.
18. Childs B, Pugliese B, Carballo C, et al. 2017. Three-dimensional kinematics of the equine metacarpophalangeal joint using x-ray reconstruction of moving morphology – a pilot study. *Vet. Comp. Orthop. Traumatol.* 30(04):1–8 Available from: <http://www.thieme-connect.de/DOI/DOI?10.3415/VCOT-16-06-0095>.
19. Hull ML. 2020. Coordinate system requirements to determine motions of the tibiofemoral joint free from kinematic crosstalk errors. *J. Biomech.* 109:109928 Available from: <https://doi.org/10.1016/j.jbiomech.2020.109928>.
20. Symons JE, Hawkins DA, Fyhrie DP, et al. 2016. Hitting the ground running: Evaluating an integrated racehorse limb and race surface computational model. *J. Biomech.* 49(9):1711–1717 Available from: <http://dx.doi.org/10.1016/j.jbiomech.2016.03.057>.



**Appendix: Description of Exercise Trends in a Subset of California Racehorses**  
**with and without Proximal Sesamoid Bone Fracture**

Overall, the laboratory had access to PSBs from 96 Thoroughbred Racehorses who were euthanized while racing or training in California. From this set of 96 horses, 30 PSBs were selected from 20 horses (10 Case, 10 Control) for morphometric analysis (Chapters 2-4). The selection of this subset of horses is described in Section 2.3.1. This appendix describes the exercise history of the larger group of 96 horses. All PSB specimens were collected via the California Horse Racing Board’s racing safety program. Of the 96 horses, 39 (40%) were Affected (died from PSB fracture; referred to as Case in a majority of this dissertation) and 57 (60%) were Controls. 65% of the horse were male (intact and castrated) and 35% were female. There was no relationship between gender (stallion, gelding, mare) and Group ( $p = 0.58$ ).

The age range for affected animals is 2-14 years and for control animals is 2-8 years; there was a statistically significant difference in age between groups (Wilcoxon  $p$ -value=0.025). A full description of age range can be seen Table SA 8.1. The average day of birth for both groups was in March, indicating there is no cohort difference in birthdate that could affect when in the season a horse starts training. Even though younger horses are at a lower risk for catastrophic injuries than older (4+ y.o.) animals, we included the young horses to get a representative sample of all animals that are actively racing.

**Table SA 8.1:** Description of available ages and genders

	<b>Affected</b>	<b>Control</b>
Mean Age $\pm$ Std (Years)	4.21 $\pm$ 2.10	3.42 $\pm$ 1.29
Median Age (Years)	4	3
Age Range (Years)	(2, 14)	(2, 8)
Percentage Male	66.6%	61.4%
Percentage Female	33.3%	38.6%

The affected group ( $n=39$ ) consisted of animals with unilateral biaxial proximal sesamoid bone (PSB) fracture; a majority (70%) of affected horses fractured PSBs in the left forelimb. The PSB fracture

types included comminuted mid-body PSB fracture, simple mid-body fracture, and oblique mid-body fracture.

Within the Control group (n=57), horses were euthanized due to non-PSB fractures, disease, soft tissue injury, or “other” causes. The non-PSB fracture group consists of fractures to the carpus (n=8), third metacarpal bone (n=7), first phalanx (n=8), pastern (n=1), pelvis (n=5), humerus (n=5), radius (n=1), scapula (n=2), and tibia (n=1). The disease group consists of enterocolitis (n=1) and pneumonia (n=4); soft tissue injuries consist of superficial distal flexor tendon rupture (n=3) and suspensory ligament rupture (n=1). The “other” group consists of collapse (n=2), surgery complications (n=1), laminitis (n=3), hoof avulsion (n=1), traumatic neck fracture (n=1), and traumatic skull fracture (n=2). The cause of death for both groups is summarized in Table SA-8.2

**Table SA-8.2:** Cause of Death for Affected and Control Horses

<b>Group</b>	<b>Cause of Death</b>	<b>Number Horses</b>	<b>% of Group</b>
Affected Group (n = 39)	Comminuted Mid-body PSB Fracture	21	54
	Simple Mid-body PSB Fracture	8	21
	Oblique Mid-body PSB Fracture	10	26
Control Horses (n=57)	Non-PSB Fracture	38	68
	Disease	5	9
	Soft Tissue	4	7
	Other	10	16

## 8.1 Description of Exercise History Information

Exercise history for each animal was accessed via the encompass database; these records contain information for official timed workouts and races. Seven base variables were given for each exercise activity (Table SA-8.3). Exercise history data only includes official high-speed timed races and work-outs.

**Table SA-8.3:** Base Variables from Exercise History

<b>Base Variable</b>	<b>Definition</b>	<b>Variable Options/Format</b>
Date	Date of Event	mm/dd/yyyy
Event Type	Type of official timed exercise activity	Race, Work-out
Distance	Distance galloped for the exercise activity	# Furlongs, # Miles
Surface Type	Type of track the exercise activity occurred on	Dirt, Turf, Synthetic
Track Condition	Qualitative description of track during exercise activity based on water content.	Hard, Firm/Fast, Good to Firm, Good, Good to Yielding, Yielding, Wet Fast, Slow, Yielding to Soft, Soft, Soft to Heavy, Heavy, Muddy, Sloppy
Date of Birth	Day animal was born	mm/dd/yyyy
Date of Death	Day animal died or was euthanized	mm/dd/yyyy

A custom MATLAB program was written to derive 350 variables from the 7 base variables to describe key events in an animal's racing career. These variables are classified as "count-" and "rate-" type variables that can be further broken down in to "distance", "event", "surface-type," or "surface-condition" descriptions. The exercise history variables are designed to highlight key times in an animal's career. A list of all variable definition used in this dissertation are provided in Section 3.7. The work presented in Chapters 2-4 did not use the exercise classified on different surface types or conditions.

## 8.2 Principal Component Analysis

A principal component analysis (PCA) was performed to reduce the number of variables to use as possible predictors to classify horses as Control or Affected. The PCA was performed using Proc PrinComp in SAS 9.4. Variables were chosen to be included in a component if the magnitude of their loading score was greater than 0.08. Principal components that contributed less than 5% of total variance were not looked at for further analysis. PCA are sensitive to outliers and cannot use a variable if it has any missing values. Fifteen variables were removed from the analysis due to multiple missing values; a majority of these were surface conditions that did not appear in many exercise histories. Six horses were removed from the analysis due to outliers: 5 were Controls, 1 was Affected. Each animal was given a component

score based on the values of each variables and its associated loading for each principal component. These were used to plot the projections of the dataset along the PC-axes.

Five principal components accounted for 64.8% of the variance in the data with no individual component contributing less than 5% of total variance; this is illustrated in the scree plot in Figure 8.1. These components are composed of 244 of the 350 exercise history variables (106 variables were removed). The variables consisted of both rate- and count-type variables; distance, event, and surface type were all included. However, no surface condition variables were included in any of the PCs.

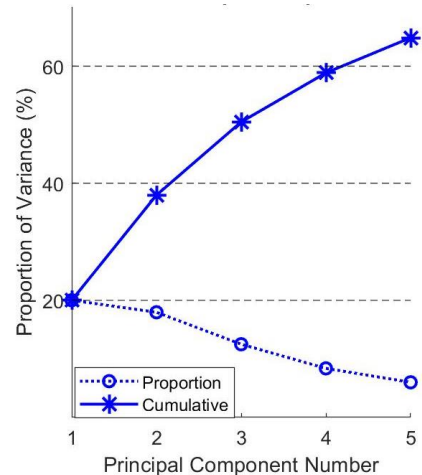


**Figure 8.1:** Scree Plot showing proportion of variance explained by each principal component and cumulative variance.

Principal Component 1 (PC1) contained primarily rate-variables describing the number of furlongs, events, and races accumulated 6 months to 1 year before death & after start on all surface types or on turf only. It also included furlongs per event, races per month active, and races per month for full career. Finally, the cumulative number of races, events, & furlongs 6 months and 1 year before death. Horses with higher values for these rates have a higher PC1 component score.

Principal Component 2 (PC2) included the same rate variables for works, furlongs, and events accumulated 6 months to 1 year before death & after starting training on dirt or synthetic surfaces. It also included count variables for number of works & events on synthetic surfaces. This component separated animals based on dirt and synthetic surface works in 6 months-1 year before death and after start. Horses with high rates on dirt have a low (more negative) PC2 component score, whereas, horses with high rates on synthetic have a high PC2 component score.

Principal Component 3 (PC3) included rate variables for cumulative works, events, races, and furlongs 2 months to 1 year before death and after starting training on turf surfaces or on synthetic. It also included count variables for number of works, events, and races on turf. Animals with high rates on turf surfaces have more negative PC3 scores, whereas, animals with high rates on synthetic have more positive PC3 scores.

Principal Component 4 (PC4) contained primarily count variables describing an animals age (in days or years), number of career days, number of active days, number of layups, average number of days between works, total days in layup, percentage of career in layup, and number of furlongs raced. It also contained rate-variables describing 1 -8 months before death or after starting training on any surface or on dirt. Older animals, those with more layups, and more time between works have a more negative (lower) PC4 score. Younger animals and those with more works or events 1-8months after starting training or before death have a more positive (higher) PC4 score.

Principal Component 5 (PC5) contains rate-variables describing cumulative number of events, races, works, and furlongs 2months – 1year before death or after start on any surface, on dirt, or on synthetic. It separates animals based on the rates before death and after start. Animals with high rates after start will have a more negative PC5 score, and animals with a high rate before death will have a more positive PC5 score.

Figure 8.2 shows the component scores of PC1, PC2, and PC3 for all horses. Ideally, Affected and Control horses would have been distinctly separated when the components were plotted against each other, but, as shown in Figure 2, the PCA did not separate the groups. A majority of the Controls have  $PC1 < 0$ , indicating fewer cumulative events/furlongs after starting training and before death. A majority of Affected animals have  $PC1 > 0$ . The Affected group tended to have either more positive or more negative PC2 scores, indicating high rates on dirt or high rates on synthetic. The Control animals PC2 scores

were less extreme, indicating they either have lower cumulative rates on dirt & synthetic or the rates on dirt and synthetic are balanced. The plot of PC2 vs PC3 indicates that there are few severely negative PC3 scores, indicating that there were low cumulative rates on turf for all animals. This match with findings that indicate few animals in this study worked on turf. The cluster of affected with high PC2 & PC3 component scores (PC2, PC3 > 5) have high cumulative history on synthetic surfaces.

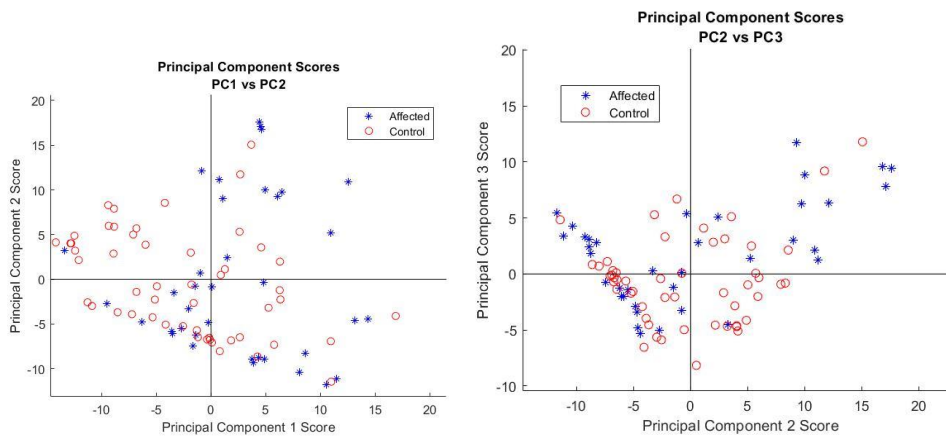


**Figure 8.2:** Left -Plots of PC1 vs PC2, Right – PC2 vs PC3. One outlier is not shown (affected animal, PC1 & PC2 > 20)

### 8.3 Classification & Regression Tree (CART) Analysis for Distinguishing Between Groups

Classification and Regression Tree (CART) analysis were performed with Group (Affected, Control) as the response variable and the exercise history variables as explanatory variables. The trees were developed using R’s statistical package “partykit” with the “ctree” function. Specifically, this R-package constructs conditional inference trees, a non-parametric class of regression tree, with a significance test ( $p=0.05$ ) to select predictor variables. CART analyses were performed for three reasons: 1) to determine which variables result in best classification of group category, 2) this type of analysis is robust to outliers,

unlike PCA or logistic regressions, and 3) it can handle missing data, and several horses did not have values for all variables.

Ten different CART analyses were performed. They analyses differ based on the potential explanatory variables that were used to predict Group membership and by the horses in the Control group (Table SA 8.4 & SA 8.5). The variable set that gave the highest accuracy was then performed to see if a CART could distinguish between Affected, Fracture-Controls, and Non-Fracture Controls when all horses were included (Group 1). These analyses were performed to determine 1) what variables best separate the Affected (PSB-fractured) and Control (no-PSB fracture) Groups, 2) if track surface information was needed to distinguish between Groups (Variable Input Sets A & B vs C), and 3) if the Control group used affected how Groups were classified (Groups 1-3).

**Table 8.4:** Variable Sets A, B, & C for CART Analysis.

	<b>Set A</b>	<b>Set B</b>	<b>Set C</b>
<b>Possible Explanatory Variables given to CART algorithm</b> (x = number of variables in Set)	All Variables (x = 350)	Only variables in first 5 PCA components  (x = 244)	Variables without surface type or condition information (x=149)

**Table 8.5:** Groups for CART Analysis. Note that Groups differ based on what horses were included in the Control set.

	<b>Group 1: All Animals</b>	<b>Group 2: Fracture Control</b>	<b>Group 3: Non-Fracture Controls</b>
<b>Control Group</b>	All Controls (n=57)	Fracture (non-PSB) only Control (n = 38)	No-Fracture in Controls (n=19)
<b>Affected Group</b>	All Affected (n=39)	All Affected (n=39)	All Affected (n=39)

The accuracy rates for each CART analysis is given in Table SA 8.6. Accuracy was defined as the percentage of true positives and true negatives (i.e., the percent of correctly classified animals). The misclassification percentage for each analysis is 100% - Accuracy. For variable Groups 2 & 3, classification accuracy did not depend on the variable Set used. For Group 1, the highest accuracy was achieved when all variables (Set A) was used. Overall, Group 2 had the lowest prediction accuracy – this could be because

the CART was trying to distinguish fracture types which could share an exercise causality. Groups 1 & 3 included non-fracture controls (i.e. soft tissue injury) which may have a different causal relationship to exercise history. Surface type did not seem to significantly increase accuracy – this could be because most animals in this study ran primarily on dirt and synthetic surfaces.

**Table SA 8.6:** CART Results for all Groups and All Variable Combinations.

<b>Possible Explanatory Variables</b>	Group 1	Group 2	Group 3
Set A- All Variables	80%	73%	79%
Set B - PCA Variables	79%	73%	79%
Set C – No Surface	73%	73%	79%

The 3 analyses run over Group 1 (all affected horses, all controls) with highest accuracy used all variables (Set A) as inputs – for 80% accuracy (20% misclassification). This model used 5 rate-variables to classify animals: cumulative number of events 6 months before death, cumulative number of races 10 months after starting training, cumulative number of works 2 months before death on synthetic, cumulative number of events 1 month before death on turf, and cumulative number of races 1 year after start on synthetic surfaces. The classification pathway used can be seen in Figure 8.3. The CART run with Group 1 & Set B, yielded a comparable accuracy to the one run over Group 1 & Set A. The only difference is that it did not use “events 1 month before death on turf” as a predictor – since this variable did not appear in the PCA. Few animals had events on turf, so using this events 1 month before death on turf as a predictor does not appear to greatly affect the results. If surface type information is removed (Group 1, Set C), the accuracy of the prediction drops by 8%; indicating that surface type information does add some value to predicting injury. The CART analysis run over all animals with no surface type information



had 72% accuracy (Group 1, Set C) and used cumulative number of events 6 months before death and cumulative number of races 10 months after start to separate animals.

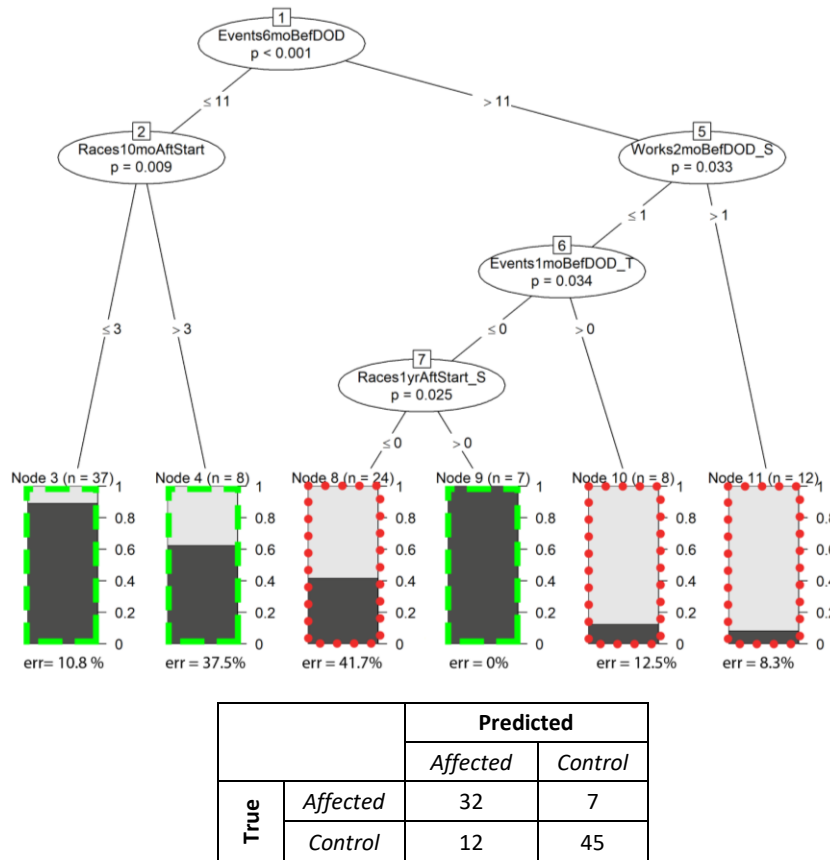
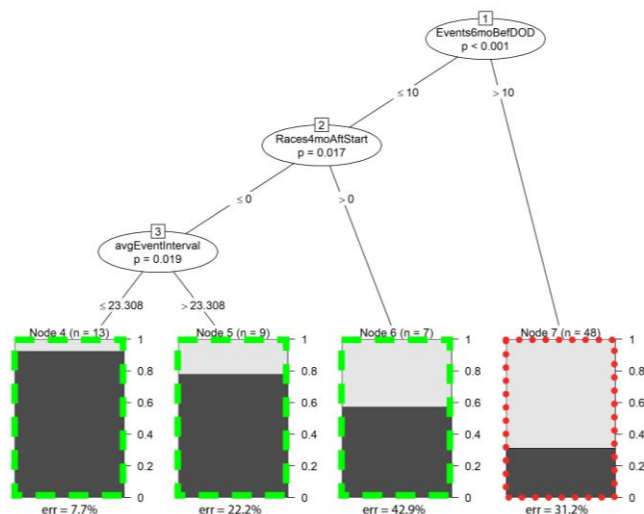


**Figure 8.3:** Top – CART for Group 1, Set A. Bar graphs show true identity of animals in terminal node (Dark Grey = True Control, Light Grey = True Affected). The green dashed box indicates Predicted Control animals, red circle border indicated Predicted Affected. Bottom – Classification Table showing 80% accuracy.

When Group 2 was used (only non-PSB fractures in control group); the CART accuracy is the same (at 73%) regardless of the explanatory variable set given (Sets A-C). In addition, the three classification variables used were the same regardless of variable set (A, B, or C). This analysis can be seen in Figure 8.4. The primary predictor for is the cumulative number of events 6 months before death. For all variable sets, all animals with less than 10 events six months before death are predicted “Controls.” The secondary predictors are number of races four months after start and the average interval (in days) between events; the secondary predictors are used to help refine which animals are considered controls.



		Predicted	
		Affected	Control
True	Affected	33	6
	Control	15	23

**Figure 8.4:** Top- CART for Group 2, Set A-C. Bar graphs show true identity of animals in terminal node (Dark Grey = True Control, Light Grey = True Affected). The green dashed box indicates Predicted Control animals, red circle border indicated Predicted Affected. Bottom- Classification Table showing 73% accuracy

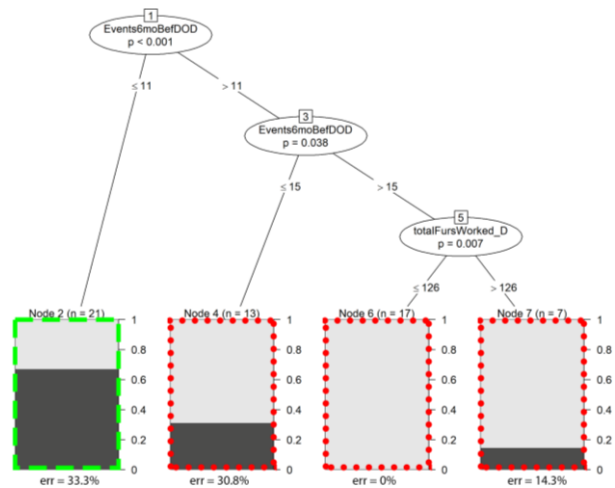
When Group 3 was used (no fractures in control group); the CART classification accuracy is 79% for all variables sets (A, B, & C). However, the variables sets used different secondary predictors. The primary predictor for all three is the cumulative number of events 6 months before death; in each tree, it was used for 2 successive nodes. The other predictor variables used are “Total Furlongs Worked on Dirt” (Set 1), “Peak 3 month furlong average 6 months after starting training” (Set 2), and “Days Between Previous Event and Death” (Set 3). The secondary predictors help to separate control from a majority of affected animals. The CART tree for Group 3, Set A is shown in Figure 8.5.

Since Set A (all variables), gave the highest overall accuracy, this Set was used to determine checked if a CART analysis could distinguish between Affected (PSB Fractures), Non-PSB Fracture Controls, and the Non-Fractured Controls. The results of the analysis is given in Figure 8.6; classification accuracy was 60.4%. Interestingly, the analysis sorted horses as Affected, Non-PSB Fracture Controls, and then Non-Fracture Controls in a sequential order down one branch based on variables relating to the amount of

work. Animals with higher amounts of work and fewer rest days between racing-speed events were more likely to be classified as “Affected”, followed by “Non-PSB Fractured Controls”, and then by a “Non-Fractured Controls.”

Overall, the CART analyses using Group 2 (only fractured controls) had the worst accuracy (73%) – this may be because the exercise variables that lead to bone fracture may be similar at various skeletal sites. Similar rate-type variables were chosen regardless of the control group used (Group 1-3). Ideally, more animals should be included in the analysis to gain a better understanding of how control group formulation changed CART analysis accuracy and variable selection.

In general, these CART results indicate that rate-variables, rather than count-variables, are more important in distinguishing group



		Predicted	
		Affected	Control
True	Affected	32	7
	Control	5	14

**Figure 8.5:** Top- CART for Group 3, Set A. Bar graphs show true identity of animals in terminal node (Dark Grey = True Control, Light Grey = True Affected). The green dashed box indicates Predicted Control animals, red circle border indicated Predicted Affected. Bottom- Classification Table indicating 79% accuracy.

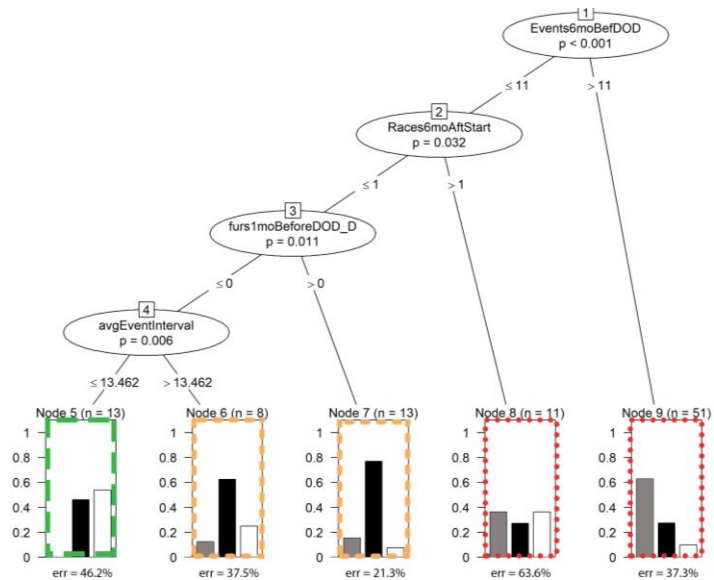


**Figure 8.6:** Top- CART Set A, All Animals. Bar graphs show true identity of animals in terminal node (Grey = Affected, Black = Non-PSB Fracture Controls, White = Non-Fractured Controls). The green dashed box indicates Predicted No Fracture Control animals, yellow dashed boarder indicated Predicted Fracture Controls, and red circle border indicates Predicted Affected

membership. In addition, a trend was seen that when rate variables had a higher magnitude (i.e., more intense exercise) Cart tended to predict horses as Affected. One variable was consistently selected for the first node (i.e., to do the initial affected or control prediction): cumulative number of events 6 months before death. If only this variable is used to predict group membership with CART, the prediction accuracy is 73% (27% misclassification rate). This indicates that the rate of events (all races and timed works) performed 6 months before injury is important in predicting injury.

The accuracy did not significantly drop when surface-type variables were excluded from possible predictors. However, a majority of horses ran on dirt and synthetic surfaces. If a wider range of exercise surface types had been examined, it is possible that the surface type variables would be more important since it has been shown that surface type is a risk factor for injury. Additionally, no surface condition variables were included in the CART analysis results.

#### **8.4 Descriptive Statistics of Study Groups**

The average, standard deviation, and other descriptive statistics are given for selected variables in the following section. Shapiro-Wilks Test for normality was run on all variables; for  $W\text{-score} \geq 0.90$  the variable was considered normally distributed. Normally distributed variables were then tested for equality of variance and run through a Pooled T-Test or Satterwaith T-test to check for significance between groups. Non-normally distributed variables had group distributions compared using the Wilcoxon T-Test. Variables with a 2-sided T-test p-value less than 0.05 are considered statistically significant. These analyses were performed in SAS. The results are given in Tables SA 8.7 – SA 8.9.

**Table SA-8.7:** Descriptive Statistics for Number of Events and Total Furlongs in Career based on Surface Type. Variables with an asterisk (\*) have significant difference between groups. Variable with a  $\psi$  are have a non-normal distribution.

	Group	Mean $\pm$ STD	(Min, Max)	Q1	Median	Q3	P-Value
<b>Number of Events*</b> , $\psi$	<b>Affected</b>	40.77 $\pm$ 29.39	(3, 153)	24.0	32.0	50.0	0.008
	<b>Control</b>	29.25 $\pm$ 29.24	(0, 150)	8.0	19.0	42.0	
<b>on Dirt</b> $\psi$	<b>Affected</b>	25.49 $\pm$ 24.99	(0, 102)	7.0	17.0	37.0	0.083
	<b>Control</b>	19.12 $\pm$ 22.85	(0, 103)	2.0	12.0	27.0	
<b>on Synthetic</b> $\psi$	<b>Affected</b>	12.31 $\pm$ 18.17	(0, 72)	0.0	5.0	17.0	0.489
	<b>Control</b>	8.96 $\pm$ 17.56	(0, 100)	0.0	3.0	8.0	
<b>on Turf*</b> , $\psi$	<b>Affected</b>	2.97 $\pm$ 9	(0, 56)	0.0	1.0	3.0	0.035
	<b>Control</b>	1.16 $\pm$ 2.66	(0, 13)	0.0	0.0	1.0	
<b>Total Event Furlongs*</b> , $\psi$	<b>Affected</b>	199.37 $\pm$ 151.36	(20, 743)	114.5	138.5	263.5	0.006
	<b>Control</b>	137.12 $\pm$ 146.19	(0, 700.5)	35.0	87.0	195.0	
<b>on Dirt</b> $\psi$	<b>Affected</b>	120.71 $\pm$ 126.56	(0, 519.5)	32.0	76.0	178.5	0.070
	<b>Control</b>	87.52 $\pm$ 112.64	(0, 532)	8.0	53.5	114.0	
<b>on Synthetic</b> $\psi$	<b>Affected</b>	58.45 $\pm$ 88.66	(0, 332)	0.0	17.0	83.0	0.555
	<b>Control</b>	41.11 $\pm$ 83.68	(0, 463.5)	0.0	9.0	38.0	
<b>on Turf*</b> , $\psi$	<b>Affected</b>	20.22 $\pm$ 53.11	(0, 324.5)	0.0	6.0	27.0	0.030
	<b>Control</b>	8.5 $\pm$ 20.59	(0, 107)	0.0	0.0	5.0	

**Table SA-8.8:** Descriptive Statistics for selected rate variables. Variables with an asterisk (\*) have significant difference between groups. Variable with a  $\psi$  are have a non-normal distribution.

	Group	Mean $\pm$ STD	(Min, Max)	First Quartile	Median	Third Quartile	P-Value
<b>Furlongs Per Event*</b>	<b>Affected</b>	4.81 $\pm$ 0.93	(3.19, 9.33)	4.4	4.8	5.1	0.004
	<b>Control</b>	4.27 $\pm$ 0.84	(1, 5.89)	3.7	4.4	4.8	
<b>Furlongs Raced Per Month Career*, <math>\psi</math></b>	<b>Affected</b>	3.51 $\pm$ 2.23	(0, 9.22)	1.9	4.0	5.2	0.002
	<b>Control</b>	2.13 $\pm$ 2.3	(0, 9.58)	0.0	1.4	3.9	
<b>Cumulative Number of Events 6 Months Before Date of Death*</b>	<b>Affected</b>	15.38 $\pm$ 5.48	(0, 23)	13.0	17.0	19.0	0.000
	<b>Control</b>	9 $\pm$ 5.99	(0, 22)	4.0	9.0	14.0	
<b>On Dirt*, <math>\psi</math></b>	<b>Affected</b>	9.46 $\pm$ 6.93	(0, 21)	2.0	10.0	16.0	0.015
	<b>Control</b>	6.09 $\pm$ 5.73	(0, 18)	0.0	4.0	11.0	
<b>On Synthetic <math>\psi</math></b>	<b>Affected</b>	4.82 $\pm$ 6.72	(0, 20)	0.0	0.0	10.0	0.322
	<b>Control</b>	2.56 $\pm$ 3.82	(0, 17)	0.0	0.0	5.0	
<b>On Turf*, <math>\psi</math></b>	<b>Affected</b>	1.1 $\pm$ 2.79	(0, 16)	0.0	0.0	1.0	0.041
	<b>Control</b>	0.35 $\pm$ 1.17	(0, 6)	0.0	0.0	0.0	
<b>Cumulative Number of Furlongs 1 Year After Start*</b>	<b>Affected</b>	110.37 $\pm$ 62.01	(11, 245.5)	55.0	116.0	142.5	0.004
	<b>Control</b>	74.78 $\pm$ 55.69	(0, 206)	30.0	64.5	112.0	
<b>On Dirt <math>\psi</math></b>	<b>Affected</b>	61.23 $\pm$ 53.37	(0, 180.5)	14.5	44.0	113.5	0.124
	<b>Control</b>	47.35 $\pm$ 50.07	(0, 206)	1.0	30.0	87.0	
<b>On Synthetic <math>\psi</math></b>	<b>Affected</b>	40.36 $\pm$ 59.97	(0, 226)	0.0	4.0	83.0	0.436
	<b>Control</b>	23.5 $\pm$ 37.26	(0, 175)	0.0	5.5	32.0	
<b>On Turf <math>\psi</math></b>	<b>Affected</b>	8.78 $\pm$ 17.59	(0, 93.5)	0.0	0.0	8.0	0.079
	<b>Control</b>	3.93 $\pm$ 9.87	(0, 54)	0.0	0.0	0.0	

**Table SA 8.9:** Univariate Odds Ratios for Selected Variables from Table SA 8.4-8.5

Variable Name	Univariate Odds Ratio	95% Confidence Interval for Odds Ratio	Standard Error in Mean, All Animals (n=96)
Number of Events	1.01	(0.99, 1.02)	3.03
on Turf	1.08	(0.94, 1.23)	0.62
Total Event Furlongs	1.00	(0.99, 1.00)	15.38
on Turf	1.01	(0.99, 1.02)	3.83
Furlongs Per Event	2.42	(1.23, 4.72)	0.10
Furlongs Raced Per Month Career	1.30	(1.07, 1.57)	0.24
Cumulative Number of Events 6 Months Before Death	1.21	(1.10, 1.31)	0.67
on Dirt	1.09	(1.01, 1.16)	0.66
on Turf	0.94	(0.93, 1.73)	0.21
Cumulative Furlongs 1 year After Start	1.01	(1.00, 1.01)	6.91